

University of Nottingham
UK | CHINA | MALAYSIA

Advanced Image Analysis to Characterise Coal and Predict Burnout Potential

by

Joseph A Perkins MSci

Thesis submitted to the University of Nottingham for the degree of

Engineering Doctorate

October 2019

Abstract

Despite a general decline in demand (from a gradual a shift towards renewable and lower carbon energy sources) pulverised coal-fired power generation remains one of the largest single contributors to global energy demands and as a key energy source for rapidly urbanizing and industrialising economies, coal will likely remain a major baseline contributor for the foreseeable future. With an increasing need to understand the consequences of fuel choice to maximise the return on shipments, meet stringent emission limits and minimise shut down time for fouling and slagging maintenance, the ability to predict the combustion performance of coals that are available on the market is valuable information to power generator, particularly coals with little documented burnout history. Image Analysis (IA) is a powerful tool that massively increases the amount of information that can be gathered during microscopic analysis. Whilst many of the behavioural aspects of coals can be 'seen' under an oil immersion and air objectives, there are very few techniques for collating this information together and the analysis of coal still relies heavily on manual analysis by trained operators.

This thesis describes the development and testing of a suite of rapidly implementable advanced image analysis techniques to accurately characterise coal samples, predict and classify combustion intermediates and simulate carbonaceous material burnout. The techniques described in this work can provide plant operators with key information about a fuel's potential for burning and can aid in monitoring the potential effects of stockpile weathering. With minimal or no input required from manual operators, these methods can improve the speed, repeatability and quality of information acquisition.

Acknowledgements

I'd like to thank the following people for all of their help and efforts throughout the course of my studies;

My academic supervisor Prof. Ed Lester, for his knowledge, patience, guidance and for always being forthcoming with opportunities and funds. I would also like to thank Dr Orla Williams for additional supervision, advice, help with publication writing and for her time proof reading this thesis.

BF2RA and the EPSRC for funding this work and the project industrial supervisors, Dr Connie Ellul and Peter Sage, for their support and guidance as the project progressed.

The CCSEFE Doctoral Training Centre and all the folks in the Chemical Engineering department for providing support and facilities to allow me to conduct this work.

Dr Silvie Koval and Graham O'Brien from CSIRO, for allowing me the opportunity to visit and to collaborate with them on their research and for encouraging and supporting my move down under.

My parents and sister, for supporting the decision to undertake this PhD and for everything they have done for me throughout my eight years at the University of Nottingham.

Finally, I'd like to thank all my friends and team mates for their encouragement and keeping me sane during my studies. You know who you are.

Table of Contents

List of Publications 13
CHAPTER 1. Thesis Introduction 15
1.1. Project Rationale, Aims and Significance 15
1.2. The Engineering Doctorate Scheme 17
1.3. Thesis Overview 17
CHAPTER 2. Literature Review 20
2.1. The Importance of Efficient Burnout and Fuel Testing 20
2.2. The Coal Power Generation Industry 21
2.2.1. Past, Present and Future 21
2.2.2. Availability of Fuel 22
2.2.3. Current and Proposed Technologies 22
2.2.4. Waste Product Utilization 23
2.3. Coal Structure and Reactivity 24
2.3.1. Organic Composition 24
2.3.2. Combustion Behaviour of Organic Material 25
2.3.2.1. Vitrinite 26
2.3.2.2. Inertinite 27
2.3.2.3. Liptinite 27
2.3.2.4. Microlithotypes 28
2.3.3. Inorganic Matter: Mineral Effects 28
2.3.4. Particle effects 29
2.3.5. Char Morphology and Reactivity 29
2.4. Image Analysis Techniques 30
2.4.1. Coal Petrography 30
2.4.2. The potential of Image Analysis 31
2.4.3. Char Characterisation 32
2.4.4. Individual Particle Analysis 33
2.5. Modelling Coal Combustion with Char Morphology 34
2.6. Applications: Coal Weathering and Combustion 38
CHAPTER 3. Laboratory Methodology 40
3.1. Coal Sample Preparation 40

3.1.1. Origin and selection of Samples 40
3.1.2. Milling and sieving 41
3.2. Coal Sample Characterisation 41
3.2.1. Proximate Analysis 41
3.2.2. Petrographic Characterisation 42
3.2.2.1. Sample block Preparation 42
3.2.2.2. The Microscope System, Mosaic Capture and Rank Analysis 42
3.2.2.3. Maceral Analysis 44
3.2.2.4. The Reactivity Assessment Program 44
3.3. Char Sample Preparation 45
3.3.1. The Drop Tube Furnace Rig 45
3.3.1.1. Input Gases, Heating Rate and Residence Time 47
3.3.1.2. Sample Feed and Collection 48
3.3.2. Char Generation: Drop Tube Furnace Experimental Conditions 51
3.3.2.1. Coal Pyrolysis Conditions 51
3.3.2.2. DTF Re-firing Experiments 51
3.3.2.3. Preparation of Artificially Oxidised Coal Samples 51
3.4. Char Characterisation 52
3.4.1. Microscopic Analysis 52
3.4.2.1. Char Block Preparation 52
3.4.2.2. Mosaic Capture and Morphological Characterisation 52
3.4.2. Intrinsic Reactivity Analysis 53
3.4.3. Loss-on-Ignition Test 53
3.5. Computer Hardware and Image Analysis Software 53
CHAPTER 4. Automated Image Analysis Techniques to Characterise Pulverised Coal Particles and Predict Combustion Char Morphology 54
4.1. Executive Summary 54
4.2. Journal Paper 56
CHAPTER 5. Automated Char Particle Analysis and Classification 65
5.1. Introduction 65
5.2. System Requirements & Approach 66
5.2.1. Stages of Analysis System Development 66
5.2.2. Pre-requisites of an automated char classification tool 67
5.3. Automated Analysis Method: Segmentation & Separation of Char Particles 69
5.3.1. Char Mosaic Segmentation 69

5.3.2. Individual Char Particle Separation....72
5.3.2.1. Char Boundary Identification....74
5.3.2.2. Char Particle Identification and Separation....79
5.4. Automated Analysis Method: Char Analysis & Classification Criteria Determination....80
5.4.1. Classification Criteria Approach....80
5.4.2. Particle Porosity....81
5.4.3. Pore Distribution....84
5.4.4. Char wall thickness distribution: 'The Pacman Function'....86
5.4.4.1. The Pacman Classification Function....86
5.4.4.2. Differentiating sphere structures....88
5.4.4.3. Differentiating network structures....89
5.4.4.4. Determining the presence of mixed structures....91
5.4.5. Char classification criteria Summarised: Logic Tree....93
5.4.6. Test Set Classification Results....95
5.5. Section 3: Comparison of Automated and Manual Analysis Results....96
5.6. Conclusions....103
CHAPTER 6. Development of an Image-Based Char Burnout Simulation: "The Pacman Model"....105
6.1. Model Design....106
6.1.1. Overview....106
6.1.2. Advantages of an Image Based Burnout Model....109
6.1.3. Approach to Development....109
6.1.4. Considerations....111
6.2. Development of the Pacman Burnout Simulation....112
6.2.1. Coal Samples for Testing and Development....112
6.2.2. Char Samples Generated in Drop-Tube Furnace....114
6.2.3. Determining Initial Internal Energy Weights....115
6.3. Initial Testing Results & Refinement of Model....124
6.3.1. Initial Simulation Results....124
6.3.2. Model Refinement....128
6.3.2.1. Char morphology dependant settings....128
6.3.2.2. Dynamic continuity factor....128
6.4. Revised Model Results....129
6.4.1. Additional Information for Power Generators....132

6.4.1.1. Implementation on whole char mosaics 132
6.4.1.2. Char Morphology Distributions 134
6.5. Conclusions 140
CHAPTER 7. Using Advanced Image Analysis Techniques to Predict and Detect Variations in Char Structure and Reactivity as a Result of Coal Oxidation 141
7.1. The Effect of Oxidation on Coal Properties 143
7.1.1. Oxidation and Proximate Composition 143
7.1.2. Oxidation and Vitrinite Reflectance 146
7.1.3. Oxidation and Maceral Composition 147
7.2. The Effect of Oxidation on Char Properties 154
7.2.1. Oxidation and Char Morphology 154
7.2.2. Predicted Char Morphology 159
7.2.3. Oxidation and Intrinsic Reactivity 164
7.3. Predicted Char Burnout 166
7.4. Conclusions 170
CHAPTER 8. Conclusions and Future Work 173
8.1 Research Summary 173
8.1.1. Automated Maceral Classification 173
8.1.2. Char Morphology Prediction 173
8.1.3. Automated Char Analysis and Char Classification 174
8.1.4. Char Burnout Simulations 174
8.1.5. Implementing Image Analysis Techniques 174
8.2. Future Work 175
References 176
Appendix A. Journal Paper Supplemental Data 184
Appendix B. Automated Char Analysis Data 198
Appendix C. Burnout Simulation Profiles 215

List of Figures

Figure 2.1 - ICCP morphologies. 30

Figure 2.2 - Evolutions of the effectiveness factor (η) of a char 36

Figure 3.1 - Zeiss Imager M1 microscope setup 43

Figure 3.2 - 50x Oil immersion objective and sample on automated sample stage 43

Figure 3.3 - Automated image capture 44

Figure 3.4 - Drop Tube Furnace (DTF) rig for preparation of char samples 46

Figure 3.5 - DTF Schematic 48

Figure 3.6 - Drop-tube screw feeder apparatus 49

Figure 3.7 - Cyclone device used to separate char particles 50

Figure 5.1 - Examples of common fractured char structures 68

Figure 5.2 - Examples of overlapping/touching char particles 68

Figure 5.3 - Flow diagram outlining char analysis system approach 69

Figure 5.4 - Visualization of Otsu's thresholding method 70

Figure 5.5 - Char mosaics illustrating implementation of Otsu's algorithm 72

Figure 5.6 - Illustration of closing function distortion 74

Figure 5.7 - Individual char separation process 75

Figure 5.8 - Migration of active contour from convex hull starting position 77

Figure 5.9 - How manipulation of the continuity factor impacts contour location 78

Figure 5.10 - How manipulation of the smoothness factor impacts contour location 78

Figure 5.11 - Using active contour perimeter detection to determine porosity 82

Figure 5.12 - Porosity distributions of the different test char morphologies. 83

Figure 5.13 - Visualisation of 'over-mend' function on sphere and network. 85

Figure 5.14 - How application of the 'over-mend' function affects morphologies 86

Figure 5.15 - Determination of the initial char particle boundary. 88

Figure 5.16 - Pacman erosion profiles of Tenui- and Crassi- network chars 90
Figure 5.17 - Comparison between the Pacman erosion profiles 92
Figure 5.18 - A logic tree constructed to categorise char into ICCP morphologies 94
Figure 5.19 - Average Pacman erosion profiles for each test char morphology.....94
Figure 5.20a-c - Comparison between manual/automated classification results 1.....98
Figure 5.21a-f - Comparison between manual/automated classification results 2. ...102
Figure 6.1 - Visualisation of combustion front location and erosion process 107
Figure 6.2 - Impact of varying user-defined inputs on pore penetration 108
Figure 6.3 - Relationship between continuity factor and burnout of tenuispheres ...117
Figure 6.4 - Relationship between continuity factor and burnout of crassispheres ..117
Figure 6.5 - Relationship between continuity factor and burnout of tenuinetworks .118
Figure 6.6 - Relationship between continuity factor and burnout of crassinetworks 118
Figure 6.7 - Relationship between continuity factor and burnout of mixed chars.....119
Figure 6.8 - Relationship between continuity factor and burnout of solid chars.....119
Figure 6.9 - Relationship between char Morphology and erosion rates 121
Figure 6.10 - Relationship between the simulated erosions of real char images.....123
Figure 6.11 - Correlation between manual and inial predicted burnouts.....126
Figure 6.12 - Correlation between manual and revised predicted burnouts 131
Figure 6.13 - Comparison of the simulated whole mosaic burnouts 133
Figure 6.14 - Predicted carboneous material distribution for Australian sample 1 ...135
Figure 6.15 - Predicted carboneous material distribution for Australian sample 2 ...136
Figure 6.16 - Predicted carboneous material distribution for Australian sample 3 ...137
Figure 6.17 - Predicted carboneous material distribution for Australian sample 4 ...138
Figure 6.18 - Predicted carboneous material distribution for Australian sample 5 ...139
Figure 7.1 - The effect of oxidation temperature on fuel ratio 146

Figure 7.2 - Correlation between manually and automated maceral distributions 149
Figure 7.3 - Cumulative greyscale distribution curves for Bentinck coal 152
Figure 7.4 - Cumulative greyscale distribution curves for La Jagua coal 152
Figure 7.5 - Cumulative greyscale distribution curves for Fila Mistra coal 153
Figure 7.6 - Cumulative greyscale distribution curves for Klein Kopje coal 153
Figure 7.7 - Cumulative greyscale distribution curves for Trans Natal coal 154
Figure 7.8 - Comparison between manual/automated classification Fila Mistra.....156
Figure 7.9 - Comparison between manual/automated classification La Jagua.....156
Figure 7.10 - Comparison between manual/automated classification Bentinck.....157
Figure 7.11 - Comparison between manual/automated classification Klein Kopje...157
Figure 7.12 - Comparison between manual/automated classification Trans Natal ...158
Figure 7.13 - Comparison between manual/predicted classification La Jagua.....161
Figure 7.14 - Comparison between manual/predicted classification Bentinck.....162
Figure 7.15 - Comparison between manual/predicted classification Fila Mistra 162
Figure 7.16 - Comparison between manual/predicted classification Klein Kopje 163
Figure 7.17 - Comparison between manual/predicted classification Trans Natal 163
Figure 7.18 - Relationship between oxidation and burnout temperature.....165
Figure 7.19 - Relationship between oxidising temp and burnout Bentinck.....168
Figure 7.20 - Relationship between oxidising temp and burnout La Jagua.....168
Figure 7.21 - Relationship between oxidising temp and burnout Fila Mistra 169
Figure 7.22 - Relationship between oxidising temp and burnout Trans Natal 169
Figure 7.23 - Relationship between oxidising temp and burnout Klein Kopje 170

List of Tables

Table 2.1 - Maceral groups and macerals in coal and their origins 26

Table 5.1 - Distribution of material removed by Pacman erosion for test particles 89

Table 5.2 - Test char set automated classification results.....95

Table 5.3 - Comparison of automated and manual char classifications coal set 1 96

Table 5.4 - Comparison of automated and manual char classifications coal set 2. 99

Table 6.1 - Australian coal sample details 113

Table 6.2 - International coal samples details.....114

Table 6.3 - Manual classification of Australian char samples 114

Table 6.4 - Manual classification of International char samples 115

Table 6.5 - Comparison between char refire results and initial predicted burnout....125

Table 6.6 - Comparison between refire and initial predicted burnout Australian 130

Table 6.7 - Comparison between refire and initial predicted burnout international. .130

Table 7.1 - Compositional details of coal set 3.....143

Table 7.2 - Proximate analysis results for the oxidation coals 145

Table 7.3 - Rank values with changing oxidation temperature 147

Table 7.4 - Manual maceral analysis 148

Table 7.5 - % Unreactives for the oxidised coals 150

Table 7.6 - Intrinsic reactivity values 165

List of Equations

Equation 5.1 - Otsu's algorithm……....70

Equation 5.2 - Parametric representation of active contour location…….77

Equation 5.3 - Active contour energy minimisation general formula……77

Equation 5.4 - Active contour internal energy equation……78

Equation 5.5 - Active contour external energy equation……...79

Equation 6.1 - Active contour overall model…….....106

Equation 6.2 - Applied force equation for active contour……106

Equation 6.3 - Thiele's modulus equation.....111

Equation 6.4 - Char effectiveness factor calculation……...111

Equation 6.5 - Combustion front internal energy equation…….116

Equation 6.6 - Kinetic constant calculation…….122

Equation 6.7 - Stoichiometric factor calculation…….122

Equation 6.8 - Visualisation of 2-stage Pacman erosion model……...124

Nomenclature

Notation	Description
A_c	Carbonaceous specific surface area (m^2/kg)
$D_{O_2}^e$	Effective diffusivity of oxygen within particle (m^2/s)
E_{con}	Image constraint forces (dimensionless)
$E_{contour}^*$	Minimised active contour energy (dimensionless)
E_{edge}	External edge energy (dimensionless)
$E_{external}$	Overall image defined external energy (dimensionless)
E_{image}	Spline energy (dimensionless)
$E_{internal}$	Internal user defined contour energy (dimensionless)
E_{line}	External line energy (dimensionless)
$F_{contour}$	Force applied to active contour (dimensionless)
k_s	Kinetic constant (m/s)
n	Number of active contour iterations
R_g	Gas constant (J/mol·K)
R_p	Particle radius (m)
t	Time (s)
(t)	Otsu's threshold (dimensionless)
T	Temperature (K)
$v(s)$	Active contour position (dimensionless)
α	Active contour continuity factor (dimensionless)
β	Active contour smoothness factor (dimensionless)
Λ	Molar stoichiometric factor, $mol^{-}C/mol^{-}O_2$
η	Particle effectiveness factor (dimensionless)
ρ_c	Density of carbonaceous particle material (kg/m^3)
σ_0^2	Class variance 0 (dimensionless)
σ_1^2	Class variance 1 (dimensionless)
$\sigma_\omega^2(t)$	Minimised interclass variance (dimensionless)
τ	Molar ratio CO/CO_2
Φ	Particle Thiele modulus (dimensionless)
ω_0	Class probability 0 (dimensionless)
ω_1	Class probability 1 (dimensionless)
ω_{edge}	User defined edge weight (dimensionless)
ω_{line}	User defined line weight (dimensionless)

List of Publications

Journal Publications

Lester, E., Avila, C., Pang, C. H., Williams, O., Perkins, J., Gaddipatti, S., Tucker, G., Barraza, J. M., Trujillo-Uribe, M. P. and Wu, T., *A proposed biomass char classification system*. Fuel. 232 (2018): 845-854

Perkins, J., Williams, O., Wu, T., and Lester, E., *Automated image analysis techniques to characterise pulverised coal particles and predict combustion char morphology*. Fuel 259 (2019).

Lester, E., Perkins, J., Cloke, M., Bailey, J., *Using Advanced Image Analysis Techniques to Predict and Detect Variations in Char Structure and Reactivity as a Result of Coal Oxidation*. Fuel. (2019) **- In preparation**

Orla Williams, Patrick Daley, Joseph Perkins, Shoaib Shah, Edward García Saavedra, Maria Trujillo Uribe, Juan Barraza Burgos, Carlos Julio Espitia, Maribel Barajas, Juan Sebastian Saltern, Ed Lester *The Forensic Thermal Thermometer: Applying Petrographic Techniques to Evaluate the Thermal History and Performance of Stoker Furnaces.* - **In preparation**

Conference Proceedings

Lester, E., Huddle, T., Wu, T., Perkins, J., (2015). Advanced Coal Characterisation Using Image Analysis. In: International Conference on Coal Science & Technology /ACSE 2015

Perkins, J., Lester, E., (2016). *Microscopic characterisation of a range of carbon-based materials.* In: 11th European Conference on Coal Research and Its Applications (ECCRIA 2016).

Perkins, J., Lester, E., (2017). *Advanced Coal Characterization to Predict Char Morphology*. In: International Conference on Coal Science & Technology/ACSE 2017

Perkins, J., Lester, E., (2018). *Using Advanced Image Analysis to Predict Coal Char Morphology, Structure and Burnout Behaviour*. In: 12th European Conference on Coal Research and Its Applications (ECCRIA 2018).

CHAPTER 1. Thesis Introduction

1.1. Project Rationale, Aims and Significance

Despite a general decline in demand (mainly across Europe) over the last decade, coal is still used extensively to meet over a quarter of global power generation demands and a key energy source for rapidly urbanizing and industrializing economies (IE.Agency, 2017). As such, coal will remain a major baseline contributor to power generation for the foreseeable future during the transition of the energy mix towards more low carbon energy sources (C.E.S.A.C, 2003). In optimising coal combustion for power generation and emission targets, generators increasingly need to understand the consequences of fuel choice to maximise the return on shipments, meet stringent NOx and SOx limits (European.Union, 2008), and minimise shut down time for fouling and slagging maintenance, whilst maximising the potential for ash sales (Jayaranjan, van Hullebusch, & Annachhatre, 2014). Thus, the ability to rapidly characterise potential fuels, stockpiles and predict how the combustion performance of coals that are available on the market is valuable information to power generator, particularly coals with little documented burnout history.

The prediction of coal combustion performance has been attempted via several approaches over the years. Laboratory techniques include the use of characterisation techniques of physical properties (rank, volatile matter, fuel ratio, intrinsic reactivity, particle size and distribution) and rely heavily on manual analysis and interpretation of trained operators (Avila, Pang, Wu, & Lester, 2011; Cloke, Lester, & Belghazi, 2002; Wells & Smoot, 1991). As a result, analysis is both slow and variable. (Bustin, 1991). Currently, there are no techniques for collating all these parameters together into automated, rapidly implementable analysis techniques, most likely due to the

heterogeneous structure of coal, the complexity of maceral reactivity and performance dependence on coal origin and combustion process variables and conditions (Cloke, Lester, & Gibb, 1997; E. Lester & Cloke, 1999). Many of these original coal characteristics are measurable using rapid and automatable image analysis (IA) techniques (Chao, Minkin, & Thompson, 1982; David & Fermont, 1993; Riepe & Steller, 1984). The potential of IA as a characterisation tool has advanced rapidly in recent years with the development of camera technology, computer processing power and IA software capabilities. IA is already being used to characterise the coking potential of coal on a particle by particle basis (Comino, Warren, & O'Brien, 2010; O'Brien, Jenkins, Ofori, & Ferguson, 2007).

With recent advances in IA, where process variables are assumed to be constant, automated coal characterisation, daughter char morphology prediction and the development of image-based burnout simulations should be possible. An automated IA method would present several advantages over manual and semi-automated techniques (Cloke et al., 1997; Cloke, Lester, & Thompson, 2002). Point counting manual petrographic analysis has remained popular due to the reliability and precision that results from a well-standardised method albeit labour and time intensive, with substantial allowable % error (Institution, 1981, 1982). A suite of fully automated coal characterisation and burnout simulation techniques has the potential to be more repeatable and faster analytical processes (O'Brien et al., 2007).

More specifically this project will develop several novel image analysis methods to rapidly characterise fuels to predict boiler performance. Fully automated tools will be able to provide plant operators with key information about a fuels potential for burning that enables power generators to understand the consequences of fuel choices (Cloke et al., 1997; Cloke, Wu, Barranco, & Lester, 2003).

1.2. The Engineering Doctorate Scheme

This research project forms part of a collaboration between the EPSRC Centre for Doctoral Training in Carbon Capture and Storage and Cleaner Fossil Energy, the Energy and Sustainability Research Division (Faculty of Engineering) at the University of Nottingham and the Biomass and Fossil Fuel Research Alliance (BF2RA). The project is co-funded between the Engineering and Physical Sciences Research Council (EPSRC) and BF2RA as the industrial partner. BF2RA consists of several industrial partners including British Sugar, Doosan Power Systems, Drax Group plc, EDF Energy plc, Electric Power Research Institute (EPRI) and Lynemouth Power and its research interests represent a broad range of biomass and fossil fuel topics targeted to meet industry needs and priorities.

1.3. Thesis Overview

This thesis consists of a further 7 Chapters split into 3 sections. Part I (Chapters 2-3) details the current literature review and research methodology respectively. Part II (Chapters 4-7) presents the results from the experimental investigations and Part III (Chapter 8) consists of the conclusions and recommendations for future work. The Chapters can be summarised as follows;

Chapter 2 - This Chapter provides the literary review and background study of the fundamental aspects of the image analysis of pulverised fuel (p.f.) coal.

Chapter 3 - This Chapter details the experimental methodology used to address the aims and objectives of this thesis and includes a detailed overview of the coal samples

used in the study, the generation of daughter char particles and the various laboratory and imaging techniques employed during characterisation.

Chapter 4 - A new automated image analysis system that analyses individual coal particles to predict daughter char morphology is presented in this Chapter. This work was published in Fuel in September 2019. (Perkins et al. 2020). This Chapter consists of an executive summary and the journal paper manuscript.

Chapter 5 - This Chapter describes the development of an automated, 1-click, image analysis system that aims to extract, separate and analyse individual char particles and classify each into one of six ICCP char morphological categories. This information can then enable researchers to use char burnout models to determine the burnout potential of different coal fuels.

Chapter 6 - This Chapter describes the development of a novel, image-based char burnout simulation to rapidly predict the burnout potential of a fuel during pulverised fuel combustion. The model, coined the 'Pacman Burnout Model', iteratively erodes individual char particles to simulate carboneous material oxidation. Being devoid of any complex kinetic calculations and generalisations surrounding particle structure and porosity distribution, this method is a relatively simple and robust tool for power generators.

Chapter 7 - This Chapter describes the analysis of 5 artificially oxidised coals and their daughter chars using traditional laboratory techniques (proximate analysis, calorific content, manual maceral composition, rank, manual char characterisation) and the image analysis techniques discussed in Chapters 4,5 and 6 to both validate and investigate the suitability of using these methods as potential tools for power generators to detect subtle changes in coal properties that may impact coal combustion potential.

Chapter 8 - This short Chapter summarises the observations and conclusions from Chapters 4 to 8, along with recommendations for future work.

CHAPTER 2. Literature Review

2.1. The Importance of Efficient Burnout and Fuel Testing

Pulverised coal fuel combustion is used widely in power plants for the generation of electricity and as of 2018, accounts for approximately 40% of the global electricity production (IEA, 2018). Conventional steam PCC technology has a maximum efficiency of approximately 35%, whilst recently developed supercritical and ultra-supercritical coal-fired technologies that produce steam at higher temperatures and pressure have recorded efficiencies of up to 45% (IEA, 2008). Plant technologies aside, the eventual efficiency level that can be achieved depends on both the type and on the quality of coal fuel used (Cloke et al., 1997).

An increase in efficiency reduces upfront fuel costs and emissions and therefore minimizes carbon levies associated with CO2 release. As a result, the selection and testing of coal samples prior to burning is vital to the efficient generation of electricity (Jones, Morley, & McCourt, 2019; Perkins, Williams, Wu, & Lester, 2020; T. Wu, Lester, & Cloke, 2006a). Where coals are to be obtained from many different sources and subjected to lengthy transportation and storage periods this may become difficult as coal quality may vary significantly over time despite originating from the same source (M. M. Wu, Robbins, Winschel, & Burke, 1988). These variations can dramatically affect a fuel's performance during electricity production (Margaretha Bengtsson, 1987). Any electricity generator investigating coals from different countries will need to know how a coal will burn and if and when the supply changes, therefore the ability to quickly and accurately determine a coals chemical composition and estimate its burnout potential is a vital tool for generators.

2.2. The Coal Power Generation Industry

2.2.1. Past, Present and Future

In terms of availability and market stability, coal has been the cheapest and most reliable source of energy worldwide for many decades, with operational costs of a conventional coal plant being approximately 50% cheaper than combined cycle gas plants (IEA, 2018; Y. Zhang et al., 2009). However, coal produces far higher amounts of carbon emissions than any other generation fuel with sub-bituminous coal producing on average 97 kg of CO2 per million British thermal units (Btu) versus only 53 kg for natural gas (Rubin, Chen, & Rao, 2007). In recent years, in response to increasing awareness of global warming and the influence of carbon dioxide on rising global temperatures, a carbon tax has been introduced by many countries in an attempt to hold generators responsible for what has been dubbed the 'social cost of carbon' (Ricke, Drouet, Caldeira, & Tavoni, 2018). The tax per kilo Watt hour (kWh) is dependent on the thermal efficiency of each power plant and therefore varies greatly, however it is estimated that the SCC for coal is approximately twice that of natural gas (Metcalf., 2009).

After a dip in coal power usage in the 1990s as a result of the first 'dash for gas', the assurgency of China as a global industrial power has been almost solely responsible for a resurgence in coal fired power since 2000, with the construction of capacity comparable to the entire UK power grid each year in order to meet exponentially growing energy demands. It is estimated that coal demand in China is projected to peak by 2020 and fall back to 2010 levels by 2030. This is driven in part by industrial restructuring, as China progressively shifts from an economic model based on industry and investment to domestic consumption and services (IEA, 2015).

Despite the UK's government announcement that all coal-fired power will close by 2025, with rapidly developing economies like India and China, it is clear that coal-fired electricity generation will remain a substantial fraction of the global energy mix for many years to come, underlining the need to continually invest in methods to improve efficiencies and reduce the impact of social cost with advanced fuel testing methods for energy generators.

2.2.2. Availability of Fuel

One of the main driving forces behind coal remaining a staple component of the global energy market is its relative abundance and easy accessibility compared to other fuels, with most coal consumed domestically and only 15% is traded internationally (BP, 2016). Most environmental agencies agree that there is approximately 120 years of proven global coal supply at current production rates, more than that of oil and gas reserve combined. Coal reserves are recoverable in over 80 countries, whereas over 50% of the world's gas and oil reserves are located in Russia and the Middle East (IEA, 2015). This global abundance, whilst beneficial economically, does also present challenges for providers as composition and burnout behaviour vary massively depending on origin and underlines importance of testing prior to purchase.

2.2.3. Current and Proposed Technologies

Largely, coal is burned around the world in a thermal power station boiler where the heat released is converted to electric power via high pressure steam driven turbines.

The loss of energy through the cooling of this steam limits coal efficiency to 30-40% (Canada, 2004). Recently developed supercritical systems have demonstrated efficiencies up to 10% higher (D. Zhang, 2013). Supercritical technology uses less coal per unit of power production in comparison with subcritical coal technologies and thus results in lower pollution levels. Individual 'cleaner' coal combustion technologies, such as flue gas desulphurisation (FGD) and low-NO_X burners can be retrofitted to existing conventional plants to reduce emissions of SO_2 and NO_x (Nihalani, Mishra, & Juremalani, 2018). Another proposed technological approach to achieving lower environmental impact is via carbon capture and storage, a process where carbon dioxide is collected before release and transporting it in super critical form to a storage site, normally an underground geological formation, where it cannot not enter the atmosphere. Capturing strategies include carbon scrubbing with amines and membrane gas separation. However, the capture and compression of CO_2 increases the energy needs of a coal-fired Carbon capture and storage (CCS) plant by an estimated 25–40% (Metz, Davidson, de Coninck, Loos, & Meyer, 2005). Whilst carbon capture and storage presents a viable carbon mitigating option for the continued use of coal as an energy source, widespread use of CSS is currently not implementable economically. Until such a time, improving plant efficiencies and consequently reducing carbon emissions with the likes of advanced fuel characterization such as image analysis is a more immediate method.

2.2.4. Waste Product Utilization

Coal power has a unique advantage over many other power generation methods as much of the waste ash product from combustion, depending on its quality, can be sold which

incentivises its continued use as an energy source. Approximately 50% of pulverised fuel ash (PFA) produced is used in the production of plasterboard, concrete and cement substitutes (Bhattacharjee & Kandpal, 2002). Strict standards govern the level of combustible carbon in ash material which can be present in many of the end products (Ahmaruzzaman, 2010) and it is therefore often beneficial to ensure that, the sale of waste ash is maximised by reducing the unburnt carbon content (by improving thermal efficiency) with accurate fuel characterisation prior to purchase.

2.3. Coal Structure and Reactivity

2.3.1. Organic Composition

Coal formation, commonly referred to as coalification, involves the physical and chemical transformation from peat organic matter to graphite via lignite, bituminous coal and anthracitic coal intermediates. In general, the degree of coalification (percentage of fixed carbon) is denoted as the coal rank and is marked by a progressive decrease in moisture and volatile functional groups with a consequent increase in the carbon content of the coal (Chandra, 1982; Smoot, 1993; Stach & Murchison, 1982). Coal has been described as “analogous to a fruitcake, formed initially as a mixture of diverse ingredients, then "baked" to a product that is visibly heterogeneous” with the different constituents consisting of microscopically distinguishable, physically and structurally distinctive, chemically different macerals (organic) and minerals (inorganic) (Smith, Neavel, Hippo, & Miller, 1981). In polished sections under the microscope, macerals are identified based on their optical properties; reflectance, degree of destruction/preservation of original material and morphological structures. Universal acceptance is given to the ICCP classification and redefinition of macerals

into vitrinite, liptinite, and inertinite categories, with there being many maceral subdivisions (ICCP, 2001; Stach & Murchison, 1982).

2.3.2. Combustion Behaviour of Organic Material

Coal will begin to combust above 300°C (Smoot, 1993). Pyrolysis is the first part of coal combustion, followed by char burnout. The combustion pathway of bituminous coals can be represented in four steps; (1) The gases from pyrolysis form a flame front around the particle, (2) these gases are then burnt leaving behind a char intermediate particle, (3) Ignition of the char and (4) char combustion follow to complete combustion leaving non-combustible ash waste product (Margaretha Bengtsson, 1987; T. Wu, Lester, & Cloke, 2006b). The types of char formed, and combustion in general, can depend on the petrographic composition of the fuel from the percentage and type of macerals present, the more reactive liptinite and vitrinite macerals will generally produce thinner combustion intermediates that burn more efficiently than those derived from inertinite (Nandi, Brown, & Lee, 1977; P., 2016; T. Wu et al., 2006b). Table 2.1 shows common macerals and microlithotypes groupings. The emphasis of rank when making informed fuel choices is due to it being particularly influential in deciding coal combustion burnout efficiency, with increasing reflectance corresponding to a decrease in reactivity of the maceral groups (E. Lester & Cloke, 1999).

Table 2.1 - Maceral groups and macerals in subbituminous, bituminous. and anthracitic coals, and their origins (Stach & Murchison, 1982)

Macerals		Origin
Group	**Maceral**	
Vitrinite	Telinite	Plant cell walls (with visible structure)
	Collotelinite	Plant cell walls (gelified, structureless)
	Vitrodetrinite	Small particles of plant attritus
	Collodetrinite	Mottled peat groundmass
	Corpogelinite	Primary and secondary cell infillings from humic gels
	Gelinite	Amorphous humic matter in crack fillings
Liptinite	Sporinite	Outer cell walls of plant spores and pollen
	Cutinite	Outer coatings of leaves, roots, stems
	Suberinite	Degraded cell walls of bark and roots
	Resinite	Plant resins, balsams, latexes, fats and waxes
	Alginite	Algae
	Bituminite	Amorphous fluorescent material of either algal or bacterial origin
	Fluorinite	Secondary crack-filling material from oil generation
	Liptodetrinite	Fragments of degradation residues of liptinites
Inertinite	Fusinite	Carbonized plant cell walls
	Semifusinite	Partly humified and dehydrated plant tissues
	Funginite	Fungal spores and other tissues
	Secretinite	Possible oxidation product of resins
	Macrinite	Dehydrated small, clumped peat matrix substances
	Inertodetrinite	Tiny, carbonized inertinite precursors
	Micrinite	Secondary coalification residues of liptinitic substances

2.3.2.1. Vitrinite

Vitrinite is derived from the cell-wall material or woody tissue of the plants from which coal was formed. Chemically, it is composed of polymers, cellulose and lignin. It is the maceral most influenced by changes in rank (N. Oka et al., 1987) and so can produce several different char 'types' (Cloke, Lester, & Belghazi, 2002; Cloke et al., 1997).

Vitrinite found in the lowest coal ranks are the most reactive in combustion with ignition and burnout occurring at the lowest temperatures, however it has been shown that low rank coals may produce thick walled chars whereas high ranked coals may produce thin walled chars (Lester, 1999). Existing predictive combustion image analysis methods have focused on characterizing coals by rank (Benfell et al., 2000; Su, Pohl, Holcombe, & Hart, 2001) and will provide an ideal starting point for development of comprehensive fuel analysis methods.

2.3.2.2. Inertinite

Inertinite is derived from oxidized organic material or fossilized charcoal. It is the maceral with the highest reflectance, carbon ratio and degree of aromaticity and the lowest hydrogen and volatile yield. (Chandra, 1982; Stach & Murchison, 1982). Despite this, it has been shown that inertinite is capable of swelling during combustion (Thomas, 1989), but manages to retain its original structure for longer than liptinite and vitrinite (M. Bengtsson, 1986). However, high rank inertinite is much less likely to be affected during pyrolysis due to its structural 'inertness' and low quantities of volatile matter (N. M. Oka, T.; Matsuoka, H.; Yamada, S.; Yamada, T.; Shinozaki, S.; Shibaoka, M.; Thomas, , 1987).

2.3.2.3. Liptinite

Liptinite is generally a minor component in bituminous coals and was formed from spores, pollen, plant resin and waxes. It has the highest volatile yield, lowest reflection and generally contains more aliphatic groups that vitrinite and inertinite. The structure and behaviour of liptinite is well known and there is little doubt concerning its nature

(Crelling, 2008), so liptinite is generally accepted as useful in obtaining flame stability (Bustin, 1991; E. Lester, Allen, Cloke, & J. Miles, 1994; N. Oka et al., 1987).

2.3.2.4. Microlithotypes

Microlithotypes are the natural groupings and collections of macerals at the microscopic level (some examples are shown in table 2.1) and are defined as having a minimum band width of 50 μm and as containing at least 5% of a maceral group (Suárez-Ruiz & Ward, 2008). The chemical properties of microlithotypes are very similar to those of the predominating macerals however their physical properties are related not only to those of the macerals but also to the combined effect of the association (Stach et al, 1982). Coals rich in vitrinite rich Microlithotypes (i.e. Vitrites and Clarites) have been found to produce low density chars with reduced combustion times (Bailey, 1990) but poorer combustion properties have been observed when there is greater association with inertinite fragments (Nandi et al., 1977). Hence particles which are made up of macerals which can freely swell during pyrolysis, without the restriction of non-swelling macerals, are much more likely to form chars which have a high surface area with large surface pores. (Benfell et al., 2000; Michele, Riccardi, & Lopez-Doriga, 1994).

2.3.3. Inorganic Matter: Mineral Effects

Mineral content in coal usually occurs as single crystals or as clusters that are intermixed with organic matter or that fill void spaces in organic coal particles. The most common minerals found in coal are clay, quartz, calcite, illite and pyrite (Stach & Murchison, 1982). A coal will be partially demineralised before it is ready for

combustion, but a proportion of the original mineral matter remains in the coal and is ‘fired' along with the coal (Mahajan & Walker, 1979, Wall et al., 1989) and flame stability and char morphology resulting after pyrolysis can be partially dictated by the presence or absence of certain minerals such as sodium, potassium, calcium (Patrick & Shaw, 1972). A comprehensive coal analysis technique to predict coal combustion behaviour, would therefore need to take any mineral matter contained within the particles into account.

2.3.4. Particle effects

It is well known that particle size affects the behaviour of coal during combustion in different ways (Cloke, Lester, & Belghazi, 2002; Gilot, Brillard, Brilhac, & Schönnenbeck, 2017; Wells & Smoot, 1991). When a raw coal is pulverized before combustion, the grinding process can cause macerals to concentrate into certain size fractions (Bustin, 1991; Jones, Morley, & McCourt, 1985). It has been shown that the smallest particle size had the highest ash level (E. Lester, Allen, Cloke, & J. Miles, 1994). %Unreactives, a reflectance-based coal reactivity measure was also found to increase with particle size and has been related to char morphology and significant differences in burnout observed for varying particle size (E. Lester, Cloke, & Allen, 1996).

2.3.5. Char Morphology and Reactivity

Coal char particles generated by rapid pyrolysis (described in 2.3.2) are mainly porous solid particles (Pyatenko, Bukhman, Lebedinskii, Nasarov, & Tolmachev, 1992). Char morphology is used to describe char appearance, its wall thickness, macroporosity, and optical anisotropy. Previous research has focused on how to describe the different

structural types of char particles and assign them into specific categories in order to best describe their combustion potential. Such a list of well defined char types is shown in Figure 2.1, which is based primarily on the ICCP classification (Alvarez, 2001; E. Lester et al., 2010) and the work of Bailey (Bailey, 1990).

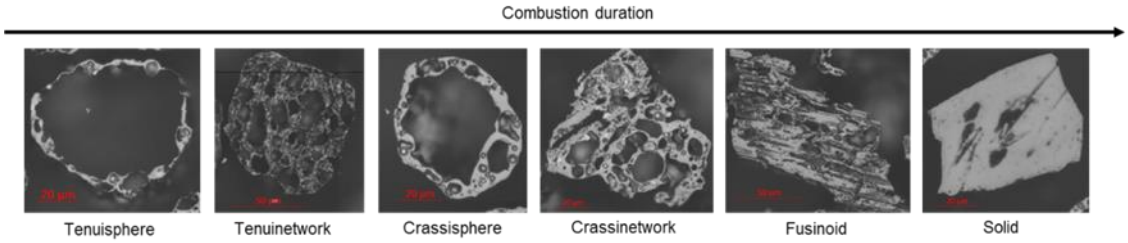


Figure 2.1 *- ICCP morphologies moving from the thinnest walled to thickest walled chars (Perkins et al., 2020).*

The significance of these char morphology groupings and the importance of obtaining accurate classification of char particles is due to the well documented effect of different char structures on fuel burnout (T. Wu et al., 2006b) and char burnout models developed using char morphology have become widely accepted kinetic models for heterogenous char oxidation reactions (Cloke et al., 2003; R. Hurt, Sun, & Lunden, 1998; R. H. Hurt & Calo, 2001).

2.4. Image Analysis Techniques

2.4.1. Coal Petrography

Historically, image analysis has involved the analysis of coal and char samples via oil immersion microscopy and much work has been performed where coal samples are characterised on the basis of their reflectance, which defines rank, and the texture and

association of the maceral content with other constituents (Chao et al., 1982; Cloke, Lester, Allen, & Miles, 1995; David & Fermont, 1993; Perkins et al., 2020; Riepe & Steller, 1984; T. Wu et al., 2006a) in accordance with a number of standards. (Institution, 1981, 1982). More recently, with technological advances, air immersion microscopy has also been used to analyse particles separately on an individual particle basis (O'Brien et al., 2007) and also to identify mineral content within coal particles (Comino et al., 2010).

Historically, heavy emphasis has been placed on the rank of a coal when attempting to make informed fuel choices. This is due to rank being particularly influential in deciding coal combustion efficiency (Bailey, 1990; Cloke et al., 1997; E. Lester, Allen, Cloke, & J. Miles, 1994; N. M. Oka, T.; Matsuoka, H.; Yamada, S.; Yamada, T.; Shinozaki, S.; Shibaoka, M.; Thomas, , 1987; Wells & Smoot, 1991) as liptinite, vitrinite and inertinite can all be 'reactive' during combustion. An image analysis technique, the reactivity assessment program (r.a.p) developed at the University of Nottingham which makes the fundamental assumption that the behaviour of a maceral is associated primarily with its reflectance and not its type, generates a value for the so called '%Unreactives' of a fuel, where material above a predetermined level is deemed 'unreactive' (E. Lester, Allen, Cloke, & Miles, 1994).

2.4.2. The potential of Image Analysis

The potential of IA as a characterisation tool has advanced rapidly with the development of imaging technology and computer and IA software capabilities yet there is no automated image-based predictive method for coal reactivity. This most likely due to the complexity of coal structure, requiring a trained petrographer, and the

effects of origin on the pyrolysis behaviour of coal (Cloke et al., 1997; Perkins et al., 2020). Manual point counting methods have remained popular due to the reliability and precision that results from a well-standardised method, despite large allowable errors (Bustin, 1991). Semi-automated histogram analysis can reduce time requirements, but it still relies on a skilled petrographer to determine maceral thresholds and verify results. An automated tool has the potential to faster, repeatable and a more widely implementable technique for power generators (O'Brien et al., 2007).

2.4.3. Char Characterisation

The majority of I.A systems developed to analyse the attributes of char morphology have previously relied heavily on manual and semi-automated identification techniques. These involve a trained petrographer to identify and assess morphological features such as porosity, shape and wall thickness to classify chars (Benfell et al., 2000). In addition to these manual point counting techniques there have attempts to use semi-automated (Cloke et al., 1997) and automated I.A systems (Chaves, Fernández-Robles, Bernal, Alegre, & Trujillo, 2018; T. Wu et al., 2006b) to speed up char classification and improve repeatability. Largely these techniques have suffered from either a lack of resolution when assessing the char structures (ability to accurately classify into the distinct ICCP morphologies) and have thus required broader morphology groupings or from problems relating to the incomplete extraction of the char information due to breakages and the varied heterogenous nature of char structures. As a result, point counting manual char analysis has remained popular, despite being a rather tedious process. Semi-automated techniques can reduce time requirements, but as with coal petrography, it still relies on a skilled petrographer to extract and process

information obtained and would benefit greatly from the development of automated systems to increase speed and repeatability of analysis.

2.4.4. Individual Particle Analysis

An alternative image analysis method known as Coal Grain analysis (CGA) has also been used for petrographic assessment of coals (O'Brien et al., 2007). CGA captures microscopic images using air objectives and assess the chemical composition of the fuel is obtained from individually separated grains. Initially this method was used for coal with few liberated mineral grains, more recently this method has been modified to also enable the acquisition of the chemical composition of raw coal samples and also a relationship between mineral content and the ash value (Comino et al., 2010). Data from the study incorporates a parameter that combines both rank and maceral type calculated from CGA which correlates strongly with chemical properties determined by ultimate and proximate analyses. Mineral content of a polished coal sample was obtained via a combination of texture and colour assignment and machine learning with SEM as a mineral reference databank (Hapugoda, Krahenbuhl, O'Brien, & Warren, 2015). The technique has only been used to identify the most common minerals found in our coal samples to-date. However, it is promising for the future potential of mineral analysis incorporation into simple image analysis processes. Analysing particles individually allows for enhanced analysis resolution, as well as enabling any predictive functions to be applied on an individual basis, rather than generalised predictions from the analysis of large mosaics.

2.5. Modelling Coal Combustion with Char Morphology

The ability to predict how a coal will perform during pulverised fuel combustion is vital as the rate of char burnout plays a very important role in determining the carbon loss in ash and the design of the boiler. Poor burnout can have significant commercial penalties associated with reduced efficiency (Wells & Smoot, 1991; T. Wu et al., 2006b), higher particulate emissions (Su et al., 2001) and waste materials that cannot be utilized (Jayaranjan et al., 2014). Therefore, knowing how a fuel is likely to behave prior to purchase would be extremely valuable information for a power generator.

Modelling coal and char combustion requires the determination of oxygen transport and kinetic parameters (R. Hurt et al., 1998; Ma & Mitchell, 2009) and is a complex challenge owing to;

1) Chars have a complex, heterogenous porous structure which continuously changes during the combustion process.

2) The combustion reactions of carboneous material takes place both within and outside the particle and is highly affected by the combustion conditions (heating rate, oxygen concentration etc) (Gilot et al., 2017).

3) At low heating rates (i.e. in a thermobalance). The active surface area is rate controlling and char burnout occurs in a uniform way. However, at high heating rates, such as those in a pf boiler, strong diffusional limitations appear, and particles no longer burn in a uniform manner (Le Manquais, Snape, McRobbie, & Barker, 2011).

The rate of char combustion is affected by particle temperature, gas temperature and oxygen concentration within the gas phase surrounding the particle and is controlled by two competing processes; the chemical reaction rate of carbon and oxygen on the char

surface and the rate of mass transfer of oxygen from the has stream through the boundary layer to particle surface (Bhatia & Perlmutter, 1980; Ma & Mitchell, 2009). At low temperatures, the chemical reaction rate is slow compared to rate of oxygen diffusion and therefore the complete porous structure is penetrated by oxygen and the reaction is reaction rate limited (known as combustion Regime I). At higher temperatures, the chemical reaction rate increases sufficiently enough that an element of diffusion limitation is introduced, and combustion rate is thought to now be the result of three interacting factors; the intrinsic reaction rate at the char surface but also the size of this surface and the extent to which oxygen diffusion through the pores restricts this reaction (Regime II). At even higher temperatures, the rate of reaction is almost completely determined by the rate at which oxygen can diffuse to the char surface (diffusion control, combustion Regime III).

Large limitations to oxygen diffusion are at work during a large part of the combustion process, at which point combustion is very close to occurring within a shell at the particle surface and can be thought of as a combustion 'front' controlled by the oxygen gradient within the char particle. As carboneous material is consumed, the combustion front progresses towards the particle centre until during late-stage combustion, the centre of the particle is also concerned by combustion. One method for visualising the change in combustion regime is by computing the effectiveness factor (η). A commonly used parameter to measure the relative balance of the chemical and diffusional limitations and depends directly on the Thiele diffusion modulus (Φ) (the relationship between the catalytic activity and the size of a particle). Equations for both can be found in Chapter 6.1.3. Estimating the effectiveness factor enables visualisation of the theoretical particle combustion rate (Gilot et al., 2017) and is displayed as function of time and carboneous material conversion in Figure 2.2.

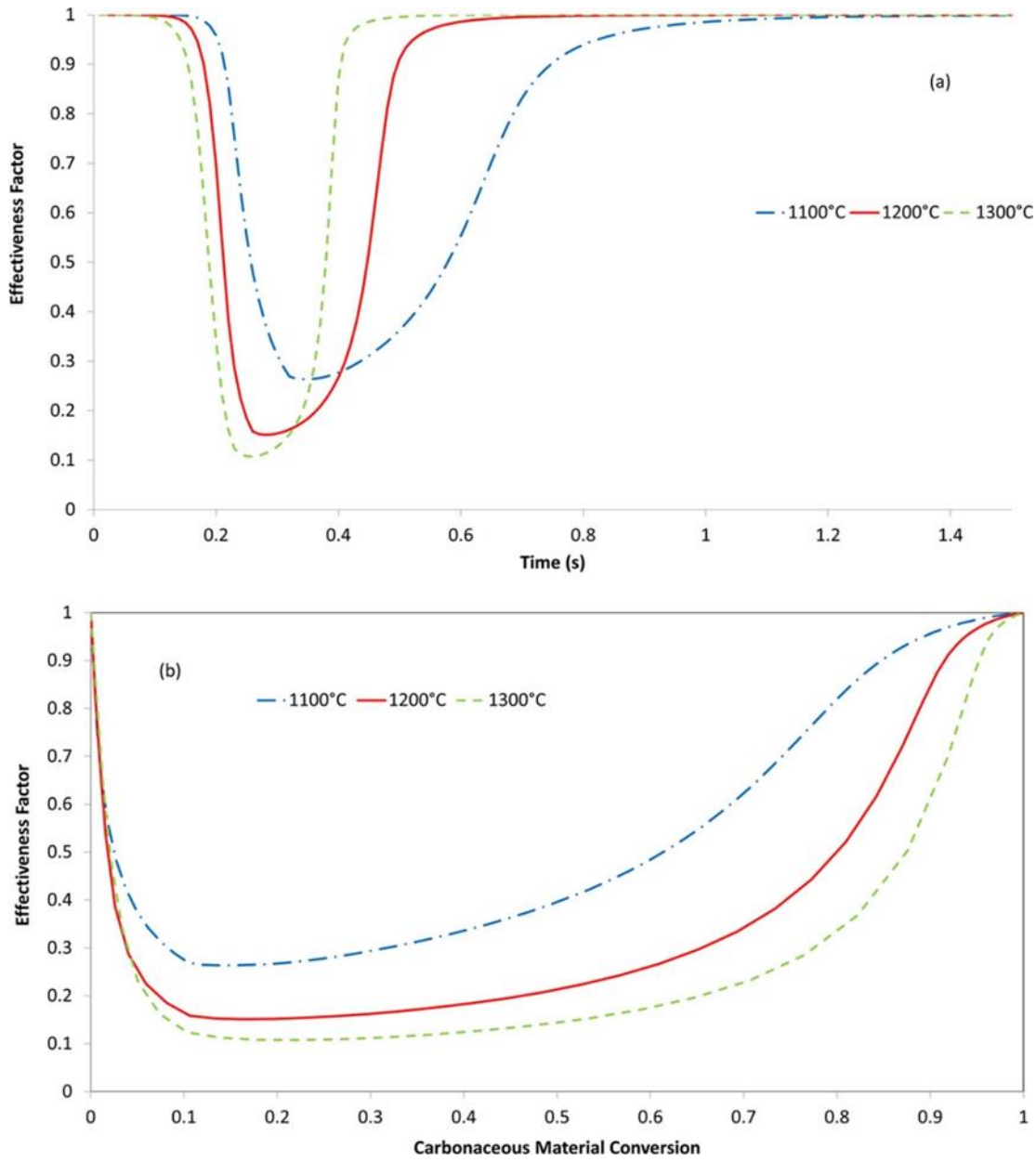


Figure 2.2 *- Evolutions of the effectiveness factor (η) of a char particle during its drop in a drop tube reactor for three regulation temperatures (1100, 1200, and 1300 °C), as a function of (a) time and (b) conversion (Gilot, Brillard et al. 2017).*

Many methods and models have been employed to predict burnout, some include particle size distribution, rank (N. Oka et al., 1987), ash content, vitrinite reflectance (Lee, Song, Lee, Chang, & Jeon, 2009) ,volatile content (Wells & Smoot, 1991), proximate and ultimate analysis data (R. H. Hurt & Calo, 2001). One of the most widely

accepted models to describe char oxidation reactions, the CBK model, was developed by Hurt (R. Hurt et al., 1998). However, the accuracy of the CBK model has been shown to be largely dependent on input distributions of particle size and density. The model was later improved by with the introduction of char morphology sub-models and 'real' char morphology data to improve the simulation of mass and heat transfer outside and inside char particle and it was shown that that different chars of the same morphology classification burn out in markedly different ways due to the significant difference in their geometric structures (T. Wu et al., 2006b).

In most char combustion models however, to simplify the effects of structure, the particles are often assumed to be spherical, uniformly porous and solid in nature when used to calculate the contribution of diffusional and chemical contributions (Ma and Mitchell 2009 (Ma & Mitchell, 2009). However, generalised assumptions concerning char structure and porosity are far from ideal, as chars from the same coal can exhibit a large range of possible structures and porosities and has led to mixed simulation results (Cloke et al., 2003).

None of the char combustion models developed so far have simulated burnout of carboneous char material on individual particle images, mainly due to the difficulties in accurately obtaining accurate and complete structural information from a combustion intermediate in sufficient quantities. Now however, the acquisition of detailed and accurate information on large numbers of individual char particles can be achieved using modern processing and automated image analysis (IA) techniques (T. Wu et al., 2006a; Yu, Lucas, Strezov, & Wall, 2003) and would enable direct analysis of actual char structures and the removal of assumed quantities and variables such as wall thickness and pore diameter from the calculations.

2.6. Applications: Coal Weathering and Combustion

Aside from general fuel analysis, another major potential application for rapidly deployable, automated image analysis techniques is the monitoring of coal stockpiles. The trade of world coals necessitates stockpiling before the final stage of combustion. A coal on a stockpile is open to potential weathering or atmospheric oxidation that can alter the organic and mineral constituents resulting in which could result in deterioration of properties essential in many utilisation processes (M. M. Wu et al., 1988) (Pisupati, Scaroni, & Stoessner, 1991). In the case of coal combustion, a coal can behave differently as a result of oxidation (Margaretha Bengtsson, 1987). Processes such as liquefaction, coking, beneficiation and gasification can also be affected by oxidation, (Gracia M., 1993; Kus, Misz-Kennan, & Iccp, 2017). Whilst a coal may behave differently when oxidised, the probability of detecting a problem before the event is low with traditional lab testing.

The effects of oxidation upon coal are manifested as changes in structural and physical characteristics. Structural changes attributed to oxidation include the formation of peroxides (M. M. Wu et al., 1988), the reduction of aliphatic hydrogen content, and increases in hydroxyl and carboxylic groups (Monthioux & Landais, 1988). Structural changes are thought to be responsible for the increase in volatile content seen after oxidation. This kind of phenomenon also explains the decrease in calorific value that can result from oxidation, and partially explains why oxidised coals may perform poorly during combustion. The changes in structure that occur are not entirely clear, although it may be possible that the oxygen bearing functional groups, which have a relatively low stability, as well as oxygen bridges, are eliminated. These bonds are known to increase the thermostability of the organic matter (Monthioux & Landais, 1988).

The principle effects of oxidation on coal macerals include the formation of oxidation rims and surface cracks. The formation of oxidation rims is particularly marked in vitrinite macerals and may be used as a measure of coal reactivity (Kus et al., 2017). Whilst oxidation may produce changes within maceral groups, maceral composition is not thought to be effected (Chandra, 1982).

Attempts to simulate oxidation have generated a plethora of techniques (Kus et al., 2017). Perhaps the most natural means of comparing the properties of oxidised and non-oxidised coal is to sample exposed outcrop coal seams and compare with coal samples from a less exposed point in the seam. This is not always possible, especially if the coal is not close to the surface and most workers therefore attempt to simulate oxidation using various laboratory techniques.

CHAPTER 3. Laboratory Methodology

3.1. Coal Sample Preparation

3.1.1. Origin and selection of Samples

A total of 21 different coals were used during this research and can be categorised into three analysis sets.

Coal Set 1 – A set of eleven coals and one coke with a wide variation in composition and reflectance were chosen to develop the initial coal and char characterisation techniques and test the versatility of the respective methods. These samples were named either by the mine or if this was unknown, the country of origin; Calenturitas, La Loma, El Cerrejon, Ostrava, Zondag, Klein Kopje, Russian, Indonesian, Vietnamese, Welsh Anthracite 1 and 2 and Chinese coke. The coke was used to increase the reflectance range of the suite of samples to well beyond the normal values for combustion coals to test the scope of the prediction and characterisation systems.

Coal Set 2 - As part of a collaborative project between University of Nottingham and The Commonwealth Scientific and Industrial Research Organisation (CSIRO) titled "Combustion Characteristics of Australian Export Thermal Coal using Advanced Imaging Techniques", five Australian thermal coals (coded 1-5 respectively) were used in this project.

Coal Set 3 - Five coal samples to investigate variations in char structure and reactivity as a result of coal oxidation were chosen to represent a wide range of volatile and petrographic contents. All five coals have previously been used in the generation of electricity in power stations around the world. The five coals originate from 4 different

countries: Bentinck (UK), La Jaguar (Indonesia), Fila Mistra (Venezuela), Klein Kopje and Trans Natal (South Africa).

3.1.2. Milling and sieving

All coals received were first dried for 12 hours in an oven set to 60 ^{o}C. They were milled using a Humbolt vibratory disc mill and then sieved into specific size fractions using an Alpine Jet Sieve.

Set 1: +53-75 μm

Set 2: +106-125 μm

Set 3: +53-106 μm

3.2. Coal Sample Characterisation

3.2.1. Proximate Analysis

Thermogravimetric Analysis (TGA) was used to analyse thermal composition of the samples and provide accurate moisture, volatile and carbon contents of each mix. Thermal profiles were produced using TA Instruments Q500 TGA. TGA tests used 10-15 mg of the milled sample. The method used was based on a slow pyrolysis method by Lester et al. (E. G. Lester, M.; Thompson, A., 2007). The sample was heated in a furnace at 5 °C.min^{-1} in 100 ml.min^{-1} of Nitrogen from atmospheric temperature to 900°C, after which the gas was switched to air at 100 ml.min^{-1}. The composition of the samples is given by moisture, dry volatile, fixed carbon, and ash content.

3.2.2. Petrographic Characterisation

3.2.2.1. Sample block Preparation

Sample blocks of each of the coal samples for petrographic analysis were prepared using a mixture of powdered Simplex Rapid clear polyester resin (Kemdent) and the coal fuel in a 1:1 ratio w/w and moulded by using either a Pressi Mecapress C or a Struers Prontopress-2 mounting presses where the mixture was subjected to a temperature of 150 °C and a pressure of 250 kPa for 10 minutes, followed by a cooling time of 5 minutes.

The blocks were then prepared for imaging by being ground flat iteratively using silicon carbide paper (800/1200/2400) and polished using a colloidal silica solution (Struers, OP-S, 0.04 µm) on a Struers Rotopol Automated Polishing System.

3.2.2.2. The Microscope System, Mosaic Capture and Rank Analysis

Manual maceral analysis was conducted on a Leitz Ortholux II POL-BK microscope as per British Standard 6127:3 (Institution, 1982). Automated rank analysis was conducted on a Zeiss Imager M1 microscope with a 50x oil immersion objective (and an internal 10x lens) providing a total of 500x magnification (Figure 3.1). An 8-bit imaging Zeiss AxioCam and Zeiss automated stage was used to generate 30×30 mosaics, representing a total area of $4.75\ \text{mm} \times 3.6\ \text{mm}$ giving a resolution of 0.1288 microns per pixel (Figures 3.2 & 3.3).

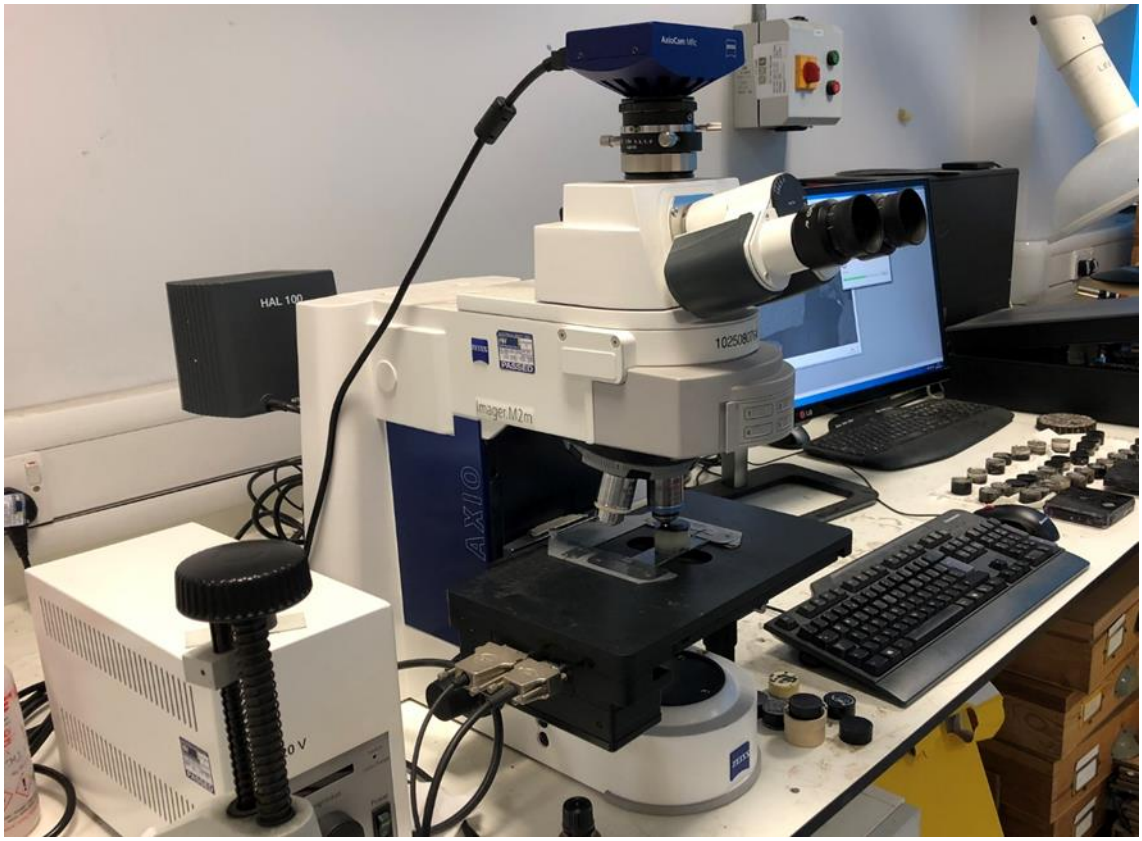


Figure 3.1 *- Zeiss Imager M1 microscope setup*

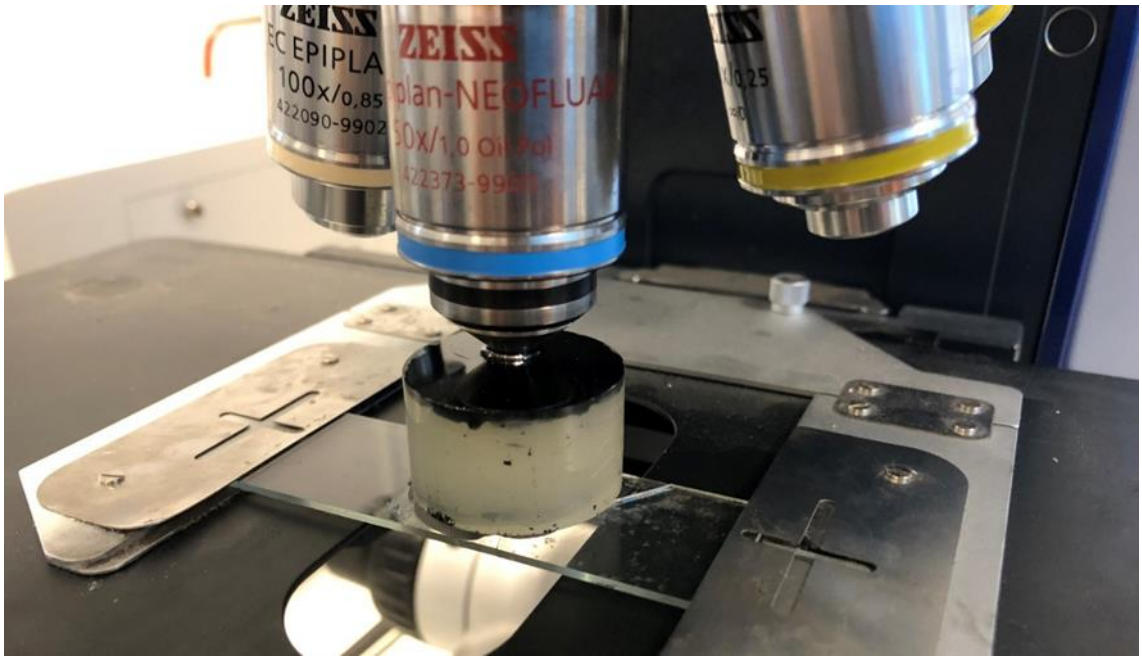


Figure 3.2 *– 50x Oil immersion objective and sample on automated sample stage*

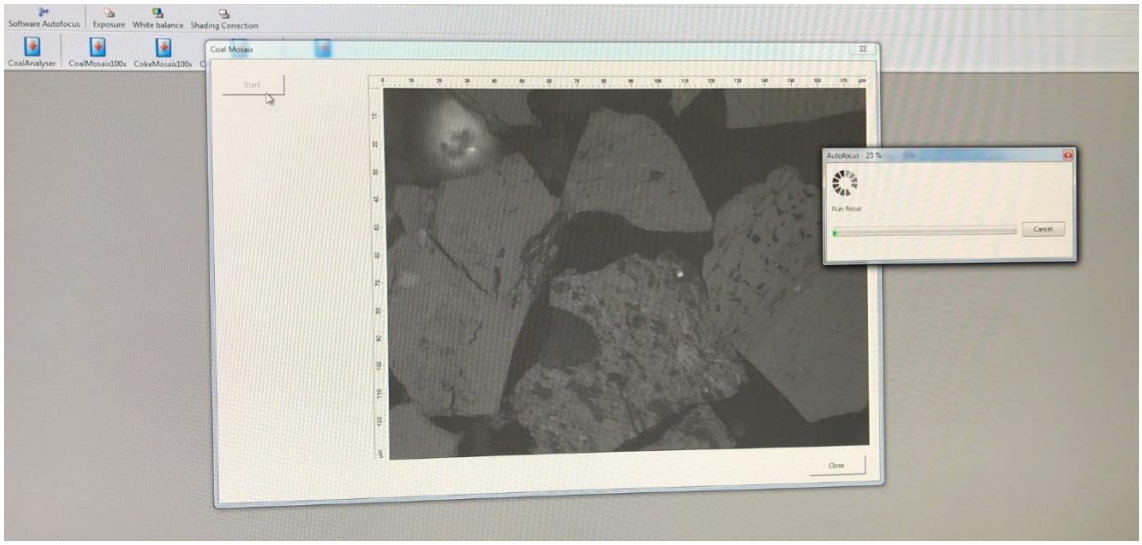


Figure 3.3 *– Automated image capture generating composite mosaic images of sample*

3.2.2.3. Maceral Analysis

Manual maceral analysis was conducted on a Leitz Ortholux II POL-BK microscope and 500 separate maceral points were counted for each analysis with stage movements of 1/3 mm in accordance with British Standard 6127:3 to determine the Liptinite, Vitrinite and Inertinite content of each coal (Institution, 1982).

3.2.2.4. The Reactivity Assessment Program

Each of the greyscale mosaic images captured were characterised using the Reactivity Assessment Program (RAP) which was developed at Nottingham (Cloke et al., 1995; E. Lester, Allen, Cloke, & J. Miles, 1994). This rapidly analyses a coal sample's reflectance histogram to determine the '% unreactives' i.e. the percentage of material that lies above a specific reflectance threshold and can be considered unreactive. The program makes the fundamental assumption that the behaviour of a maceral is associated primarily with its reflectance and not its type. The determination of this

boundary is arbitrary, and it has been found to be dependent on the rank of the coal (Cloke et al., 1997).

3.3. Char Sample Preparation

3.3.1. The Drop Tube Furnace Rig

A Drop Tube Furnace (DTF), which was developed at Powergen UK plc, was used to produce intermediate char structures under similar conditions to those of industrial pulverised fuel combustors at a power station (Figures 3.4-7). The main components of the system include a fuel feeder, a work tube and probe, ancillary equipment for gas supply and flow regulation, a product collector, a gas filter, and temperature monitoring.



Figure 3.4 *– Drop Tube Furnace (DTF) rig for preparation of char samples*

3.3.1.1. Input Gases, Heating Rate and Residence Time

This particular DTF apparatus is able to achieve heating rates of the order of 10^4-10^5 $K.s^{-1}$, a maximum temperature of 1400°C, and the composition of the carrier gas can be predetermined using air and nitrogen cylinder so that oxygen levels can be regulated to simulate the atmosphere found during a full-scale combustion process.

The heating system is comprised of three sections outlined in DTF schematic Figure 3.5. A preheater firstly heats the input gases as they enter the feeder probe. The main heating system consists of a quartet of carbon graphite rods surrounding the work tube. Finally, a trim heater offsets the temperature difference between the water-cooled collector probe and the work-tube.

The residence time of the particles falling through the high temperature region is controlled by the separation of the feeder and collector probes, and the temperature and flow rate of the gas and was tuned to an estimated 200 ms.

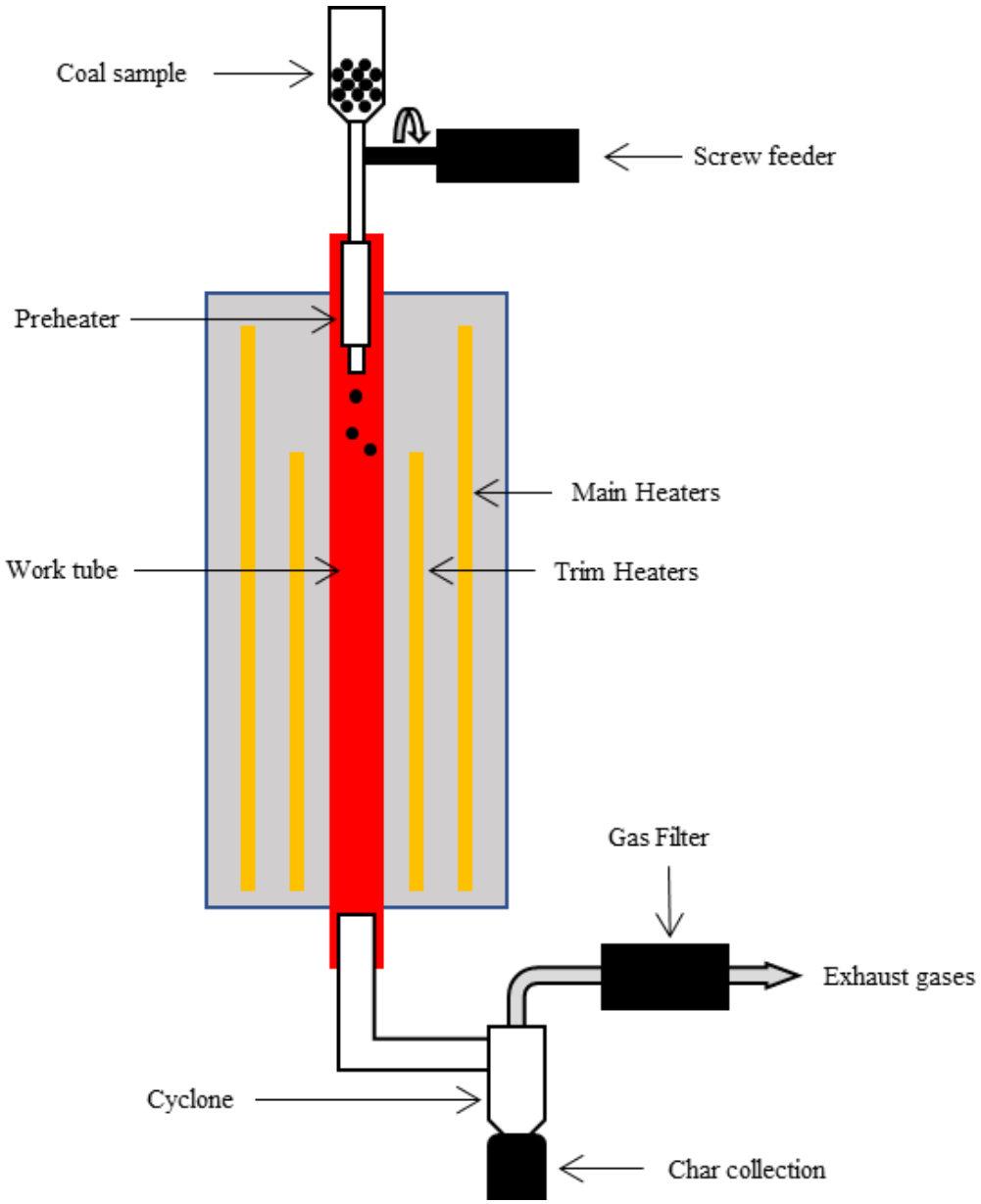


Figure 3.5 *– DTF Schematic*

3.3.1.2. Sample Feed and Collection

A specially designed feeder system, made in the Chemical Engineering workshop at Nottingham University, was utilised to provide a steady flow rate throughout each experiment shown in Figure 3.6. The same system was used in the work of Lester (E. Lester, Allen, Cloke, & J. Miles, 1994; E. Lester et al., 2010), Cloke (Cloke, Lester, &

Belghazi, 2002; Cloke, Lester, & Thompson, 2002), and Gilfillan (Gilfillan, Lester, Cloke, & Snape, 1999) and Barranco (Cloke et al., 2003). The milled and sieved coal sample is placed in a hopper and is fed onto a rotating screw thread where falls under gravity and is swept into the DTF nitrogen/air stream of 12.2 $lmin^{-1}$.



Figure 3.6 *– Drop-tube screw feeder apparatus*

A vibrating device was added to the assembly to prevent hold-up of the coal particles in the hopper. Feed rates varied considerably depending upon the coal sample and particle size and were in the range 5 to 10 grams per hour.

A cyclone device at the end of the collector probe (Figure 3.7) allows the char material to be separated from any gaseous volatiles that may remain in the carrier gas. The carrier gas itself contains a circular piece of filter paper and a pad of fibreglass to remove tar and particulate matter and are changed at regular intervals.

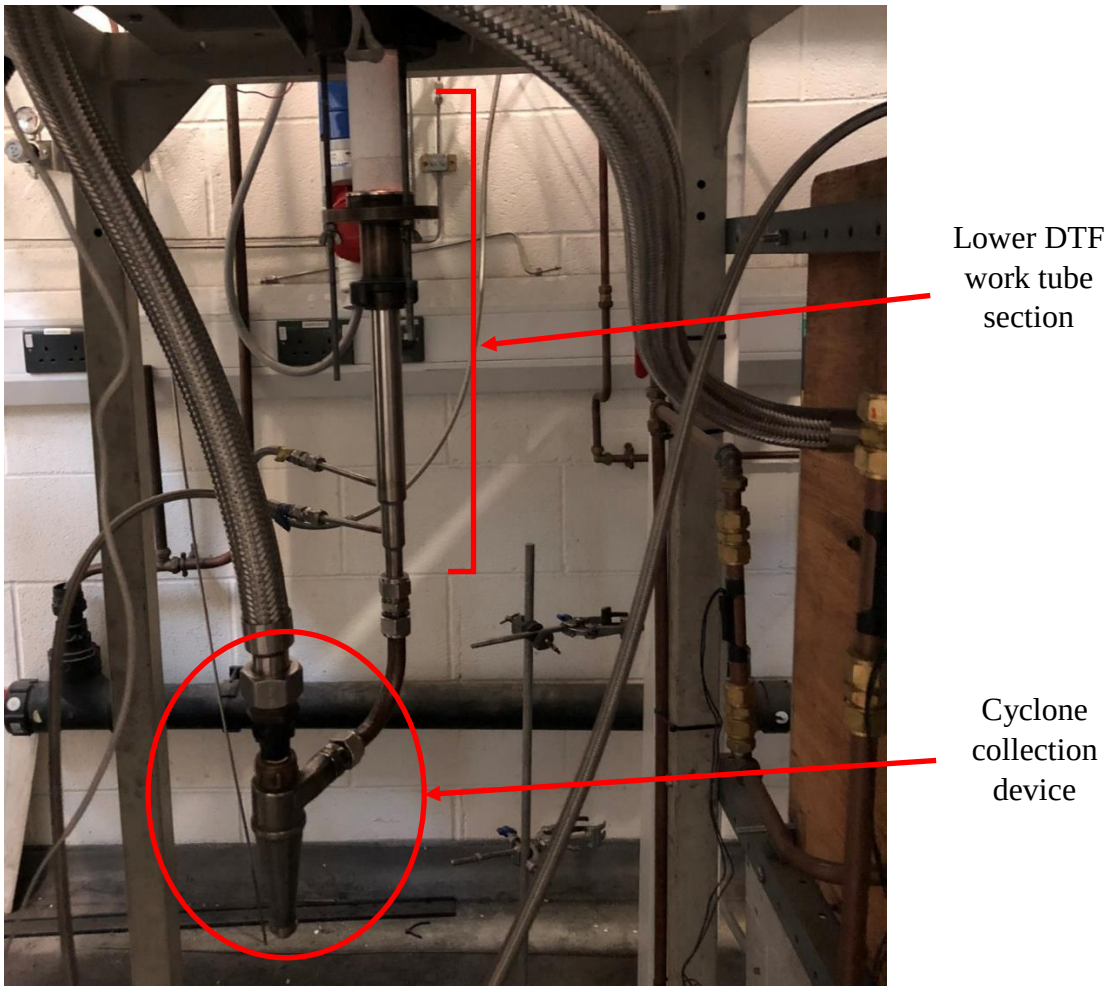


Figure 3.7 *– Cyclone device used to separate char particles from carrier gas stream*

3.3.2. Char Generation: Drop Tube Furnace Experimental Conditions

3.3.2.1. Coal Pyrolysis Conditions

1 g of each milled coal sample was pyrolysed in a vertical drop-tube furnace (DTF) (Severn Thermal Solutions, R765A) operating at 1300°C, with a 200 ms residence time, and air flow set to 1% oxygen (Cloke, Lester, & Belghazi, 2002; Cloke, Lester, & Thompson, 2002; Cloke et al., 2003). These conditions were used to reproduce the conditions experienced by coal in the initial stage of combustion to generate combustion intermediates.

3.3.2.2. DTF Re-firing Experiments

To provide a relative comparison of the combustion rates of sample coals, samples were re-fired through the DTF to acquire char sample at different residence times. For these experiments, coals from coal sets 2 and 3 were first passed though the DTF, operating at 1300 °C in a 1% oxygen in nitrogen atmosphere with a residence time of 200 ms and then were re-fired in the DTF, again at 1300°C, over a series of different residence times (200, 400 and 600 ms), in an atmosphere containing 5% oxygen in nitrogen. The coal and the chars (collected at the bottom of the cyclone), were then carefully weighed.

3.3.2.3. Preparation of Artificially Oxidised Coal Samples

Ten 2 g portions of each of the 5 coals in coal set 3 were weighed out. All 50 samples were then placed inside an oven at ambient temperature. After 24 hours one sample of each coal was removed, and the oven allowed to heat up to 50 ^{o}C at a ramp rate of approximately 2 ^{o}C.min^{-1}. In this way the oven was heated from 25 to 250 ^{o}C over a

period of 10 days with graduated intervals of 25 ºC. One sample from each coal type was removed after 24 hours at any given temperature. The whole oxidation procedure took 11 days from taking the initial removal at 25 ºC to the final sample being removed after 24 hours at 250 ºC. Each sample was stored in an airtight container after removal from the oven.

3.4. Char Characterisation

3.4.1. Microscopic Analysis

3.4.2.1. Char Block Preparation

After collection from the DTF, the char samples were prepared in blocks using a liquid resin (EPOFIX, Struers Ltd.) and vacuum infused for 30 mins before being left to cure for 24 hours. Blocks were then polished in the same manner as those for coal samples described in Section 2.2.2.1.

3.4.2.2. Mosaic Capture and Morphological Characterisation

Mosaic capture of the sample blocks and char morphology analysis was performed using the same equipment as for the point counting the coal sample blocks. In this case, 250 morphological points were identified for each char block and each char categorised by the established nomenclature via the International Committee of Coal and Organic Petrology (ICCP), which divides char structures into thin walled and thick-walled spheres and networks, mixed dense and mixed porous, fusinoids and solids (Alvarez, 2001; E. Lester et al., 2010).

3.4.2. Intrinsic Reactivity Analysis

Char intrinsic reactivity of was determined via a non-isothermal technique (Unsworth, Barratt, & Roberts, 1991) whereby 10-12 mg of char was loaded into the sample cup of the TA Instruments Q500 TGA and the following program used. Initial heating to 300^{o}C at 50 ^{o}C min^{-1} was followed by 10 ^{o}C min^{-1} to 900 ^{o}C in the presence of air. The temperature where the rate of combustion was the greatest (dW/dt = maximum) was called the peak temperature. The temperature at which the rate of combustion equalled 1% per minute (dW/dt = 1% min^{-1}) was called the burnout temperature.

3.4.3. Loss-on-Ignition Test

A measurement of the loss-on-ignition of the samples obtained from the DTF was performed using the same TA Instruments Q500 TGA. This test involved the heating of 10-12 mg of char sample in air at a ramp rate of 25 ^{o}C.min^{-1} to 900°C and held for 60 mins. Any weight changes during this process were assumed to be as a result of the remaining carbonaceous material present in the samples (Payá, Monzó, Borrachero, Perris, & Amahjour, 1998).

3.5. Computer Hardware and Image Analysis Software

All the image analysis techniques described in this work were developed and tested using Mathwork's Matlab™ version 2019a and utilizing the Image Processing Toolbox™ application. All of the program scripts were run using a Lenovo ThinkStation with an Intel Core i7 processor and 32GB of RAM.

CHAPTER 4. Automated Image Analysis Techniques to Characterise Pulverised Coal Particles and Predict Combustion Char Morphology

A new automated image analysis system that analyses individual coal particles to predict daughter char morphology is presented in this Chapter. This work was published in Fuel in September 2019 (Perkins et al., 2020). This Chapter consists of an executive summary and the journal paper manuscript. Supplemental material is attached in Appendix A along with annotated program scripts.

4.1. Executive Summary

The ability to accurately predict the char morphology distribution for a given coal would be of particular use during the fuel selection process and when making coal burnout predictions, as the general rate of the combustion reaction is determined by the structure of these 'daughter' particles. It is generally agreed that the rate of char oxidation is dependent on the heat transfer and the diffusion of reactant gases through 1) the char surface and 2) the char pore structures to permit the chemisorption of these gases and desorption of combustion products. The performance of a particular coal in a furnace will therefore depend on how it reacts during pyrolysis and combustion.

An automated I.A method would present several advantages over manual and semi-automated techniques. Point counting manual petrographic analysis has remained popular, despite being a rather tedious process, due to the reliability and precision that results from a well-standardised method albeit labour and time intensive, with

substantial allowable % error. Semi-automated histogram analysis can reduce time requirements, but it still relies on a skilled petrographer to ascertain maceral thresholds and verify the results. A fully automated coal characterisation technique has the potential to be a more repeatable and faster analytical process. The first Section comprises of the traditional analysis of coal and char samples generated in a DTF to obtain trends between coal properties and daughter char morphology to enable the development and subsequent performance evaluation of the new system outlined in Section 2.

Fuel 259 (2020) 116022

Contents lists available at ScienceDirect

Fuel

journal homepage: www.elsevier.com/locate/fuel

Full Length Article

Automated image analysis techniques to characterise pulverised coal particles and predict combustion char morphology

Joseph Perkins[a], Orla Williams[a], Tao Wu[b], Edward Lester[a,*]

[a] Faculty of Engineering, University of Nottingham, University Park, NG7 2RD Nottingham, United Kingdom
[b] Department of Chemical and Environmental Engineering, The University of Nottingham Ningbo China, Ningbo 315100, PR China

ARTICLE INFO

Keywords:
Coal characterisation
Macerals
Char morphology
Automated image analysis
Combustion
Vitrinite

ABSTRACT

A new automated image analysis system that analyses individual coal particles to predict daughter char morphology is presented. 12 different coals were milled to 75–106 μm, segmented from large mosaic images and the proportions of the different petrographic features were obtained from reflectance histograms via an automated Matlab system. Each sample was then analysed on a particle by particle basis, and daughter char morphologies were automatically predicted using a decision tree-based system built into the program. Predicted morphologies were then compared to 'real' char intermediates generated at 1300 °C in a drop-tube furnace (DTF). For the majority of the samples, automated coal particle characterisation and char morphology prediction differed from manually obtained results by a maximum of 9%. This automated system is a step towards eliminating the inherent variability and repeatability issues of manually operated systems in both coal and char analysis. By analysing large numbers of coal particles, the char morphology prediction could potentially be used as a more accurate and reliable method of predicting fuel performance for power generators.

1. Introduction

Despite a general decline in demand (mainly across Europe) over the last decade, coal is still used extensively to meet over a quarter of global power generation demands [1] and a key energy source for rapidly urbanizing and industrializing economies. As such, coal will remain a major baseline contributor to power generation for the foreseeable future during the transition of the energy mix towards more low carbon energy sources [2]. In optimising coal combustion for power generation and emission targets, generators increasingly need to understand the consequences of fuel choice to maximise the return on shipments, meet stringent NOx and SOx limits [3,4], and minimise shut down time for fouling and slagging maintenance, whilst maximising the potential for ash sales [5]. Thus, the ability to predict how the combustion performance of coals that are available on the market is valuable information to power generator, particularly coals with little documented burnout history.

The prediction of coal combustion performance has been attempted via several approaches over the years. Laboratory techniques include the use of characterisation techniques of physical properties such as volatile matter [6] and ash content [5], fuel ratio [6], particle size distribution [6,7] and intrinsic reactivity of char intermediates [8,6]. Visual petrographic methods of predicting coal combustion performance include rank [11], vitrinite reflectance [12], full maceral reflectance [9,10], maceral content [11], and maceral microlithotypes [12]. Currently, there is no technique for collating all these parameters together into a single predictive technique. This is most likely due to the heterogenous structure of coal, the complexity of maceral reactivity and performance dependence on coal origin and combustion process variables and conditions [9,10].

The ability to accurately predict the char morphology distribution for a given coal would be of particular use during the fuel selection process and when making coal burnout predictions, as the general rate of the combustion reaction is determined by the structure of these 'daughter' particles [10,13]. It is generally agreed that the rate of char oxidation is dependent on the heat transfer and the diffusion of reactant gases through 1) the char surface and 2) the char pore structures to permit the chemisorption of these gases and desorption of combustion products [12,14,15]. The performance of a particular coal in a furnace will therefore depend on how it reacts during pyrolysis and combustion.

Three fundamental chars characteristics have been taken as key differentiators: porosity, pore structure and wall thickness [6,16]. Chars have subsequently classified as either thin walled 'tenui-', thick walled 'crassi-' or solid/fused type structures [12,17], the assumption that thin chars will burn out more rapidly than thick chars has been applied to several char combustion modelling systems [14,15]. These char

* Corresponding author.
E-mail address: Edward.Lester@nottingham.ac.uk (E. Lester).

https://doi.org/10.1016/j.fuel.2019.116022
Received 31 May 2019; Received in revised form 9 August 2019; Accepted 13 August 2019
Available online 19 September 2019
0016-2361/ © 2019 The Author(s). Published by Elsevier Ltd. This is an open access article under the CC BY license (http://creativecommons.org/licenses/BY/4.0/).

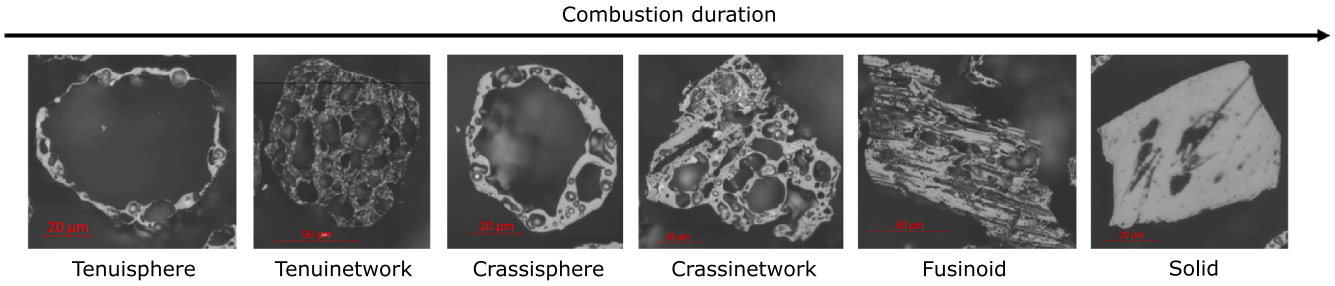


Fig. 1. ICCP morphologies moving from the thinnest walled to thickest walled chars.

morphologies are dependent on the original coal's characteristics, such as maceral type, rank, particle size, mineral matter and on process variables such as formation temperature, heating velocity, gaseous atmosphere and residence time [12,14,18,19]. Generally, the more reactive liptinite and vitrinite macerals will produce thinner combustion intermediates that burn more efficiently than those derived from inertinite [20–23]. Rank affects the reactivity of the maceral groups, with increasing reflectance corresponding to a decrease in reactivity [9]. Many of these original coal characteristics, such as rank, maceral content, %Unreactives and particle size/shape are measurable using rapid and automatable image analysis (IA) techniques [24–27], yet there is no automated image-based predictive method. This is possibly due to hardware and software limitations, the complexity of coal structure, requiring a trained petrographer, and the effects of origin on the pyrolysis behaviour of coal [7,9,28,29].

The potential of IA as a characterisation tool has advanced rapidly in recent years with the development of camera technology, computer processing power and IA software capabilities. Mineral Liberation Analysis (MLA Computer Controlled Scanning Electron Microscopy (CCSEM)) [30,31] is a well-established technique for imaging and characterising mineral content. Maceral detection using SEM is difficult owing to the similarity of maceral backscatter signals [32]. However, recently mineral detection combined with semi-automated maceral classification has been undertaken using traditional microscopy [33]. Furthermore, IA is already being used to characterise the coking potential of coal on a particle by particle basis [33,34]. With recent advances in IA, where process variables are assumed to be constant, automated coal characterisation and daughter char morphology prediction should be possible. An automated IA method would present several advantages over manual and semi-automated techniques. Point counting manual petrographic analysis has remained popular due to the reliability and precision that results from a well-standardised method [35–37] albeit labour and time intensive, with substantial allowable % error [38].

Semi-automated histogram analysis can reduce time requirements but it still relies on a skilled petrographer to ascertain maceral thresholds and verify the results [39]. A fully automated coal characterisation technique has the potential to be a more repeatable and faster analytical process [33].

This study describes the implementation of a new automated image analysis system using Matlab to accurately characterise individual coal particles and predict their daughter char morphology. The automated coal data was first compared to manual petrographic analysis to ensure parity and then the automated data was used to predict char types. The predicted morphology datasets were then compared to an actual set of chars generated using a drop-tube furnace at 1300 °C, 200 ms and 1% oxygen.

2. Methodology

2.1. Coal sample maceral and rank characterisation

To test the versatility of the predictive method, eleven different coals and one coke with a wide variation in composition and reflectance were chosen and included samples from Colombia, Czech Republic, Russia, Indonesia, South Africa, Wales, Vietnam and a Chinese coke. The coke was used to increase the reflectance range of the suite of samples to well beyond the normal values for combustion coals in order to test the scope of the prediction system. The coal samples were first milled using a Humbolt vibratory disc mill and then dry sieved into 75–106 µm range using an Alpine Jet Sieve. Blocks of each of the coal samples were prepared using a mixture of powdered 'Simplex Rapid' polyester resin and the coal fuel in a 1:1 ratio w/w and ground flat using Silicon carbide paper (800/1200/2400) and polished using a colloidal silica solution (Struers, OP-S, 0.04 µm) on a Struers Rotopol Automated Polishing System.

2.2. Manual maceral and automated rank analysis

Manual maceral analysis was conducted on a Leitz Ortholux II POL-BK microscope as per British Standard 6127:3 [35] to determine the Liptinite, Vitrinite and Inertinite content of each coal. Inertinite macerals were sub-divided into semi-fusinite and fusinite – representing the main inertinite sub-macerals. Automated rank analysis was conducted on a Zeiss Imager M1 microscope using an 8 bit imaging Zeiss AxioCam of the blocks.

2.3. Thermogravimetric analysis of the coals

Thermogravimetric Analysis (TGA) was used to analyse thermal composition of the samples and provide accurate carbon contents of each mix. Thermal profiles were produced using TA Instruments Q500 TGA (New Castle, DE, USA). TGA tests used 10–15 mg of the milled sample. The method used was based on a slow pyrolysis method [40]. The sample was heated in a furnace at 5 °C.min^{-1} in 100 ml.min^{-1} of Nitrogen from atmospheric temperature to 900 °C, after which the gas was switched to air at 100 ml.min^{-1}. The composition of the samples is given by moisture, dry volatile, fixed carbon, and ash content [41].

2.4. Char sample preparation

1 g of each 75–106 µm sample was pyrolysed in a vertical drop-tube furnace (DTF) (Severn Thermal Solutions, R765A) operating at 1300 °C, with a 200 ms residence time, and air flow set to 1% oxygen [7,9,14]. After collection, the char samples were prepared in blocks using a liquid resin (EPOFIX, Struers Ltd.) and vacuum infused for 30 mins before being left to cure for 24 h.

2.5. Mosaic image capture

For the development of the automated IA system, large mosaics of the coal and corresponding the daughter char samples were obtained using a Zeiss Image M1 microscope with a 50x oil immersion objective (and an internal 10x lens) providing a total of 500x magnification. The Zeiss automated stage was used to generate a 30 × 30 mosaic, representing a total area of 4.75 mm × 3.6 mm.

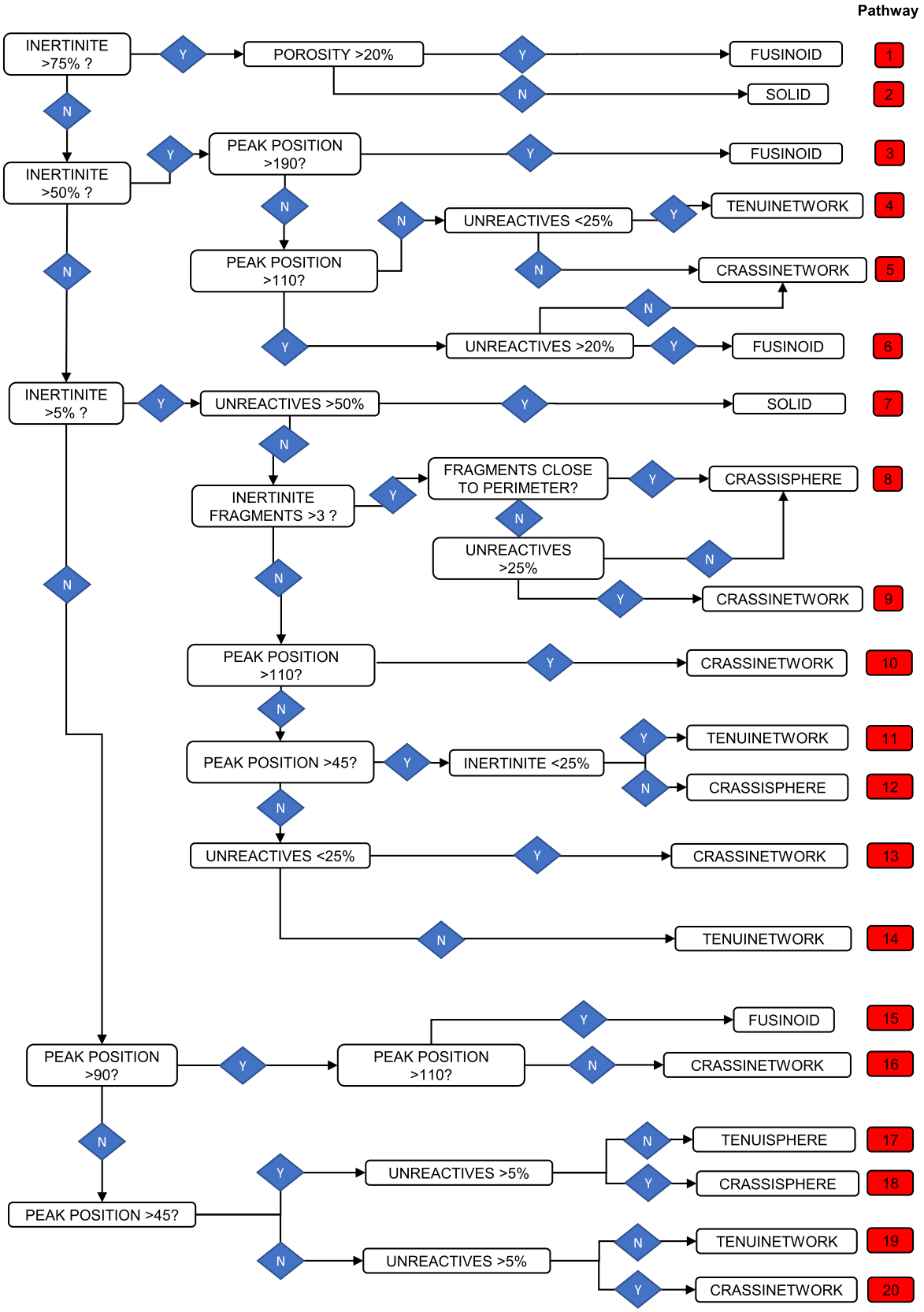


Fig. 2. Char morphology prediction decision tree.

3. Char morphology predictive system

Based on the assumption that thinner chars (that have proportionally more carbon material near the particle perimeter) burn faster than thicker chars [42], the morphologies can be ranked generally from fastest to slowest as shown in Fig. 1. For char morphology prediction, a decision based system (Fig. 2) was devised using the maceral distribution, rank, individual pixel greyscale values and the %Unreactives

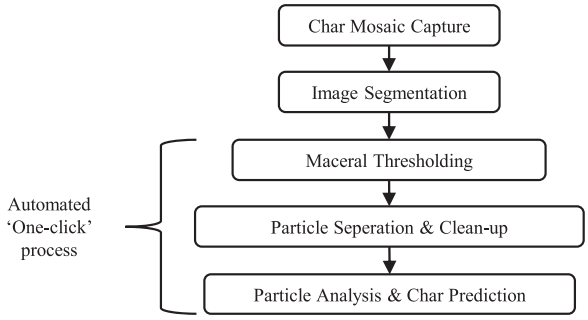


Fig. 3. Process flow for image analysis characterisation and prediction technique.

of each coal particle image to predict the different char morphologies as described in the International Committee for Coal and Organic Petrology (ICCP) Char Atlas [17], which was implemented in Matlab as a decision tree.

3.1. Maceral content

The predictive system classified each coal particle into high (> 75%), medium (> 50%), low (> 5%) and very low (0–5%) inertinite content categories due to the general trend of high inertinite content particles generally producing thicker and slower burning char morphologies, with the prevalence of faster burning morphologies increasing as inertinite content decreases [43].

3.2. Rank

Vitrinite is the maceral most influenced by changes in vitrinite reflectance (also referred to as rank) [44] and produces a variety of different char morphologies during pyrolysis [45]. Lower rank vitrinite generally produces more networked chars than higher ranked coals [46], with very high rank vitrinite showing little reactivity at all. Network-type chars were predicted for lower reflectance coal particles, and sphere-type morphologies predicted for higher reflectance vitrinite.

3.3. Percentage unreactives

The final morphology predictions were also dependant on the amount of unreactive material (%Unreactives) in the coal [10,16]. % Unreactives accounts for high reflectance macerals which have been shown to be lower in reactivity and produce slow burning char [13]. It has been previously shown that the %Unreactives parameter can be used to predict thickness of daughter chars for bituminous coal and the lower the %Unreactives the thinner the char type produced [32]. Whilst the %Unreactives parameter links to burnout, it is not sufficient (as a single number) to predict char morphology outright. However, char wall thickness can be related to this value [20], it provides a useful criterion for differentiating between thick and thin morphology predictions when combined with rank and quantities of inertinite.

4. Image analysis techniques

An outline of the automated IA process is shown in Fig. 3. After microscope mosaic capture, the image segmentation was a semi-automated process using Matlab with an operator ensuring that the thresholds had been correctly determined after segmentation. The coal maceral thresholding, particle separation, analysis and char morphology prediction was a continuous automated process and was implemented using Matlab 2018a + image processing toolbox add-on.

4.1. Semi-automated image segmentation

After initial image capture, the first step in the IA process was the accurate segmentation of the particles from the background resin. Attempts to remove the resin by traditional thresholding processes or traditional edge detection (ie. Canny edge detection [47]) can prove difficult due to the overlap of resin grayscale values with that of the coal particles, particularly those corresponding to liptinite and subsurface blemishes, either standalone or attributed to partly exposed polished particles.

The segmentation process itself was twofold. A variant of the Lazy Snapping Algorithm [48] was first used to separate foreground and background values into distinct areas using a K-means method [49], which removes background pixels as well as removing sub-surface and unfocused areas from around exposed particles (Fig. 4).

The Lazy Snapping method also segmented any background resin that was present within the particle boundaries. To remove this residual resin, a K-means clustering method which clusters pixels based on their intensity and neighbouring associations was used to determine the resin greyscale threshold (Fig. 5). 20 clusters proved effective enough to remove residual resin and leave liptinite mostly untouched. The binary mask generated was then overlaid on the original, unaltered mosaic, to generate a masked segmented image.

4.2. Automated particle separation & clean up

To separate touching and overlapping coal particles were the binary sample mask was subjected to a Watershed Transformation [50] (Fig. 6). The watershed transform finds "watershed ridge lines" in an image by treating it as a surface where light pixels represent high elevations and dark pixels represent low elevations. For a binary image such as the coal mosaic mask, a distance transform function [51] generated the topography in the image and any minima within the image would constitute the most likely area where two particles are touching. Whilst this method is generally successful with most touching particles, it does not work well where long edges are touching or where there was no obvious catchment basin. These were removed by a particle size filter and from the predictive process along with any small blemishes also liberated by the separation function.

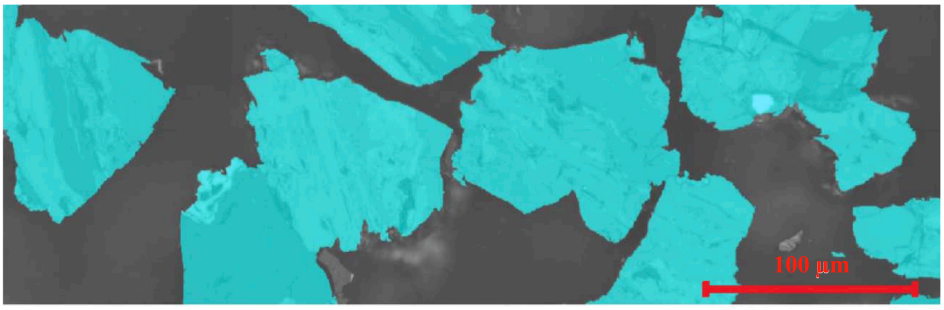


Fig. 4. Lazy Snapping segmentation of coal particles.

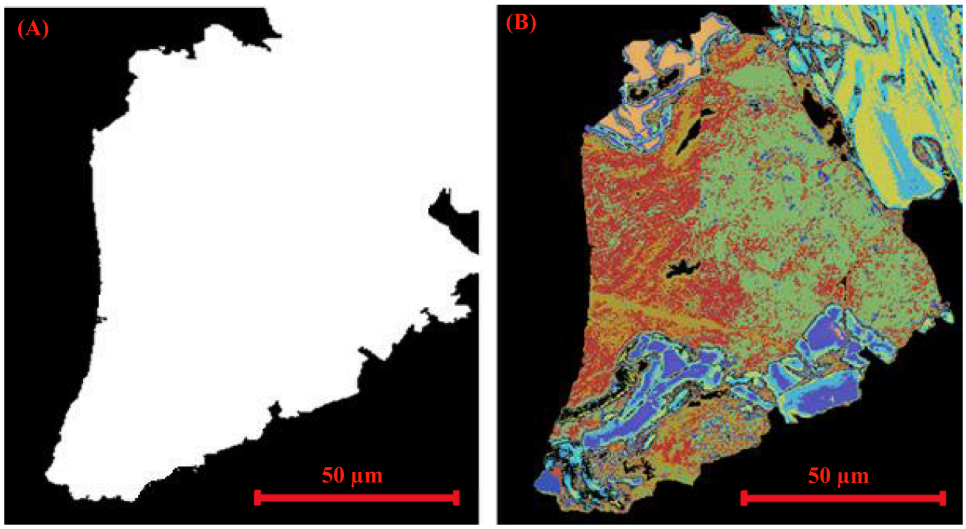


Fig. 5. Clustering segmentation of residual background resin. A) Lazy snapping segmentation result with residual resin and B) Clustering result showing with residual resin removed.

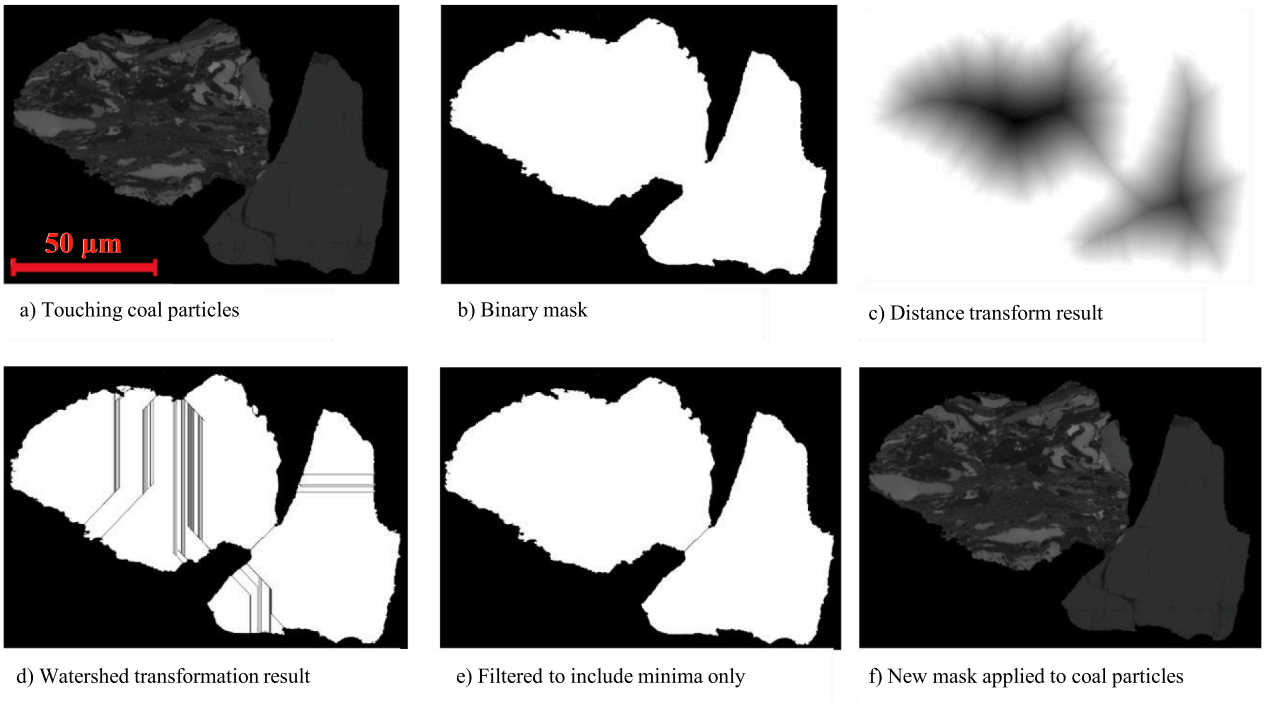


Fig. 6. Touching particle separation via distance transform and watershed transformations.

4.3. Automated maceral thresholding

The maceral thresholds were obtained using the greyscale histogram of the segmented mosaic. Firstly, the liptinite threshold was determined by the presence of any minima in the greyscale region below the vitrinite peak. The minima was calculated using a triangle threshold method [52] which computes the maximum distance between the histogram plot and a line from 0 to the vitrinite peak value.

It is thought that the threshold between vitrinite and inertinite lies within the semi-fusinite group, a maceral intermediate with properties between inertinite and vitrinite [53]. Depending on the rank of the sample, the peaks for vitrinite and semi-fusinite can be well separated or lie partially or directly over each other and the automated classification system determined the inertinite threshold depending on the shape of the reflectance histogram as follows;

1) **'No Overlap'** – The histogram plot is bimodal (i.e. there is a significant reflectance difference between vitrinite and semi-fusinite) then a value corresponding to 30% of the semi-fusinite peak height was found to match the manually obtained data closest.
2) **'Partial Overlap'** – There is some peak overlap but there remains a distinct transition point from vitrinite to inertinite, the threshold was set as half-way between the peaks due to increased overlap of higher reflectance vitrinite with semi-fusinite.
3) **'Complete overlap'** – If the vitrinite peak almost or completely conceals the semi-fusinite peak then a value corresponding to 28% of the vitrinite peak height was found to correlate with manual maceral data.

A graphical representation of the different histogram profiles and threshold locations is shown in Supplementary Figs. S1–4.

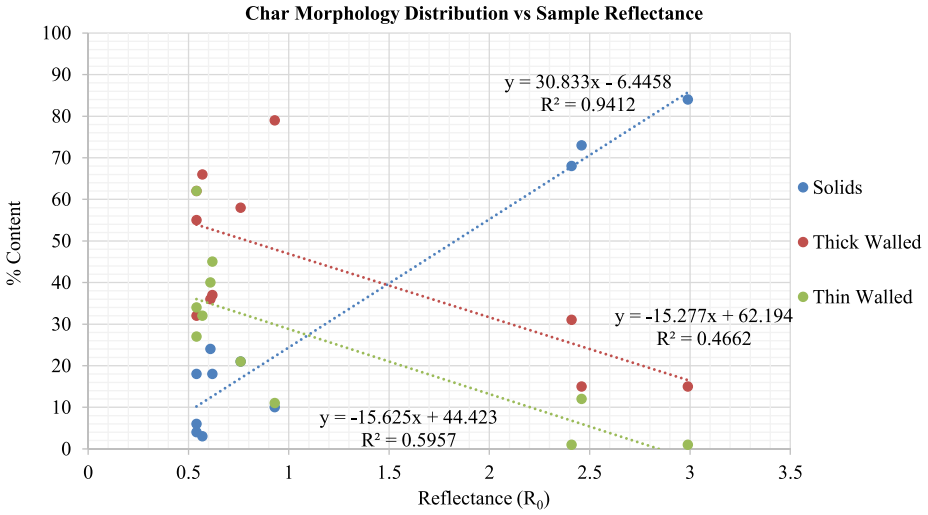


Fig. 7. Relationship between reflectance and general char morphology for 'real' chars generated in DTF.

4.4. Automated particle analysis and char morphology prediction

During the predictive process, each segmented and separated particle was automatically uploaded and analysed in a loop using Matlab to determine peak vitrinite position and maceral composition from the particle histogram, the position of the maceral components and the percentage of pixels that fall above the reactive threshold (set by % Unreactives) [10]. These values were then fed into the prediction decision tree model (Fig. 2), which was trained using Mathwork's Classification Learner using an initial dataset of manually compiled input values for the criteria outlined in 3.1–3.3 and their corresponding char morphology outputs.

5. Results & discussion

5.1. Proximate analysis

The proximate analysis data and vitrinite reflectance data for the 12 samples is presented in Supplemental Table 1. The vitrinite reflectance (for the coals) shows a wide range of values from La Loma at 0.51% through to the Vietnamese anthracite at 2.99%. The Chinese coke has a typical reflectance value around 7%. Clearly the proximate contents (particularly the fuel ratio) correlate with these vitrinite reflectance values but this has been described earlier [54].

5.2. Manual vs predicted maceral analysis

Supplementary Table 2 shows a good correlation between the automated and predicted maceral distributions was observed with 9 of the 11 coal samples differing by < 5%, and all 11 differing by < 10%. From ISO standards for petrographic analysis, these results would be considered to be comparable [38,55]. Image analysis can now provide a rapid and repeatable alternative to traditional maceral analysis to provide more reliable and comparable information. With the exception of the very high reflectance (%R_o = 2.46) Welsh sample 1 and the Chinese coke material, the automated thresholding method proved to be an effective tool to threshold a wide variety of coal samples into their major maceral constituents. Given that allowable operator-based manual point counting results between users for a maceral determined to be 50% of the sample, can fall between 43% and 57%, a variance of 5% from manually determined data using this method is well within the acceptable boundary of error [38]. In the case of the Welsh coal, the very high vitrinite reflectance resulted in a significant overlap of the vitrinite and semi-fusinite peaks, which is a limitation to a greyscale based automated thresholding. In this case, a trained operator would be required to distinguish between the semi-fusinite and vitrinite by way of morphological differences.

Whilst constituting the smallest percentage of the coal matrix, the classification of the liptinite maceral illustrated the largest relative discrepancy between manual and automated results. For the Indonesian and Klein Kopje samples, the predicted value was lower than the manual value, due to the variation in over segmentation during the K-mean clustering step, where too much liptinite is being removed along with residual background resin. There are many ways around this problem including colour imaging with fluorescence lighting [56], morphology manipulation [57] and air objectives [33]. However, as liptinite does not form a critical component in this predictive system and so it was of little consequence to the char morphology prediction processes. The characterisation system was unable to characterise the Chinese coke sample, not least because of the position of the reflectance peaks and absence of macerals. A separate characterisation system would be required to accurately characterise coke material with a different light setting and polarised optical filters.

5.3. Manual vs automated char prediction

The char morphology prediction results are summarized in Supplemental Tables 3 and 4. Table 3 shows a strong correlation between the manually analysed 'real' char and the predicted morphologies. However with certain specific char morphologies (most notably the tenuisphere and crassinetworks), there was variation of up to 16% between manual and predicted results. These observations indicate that there are still factors that were not measured by image analysis discussed in Section 1.

Table 4 shows a simple version of the data in Table 3 where general wall thickness is used to combine the 6 different morphologies i.e. 'thin', 'thick' and 'solid'. In all 12 carbon samples the predictions are within 8% of the manual data which is an excellent correlation between predicted and measured values.

Generally, as rank increases, char reactivity decreases due to the increasing prevalence of thicker and solid pyrolysis products (Fig. 7), a trend that supports previous research [10–13]. The relationship is strongest for the 'solids' grouping and higher reflectance samples, whereas there is more variation observed for the lower reflectance samples. This is entirely due to changes in maceral composition. Vitrinite reflectance can show trends between coals across a wide reflectance range but it is not sufficient as a parameter to predict char morphology at low rank ranges. Maceral composition can vary widely between two coals, even though the vitrinite reflectance is the same, and therefore both coals would generate quite different char types. e.g

the Russian and Indonesian samples produced a relatively high proportion of solid chars (~18%) despite their low rank. In terms of the three general morphology groupings, the predicted distributions of 'thin', 'thick' and 'solid' char morphologies are very close to those from those generated in the DTF with a maximal variance of 9% (Fig. 8a-c).

The largest discrepancies occurred in the lower reflectance coals, particularly those from Colombia. La Loma, El Cerrejon, Calenturitas all possess very similar proximate analysis, peak vitrinite values (42–45), vitrinite contents (88%, 90% & 90% respectively), however their chars generated in the DTF display very different distributions with La Loma producing a high proportion of tenuinetworks (40%) and crassispheres (26%), with El Cerrejon favouring tenui-(24%) and crassispheres (46%) and Calenturitas devolatilising to crassispheres (45%) and an even spread of networks. The prediction system accurately predicted the proportion of crassispheres for all these coals via route 8 (Fig. 2), however when it came to predicting char morphologies for those particles containing a high proportion of vitrinite (routes 15–20), there were significant discrepancies between predicted and manual results for tenuispheres, and networks. El Cerrejon for example, despite being very low rank, produced a higher proportion of 'Sphere' type chars (~70%) compared to the higher rank La Loma (~45%), contrary to previous work discussed earlier that indicated network-type structures should have been the preference. These variances can be attributed to natural variance due to the presence of inertodetrinite which can influence char morphology [58]. As the predictive system cannot currently account for these differences, a disparity was observed between manual and predicted results for some morphologies. For the higher rank coals; Ostrava, Zondag and Klein Kopje, the manual and predicted results were close, with a maximal variance range of just 7%. These coals do not tend to contain inertodetrinite and the % of inertinite is an accurate parameter in the predictive logic tree. Despite the note variations in the 6 specific char classes, the overall proportions of predicted 'thin', 'thick' and 'solid' char morphologies remain very close to these 'real' chars.

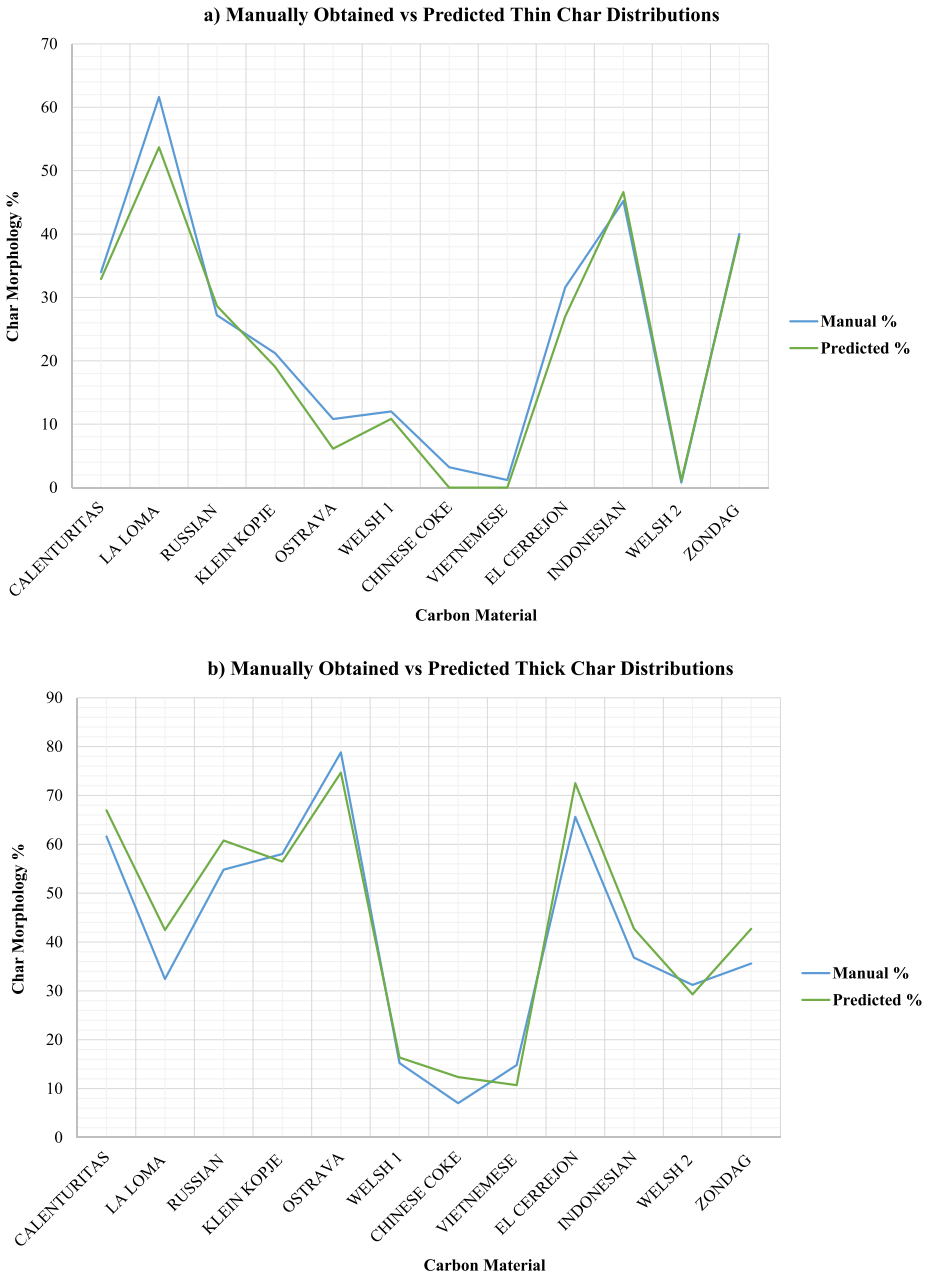


Fig. 8. a-c – Comparison between manual and predicted data for a) thin, b) thick and c) solid chars.

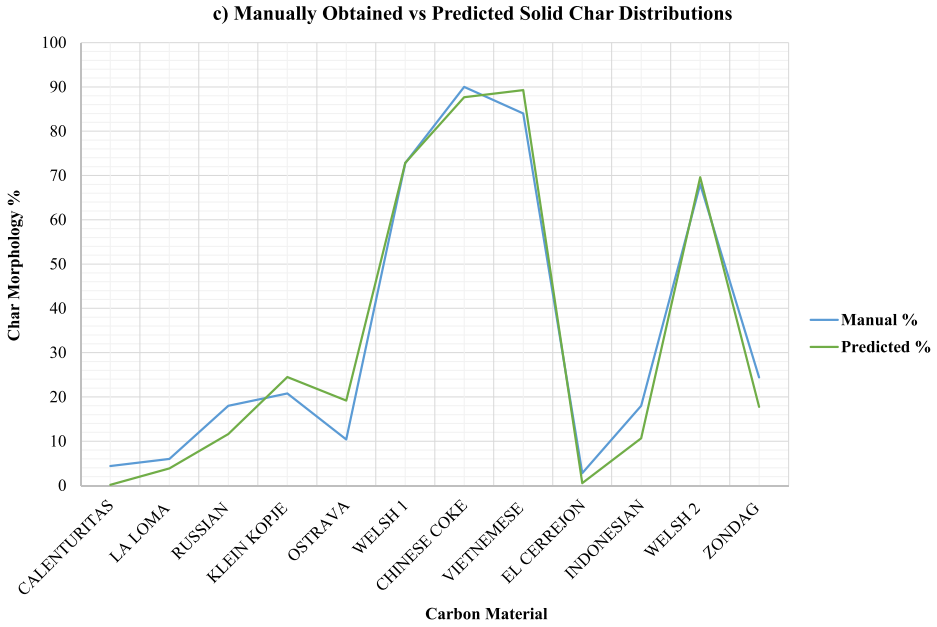


Fig. 8. (*continued*)

6. Conclusions and future work

A new image-based coal characterisation system to predict char morphology has been devised and developed. The system can separate coal particles and automatically segregate the particles into macerals groups and measure other features such as the dispersion of macerals within each particle. The predicted maceral composition vs actual composition appeared to be within standard prescribed by ISO standard.

The system then uses the information gathered from individual coal particles including reactivity (%Unreactives), inertinite content (with positional data) and vitrinite reflectance to predict char type.

In addition to rapid fuel characterisation, this IA system can predict the distribution of major char morphologies, matching closely with actual chars generated using a drop-tube furnace. This data could be used in the future by generators who are interested in predicting combustion characteristics of unknown coals.

Acknowledgements

This work was funded by the EPSRC Centre for Doctoral Training in Carbon Capture and Storage and Cleaner Fossil Energy [grant number EP/L016362/1].

Appendix A. Supplementary data

Supplementary data to this article can be found online at https://doi.org/10.1016/j.fuel.2019.116022.

References

[1] Agency IE. Coal Report 2017: Analysis and Forecasts to 2022. 2017.
[2] Committee, M.C.E.S.A., The Future of Coal 2003.
[3] Directive 2008/50/EC of the European Parliament and of the Council of 21 May 2008 on ambient air quality and cleaner air for Europe. 2008, Official Journal of the European Union. p. Chapter 15 Volume 029 P. 169–212.
[4] Regulation (EU) No 525/2013 of the European Parliament and of the Council of 21 May 2013 on a mechanism for monitoring and reporting greenhouse gas emissions and for reporting other information at national and Union level relevant to climate change and repealing Decision No 280/2004/EC. 2013, Official Journal of the European Union. p. Chapter 15 Volume 031 P. 251–278.
[5] Jayaranjan MLD, van Hullebusch E, Annachhatre A. Reuse options for coal fired power plant bottom ash and fly ash. Vol. 13. 2014.
[6] Wells WF, Smoot LD. Relation between reactivity and structure for coals and chars. Fuel 1991;70(3):454–8.
[7] Cloke M, Lester E, Belghazi A. Characterisation of the properties of size fractions from ten world coals and their chars produced in a drop-tube furnace. Vol. 81. 2002. 699–708.
[8] Avila C, et al. Morphology and reactivity characteristics of char biomass particles. Bioresour Technol 2011;102(8):5237–43.
[9] Lester E, Cloke M. Characterisation of coals and their respective chars formed at 1300°C in a drop tube furnace. Vol. 78. 1991. 645–1658.
[10] Cloke M, Lester E, Gibb W. Characterization of coal with respect to carbon burnout in p.f.-fired boilers. Fuel 1997;76(13):1257–67.
[11] Su S, et al. A proposed maceral index to predict combustion behavior of coal. Fuel 2001;80(5):699–706.
[12] Bailey JG, et al. A char morphology system with applications to coal combustion. Fuel 1990;69(2):225–39.
[13] Cloke M, Lester E, Thompson AW. Combustion characteristics of coals using a drop-tube furnace. Fuel 2002;81(6):727–35.
[14] Cloke M, et al. Char characterisation and its application in a coal burnout model☆. Fuel 2003;82(15):1989–2000.
[15] Benfell KE, et al. Modeling char combustion: the influence of parent coal petrography and pyrolysis pressure on the structure and intrinsic reactivity of its char. Proc Combust Inst 2000;28(2):2233–41.
[16] Borrego AG, Alvarez D, Menéndez R. Effects of inertinite content in coal on char structure and combustion. Energy Fuels 1997;11(3):702–8.
[17] Alvarez DL, E, Atlas of Char Occurrences. 2001: Combustion Working Group, Commission III. ICCP.
[18] Jones RB, Morley C, McCourt CB. Maceral effects on the morphology and combustion of coal char. 1985.
[19] Lee B. et al., Effect of coal properties on combustion characteristics in a pulverized coal fired furnace. Vol. 33. 2009. 737–747.
[20] Wu T, Lester E, Cloke M. A burnout prediction model based around char morphology. Energy Fuels 2006;20(3):1175–83.
[21] P., J., A new classification system for biomass and waste materials for their use in combustion. 2016, University of Nottingham.
[22] Nandi BN, Brown TD, Lee GK. Inert coal macerals in combustion. Fuel 1977;56(2):125–30.
[23] Smoot LD. Fundamentals of coal combustion: for clean and efficient use. Amsterdam; New York: Elsevier; 1993.
[24] Riepe W, Steller M. Characterization of coal and coal blends by automatic image analysis: use of the Leitz texture analysis system. Fuel 1984;63(3):313–7.
[25] Chao ECT, Minkin JA, Thompson CL. Application of automated image analysis to coal petrography. Int J Coal Geol 1982;2(2):113–50.
[26] David P, Fermont W. Application of colour image analysis in coal petrology. Vol. 20. 1993. 747–758.
[27] Wu T, Lester E, Cloke M. Advanced automated char image analysis techniques. Energy Fuels 2006;20(3):1211–9.
[28] Sarofim AF, Bar-Ziv E. The influence of coal type on the evolution of polycyclic aromatic hydrocarbons during coal devolatilization AU – Mitra, Amitava. Aerosol Sci Technol 1987;6(3):261–71.
[29] Michele GD, Riccardi J, Lopez-Doriga E. Influence of coal type and operating conditions on the formation of incomplete combustion products. Pilot plant experiments AU – BONFANTI, L. Combust Sci Technol 1994;101(1–6):505–25.
[30] Waanders F, Mulaba-Bafubiandi A, Lodya L. The South African industry use of

Mössbauer spectroscopy to solve operational problems. Vol. 226. 2013. 721–735.
[31] Wells J. et al., The nature of mineral matter in a coal and the effects on erosive and abrasive behaviour. Vol. 86. 2005. 535–550.
[32] Cardott B, Curtis ME. Identification and nanoporosity of macerals in coal by scanning electron microscopy. Vol. 190. 2017.
[33] O'Brien G. et al., Semi-automated petrographic assessment of coal by coal grain analysis. Vol. 20. 2007. 428–434.
[34] Comino P, Warren K, O'Brien G. Applying the Coal Grain Analysis (CGA) method on liberation studies in coal. 2010.
[35] British Standard (BS) 6127, 1982. Petrographic analysis of bituminous coal and anthracite, Part 3: Method of determining maceral group composition of bituminous coal and anthracite, Database Section, BSI Milton Keynes, Milton Keynes, U.K.
[36] British Standard (BS) 6177, 1981. Petrographic analysis of bituminous coal and anthracite Part 2: Method of preparing coal samples for petrographic analysis. Database Section, BSI Milton Keynes, Milton Keynes, U.K.
[37] Materials, A.S.o.T., in Microscopical determination of volume percent of physical components in a polished specimen of coal. 1980: Philadelphia, Pa.
[38] Bustin RM. Quantifying macerals: some statistical and practical considerations. Int J Coal Geol 1991;17(3):213–38.
[39] Lester E, et al. An automated image analysis system for major maceral group analysis in coals. Fuel 1994;73(11):1729–34.
[40] Lester EGM, Thompson A. A method for source apportionment in biomass/coal blends using thermogravimetric analysis. Anal Appl Pyrolysis 2007;80:111–7.
[41] Institution, B.S., Coal – proximate analysis, in BS ISO 17246. 2010.
[42] Lester E, Cloke M, Allen M. Char characterization using image analysis techniques. Energy Fuels 1996;10(3):696–703.
[43] Rojas-González AF, Barraza J. Volatile matter release and thin and thick char formation as a function of vitrinite content, coal rank, time and temperature devolatilization. Ingeniería y competitividad 2013;15:171–9.
[44] Oka N, et al. The influence of rank and maceral composition on ignition and char burnout of pulverized coal. Fuel Process Technol 1987;15:213–24.
[45] Rojas A, Barraza J. Caracterización morfológica del carbonizado de carbones pulverizados: estado del arte. Revista Facultad de Ingeniería Universidad de Antioquia 2007:84–97.
[46] Vargas D, et al. Beneficiated coals' char morphology. Ingeniería e Investigación 2013;33:13–7.
[47] Canny J. A computational approach to edge detection. IEEE Trans Pattern Anal Machine Intelligence 1986;PAMI-8(6):679–98.
[48] Li Y, et al. Lazy snapping. ACM Trans Graph 2004;23(3):303–8.
[49] MacQueen J. Some methods for classification and analysis of multivariate observations. Proceedings of the fifth Berkeley symposium on mathematical statistics and probability, Volume 1: Statistics. Berkeley, Calif.: University of California Press; 1967.
[50] Meyer F. Topographic distance and watershed lines. Signal Process 1994;38(1):113–25.
[51] Maurer Calvin R, Qi R, Raghavan V. A linear time algorithm for computing exact euclidean distance transforms of binary images in arbitrary dimensions. IEEE Trans Pattern Anal Mach Intell 2003;25(2):265–70.
[52] Zack GW, Rogers WE, Latt SA. Automatic measurement of sister chromatid exchange frequency. Vol. 25. 1977. 741–53.
[53] The new inertinite classification (ICCP System 1994). Fuel, 2001. 80(4): p. 459–471.
[54] Stach E, T.b.M.-T.M., Teichmüller M, et al. a.E.r.b.D.G. Murchison, Stach's textbook of coal petrology. 1982.
[55] ISO 7404-3 – Methods for the petrographic analysis of bituminous coal and anthracite – Part 3: Method of determining maceral group composition. 1994.
[56] Cloke M, et al. Automated maceral analysis using fluorescence microscopy and image analysis. Vol. 74. 1995. 659–669.
[57] Lester E. et al. An automated image analysis system for major maceral group analysis in coals. Vol. 73. 1994. 1729–1734.
[58] Neomagus H. et al. Properties of high ash char particles derived from inertinite-rich coal: 1. Chemical, structural and petrographic characteristics. Vol. 87. 2008.

CHAPTER 5. Automated Coal Char Particle Analysis and Morphology Classification

5.1. Introduction

The significance of coal char morphology and the importance of obtaining accurate classification of char particles is due to the well documented effect of different char structures on fuel burnout (Ma & Mitchell, 2009; T. Wu et al., 2006b). Char burnout models developed incorporating char morphology have become widely accepted kinetic models for heterogenous char oxidation reactions. (Gilot et al., 2017; R. H. Hurt & Calo, 2001).

The majority of I.A methods developed to analyse the attributes of char morphology have previously relied heavily on manual and semi-automated identification techniques which involve a trained petrographer to identify and assess morphological features such as porosity, shape and wall thickness to classify chars (Alvarez, 2001; Bailey, 1990). In addition to these manual point counting techniques, semi-automated (Cloke et al., 1997) and automated I.A systems (Chaves et al., 2018; T. Wu et al., 2006a) have also been developed to speed up char classification and improve repeatability. Largely these techniques have suffered from either a lack of resolution or problems associated with char material separation.

As a result, point counting manual char analysis has remained popular, despite being a rather tedious and time intensive process, due to the reliability and precision that results from a standardised manual method. A fully automated char analysis characterisation technique has the potential to be a more repeatable and faster analytical process

(O'Brien et al., 2007) as well as being a more widely employable technique without the prerequisite of a trained manual operator.

This Chapter describes the development of an automated, 1-click, image analysis system that aims to extract, separate and analyse individual char particles and classify each into one of six ICCP char morphological categories. This information can then enable researchers to use char burnout models to determine the burnout potential of different coal fuels.

5.2. System Requirements & Approach

5.2.1. Stages of Analysis System Development

The development and testing phases of the classification system described in the following sections can be broken down into three parts.

1) The automated segmentation of large char mosaic images and the extraction and analysis of individual char particles.
2) Implementation of several char particle analysis techniques to determine classification criteria for a test set of 550 manually classified char particle images.
3) Testing and validation compared to manually obtained classification data using chars generated in a drop-tube furnace (DTF) from coal sets 1 and 2 described in Chapter 3 (Totalling 17 different coals and 6000+ char particles in total).

5.2.2. Pre-requisites of an automated char classification tool

Three of the major problems that have hindered automated image analysis characterisation of individual char particles are summarized below;

1) Char structures are fragile which can lead to breakages in the char wall during sample preparation or the pyrolysis step itself, examples of broken chars are shown in Figure 5.1. Breakages make segmentation and the subsequent separation of whole char particles difficult as pieces are often completely detached from the main body of the char and therefore difficult to re-associate. Obtaining accurate porosity values with broken and incomplete chars is also problematic as an accurate particle boundary measurement to determine total area is difficult to ascertain.
2) Touching particles, as illustrated in Figure 5.2, also present an obvious difficulty as any properties measured of the adjoining particles will be assumed to originate from a single particle. This will result in both particles being misclassified, or if a size filter is employed, then the agglomeration could be disregarded completely.
3) Difficulty in transferring the morphological 'rules' discussed used by operators during manual classification (Alvarez, 2001). Whilst the identification of morphological features such as wall thickness and porosity can be described in clear terms, it is often difficult to transfer these to a computer-based system due to the general heterogenous nature of char structures and the variability in structure and pore distribution between chars in the same morphological group.

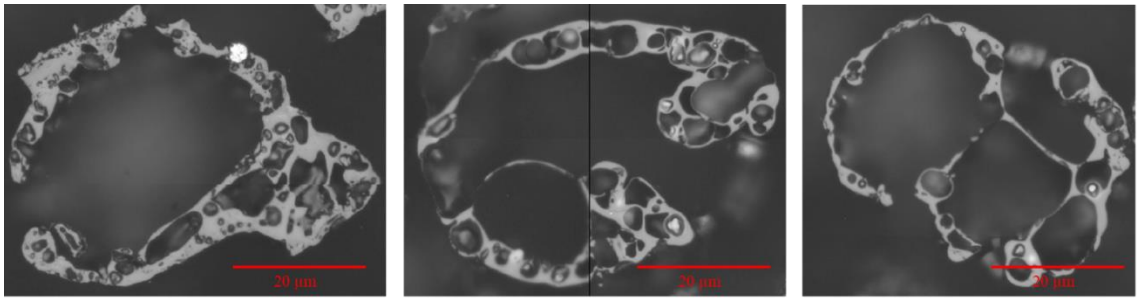


Figure 5.1 *– Examples of common fractured char structures*

An effective system therefore would have the capability to identify and separate individual chars, repair fractures whilst leaving morphological features intact and then classify each particle by recreating the decisions made by a skilled petrographer as closely as possible. Figure 5.3 shows a flow diagram breakdown of the proposed char classification system; each step is described in detail in sections 5.3-5.4. Annotated program scripts are attached in Appendix B.

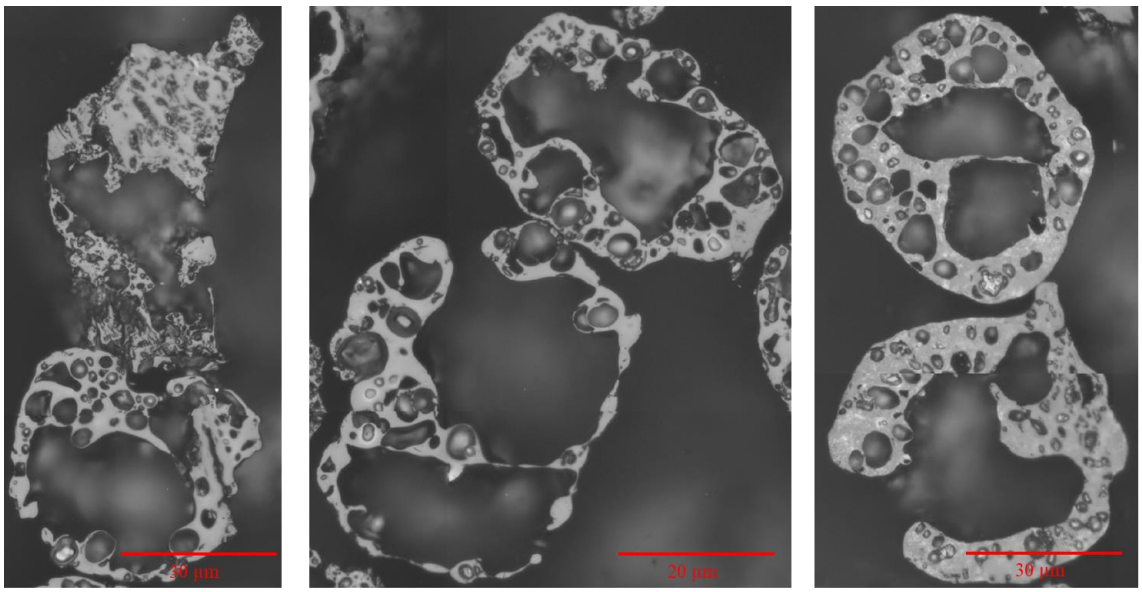


Figure 5.2 *– Examples of overlapping/touching char particles*

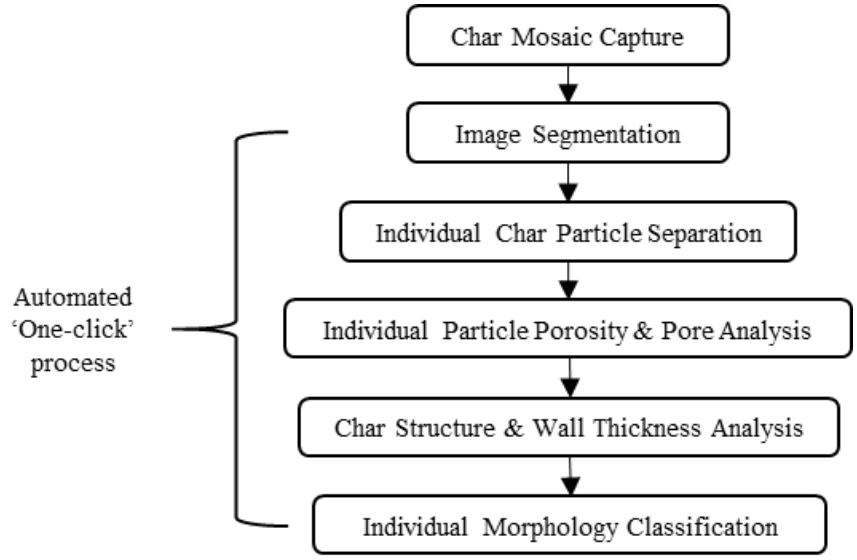


Figure 5.3 *- Flow diagram outlining char analysis system approach*

5.3. Automated Analysis Method: Segmentation & Separation of Char Particles

5.3.1. Char Mosaic Segmentation

The first step in the development of the I.A classification system was to develop a versatile and repeatable method to accurately separate individual char particle pixels from the background resin and other char particles. The reflectance of the char wall material is significantly higher than the epoxy resin used in the block preparation resulting in a bimodal greyscale distribution. Therefore, only one threshold value was required to separate foreground char from background resin pixels. One widely known global thresholding method, Otsu's algorithm (equation 5.1) is defined as a weighted sum of variances of two classes. Weights ω_0 and ω_1 are the probabilities of the two classes separated by a threshold (t) and σ_0^2 and σ_1^2 are the variances of these two classes (Otsu, 1979).

$$\sigma_{\omega}^{2}(t) = \omega_0(t)\sigma_0^2(t) + \omega_1(t)\sigma_1^2(t) \quad \textbf{(eq. 5.1)}$$

Otsu's algorithm is based on a very simple idea; to find the threshold that maximizes the between-class variance between two peaks and can operate directly on the graylevel histogram (Chaubey, 2016). A visualisation of the method for a coal char mosaic is shown in Figure 5.4. Otsu's method is well suited to char mosaic segmentation due to the bimodal image greyscale distribution and a defined intensity valley between the two peaks. By operating directly on the graylevel histogram it is computed very quickly and this, along with its relative simplicity compared to other thresholding algorithms such as Clustering (Awangga, 2018) and Region Growing (Rafael C. Gonzalez, 2007) , were the reasons it was selected generate binary char mosaics (H.S.Prasantha, 2010).

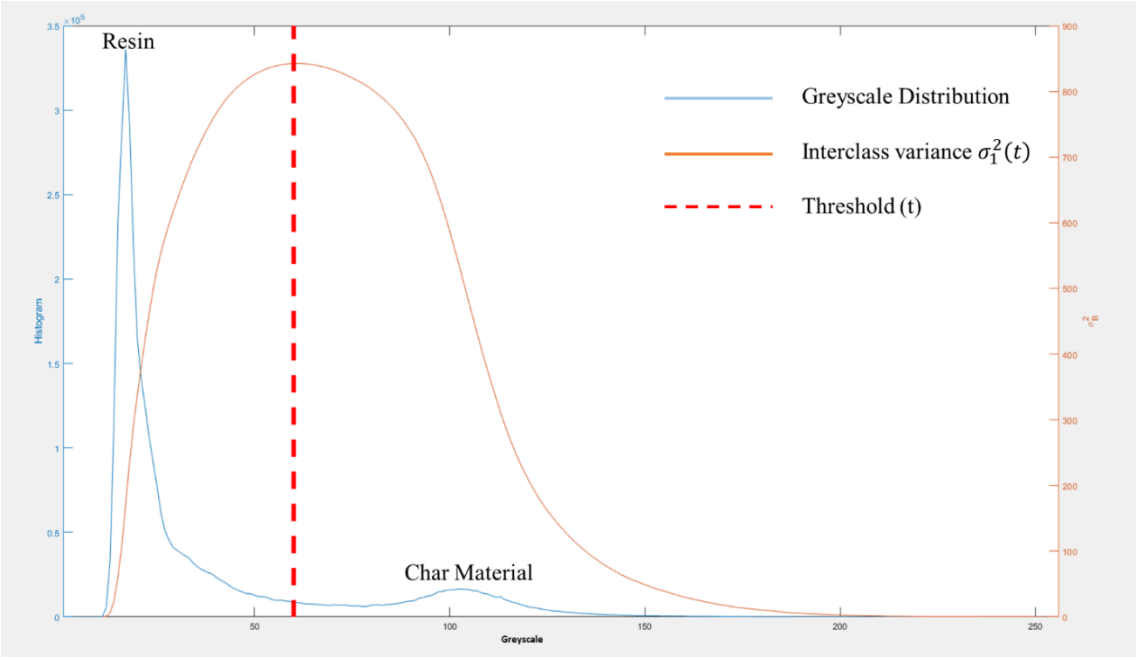


Figure 5.4 *– Visualization of Otsu's thresholding method*

Figure 5.5 shows an example starting char mosaic and the corresponding binary mosaic image after background removal using Otsu's algorithm. From this point onwards, the char images remained in binary format for the remainder of the analysis. The decision to use binary representation of the char particles was based on a number of factors;

1) Whilst greyscale and multi-channel imaging has shown potential in identifying some of the mineral content within chars it is often difficult to resolve, colour images can often lead to mis-classification due to the inclusion of unwanted artefacts such particle relief and background blemishes due to the requirement of complicated multi-level segmentation methods (Chaubey, 2016).

2) Binary images enable the simplification of any morphological functions and char structure manipulation steps during the analysis phase of the system.

3) Enough essential information to determine char morphology (fused/unfused structure, size/shape, porosity and wall thickness) can be obtained from a binary image so a simpler representation will speed up processing times and improve repeatability of analysis techniques.

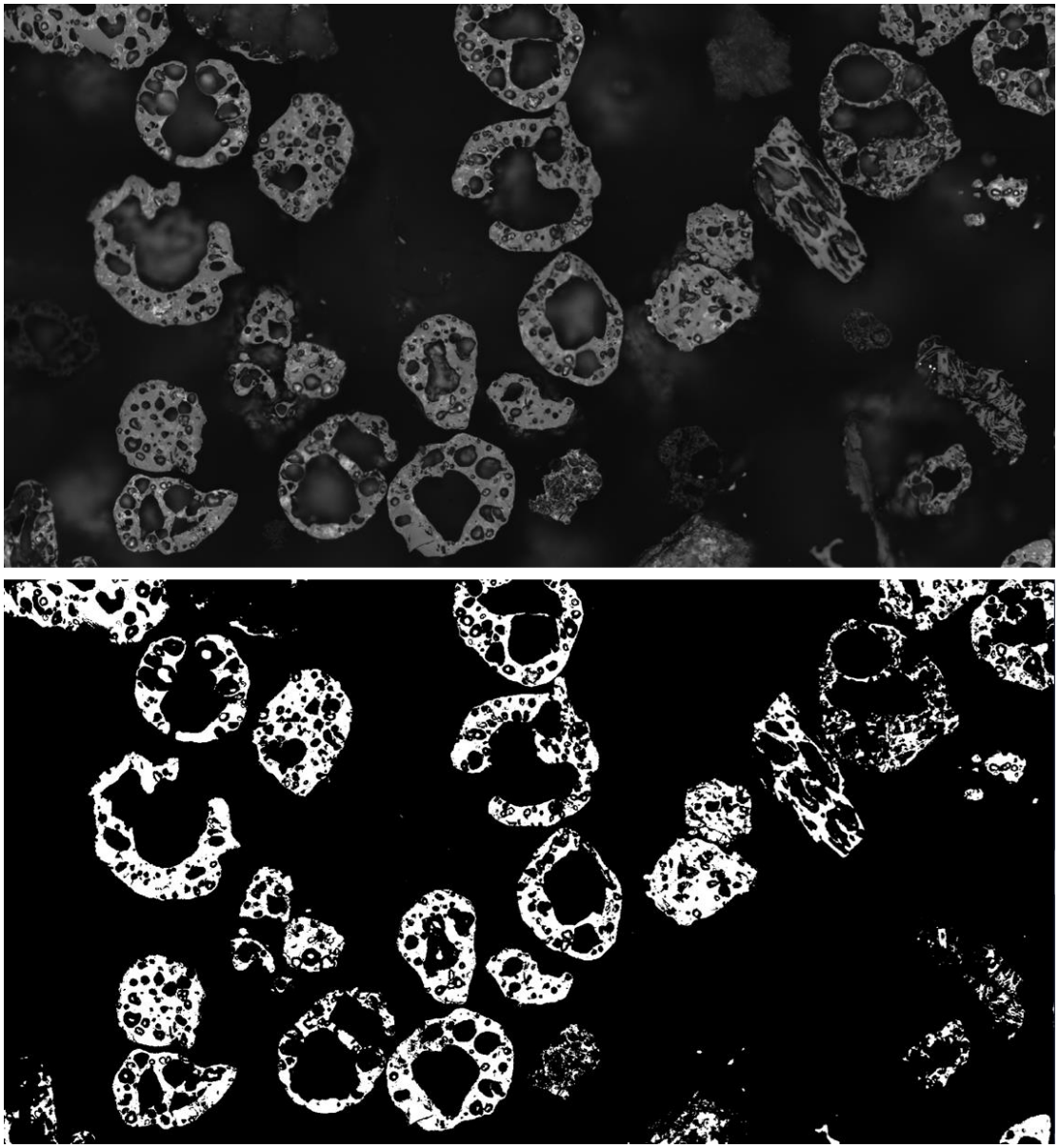


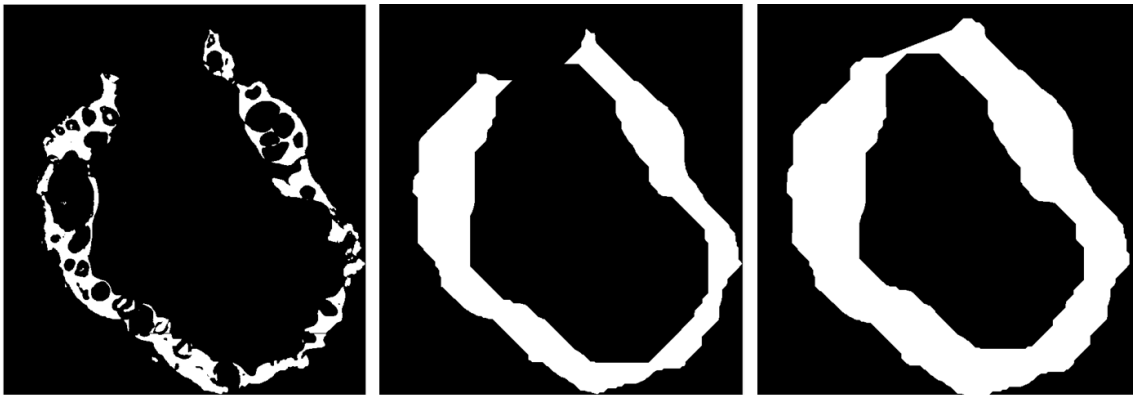
Figure 5.5 *- Char mosaics illustrating before and after implementation of Otsu's algorithm*

5.3.2. Individual Char Particle Separation

In order to analyse and then classify individual chars, each structure is required to be isolated from other particles in the mosaic image. As already discussed, touching particles are a common hurdle in the segmentation of char particle mosaic images. Even to the eye of an untrained observer it is easy to distinguish between the two and

recognise that each is a separate entity during manual analysis. However, enabling a computer program to cleanly separate two char structures presents more problems than the separation of coal particles discussed in Chapter 4. Unlike coal particles, where corresponding binary masks are mostly uniform and well-defined shapes, the sporadic pixel distributions of porous char structures make automated identification of the geometric centre of gravity, and subsequent identification of individual chars difficult.

These separation problems are further complicated as after polishing, many char particles are broken or fragmented, often substantially. Therefore, to avoid analysis of each separate fragment as standalone particles, a reconstruction step is often required, ideally without compromising or altering the structure of the char particle. Various methods including manual mending and image processing techniques such as erosion-dilation and closing functions (T. Wu et al., 2006a) have been previously employed to reconstruct chars. Manual mending is tedious and time consuming and whilst closing functions can be effective at closing small gaps, these functions can significantly distort the shape of the char particles, particularly if the breakage is substantial as illustrated in Figure 5.6. Often the fracturing is so extensive that the breakage cannot be effectively closed at all, and these damaged particles are often removed accidently by filtering functions or mis-classified as a result.



a) Substantially fractured particle

b) Incomplete closing function

c) Further closing distorting char structure

Figure 5.6 *– Illustration of how closing functions can distort the shape of significant broken char particles resulting in loss of incomplete secondary pore structure*

To overcome these separation problems, a 2-stage separation technique was developed to;

1) Determine the boundaries of char structures without subjecting the char structure to any morphological or structural changes which could inhibit later separating and classification functions

2) Accurately identify individual char structures within touching agglomerates and separate each into separate images.

5.3.2.1. Char Boundary Identification

To overcome the problem of fragmented chars, it was first important to ensure all the fractured pieces associated with each char particle are first included before further processing. An aggressive initial closing function, like that illustrated in Figure 5.6c was first implemented to join neighbouring fragments together. An 8-connected radius of 75 pixels (equivalent to 9.66 µm) was used, enabling detached fragments separated

by 150 pixels (19.32 µm) or less to be re-joined to the main body of the char as illustrated in Figure 5.7a and b. Complete boundary restoration was not essential at this stage, just the inclusion of any fragments with the char main body.

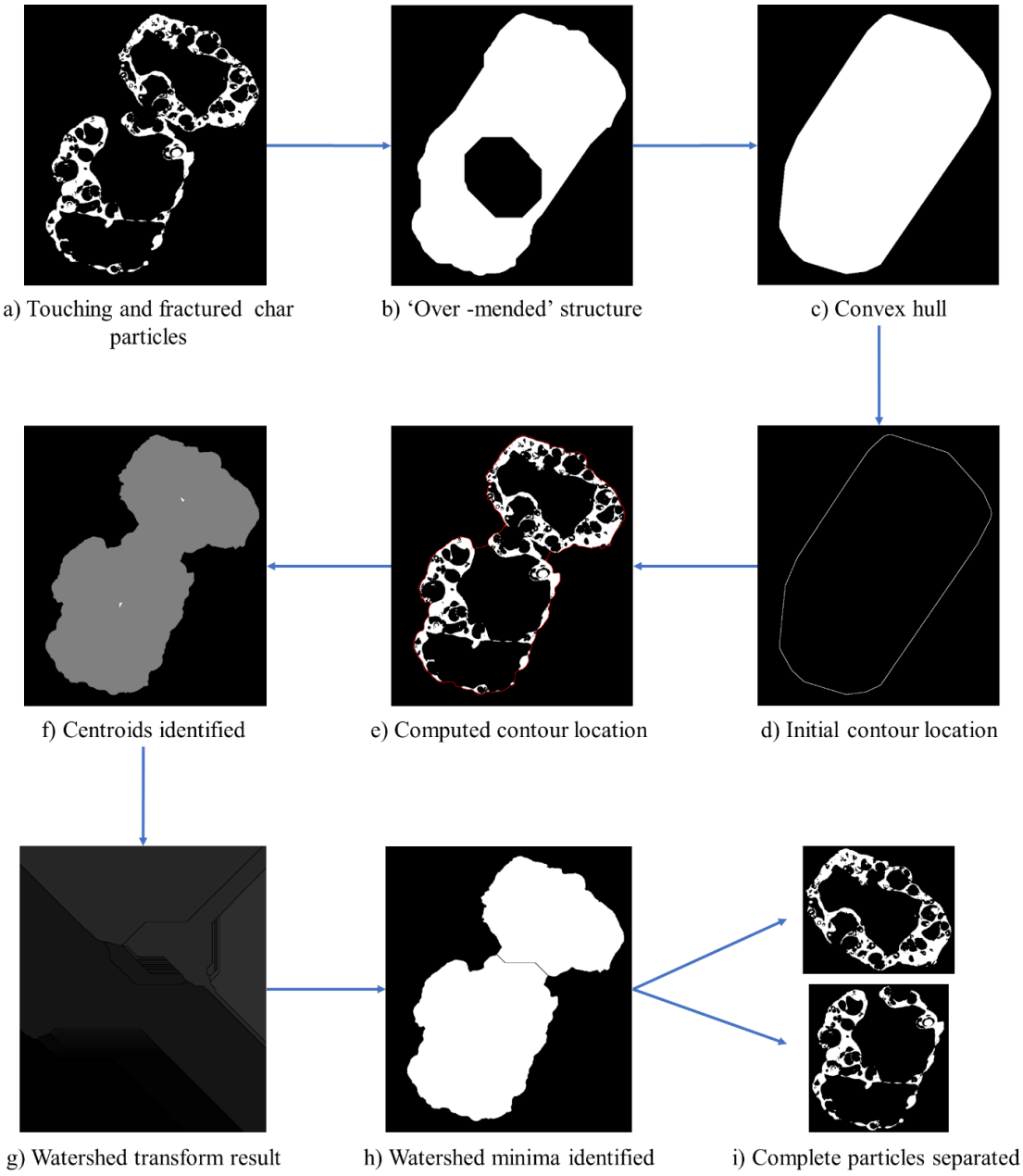


Figure 5.7 *– Individual char separation process*

This ‘over-mending’ process will obviously exacerbate any overlapping/joining of particles and potentially create new char agglomerates by joining closely neighbouring particles, this was inconsequential at this stage, as the system dealt with overlapping particles later. The focus at this phase was the complete inclusion of all char material associated with each particle, minimising the separation and analysis of incomplete chars.

The next step was the computing of the convex hull of the modified char structures. The convex hull/envelope/closure is the smallest convex shape that contains a set of points, in this case the pixels corresponding to char structure/agglomerate as illustrated in Figure 5.7c. A convex hull encloses all the char material within its boundaries and importantly, these boundaries lie close to those of char structure, two vital prerequisites for the effective implementation of an *active contour* model used in the next step to determine outer boundary of the particles.

The active contour or ‘snake’ model is a commonly used feature detection method to determine object boundaries in greyscale images (Kass, Witkin, & Terzopoulos, 1988) given an initial guess, (i.e., an initial contour). In this implementation, the initial contour is the boundary of the char convex hull as shown in Figure 5.7d. This contour is then driven by internal forces (user-defined weights to control the stretch, smoothness and curvature of the function and essentially dictate the shapes that the contours can form) and external forces, which are computed from the underlying image data. These forces iteratively move the contour inwards from a starting point toward an object boundary or defined feature within an image.

By representing the position (v) of the contour (s) parametrically (equation 5.2), the energy minimization model for a simple elastic contour can be written as equation 5.3,

where $E_{internal}$ represents the internal energy (user inputs) of the spline, E_{image} gives rise to the image forces (pixel gradients) and E_{con} gives rise to the external constraint forces.

$$v(s) = (x(s), y(s)) \quad \textbf{(eq. 5.2)}$$

$$E^*_{contour} = \int_0^1 E_{contour}(v(s))ds = \int_0^1 \left(E_{internal}(v(s)) + E_{con}(v(s))\right) ds \quad \textbf{(eq. 5.3)}$$

An illustration of the char boundary identification as a result of the iterative active contour implementation for an example particle is shown in Figure 5.8. The active contour proceeds to advance towards the boundary between char and background as the function progresses.

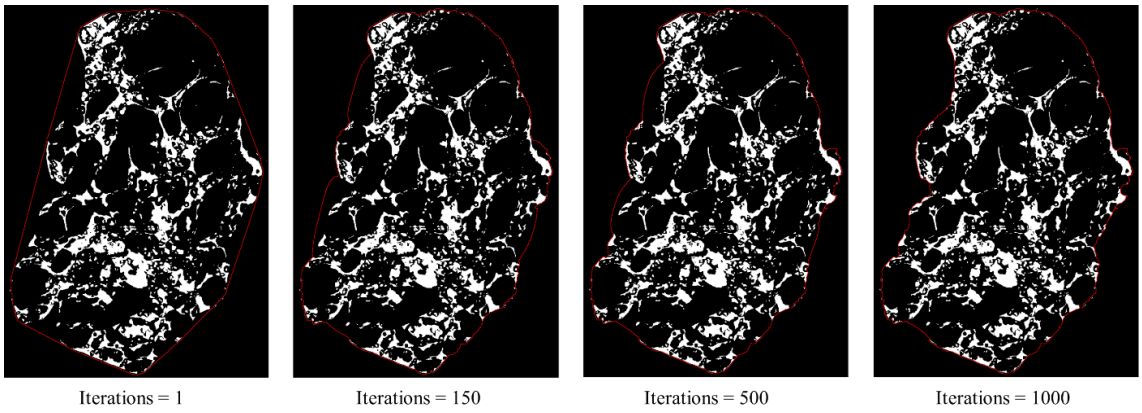


***Figure 5.8** – Migration of active contour from convex hull starting position to char wall boundary*

The internal energy can be written as equation 5.4 and is composed of a first order term controlled by α (s) and a second-order term controlled by β (s). Both are user-defined weights and control the internal energy function's sensitivity to the amount of stretch and curvature possible as the contour deforms. α = 'Continuity Factor' and is a control of the contours tendency to shrink inwards. β = 'Smoothness factor' where higher

values produce smoother region boundaries and filter out finer details, whilst lower values produce more irregularities in the region boundaries.

$$E_{internal} = \frac{1}{2}(\alpha(s)|V_s(s)|^2) + \frac{1}{2}(\beta(s)|V_{ss}(s)|^2) \quad \textbf{(eq. 5.4)}$$

Figures 5.9 and 5.10 illustrate the impact of varying α and β on char particle boundary identification over 500 iterations. An increasing weight of α allows the contour to bend and migrate inwards both around and through the fractured char wall to begin tracing the internal wall structure also. Lower β weights allows finer details of the char wall structure to be resolved.

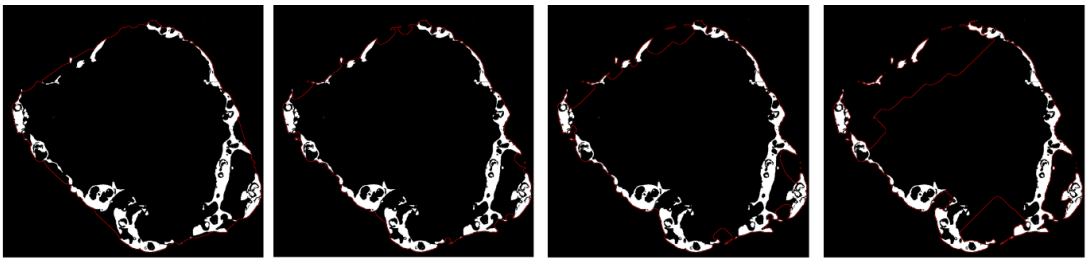


Figure 5.9 *- How manipulation of the continuity factor (α) impacts final contour location for a char particle*

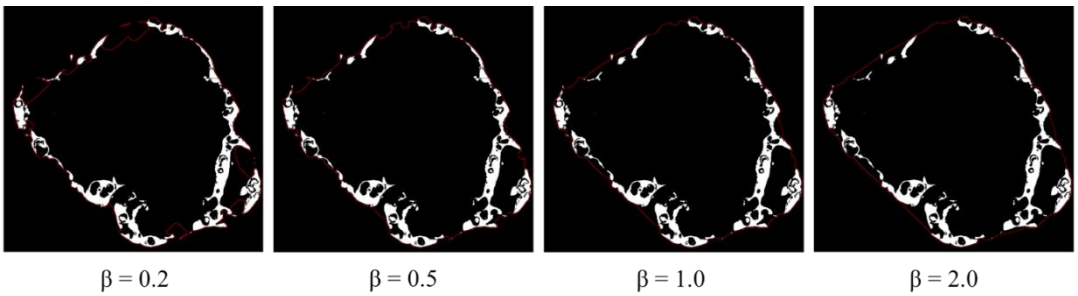


Figure 5.10 *- How manipulation of the smoothness factor (β) impacts final contour location for a char particle*

The external energy can be written as equation 5.5. E_{line} dictates whether the contour migrates towards bright or dark areas, whilst E_{edge} attracts the contour to the areas of the image with the largest image gradients.

$$E_{image} = \omega_{line}E_{line} + \omega_{edge}E_{edge} + \omega_{term}E_{term} \quad \textbf{(eq. 5.5)}$$

In a greyscale representation of a binary image, where only two-pixel intensities exist (0 or 255), the largest gradients are therefore located at the char particle wall boundaries, and the contour will migrate to these locations before terminating. The way in which the contour will 'bend' and 'stretch' over breakages and the general char structure were user manipulated to enable active contours to effectively mould themselves around the char structure. This allows the precise determination the particle boundaries (Figure 5.7e) regardless of substantial fractures in the char wall structure and without the need to repair particle walls and potentially distort char structure. α and β values of 0.03 and 0.2 respectively over 500 iterations were found to accurately trace the boundary of the test char particles.

5.3.2.2. Char Particle Identification and Separation

By determining the boundary of particles with an active contour, each can be filled and centre of gravity determined prior to separation as illustrated in Figures 5.7e-f using methods similar to those used on coal particles in Chapter 4. Due to the user defined fluid behaviour of the spline, pinch points between touching particles are maintained, which aid the separation of these particles via a watershed segmentation process (previously described in Chapter 4.4.2) for the separation of touching coal particles. Once separated, each char particle was subjected to a scrap function to remove small noise material from the image before being saved individually. It is at this point that the

user can confirm with a manual check the saved images and easily edit/or remove any images if required. If zero user input is desired, then a size filter can be used to remove all images that contain particles that fail certain shape or size criteria to ensure char agglomerates/small individual fragments are not subjected to further analysis.

5.4. Automated Analysis Method: Char Analysis & Classification Criteria Determination

In order to develop and assess the performance of the char analysis techniques described in this Section, a test set of 500 manually classified char images for six ICCP char morphologies was assembled. The test set consisted of 100x Tenui-/Crassispheres and Tenui/Crassinetworks + 50x Fusinoid and Solid chars. Due to their relatively low occurrence and to simplify the classification of the char samples, mixed porous/dense chars were categorised as either crassispheres or crassinetworks depending on their pore distribution (E. Lester et al., 2010). To test the capability of the program and the potential for expanding the system to include these morphologies in the future, an additional set of 50x Mixed chars was also compiled and tested but not included in the final classification system.

5.4.1. Classification Criteria Approach

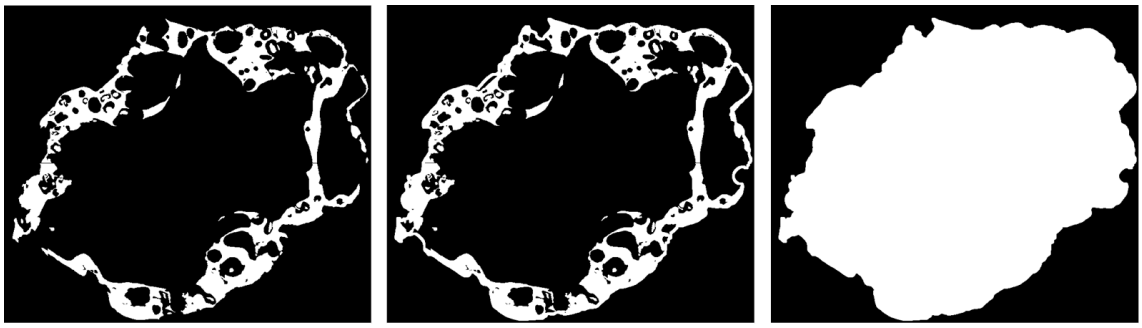
To classify individual char images obtained from methods described in sections 5.2 and 5.3, each image was uploaded into an automated loop and subjected to a series of assessment functions designed to ascertain key structural and morphological characteristics to classify each char into one of six char morphologies.

The aim when designing this system was to, as close as possible, replicate the decision-making process of a manual operator with the repeatability of a computer driven method. Whilst many have been described in literature, there are essentially three fundamental characteristics that are used to differentiate between different char structures, namely; porosity, pore structure, and wall thickness distribution (Bailey, 1990; Benfell et al., 2000; Chaves et al., 2018; Cloke et al., 2003). An automated system however has the capability to collect and measure more information than is possible with manual analysis (ie. geometric characteristics such as primary and secondary pore data, perimeter and wall distribution data etc) and this is one of the main drivers for development of such techniques. Sections 5.4.2-5 describe the implementation of a series of automated I.A techniques to classify char structures by accurately determining the three characteristics mentioned above.

5.4.2. Particle Porosity

Two kinds of porosity can be identified from char image analysis. Primary porosity; which describes the size and distribution of central pores and secondary porosity; which includes porous voids located on the char boundaries (Alvarez, 2001; Bailey, 1990). Whilst an operator can qualitatively assess these features, quantifying and measuring these properties manually has remained difficult due to fracturing and the varied heterogenous nature of the walls and internal pore structures. The relationship between overall porosity and char morphology however is well documented, and generally follows, in order of decreasing porosity; Tenuisphere > Tenuinetwork > Crassisphere > Crassinetwork > Fusinoid > Solids (E. Lester et al., 1996).

To determine area and ultimately the overall porosity of the individual structures the integrity of the char walls is vital. In Section 5.3.2.1, char fragments were grouped with the main char body and segmented from the mosaic without the need for the addition of extra material, however to determine porosity the system must fill the internal void space, which cannot be achieved with holes in the external walls. To do this, a modified implementation of the *active contours* method was used to accurately trace a 1x pixel thick char wall boundary before computing the particle area. Char void porosity was determined by calculating the difference in area between the filled and unfilled char structures after wall mending, as illustrated in Figure 5.11. As previously demonstrated, this method is particularly effective as it accurately traces the boundary of a char particle and can bridge large gaps without distorting or altering the char shape or internal pore structure.



a) Individual char structure with broken walls

b) Mended char structure. No. true pixels = 83910

c) Filled char area. No. true pixels = 337946 (75.1% total porosity)

Figure 5.11 *– Using active contour perimeter detection to determine overall porosity of chars*

The porosity distributions for each test char morphology are displayed in Figure 5.12. The results are consistent with those from previous researchers, with thin walled

tenuistructures exhibiting higher average porosity (75-95%), than thicker walled crassistructures (30-85%) and mixed/solid types structures respectively (1-20%). As with other works, this general relationship between morphology and porosity can be used an initial means of classification and a means of differentiation for particles that may have other similar characteristics (pore distribution, etc) which may otherwise make automated classification difficult. Notable though, is the spread and overlap of porosity between the different categories, which highlights the general unsuitability of purely porosity driven classification decisions.

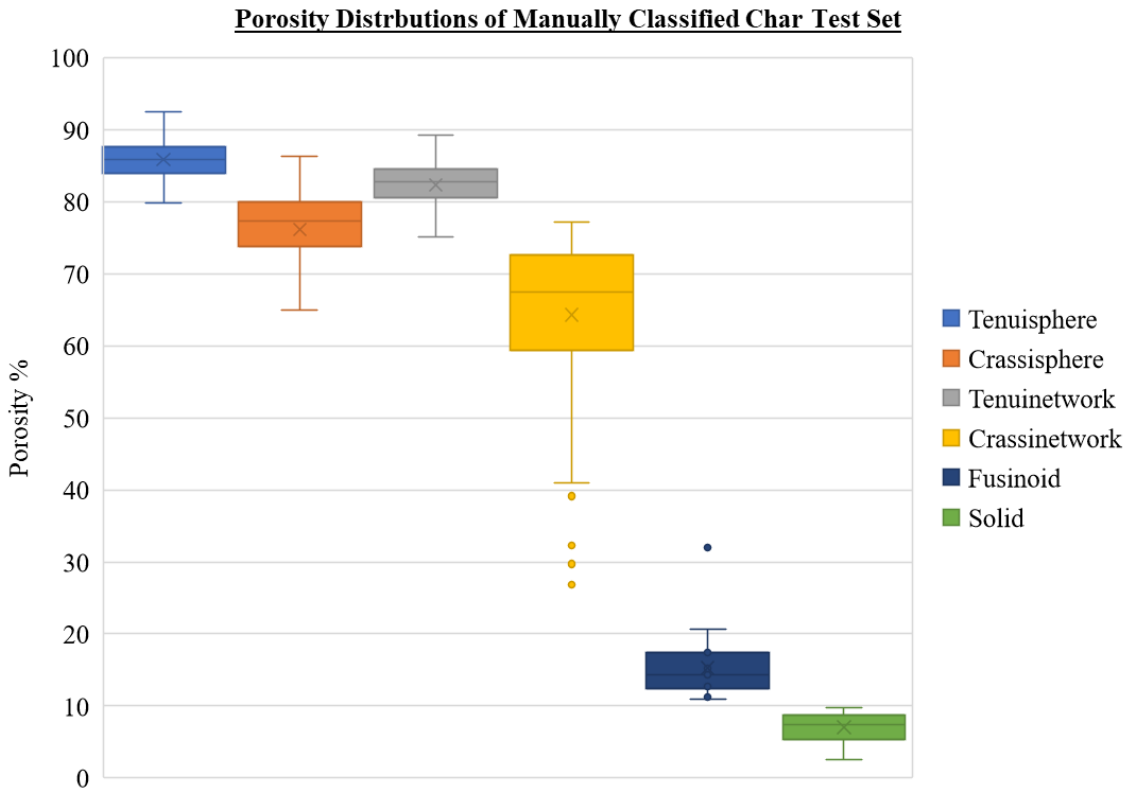


Figure 5.12 *- Porosity distributions of the different test char morphologies.*

5.4.3. Pore Distribution

During manual classification, an operator differentiates spheres from networks if they contain only 1-2 dominant voids and are therefore cenospheric in arrangement. Once the outer boundary has been determined, the area of the two largest pores as a percentage of overall porosity was computed. However, akin to fractured external char boundaries, problems can often arise if the internal structure of the chars is also compromised and incomplete. These broken pores then no longer have an enclosed perimeter and neighbouring pores can join and lead to the formation of 'super-pores'. An automated system using average pore size as a criterion will then often mis- classify networks as spheres as illustrated by Figure 5.13. To overcome this problem, an 'over-mend' closing function was implemented with a closing diameter of 150 pixels (19.32 µm) and 275 pixels (32.2 µm) for 53-75 µm and 106-125 µm chars respectively, which equates to ~33% average char diameter. Such an aggressive close was implemented to 1) ensure that even the largest broken pores were closed and 2) to deliberately 'over-mend' the internal walls, distorting the char structure and closing small pores, even if already intact. A visualisation of this process is illustrated in Figure 5.13c & f.

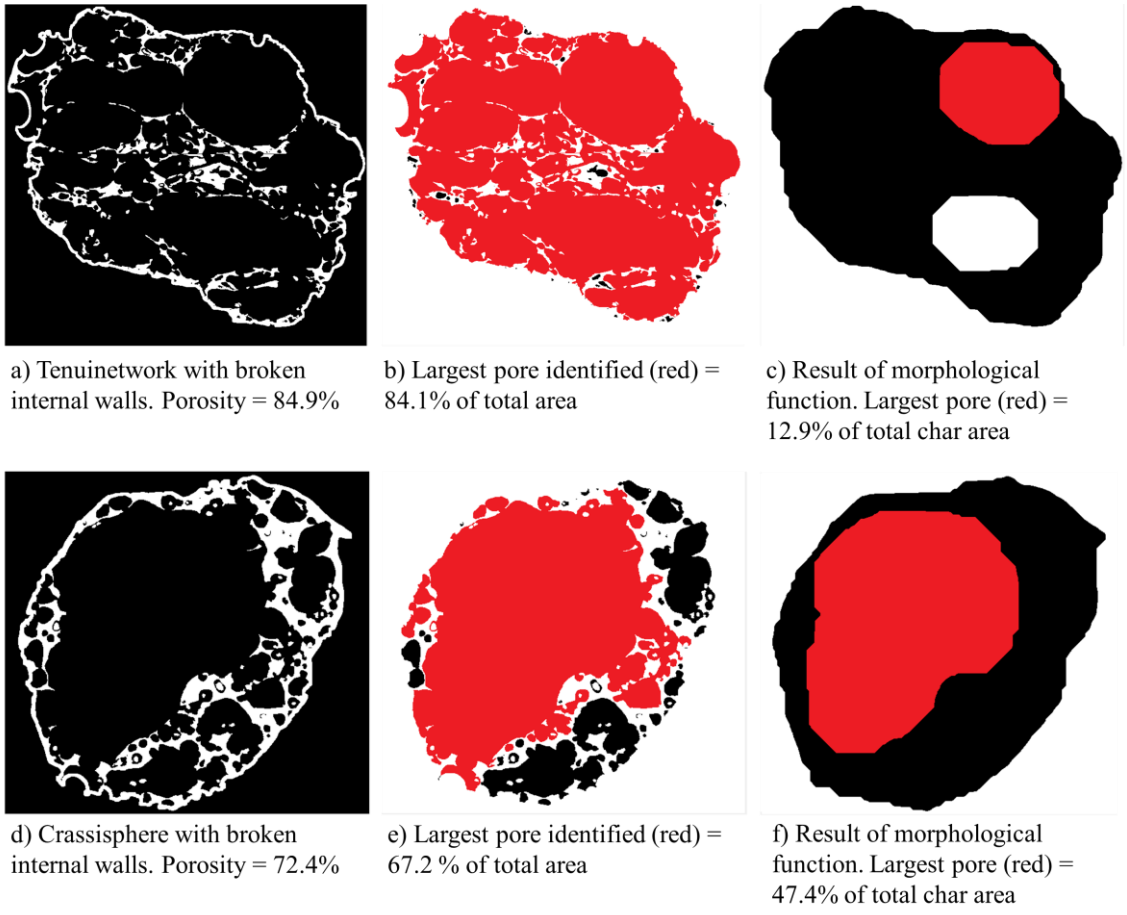


Figure 5.13 *– High largest void porosity values measured for networks with structurally compromised internal walls and a visualisation of 'over-mend' function on sphere and network structures.*

A comparison of this morphological change on then overall porosity of sphere and network morphologies is shown in Figure 5.14. The porosity of networks decreases dramatically (29% & 63%) as a result of the over-mending, whilst the larger dominant voids in spheres were large enough to remain relatively unchanged and exhibited a decrease of only 10% & 16% respectively. Crucially, the two ranges for the test set chars exhibit very little overlap, demonstrating the suitability of this relatively simple method as an effective classification discriminant for spheres and networks.

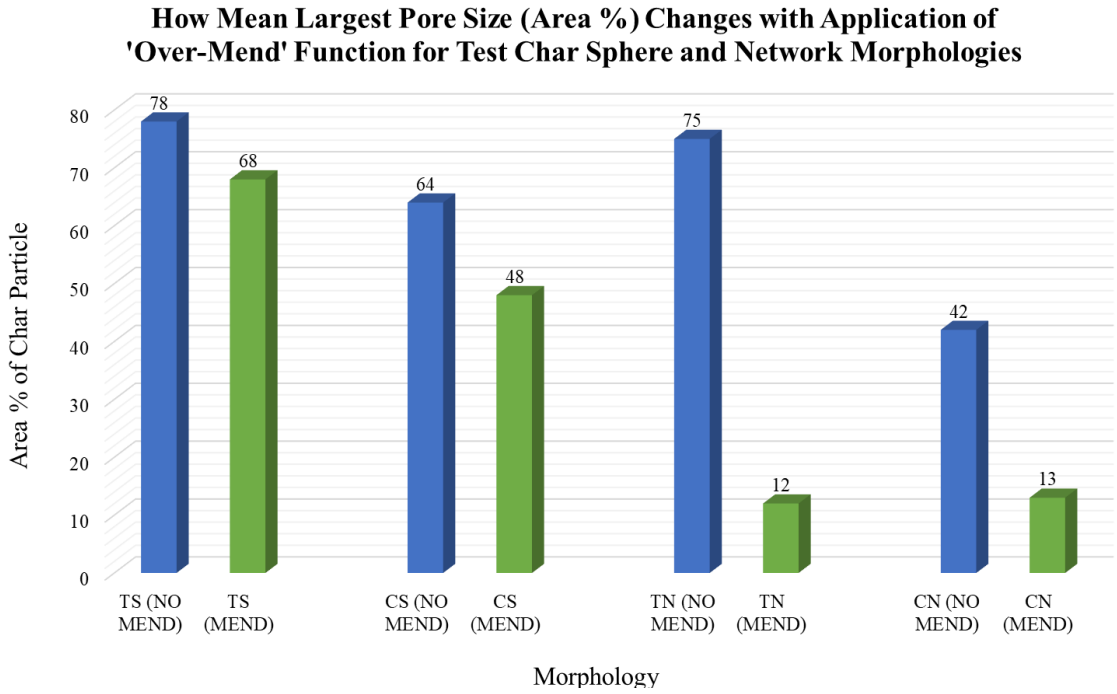


Figure 5.14 *– How application of the 'over-mend' function affects spheres and network type structures differently. (TS = Tenuisphere, CS = Crassisphere, TN = Tenuinetwork, CN = Crassinetwork)*

5.4.4. Char wall thickness distribution: 'The Pacman Function'

5.4.4.1. The Pacman Classification Function

Due to the inherently heterogenous nature of chars, determining the wall thickness of a char is the most subjective decision for a manual operator as it relies on an operator gauging by eye whether 50% of the wall material is above or below 3 µm. This introduces elements of judgement and interpretation which make obtaining consistent and repeatable results difficult. As described earlier, there has been previous work focused at automating the measurement char wall thickness with mixed success. Wu & Lester et al. measured wall thickness by drawing a series of chords from the centre of gravity. The overlap of the chords with the char walls enabled a series of thickness measurements to be made (T. Wu et al., 2006a). Chavez & X et al. used a machine

vision process to analyse shape and texture features in order to determine morphology (Chaves et al., 2018). The former suffered from the long processing times required to obtain accurate char wall data, whilst the later method was unable to accurately resolve chars into more than three classifications (High, Med and low reactivity) as a result of the greatly varying heterogenous structures of chars and the complexity of the analysis method.

In this section, a novel analysis method to classify chars by wall thickness and distribution coined ‘The Pacman Function’ is described, with the aim to rapidly compute information to enable the differentiation of thin and thick-walled morphologies. The Pacman Function is an evolution of the active contours process described in Section 5.3.2 and is so named as outer char particle pixels are eroded or ‘eaten’ away iteratively each time a new boundary is computed. With each ‘bite’, geometric measurements are performed to determine the change in voidage, char structure and the rate of char material removed within each iteration.

The function was implemented in two stages, described in sections 5.4.4.1-3 respectively, with the user defined variables differing in each to maximise the detection of key morphological differences in char structures.

The first stage is the initial differentiation of tenui- and crassispheres by a ‘gentle’ approach, where only the outer surface of the char structure is eroded. The second is the implementation of a more aggressive function where both internal and external structures are eaten in order to differentiate between networks.

5.4.4.2. Differentiating sphere structures

As with the boundary identification step described earlier, the active contour first identifies the outer boundary of each char particle. The program then erodes a 23 pixel (2.96 µm/~3 µm) layer of the char outer char wall and calculates the percentage of char material removed. Figure 5.15 shows examples of the determination of the initial boundary and removal of char material within ~3 µm of initial contour.

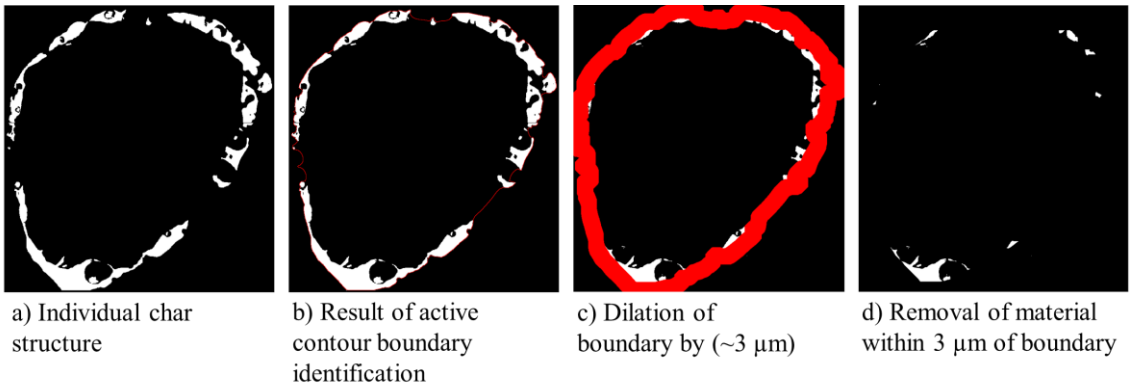


Figure 5.15 *- Determination of the initial boundary and the stages of removal for example char particles.*

This number of pixels was chosen as it gave the closest value to that of the 3 µm wall thickness value used in manual classification. Table. 5.1 displays the results of the function and the relationship between char morphology and the percentage of material removed after the 3 µm bite. On average, 73% of tenuisphere were eroded compared to 51% of crassinetworks, more crucially, is the only slight overlap (<4%) between the maximum erosion observed for crassispheres and minimum for tenuisphere test set chars, indicating that threshold of ~60% would be effective at distinguishing between most sphere structures. There was little difference observed between tenui- and

crassinetworks at this stage and was to be expected. Despite the inherent difference in char wall thickness, material is distributed throughout the whole network structure and not concentrated at the border region and differentiation made from this boundary based method could not be. In the original development of the program, 21 x 1-pixel bites were taken and measured iteratively, which increased processing times dramatically. Due to re-initialisation of the contour and retracing of the new char wall boundary with each step, more char material was removed for the same number of bites. However, there was not a substantial increase in precision or resolution observed when differentiating between the thin and thick spheres to justify increasing the processing time by a factor of 20.

Table 5.1 – Distribution of material removed by 3 μm Pacman erosion for char test set particles

Char Morphology	Mean % Removed	Max % Removed	Min % Removed
Tenuisphere	72.8	99.1	57.2
Crassisphere	50.8	60.7	39.4
Tenuinetwork	40.1	54.1	19.1
Crassinetwork	42.4	57.5	21.6
Fusinoid	24.7	32	14.1
Solid	22.0	32.6	18.5

5.4.4.3. Differentiating network structures

The second implementation of the Pacman Model was a more aggressively penetrating function. Unlike in the previous section, where active contours were used to identify char outer boundaries for separation and to distinguish between tenui-/crassispheres, a

more fluid version of the model was employed to penetrate the char structure and erode both internal and external wall structures iteratively in 3-pixel (0.39 µm) bites. Thinner walled tenuinetworks, with less internal char wall material, would then be eroded faster than thicker-walled crassispheres. This process was used in conjunction with the previous step to gradually erode the char particles iteratively. A comparison between the average erosion profiles for tenui- and crassinetworks is shown in Figure 5.16. Individual Pacman erosion profiles for all test char morphologies are attached as Figures B.1-7 in Appendix B.

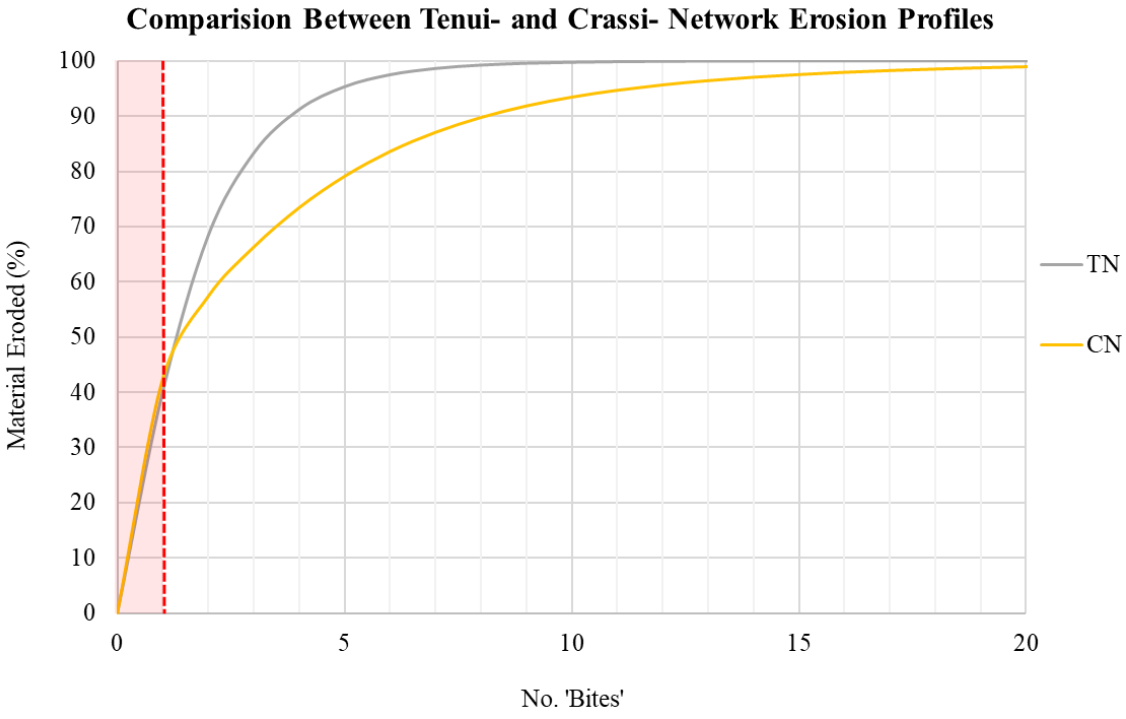


***Figure 5.16** – Pacman erosion profiles of Tenui- (TN) and Crassi- (CN) network test chars*

The area highlighted in red corresponds to the one-step erosion described in Section 5.4.4.1 used to distinguish between thick and thin sphere structures and the remaining profile (bites 2-20) therefore correspond to the second Pacman Model implementation. As the material within networks can be distributed anywhere throughout the structure,

almost identical 1x bite erosion values for both thick and thin network structures. However, when the more aggressive model is applied there is clear divergence in the profiles of the two-test char sets and the sub-structures are exposed to erosion and the thinner tenuinetwork structures are eroded substantially faster than the thick-walled crassinetworks and by 6 bites total (2.31 µm), ~99% of tenuinetwork material has been removed. This is to be expected as erosion is now occurring from both sides of the char walls (corresponding to 4.63 µm total) whilst only ~85% of crassinetwork material has been removed by this point as by definition more of their wall structure must exceed 3 µm in width. This difference in erosion profile, along with overall porosity discussed earlier, was then implemented in the system to discriminate between thin and thick-walled network structures.

5.4.4.4. Determining the presence of mixed structures

Differentiating mixed char structures from others is difficult due to the irregularity and the spread of morphological features observed within the morphology, and as they normally occur in relatively low quantities, previous studies have grouped mixed-dense/porous particles into to the crassisphere or crassinetwork categories respectively to simplify the classification process. In addition to information described above however, there is potential for the erosion model to be implemented to differentiate mixed dense/porous chars from others. Figure 5.17 shows a comparison of the profiles for crassistructures and the mixed test set chars; the areas in red and blue highlight the portion of the profiles used in the determination of classification thresholds discussed in previous sections whilst the threshold illustrated in red indicates a potential threshold for distinguishing mixed structures.

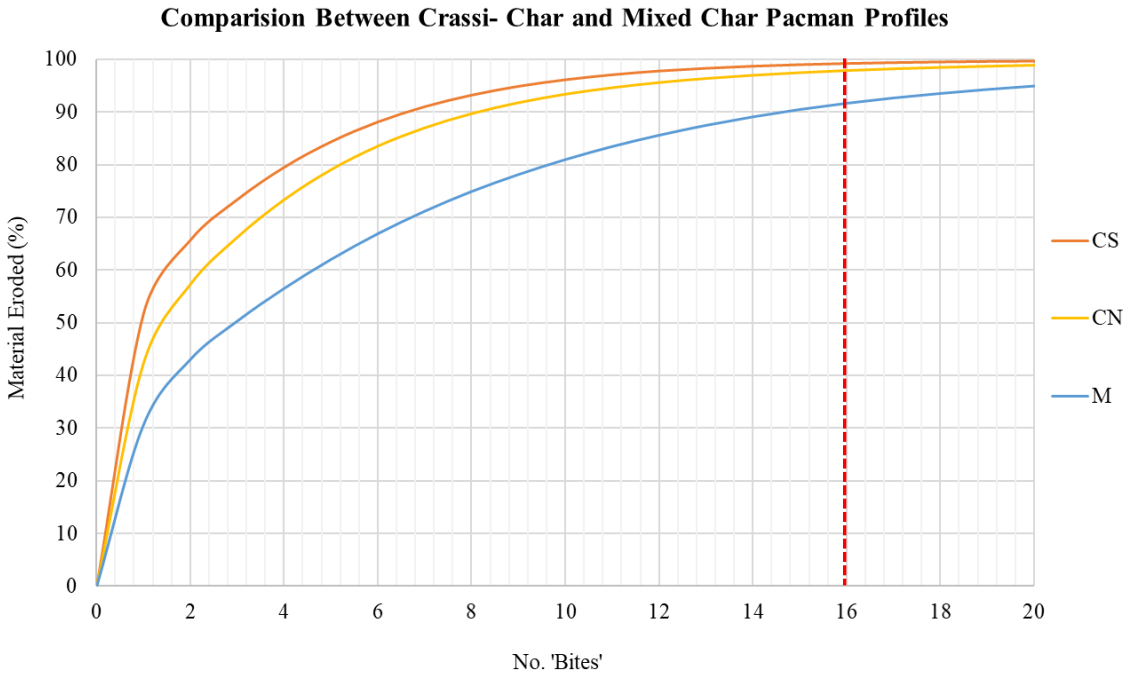


Figure 5.17 *– Comparison between the Pacman erosion profiles of Crassi-sphere/networks and mixed char morphologies*

Mixed chars often contain substantial areas of solid/low porosity which due to low surface area is eroded slowly. The residue of this structural element that remains after significant erosion has occurred could be used to as a distinguishing criterion for future developments of the classification system. This feature combined with porosity data obtained in previous sections can allow for the effective differentiation of mixed chars from other morphologies.

5.4.5. Char classification criteria Summarised: Logic Tree

The criteria determined in sections 5.4.4.1–4 are summarized as the logic tree shown in Figure 5.18. The basis for the classification is that an initial separation of the char morphologies is made using overall porosity of the particles before those chars that cannot be categorised solely with porosity are classified by information obtained by deliberate distortion of the internal wall structure of the chars and the individual Pacman Model profile for each char. Mean erosion profiles for each char morphology test set illustrating the difference in erosion for thick and thin chars are shows in Figure 5.19. Another observation that can be made at this point is how the Pacman erosion profiles are akin to proposed burnout profiles of different char morphologies (T. Wu et al., 2006b) with thinner chars are eroded faster than thicker chars with slower erosion, like char burnout. There could therefore be potential to develop the Pacman model into a novel, completely image-based burnout system, negating the need for complicated kinetics.

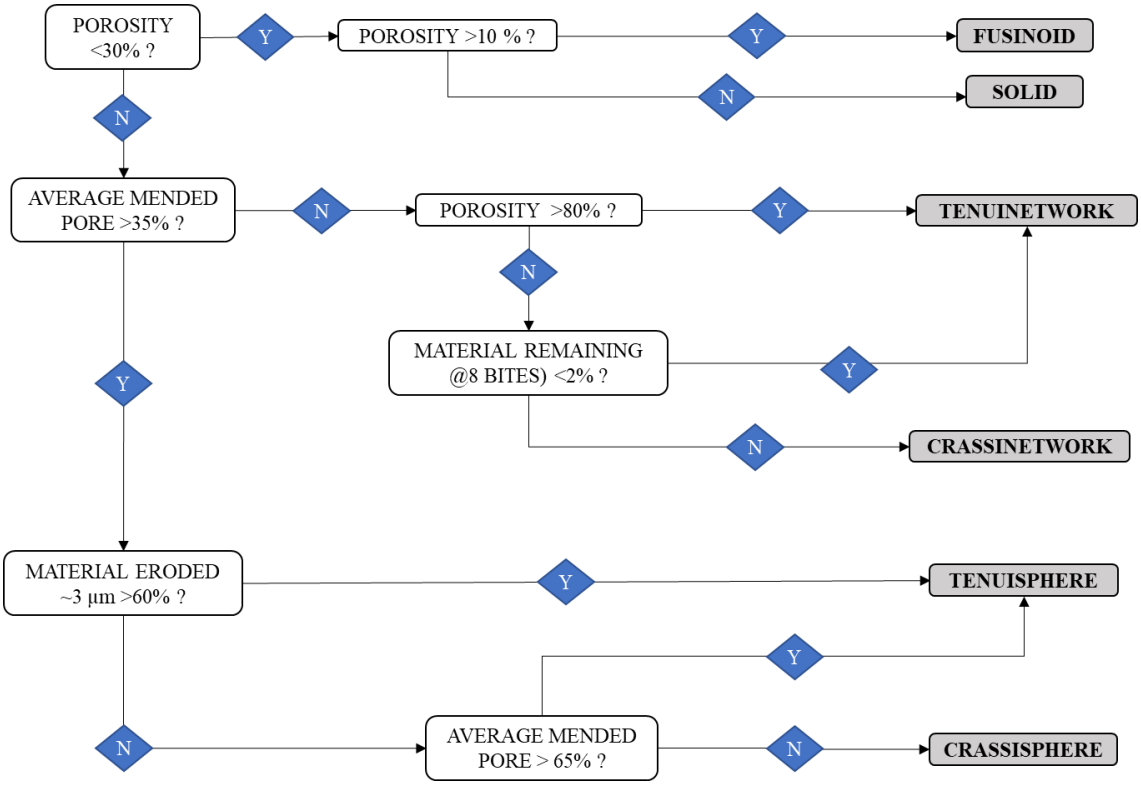


Figure 5.18 *– A logic tree constructed to categorise each individual char into a specific ICCP morphology*

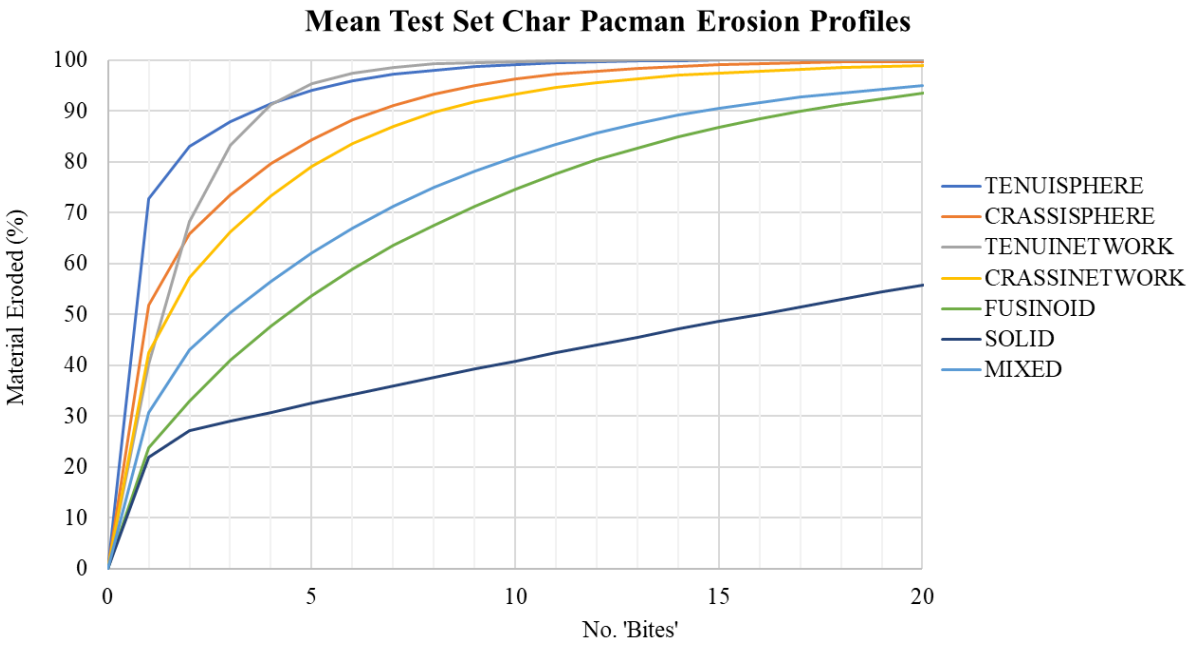


Figure 5.19 – *Average Pacman erosion profiles for each test char morphology used to determine thresholds for classification system.*

5.4.6. Test Set Classification Results

The automated results for the test set chars are shown in Table 5.2. Generally, the system was very effective at accurately classifying the test set chars, particularly when classifying thin-walled morphologies, with 479 of the 500 test chars correctly classified. The classification of crassinetworks performed the worst (93%), indicating that some crassinetworks exhibit wider discrepancy in wall thicknesses than tenuinetworks (98%) resulting in overlap of the threshold. Fusinoid and Solid structures performed best (96% and 100% respectively) which is to be expected these chars exhibit the smallest inherent variation in morphological features. It must be noted that only 'ideal' example chars, with definitive and distinctive morphological features unique to each char type were compiled into each test category. This was to reduce ambiguity during the development of the logic tree criteria described above. Difficult to categorise particles with features that lie closer to the discriminative thresholds that would rely more on the judgement and experience of the operator may present more of a challenge to the system.

Table 5.2 – Test set automated classification results

	Automated Classification %					
Test Set	**TS**	**TN**	**CS**	**CN**	**F**	**S**
Tenuisphere (TS)	99	0	1	0	0	0
Tenuinetwork (TN)	0	2	0	98	1	0
Crassisphere (CS)	7	0	91	2	0	0
Crassinetwork (CN)	0	5	0	93	2	0
Fusinoid (F)	0	0	0	4	96	0
Solid (S)	0	0	0	0	0	100

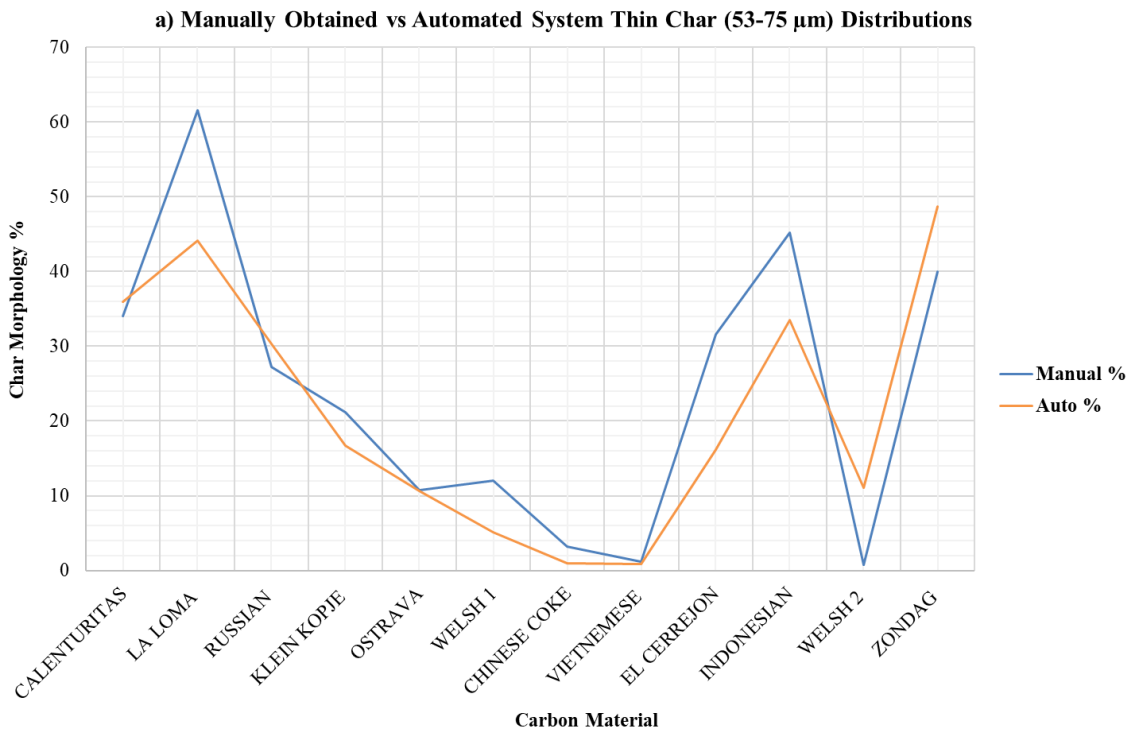
5.5. Section 3: Comparison of Automated and Manual Analysis Results

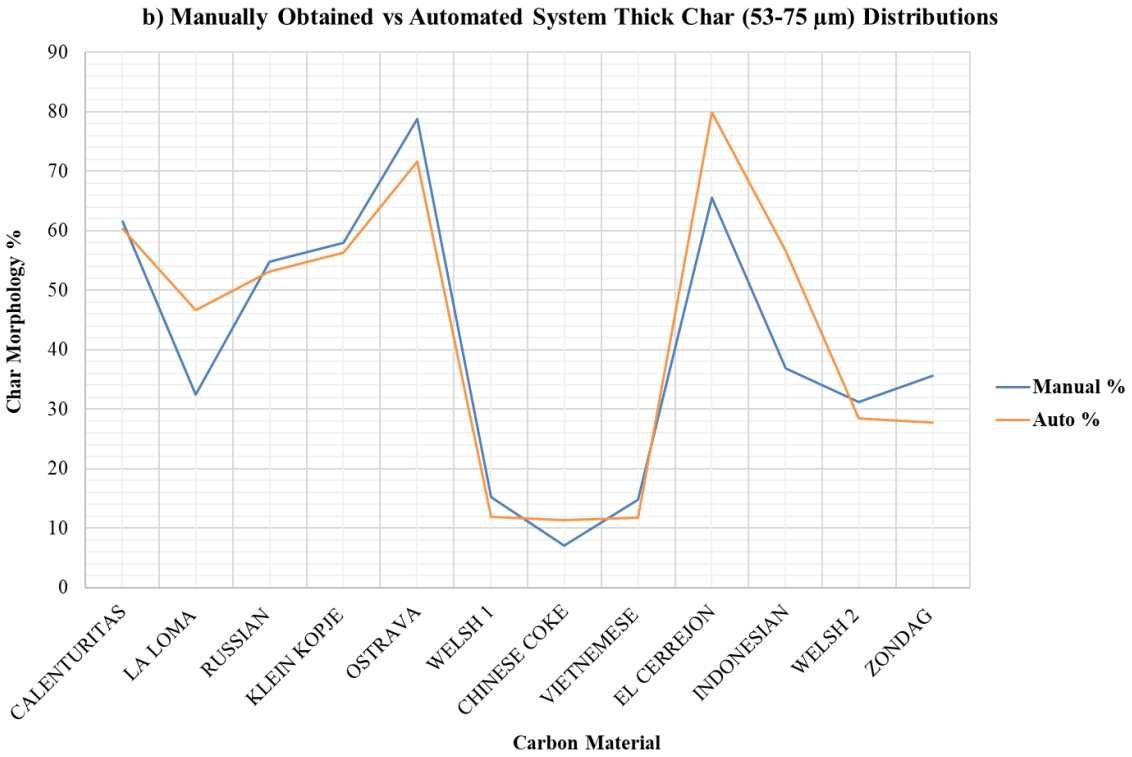
To test the capability of the automated image analysis classification technique described in this Chapter, 'real' chars generated in a drop-tube furnace from coal sets 1 and 2 (totalling 17 different coals in two size fractions) were analysed. As discussed earlier, to simplify the classification system and allow comparison to previous methods, mixed char (dense/porous) particles were added to the crassisphere or crassinetwork groups based on their pore structure. Individual Pacman erosion profiles for all samples are attached in Appendix B.

The results of the automated and manual char analysis for the 12 samples in coal set 1 (53-75 μm) are shown in Table 5.3. Figures 5.20a-c plot the comparison between automated and manually classified thin, thick and solid chars respectively.

Table 5.3 - Comparison of Char Morphology Data Obtained by Automated and Manual Char Image Analyses for Coal set 1.

CHAR SAMPLE	CHAR MORPHOLOGY											
	TS		TN		CS		CN		F		S	
	M %	A%	M %	A%	M %	A%	M %	A%	M %	A%	M %	A%
CALENTURITAS	8	11	26	25	45	39	16	22	3	2	1	2
LA LOMA	21	14	40	30	26	37	6	10	4	2	2	7
RUSSIAN	14	19	14	12	40	32	14	21	12	13	6	4
KLEIN KOPJE	9	12	12	5	22	25	36	31	13	15	8	12
OSTRAVA	6	5	4	6	56	52	23	19	10	18	1	0
WELSH 1	4	1	8	4	9	9	6	3	12	13	61	70
CHINESE COKE	1	0	2	1	2	1	5	10	70	63	20	25
VIETNEMESE	1	0	0	1	6	0	9	12	2	6	82	81
EL CERREJON	24	13	8	3	46	60	19	20	2	2	0	2
INDONESIAN	21	25	24	9	27	37	10	20	14	8	4	2
WELSH 2	0	0	0	11	6	14	25	14	1	2	67	59
ZONDAG	1	1	39	48	6	10	30	18	18	14	7	10


a) Manually Obtained vs Automated System Thin Char (53-75 µm) Distributions
Char Morphology %
70
60
50
40
30
20
10
0
CALENTURITAS
LA LOMA
RUSSIAN
KLEIN KOPJE
OSTRAVA
WELSH 1
CHINESE COKE
VIETNEMESE
EL CERREJON
INDONESIAN
WELSH 2
ZONDAG
Carbon Material
Manual %
Auto %


b) Manually Obtained vs Automated System Thick Char (53-75 µm) Distributions
Char Morphology %
90
80
70
60
50
40
30
20
10
0
CALENTURITAS
LA LOMA
RUSSIAN
KLEIN KOPJE
OSTRAVA
WELSH 1
CHINESE COKE
VIETNEMESE
EL CERREJON
INDONESIAN
WELSH 2
ZONDAG
Carbon Material
Manual %
Auto %

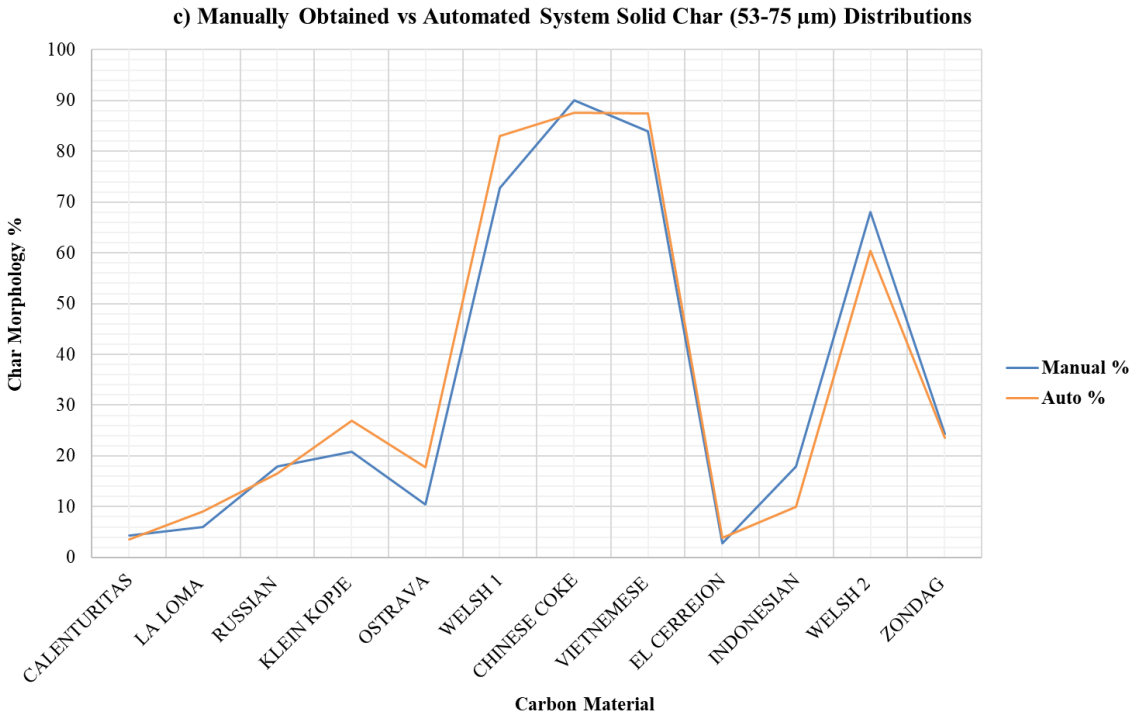


Figure 5.20a-c *- Comparison between manual and automated classification results for a) thin, b) thick and c) solid chars for 53-75 µm char set.*

Generally, manual and automated analyses correlate well. Of the 84 individual morphology categories, 73 differ by less than 8% with all results varying by less than 15%. Similar correlation is observed when the morphologies are grouped as the major thin/thick/solid categories; a particularly important classification as many of the morphology-based burnout models use these classifications (Cloke et al., 2003; T. Wu et al., 2006b). There are some samples where results do differ significantly; e.g. the manual analysis of the percentages of thin and thick char morphologies in Indonesian coal were approximately 45% and 37% respectively, whilst the automated analysis found 34% and 57% respectively. The possible explanation for this is that during the repair stage of the char analysis, some of the broken/fractured internal walls of the networks were not being mended properly and this led to these structures being

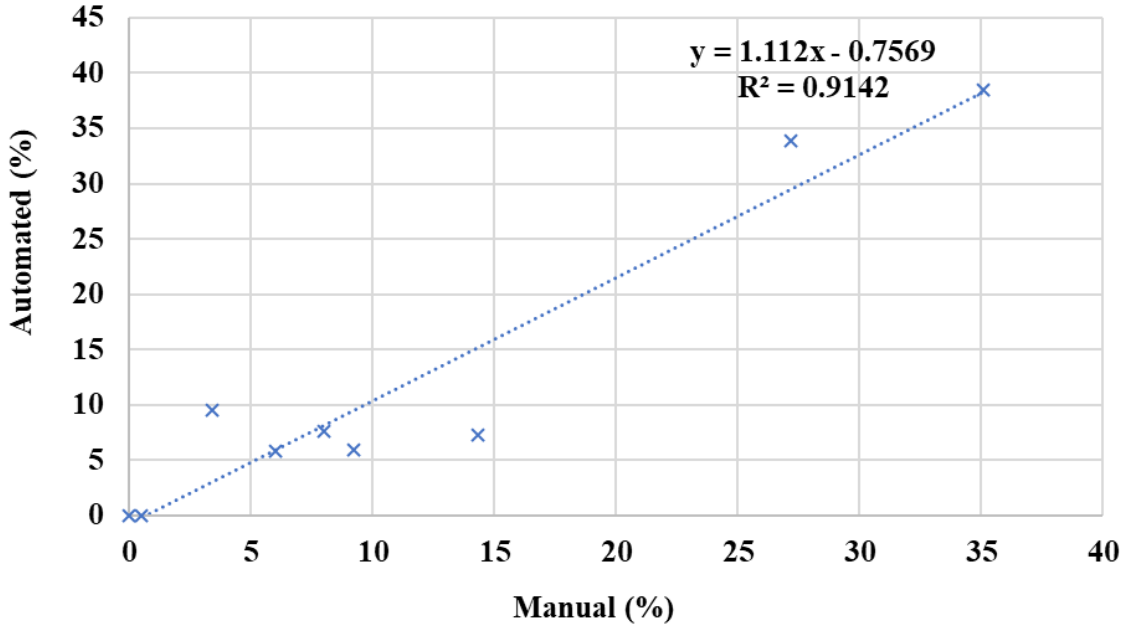
classified as either tenui-/crassisphere instead. In the case of La Loma and El Cerrejon, the image analysis system identifies more tenuispheres than with manual analysis. By implementing a logic tree of decisions, the system criteria for each char type are predefined and absolute and measurements of wall material eroded made to 4 decimal places. During manual analysis only a basic estimate of wall thickness and porosity is needed, which requires discretion as well as experience. For this reason, it is unlikely that the manual and automated analyses will be in absolute agreement.

Table 5.4 displays the results of automated and manual char analysis of coal set 2 (106-125 μm) for thin thick and solid chars whilst Figures 5.21a-f displays the correlation between automated and manually obtained techniques. Raw classification results are attached as Table B.1 in appendix B.

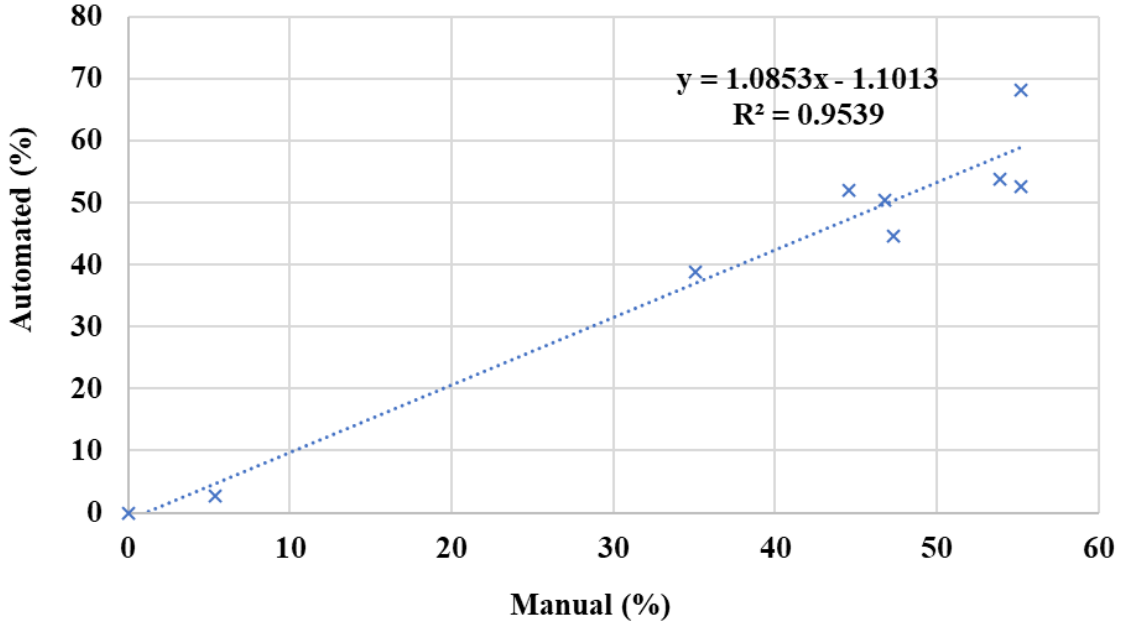
Table 5.4 - Comparison of Char Morphology Data Obtained by Automated and Manual Char Image Analyses for Coal set 2.

CHAR SAMPLE	MORPHOLOGY					
	THIN		THICK		SOLID	
	M %	A %	M %	A %	M %	A%
1	12	17	63	59	25	23
2	17	21	64	60	19	19
3	23	14	63	70	13	16
4	19	12	64	79	17	9
5	45	43	55	56	0	1
INDONESIAN	23	30	52	49	25	22
OSTRAVA	14	13	61	65	25	23
EL CERREJON	33	37	64	58	3	5
VIETNEMESE	0	0	0	0	100	100

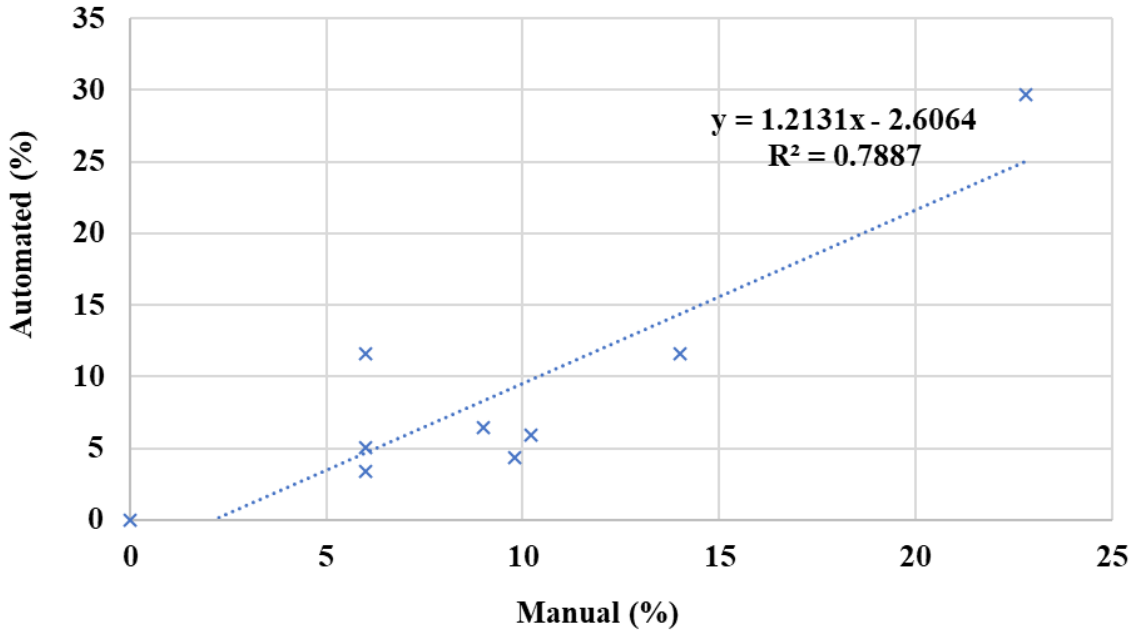
a) Correlation between Manual and Automated Char Classification: Tenuisphere



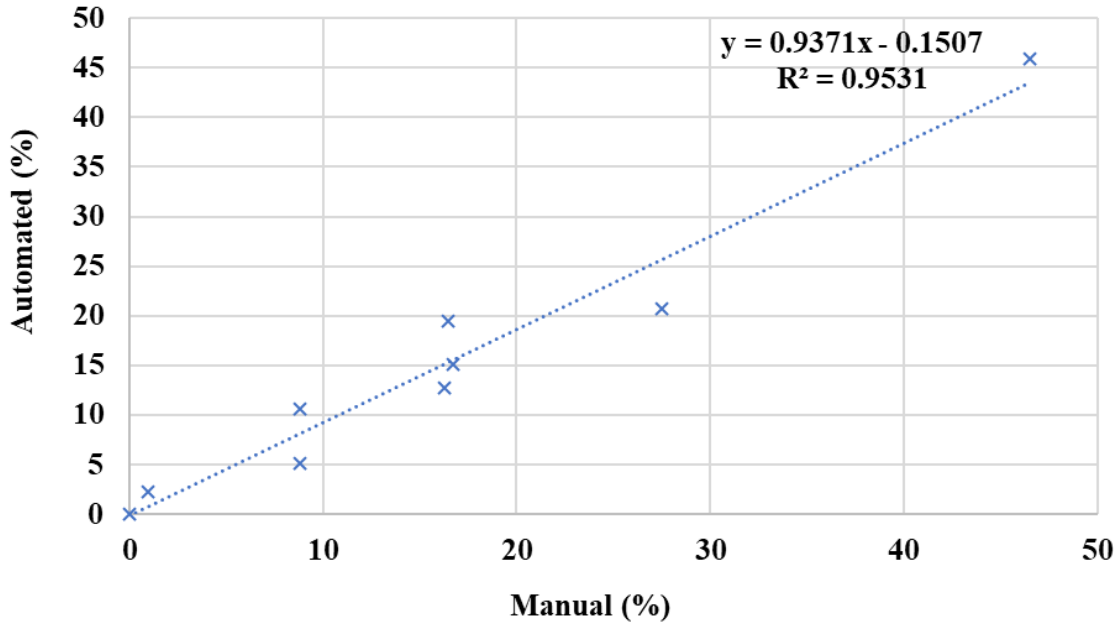
b) Correlation between Manual and Automated Char Classification: Crassisphere

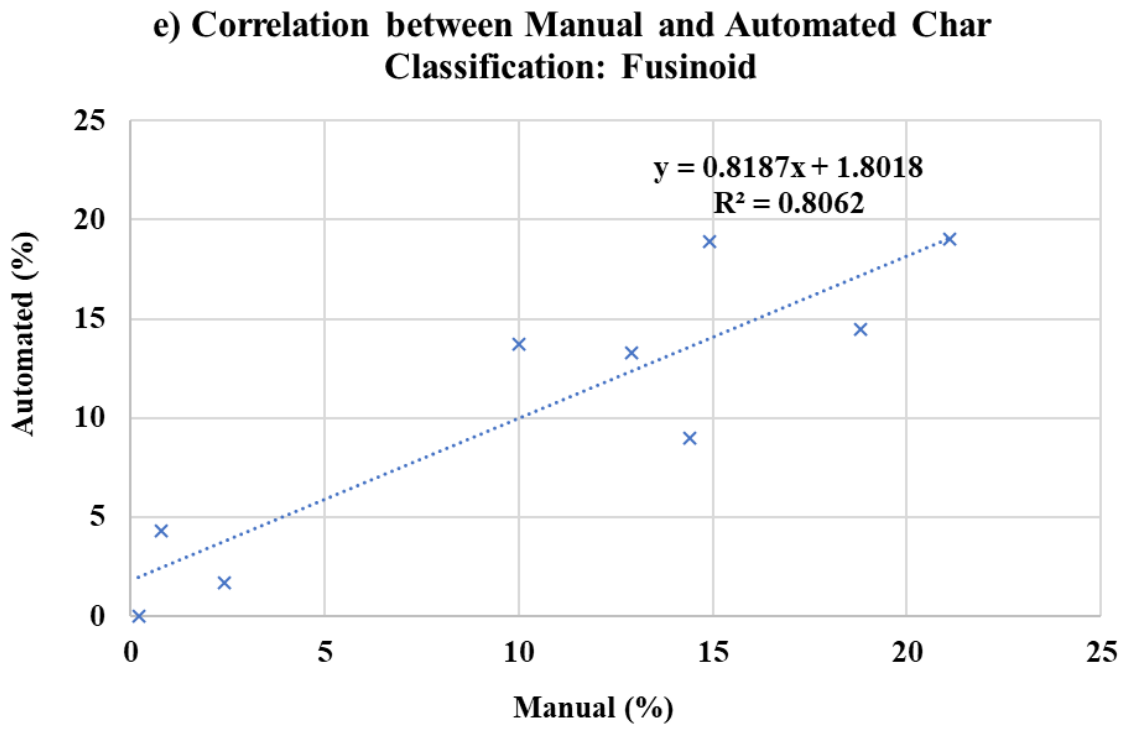


c) Correlation between Manual and Automated Char Classification: Tenuinetwork



d) Correlation between Manual and Automated Char Classification: Crassinetwork





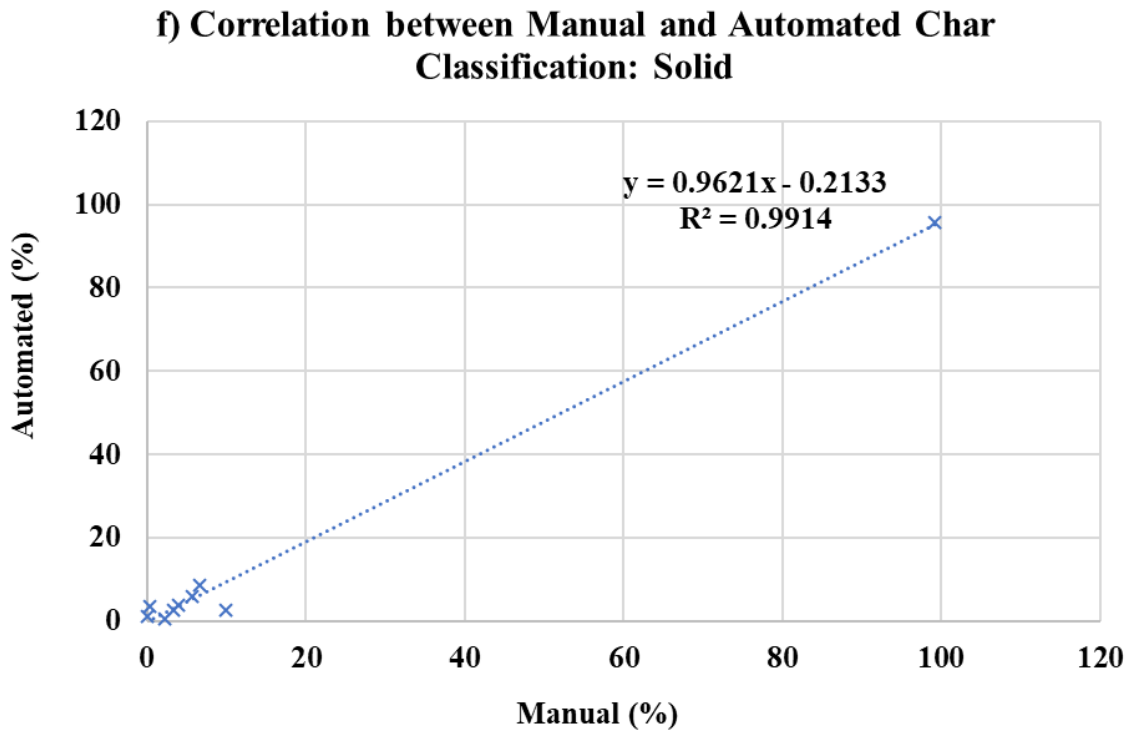


Figure 5.21a-f *- Comparison between manual and automated classification results for a) Tenuisphere, b) Crassisphere, c) Tenuinetwork, d) Crassinetwork, e) Fusinoid and f) solid chars for 106-125 µm char set.*

For this larger size fraction, classification results from the image analysis system generally match more closely with those from manual analysis with all but one sample varying by a maximum of just 8% with a maximum variance of 13%. The possible explanation for this could be due to the increased prevalence of solids (which are generally easier to segment and classify by porosity as discussed earlier) and thicker walled chars which are less likely to fracture and more likely to be successfully extracted completely from the mosaic image.

The speed at which individual char images are analysed and classified by the automated system is approximately 3 min^{-1}. There are no official standards regarding char analysis, however if the same standards for error are adopted as those for manual maceral analysis standards, 500 particles could be assumed to be sufficient with respect to repeatability/reproducibility and would therefore require approximately 25 mins. This is approximately 6 times faster than previous work from (T. Wu et al., 2006a) analysing individual char particles and whilst this system remains slower than that developed by Chavez et al., the classification capabilities are far greater.

5.6. Conclusions

This Chapter describes the development of a fully automated image analysis technique for the assessment and morphological classification of char particles into one of six morphological categories that are relevant to determining combustion potential of a pf fuel. The system displays similar classification capabilities and enhanced processing speed compared to previous binary morphological analysis work and superior precision compared to machine learning and porosity based-systems. Novel use of several active contour implementations to separate, repair and analyse the morphological properties

of individual char particles is proposed. There is also the potential to expand the current capability to include mixed porous/dense structures in the future. One key feature of the program is the versatility of the wall mending process that, without distorting the char structure or morphological features, can rebuild even substantially splintered structures and appears to be effective on chars of various sizes. There is potential of further developing one proposed technique, the “Pacman Model”, to simulate char burnout in an entirely image-based, kinetics free char combustion model which is described in Chapter 6.

CHAPTER 6. Development of an Image-Based Char Burnout Simulation: "The Pacman Model"

The ability to predict how a coal will perform during pulverised fuel combustion is vital, as the rate of char burnout plays a important role in determining the carbon loss in ash and the design of the boiler. Modelling coal and char combustion requires the determination of oxygen transport and kinetic parameters (R. Hurt et al., 1998) (Ma & Mitchell, 2009) and is a complex challenge owing to the complex heterogenous nature of char structures. In most char combustion models, to simplify the effects of structure, the particles are often assumed to be spherical, uniformly porous and solid in nature when used to calculate the contribution of diffusional and chemical contributions (Gilot et al., 2017). Generalised assumptions concerning char structure and porosity are far from ideal, as chars from the same coal can exhibit a large range of possible structures and porosities, which has led to mixed simulation results (T. Wu et al., 2006b). None of the char combustion models developed so far have simulated burnout of carboneous char material on individual particle images, mainly due to the difficulties in accurately obtaining accurate and complete structural information from a combustion intermediate in sufficient quantities.

This Chapter describes the development of a novel, image-based char burnout simulation to rapidly predict the burnout potential of a fuel during pulverised fuel combustion. The model, coined the 'Pacman Burnout Model', iteratively erodes individual char particles to simulate carboneous material oxidation. Being devoid of any complex kinetic calculations and generalisations surrounding particle structure and porosity distribution, this method is a relatively simple and robust tool for power generators

6.1. Model Design

6.1.1. Overview

The Pacman Burnout Model is an evolution of the active contour method described in Chapter 5.3, which was employed to first separate and then differentiate chars of different wall thicknesses. Active contours were used to first compute a 'combustion front' around a char particle before subsequent erosion of the carboneous material situated at this boundary. The front is then recalculated on the new char structure and the process is repeated as shown in Figure 6.1. The active contour model, first developed by Kass 1988, can be represented in its simplest form as equation 6.1, where the contour is computed from an initial position (char particle boundary) to a new location based on a gradient descent minimisation method (Kass et al., 1988). An applied force ($F_{contour}$) shrinks or expands the contour in a manner controlled by image content and predefined user inputs (equation 6.2). Definitions and full set of energy minimisation equations were discussed in Chapter 5.3.

$$F_{contour} = -\sum_{i=1}^{n} \nabla E_{contour}(\bar{v}_i) \quad \textbf{(eq. 6.1)}$$

$$(-/+)\, \nabla E_{contour}(\bar{v}_i) = -(\omega_{ext} \nabla E_{ext}(\bar{v}_i) + \omega_{int} \nabla E_{int}(\bar{v}_i)) \quad \textbf{(eq. 6.2)}$$

$\bar{v}_i$ = Initial contour position
$E_{contour}$ = Calculated energy minima
E_{ext} = External energy
E_{int} = Internal energy
ω = User defined weights
n = Number of iterations

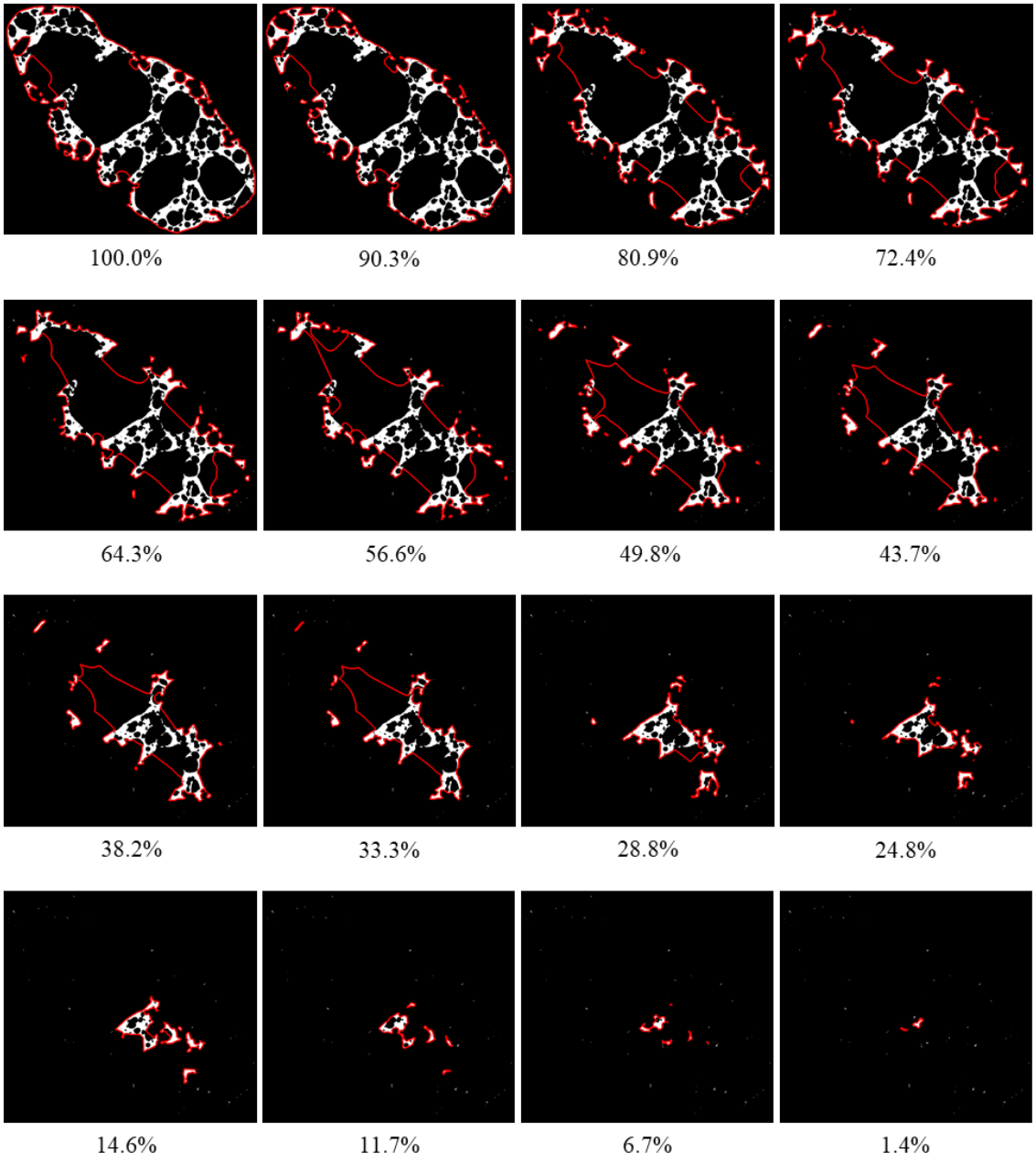


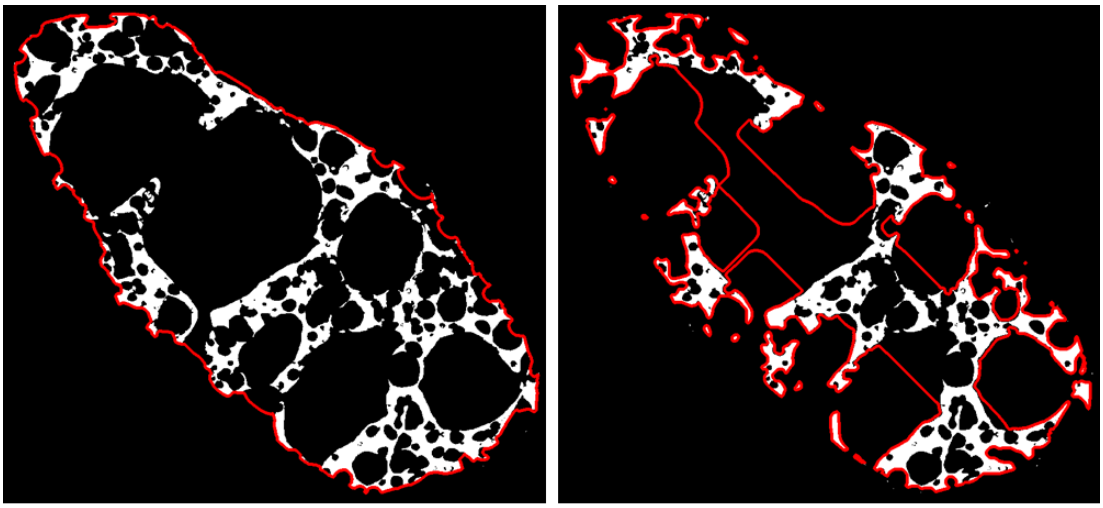
Figure 6.1 *– Visualisation of combustion front location and char erosion process computed using the Pacman Model as function of % material eroded.*

Implementing active contours in this way is well suited for simulating char combustion owing to;

- The nature of the energy minimisation function shrinks the contour inwards in a unidirectional fashion simulating oxygen diffusion from the gas stream to the particle surface.

- The 'bend' and 'stretch' behaviour of the contour and how it interacts with different pore sizes and char morphology can be predetermined to control the degree of contour penetration into the structure, as illustrated in Figure 6.2 and the iterative nature of the process allows user-inputs to be varied with each computation if necessary.

- The rate and progress of char removal, along with other parameters can be visualized and measured during simulated combustion, thus enabling the balance of kinetic and diffusional control for each char image to be estimated during simulated combustion by computing an estimation of the effectiveness factor (η) first described in Chapter 2.5 and defined in equation 6.4.



a) Combustion front computed at particle surface

b) Increased pore penetration computed using modified model settings

Figure 6.2 *– Impact of varying user-defined inputs on pore penetration of simulated combustion front*

6.1.2. Advantages of an Image Based Burnout Model

Computing a combustion front using individual char particle information contained within images presents a number of distinct advantages over more traditional kinetic modelling techniques. As a char particle's structure drastically evolves locally during the combustion process, parameters such as particle porosity, pore size, apparent carbon density, and specific surface area should be considered as local quantities, which evolve inside the particle along this combustion process. As a result, the application of active contours directly with 'real' char data contained within particle images has a distinct advantage over traditional char combustion modelling which cannot account for this uniquely evolving porosity gradient that appears for each individual particle during combustion. The only way to account for the evolution of the porous structure during the combustion process is to consider local pore and char material parameters to determine particle behaviour during the combustion process.

6.1.3. Approach to Development

As shown in Chapter 5, the outer boundary of char particles can be accurately traced using active contours. The process of determining the degree of pore penetration and the rate of material removal required with each iteration began by testing how varying active contour settings would affect the simulated combustion of different char morphologies. An estimation of the effectiveness factor (η) was calculated for each contour setting to visualise these changes using equation 6.4

As discussed in Chapter 2.5, the effectiveness factor defines the degree of kinetic and diffusional control during char combustion and can be visualised for a char particle during combustion as a function of time and conversion as shown in Figure 2.2 (Gilot, 2017). At high temperatures and heating rates (~1300 ^{o}C and >10/5 Ks^{-1}

respectively), like those in industrial furnaces and replicated in a drop tube furnace (DTF) it is thought that char combustion occurs primarily between combustion regimes II & III (Hurt, 1998, Ma, 2009). At the very beginning of the combustion process the combustion rate is very slow due to low particle temperatures ($\eta \approx 1$) but after rapid heating a mixed diffusional and kinetic regime occurs that is primarily under diffusional control ($\eta \approx 0.1$). Towards the end of combustion, the diffusional limitations decrease due to extensive mean pore size increase and the reaction here is close to being under kinetic control ($\eta \approx 1$). Initial investigations were therefore aimed to design and implement the Pacman model on individual particle images to simulate the above into two distinct stages;

Stage 1: Diffusional control/ Regime III (~0-50% conversion) – Material conversion occurring primarily within a shell at the particle surface with minimal pore penetration.
Stage 2: Decreasing diffusional control/ Regime II (~50-100% conversion) – Progression of the diffusion front through the char structure with increasing porosity.

The initial phase of kinetic control accounts for only approximately <2.5% of carbonaceous material conversion and is sufficiently short-lived and relatively inconsequential to overall burnout to not be considered in the model.

The effectiveness factor (η) depends directly on the Thiele diffusion modulus (Φ), which is defined as the relationship between the catalytic activity (determined by specific surface area, density, stoichometry, kinetic rate and diffusibility) and the size of a particle (Gilot et al., 2017). By analysing the changing char particle structure with each iteration, the rate of material eroded/converted at the 'combustion front', the

surface area, effective diffusibility and char radius can all be measured with each iteration to enable the estimation of the effectiveness factor via equations 6.3 and 6.4. This was used to tailor the balance of kinetic and diffusional control on particles in agreement with stages 1 and 2 described above. Initial investigations consisted of measuring the impact of varying user-defined inputs on the effectiveness factor for a test set of manually classified char particles and consisted of 100x Tenuisphere, Crassisphere, Tenuinetwork, Crassinetwork examples and 50x each of Mixed and Solids obtained from large mosaic images by way of the methods discussed in Chapter 4.

$$\Phi = R_p \sqrt{\frac{k_s A_c \rho_c}{\Lambda D^e_{O_2}}} \quad \textbf{(eq.6.3)}$$

$$\eta = \frac{3}{\Phi}\left(\frac{1}{\tanh \Phi} - \frac{1}{\Phi}\right) \quad \textbf{(eq.6.4)}$$

R_p = particle radius, m
k_s = kinetic constant, m/s
A_c = Carbonaceous specific surface area, m^2/kg
ρ_c = Density of carbonaceous particle material, kg/m^3
Λ = molar stoichiometric factor, mol-C/mol-O_2
$D^e_{O_2}$ = Effective diffusivity of oxygen within the particle, m^2/s

6.1.4. Considerations

As previously discussed, as the initial phase of kinetic control accounts for only a small fraction of material conversion and is sufficiently short-lived to be disregarded. Also, in this model, the boundary layer that accounts for the diffusional limitation of oxygen

transport is assumed to be at the particle surface and char material is assumed to burn evenly and with constant density at the computed combustion front. Although chars often have irregular shapes which introduces a multidimensional temperature gradient over the whole particle, char particles are assumed to behave as if they were spherical to allow radial and angular variations in surface temperature to be ignored. The impact of ash films or other mineral interactions, whilst considered in other simulation work, does not feature in this model and it is assumed that the ash distribution is uniform and has no impact on the char reaction kinetics and oxygen diffusion. This is in part due to the little evidence for the common existence of ash films encapsulating char structures (Lunden, Yang, Headley, & Shaddix, 1998) (R. H. Hurt & Davis, 1994) (Senneca, 2008). Rather, it has been shown that the high particle temperatures attained during active char combustion may soften or melt the ash back into the char matrix or either bead into distinct ash structures on the surface instead (Murphy & Shaddix, 2010). This assumption allowed simulation calculations to be performed based on the ash-free particle properties. Incorporating inhibitory mineral effects could be an area for further development in the future, but whilst mineral location and degree of liberation can be detected by optical microscopy (Comino et al., 2010), specific minerals could not be identified in these images and their effects were not included in the burnout simulation.

6.2. Development of the Pacman Burnout Simulation

6.2.1. Coal Samples for Testing and Development

As part of a collaborative project, funded by the Australian Coal Industry's Research Program (ACARP), researchers from University of Nottingham undertook work with the Commonwealth Scientific and Industrial Research Organisation (CSIRO) to assess

a suite of Australian thermal coals. The primary goals were to use several image analysis techniques, including CSIRO's commercially available *Coal Grain Analysis (CGA)* (Comino et al., 2010; O'Brien et al., 2007) to analyse and assess the combustion potential of a suite of five Australian thermal coals (Coal Set 2: 106-125 µm size fraction) and their daughter chars. This project presented a unique opportunity to use a set of 'real' chars generated in conditions like that of an industrial boiler at different residence times to develop the model. In order to further validate the predictive capabilities and to test the versatility of the model in regards different particle sizes, another set of five coals (Coal set 3: 53-106 µm) from Indonesia, Venezuela South-Africa and United Kingdom were also analysed. Maceral analysis, %unreactives and Rank information of the Australian and international coals used in this study are presented in tables 6.1 and 6.2 respectively.

Table 6.1 – Australian coal sample details (106-125 µm)

	% Composition and Rank				
Sample Ref	**1**	**2**	**3**	**4**	**5**
Vitrinite	44.4	46.8	67.6	64.8	98.4
Liptinite	0.4	0.0	0.0	0.0	1.6
Inertinite	55.2	53.2	32.4	35.2	0.0
% Unreactives	69.9	58.5	95.5	27.4	2.8
Rank	1.2	1.2	1.6	1.0	0.4

Table 6.2 –International coal samples details (53-106 µm)

	% Composition and Rank				
Sample Name	**Fila Mistra**	**La Jagua**	**Bentinck**	**Trans Natal**	**Klein Kopje**
Origin	Indonesia	Venezuela	UK	South Africa	South Africa
Vitrinite	96.8	87.2	86.6	56.4	31.6
Liptinite	1.6	1.6	4.8	4.8	3.4
Inertinite	1.6	11.2	7.6	38.8	65.0
% Unreactives	0.3	1.3	1.8	17.2	29.5
Rank	0.50	0.49	0.65	0.62	0.63

6.2.2. Char Samples Generated in Drop-Tube Furnace

The manual char classification results for the Australian and international samples generated in the drop-tube furnace are shown in Tables 6.3 and 6.4 respectively.

Table 6.3. Manual classification of Australian char samples (106-125 µm)

	% Composition Australian Char Samples				
Classification	**1**	**2**	**3**	**4**	**5**
Tenuisphere	6.0	3.4	14.3	9.2	35.1
Crassisphere	35.1	47.3	46.8	55.2	53.9
Tenuinetwork	6.0	14.0	9.0	10.2	9.8
Crassinetwork	27.5	16.7	16.5	8.8	1.0
Fusinoid	18.8	12.9	10.0	14.4	0.2
Solids	6.6	5.7	3.4	2.2	0.0

Table 6.4 – Manual classification of International char samples (53-106 µm)

	% Composition International Char Samples				
Classification	**Fila Mistra**	**La Jagua**	**Bentinck**	**Trans Natal**	**Klein Kopje**
Tenuisphere	24	27	30	19	2
CrassiSphere	4	7	21	11	12
TenuiNetwork	69	58	35	35	45
CrassiNetwork	3	8	10	17	20
Fusinoid	0	0	2	15	16
Solids	0	1	2	2	5

6.2.3. Determining Initial Internal Energy Weights

It has been shown that generally thin-walled chars require the shortest time to burnout compared to thick-walled and denser still solid char structures (T. Wu et al., 2006b). Chars with a dense carbon structure have a low available surface area for the reaction of oxygen and the process of oxygen diffusion from outside the particle is slower and more difficult than in thinner char structures. In cenosphereical char particles (tenui-/crassispheres), the high porosity and proximity of macrospores to the surface allows for rapid diffusion of reaction gases and burning rate consists of both external and internal carboneous material conversion. (i.e. combustion occurs low in Regime II). In networks, wall thickness can significantly impact char particle reaction rate by influencing the reactant gas diffusion into the particle. It has been shown that due to the high porosity often observed within thin-walled network structures, their reaction rate can be like that of some cenosphereical particles (Ma & Mitchell, 2009; Niu & Shaddix, 2015). Carboneous material conversion in networks is hence thought to occur across a range of low- high Regime II. In very dense chars, combustion is very slow as reaction

progresses under almost complete diffusional control (high combustion Regime II/III). Initial investigations were aimed at replicating these general burnout behaviour trends on sets of manually classified char morphologies by trialling different user input settings and eroding char material at the combustion front computed by internal energy equation 6.5. These initial values formed the basis for the first model iteration.

$$E_{internal} = \frac{1}{2}(\alpha(F)|V_F(F)|^2) + \frac{1}{2}(\beta(F)|V_F(F)|^2) \quad \textbf{(eq.6.5)}$$

Both α and β are user-defined weights and control the internal energy function's sensitivity to the amount of stretch and curvature possible as the contour deforms. β = 'Smoothness factor' where higher values produce smoother region boundaries and filter out finer details, whilst lower values produce more irregularities in the region boundaries. In Chapter 5, a β value of 0.2 was found effective at accurately tracing the topography of char particles and was therefore kept constant during this testing. In order to reduce processing times, 3 pixels (0.386 μm) were eroded over 30 iterations and the contour was computed over a fixed value of 500 energy minimisations. The 'Continuity Factor' (α) is a control of the contours tendency to shrink inwards around shapes and into gaps and can be considered as a control of the contour's ability to penetrate char structures. The relationship between varying α and the combined simulated burnout of the char test sets are shown in Figures 6.3-8. ('All' = erosion at every surface).

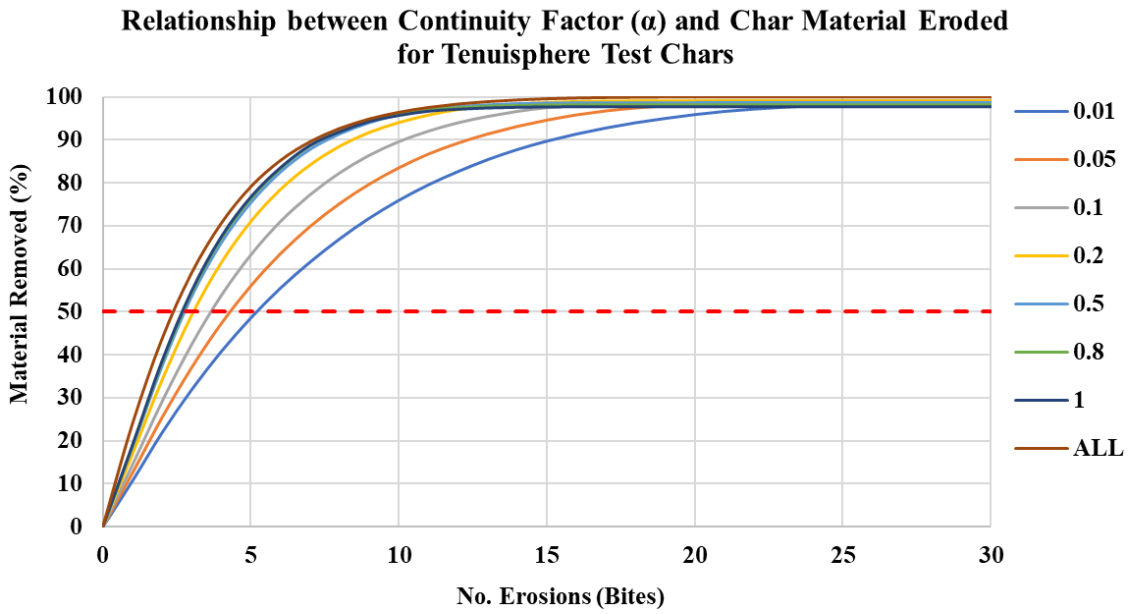


Figure 6.3 *– Relationship between varying continuity factor and simulated burnout of tenuisphere char test set*

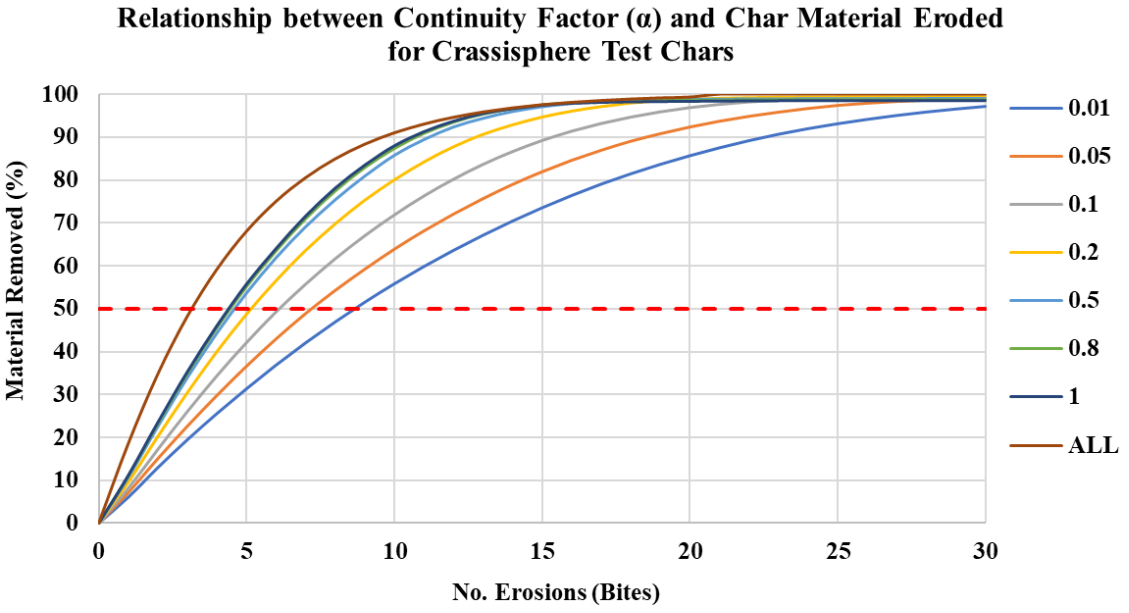


Figure 6.4 *– Relationship between varying continuity factor and simulated burnout of crassisphere char test set*

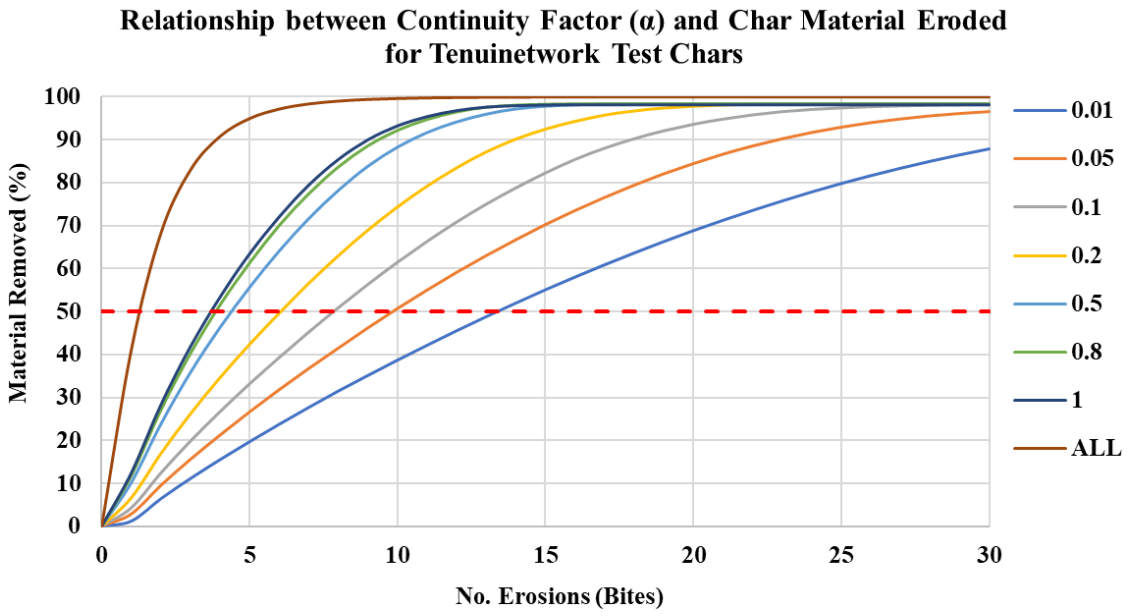


Figure 6.5 *– Relationship between varying continuity factor and simulated burnout of Tenuinetwork char test set*

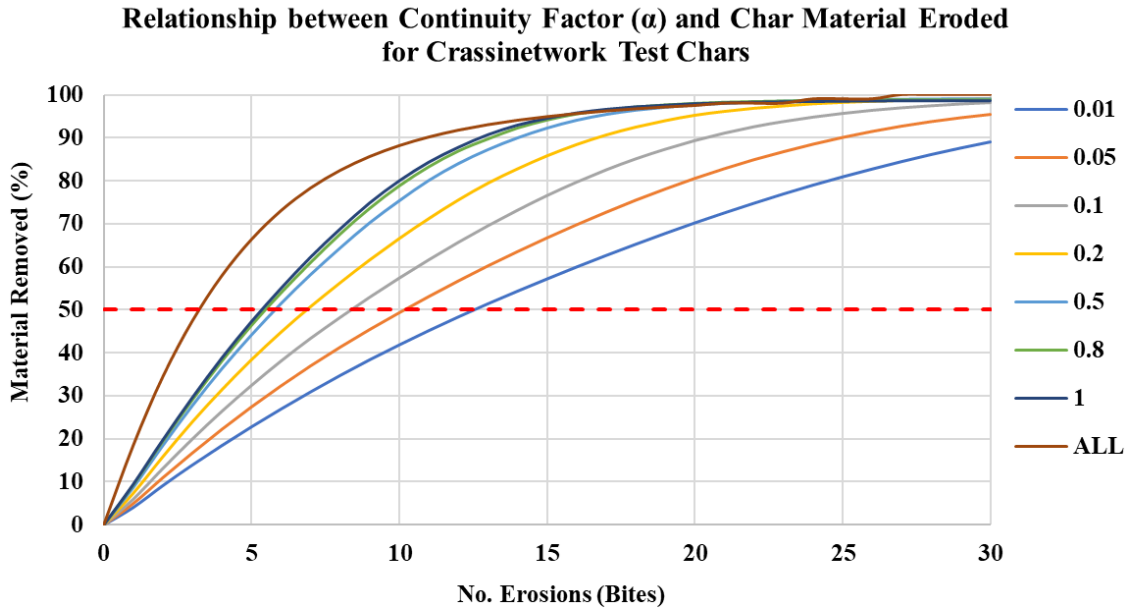


Figure 6.6 *– Relationship between varying continuity factor and simulated burnout of Crassinetwork char test set*

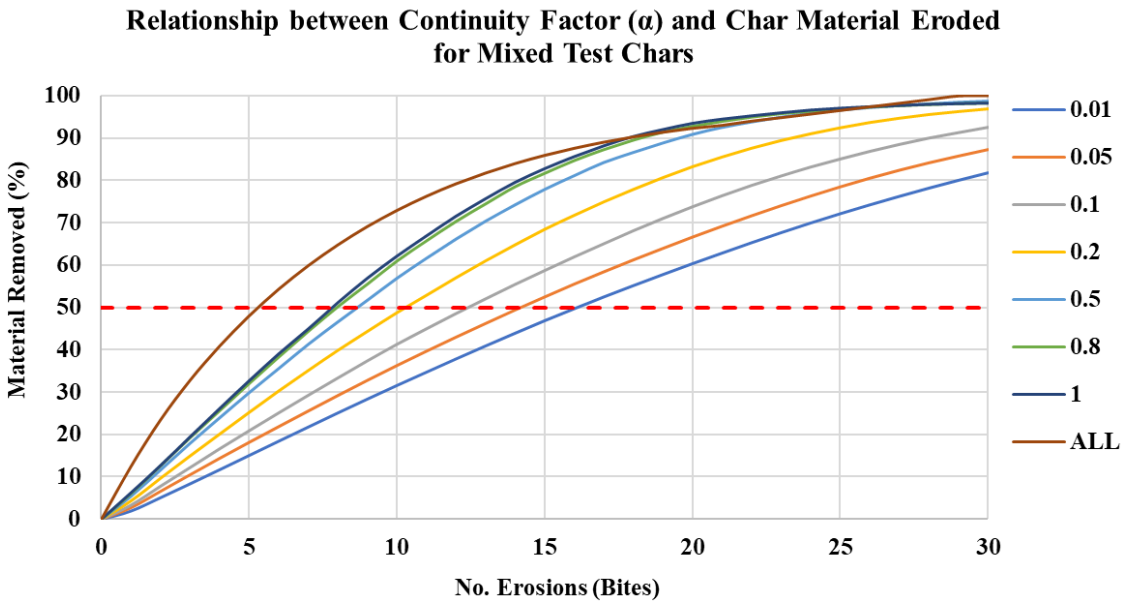


Figure 6.7 *– Relationship between varying continuity factor and simulated burnout of Mixed char test set*

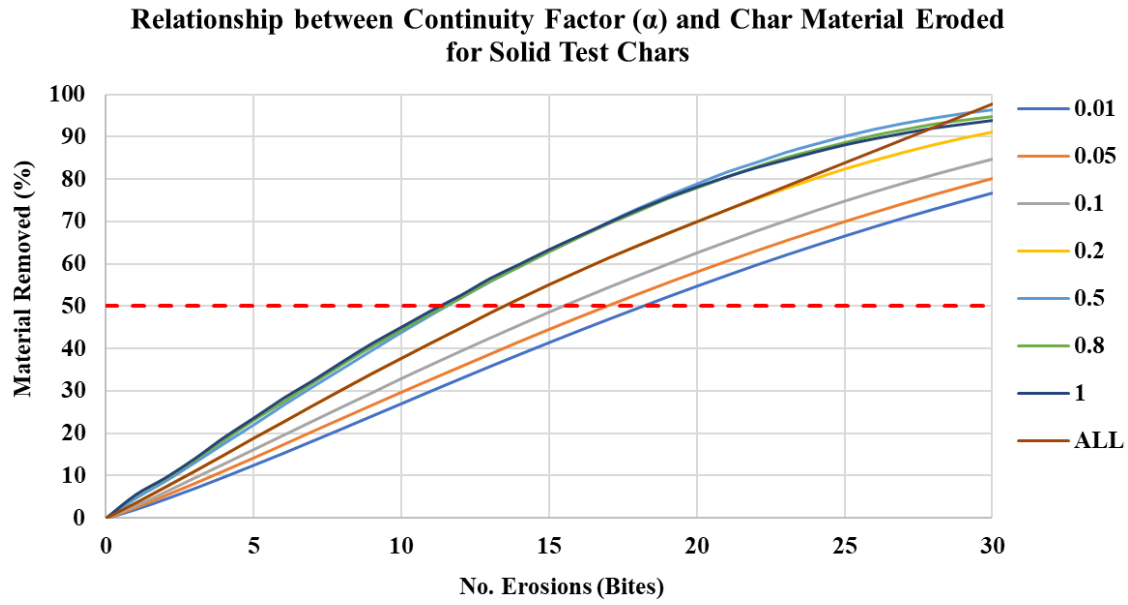


Figure 6.8 *– Relationship between varying continuity factor and simulated burnout of Solid char test set*

As expected, for all six sets of test chars, increasing the continuity factor (α) resulted in an increase in the rate of char material removal due to greater pore penetration and a

larger combustion surface area computed and then eroded. The degree of increase, and the point at which increasing α further had little or no additional impact on the removal rate differed between the char types. The largest observed increase was seen for tenuinetworks, with 50% removal requiring only four 'Pacman bites' at an α value of 1.0 versus thirteen bites required when α was set at 0.01. This is unsurprising due to the inherent open porous nature of tenuinetworks (up to 75-80% porosity) and the large corresponding surface area for the combustion front to trace its way around at higher continuity values. Again unsurprisingly, solids exhibited the smallest increase in rate removal due to the lack of any substantial macro or micro-porosity features. The point at which further increase in α resulted in a minimal or no change in combustion rate did differ between cenospheres and networks and was an important factor used to determine initial model settings. Minimal increase in char erosion rates was observed for tenui-/crassispheres above α values of 0.2, as the majority of the cenospherical wall material would already have been surrounded by the simulated combustion front at this point. For networks however, this structure: contour equilibrium was not reached until α values of 0.5/0.8. This observation is highlighted in Figure 6.9, which shows the relationship between the different char morphologies and erosion rates at α values of 0.2 and 0.5 respectively where the general trend of simulated combustion duration observed at 0.2 was; tenuispheres < crassispheres < tenuinetworks < crassinetworks < mixed < solids. At the lower α value, due to more limited pore penetration, tenuinetworks exhibit very similar simulated combustion rates to crassinetworks, particularly during the early phases of erosion until erosion begins to expose the more porous tenuinetwork structures. At the higher α values, the erosion rate of tenuinetworks is markedly faster and now very similar to that of crassispheres. As previously discussed, in terms of combustion potential, there has been a degree of

overlap observed for these two morphology groups. In terms of the other morphologies, the overall burnout trend remains as before.

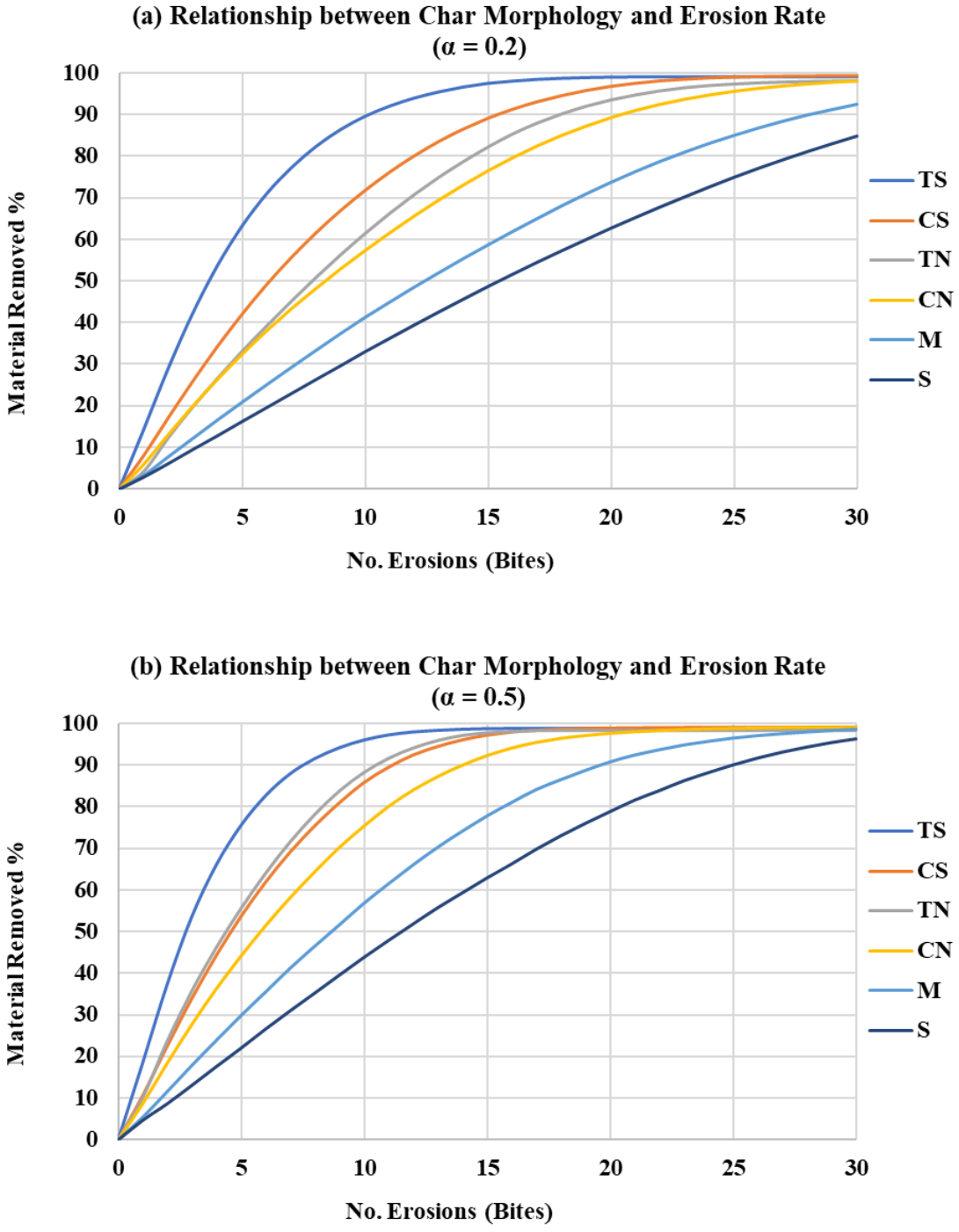


Figure 6.9 *– Relationship between Char Morphology and Erosion Rate for (a) α = 0.2 and (b) α = 0.5*

In order to further visualise the relationship between active contour continuity factor and the simulated combustion regime, and to aid in selection of the initial model settings, an approximation of the effectiveness factor (η) was calculated for each (α) value using equations 6.3 and 6.4 and information obtained from the simulated erosion of the test set char images. As the size of each pixel is known, many of the equation parameters can be measured or estimated from the char images during erosion. To simplify the calculation, the feret max of the particle during the erosion process was used to approximate particle radius and the rest of the particle was assumed to be spherical in relation to this. The kinetic constant (k_s) was found equal to equation 6.6:

$$k_s = 1050\ exp(-153200/(R_gT)) \quad \textbf{(eq.6.6)}$$

assuming first order kinetics and the stoichiometry factor (Λ) was calculated as equation 6.7 (Gilot et al., 2017):

$$\Lambda = (\tau + 1)/(\tau/2+1) \text{ where } \tau = 10^{2.5}\ exp(-25000/(R_gT)). \quad \textbf{(eq.6.7)}$$

R_g = Gas constant (J/mol/K)
T = Temperature (K)
τ = Molar ratio CO/CO_2

Particle density was calculated using approximated radius, porosity and an assumed ash-free carboneous material density value of 1.5 g cm^{-3}. Effective diffusivity was approximated using particle area and the percentage of material removed compared to a theoretical maximum (using total exposed surface area of the particle, 'All'). The initial specific surface area was estimated by determining both the internal and external perimeters of the char structure. The estimated effective factor profiles for different continuity factors are shown in Figure 6.10 as a function of material conversion.

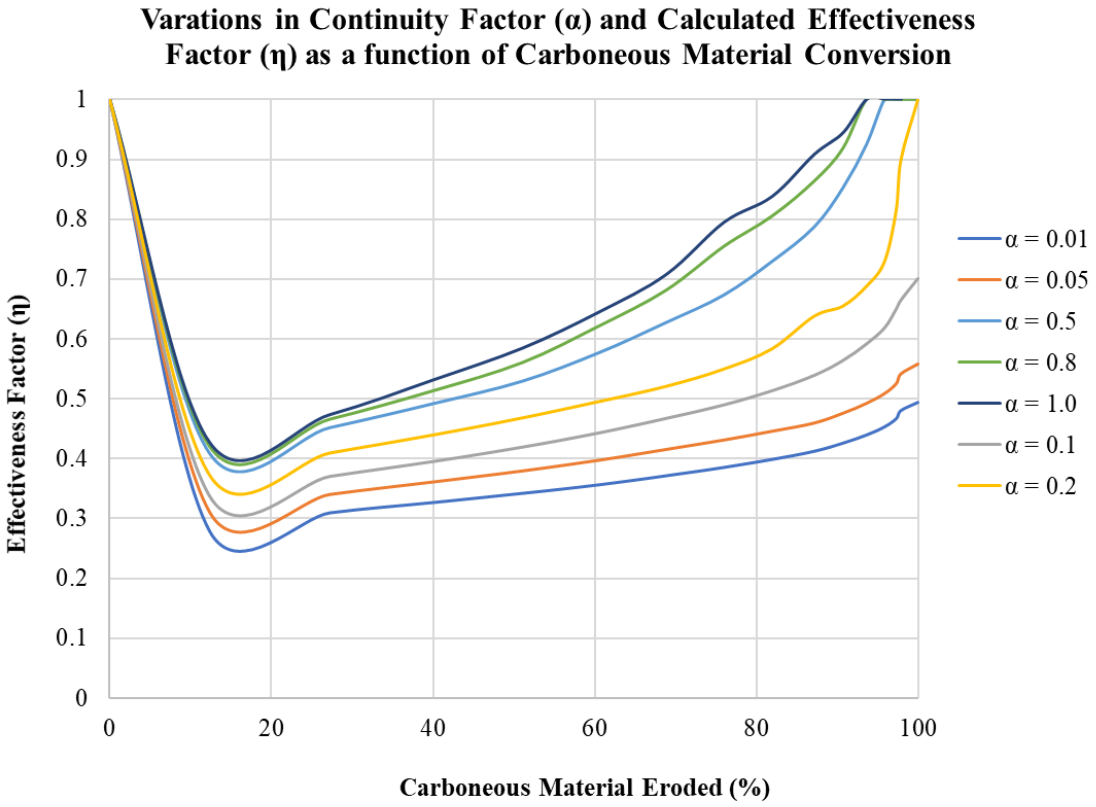


Figure 6.10 *– Relationship between the simulated erosions of real char images for varying active contour continuity factor (α).*

Unsurprisingly it was observed that as α increases, the degree of early-combustion diffusional limitation decreases due to increased pore penetration. Synonymous with the observations made from figs 6.3-8, after a point (~α = 0.5) there is little further increase in pore penetration during simulated early combustion. What is also clear is that for α values of 0.01-0.1, return to kinetic control is never fully reached before the end of the simulation, even as the particles fragment and porosity increases rapidly, indicating that the bend and stretch capabilities of the contours are still too greatly hindered and cannot sufficiently penetrate the large voids to accurately simulate late stage combustion. For α values greater than 0.1, kinetic control was restored during late stage combustion as η returned to 0. As a result of these observations and those trends

displayed in figs 6.4-10, initial α values of 0.1 and 0.5 were selected as user-defined inputs for the two stage combustion model outlined in Section 6.2, where stage 1 concerns combustion occurring primarily within a shell at the particle surface with minimal pore penetration, whilst stage two represents a progression of the diffusion through the char as local structural features evolve.

6.3. Initial Testing Results & Refinement of Model

6.3.1. Initial Simulation Results

By combining equations 6.1 and 6.2 and implementing as a two-part system as described in Section 6.2, the minimised energy of the contour and its location after 500 iterations can be calculated using the two-part equation 6.8. For this initial testing, each erosion (k) was chosen to represent 20 ms of combustion time and each bite remained as 3 pixels in size (0.386 μm).

Part 1 *– Diffusional control*

For k = 1:10 (a = 0.1, B = 0.2, n = 500)

$$\left(E_{contour} = -\sum_{1}^{500} E_{contour}\left(\bar{v}_i\right) \right)$$

Part 2 *– Decreasing diffusional control*

For k = 11:30 (a = 0.5, B = 0.2, n = 500)

$$\left(E_{contour} = -\sum_{1}^{500} E_{contour}\left(\bar{v}_{k=10}\right) \right)$$

(eq.6.8)

The manually obtained refire results and predicted burnouts for the Australian coal samples are presented in Table 6.5. The refired char samples were generated in the DTF by Dr David Nichols (University of Nottingham) and Thermogravimetric analysis performed by Dr Orla Williams (University of Nottingham). Unfortunately, it was not possible to obtain a full burnout history for Australian coal 75 as the sample would fully combust after 1 refire in the DTF. The correlation between these manual and predicted burnouts is shown in Figure 6.11.

Table 6.5 – Comparison between char refire results and initial predicted burnout

	Carbon Conversion % (Char Basis)					
	200 ms		**400 ms**		**600 ms**	
Coal Sample	**M**	**P**	**M**	**P**	**M**	**P**
1	36	39	61	57	86	77
2	30	45	72	64	86	83
3	20	36	53	53	73	73
4	23	35	86	52	94	72
5	79	57	-	78	-	97

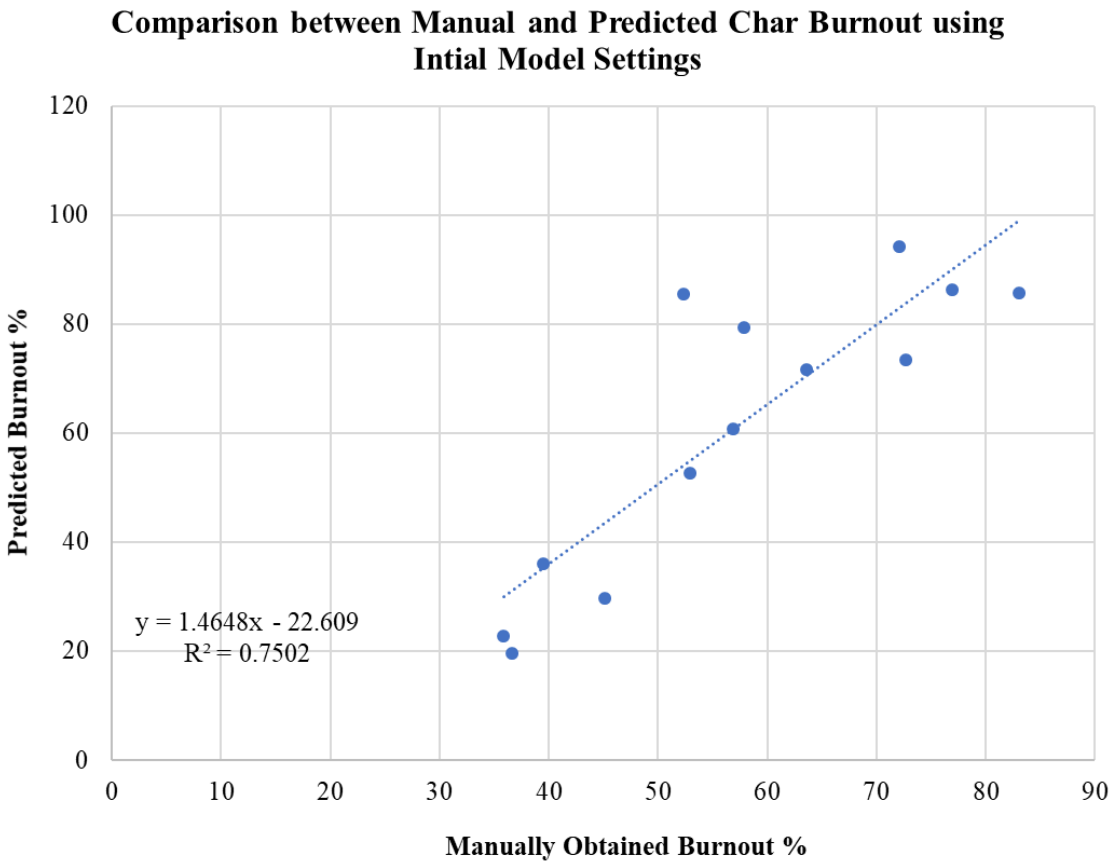


***Figure 6.11** – Correlation between manual refire and predicted burnout for initial model settings*

Whilst there is some correlation between manual and predicted results, several key observations can be made concerning the performance of the initial predictive model;

1) The initial phase (0-200 ms) is generally too aggressive and is only partly effective at differentiating between samples with higher proportions of faster burning material (i.e. cenospheres/tenuinetworks). The predicted burnout at 200 ms for all samples, except for sample 5, was 3-17% higher than manually obtained refire data. However, whilst initial predicted burnout for sample 5 was considerably higher than the other samples, predicted burnout was still 21%

lower than the experimental data despite the sample containing approximately 98% cenospherical or thin-walled material. These observations imply that the use of a universal α value of 0.2 during this initial phase resulted in too much pore penetration by the combustion front in thicker chars yet, not enough pore penetration for thin and cenospherical char particles.

2) Generally, predicted 'mid' combustion (400 ms) results correlated well with those of manually obtained data with a maximum variance of 8% between in all samples except sample 4. This implies that the active contour function ($\alpha = 0.5$) is effective at simulating a gradual increase in effective diffusibility as porosity of eroding particles begins to increase. However, any changes to model settings to rectify the overly aggressive early combustion simulations described above, may require the implementation of a more aggressive version at this phase to balance out the change. There is still evidence that the model still exhibits limited differentiation between morphology at this phase with the predicted burnout of sample 4 (consisting of ~75% cenospherical and thin material) being 34% lower than that of manual results.

3) Predicted late stage combustion is generally not aggressive enough. Whilst a fixed α value of 0.5 is effective at simulating the gradual increase in diffusibility as material is eroded during the mid-combustion phase (~ 400 ms), it is not effective enough at simulating the rapid increase in diffusibility during late stage combustion where there is almost no diffusional limitation.

6.3.2. Model Refinement

From the above findings, several refinements were made to the model to increase sensitivity to different char morphologies and to increase the rate of effective diffusion during later stage combustion.

6.3.2.1. Char morphology dependant settings

To enable the model to differentiate between cenospheres and slower combusting char morphologies during the initial phase of combustion simulation, a char classification function (described in Chapter 5.4.3) was introduced to classify chars as either cenospherical in nature, or 'other'. The initial combustion phase (0-200 ms) of those chars classified as spherical was then simulated using an alpha value of 1.0 to increase the percentage of wall material eroded. Those classified as 'other' were eroded using $\alpha = 0.03$, which ensured that combustion occurred almost entirely at the char surface. This incorporation of a 'cenospherical' and 'dense' distinction has also been used in a combustion model by Ma et al., where in particles with outer wall thickness <10 μm, carboneous material conversion occurred at both the external and internal char surfaces, whilst conversion was strictly restricted to the surface of denser particles (Ma & Mitchell, 2009).

6.3.2.2. Dynamic continuity factor

From the initial testing results, it was observed that the use of a constant α value was not effective at differentiating between some char types and simulating the rapid increasing in diffusibility during late stage combustion. To solve this, α was set to increase from 0.5 by 0.02 with each erosion. As a result, in addition to the local changes

in char structure influencing diffusibility, increased pore penetration is also computed as a result of a dynamic increase in contour continuity factor.

The refined model settings can now be defined with user input settings of;

Part 1 *– Diffusional control*

For k = 1:10 (a = 1.0 or 0.03, B = 0.2, n = 500)

Part 2 *– Decreasing diffusional control*

For k = 11:30 (a = 0.5+0.02, B = 0.2, n = 500)

6.4. Revised Model Results

The manually obtained refire results and revised predicted burnouts for the Australian coal samples are presented in Table 6.6. To further test and validate the revised settings, the model was also run implemented on the five international coal samples (described in 5.3.2) and these results are shown in Table 5.7. The correlation between manual and predicted results for all char samples is shown in Figure 6.12. Plots of the individual particle burnout profiles for all the samples are attached in Appendix C.

Table 6.6 – Comparison between char refire results and initial predicted burnout for Australian coal samples

	Carbon Conversion % (Char Basis)					
	200 ms		400 ms		600 ms	
	M	P	M	P	M	P
1	36	26	61	60	86	84
2	30	30	72	67	86	88
3	20	25	53	57	73	77
4	23	36	86	77	94	89
5	79	70	-	100	-	100

Table 6.7 – Comparison between char refire results and initial predicted burnout for international coal samples.

	Carbon Conversion % (Char Basis)					
	200 ms		400 ms		600 ms	
	M	P	M	P	M	P
Bentinck	45	43	83	79	92	90
Klein Kopje	38	28	56	61	74	74
La Jagua	45	50	89	85	98	95
Fila Mistra	66	59	94	87	95	94
Trans Natal	43	37	65	74	79	86

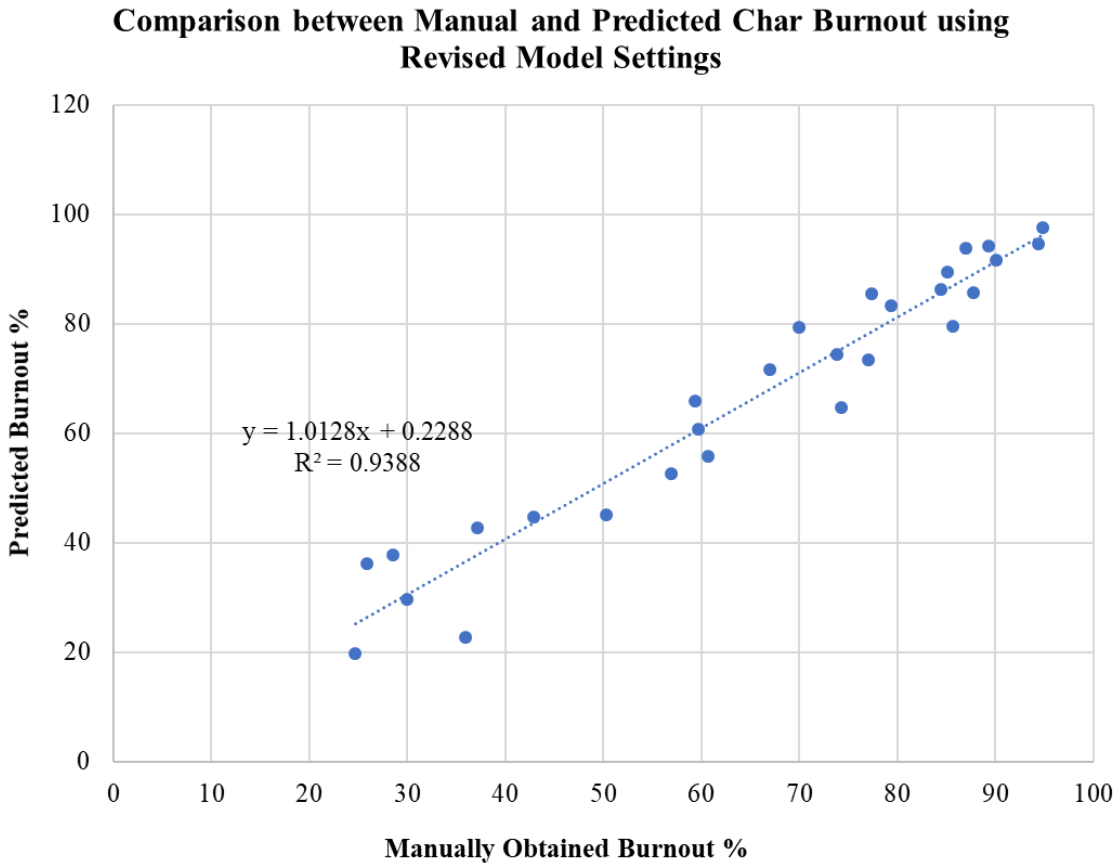


***Figure 6.12** – Correlation between manual refire and predicted burnout for revised model settings*

With the introduction of a morphology differentiator and a progressively increasing continuity factor, there was a marked improvement in the correlation (R^2 = 0.94 compared to 0.75 previously) between manually obtained burnout and that simulated by the revised Pacman Model settings. The discrepancies between manual and simulated results were at their largest during the early phases of simulated combustion with an average and maximum variance of 6.7% and 13% respectively. One reason for this is that whilst a differentiator for cenosphereical and denser chars was used, burnout between different 'denser' chars can be markedly different (T. Wu et al., 2006b) and have not been accounted for at this stage. For mid- and late stage combustion, simulated

results were generally a lot closer to those obtained manually (mean variance = 4.1%, max = 9%), indicating that a combination of iteratively computing a combustion front as char structure evolves and a gradual increase in continuity factor could effectively simulate the changes in diffusional control exhibited by char particles during later stage combustion. In addition to the improved correlation with experimentally obtained refire data, the model was also effective at simulating burnout for both char size fractions. This is unsurprising, as the pixel size and therefore the amount of material removed with each iteration remained constant, the smaller chars were therefore eroded proportionally faster. It must be noted that as the size fractions were close in size, the full extent of this inherent feature within the model is still unknown and would require further testing to validate its versatility for modelling other size fractions.

On average, the program requires 6-7 seconds to simulate combustion on a single char particle. If the same sample size of 500 is used as in manual coal and char analysis, predicted burnout results are obtainable in less than an hour, far quicker than refiring the samples in a drop-tube and conducting thermobalance analysis which takes several days.

6.4.1. Additional Information for Power Generators

6.4.1.1. Implementation on whole char mosaics

In addition to processing time, one of the other main drawbacks in using individual particle images is the potential for the loss of material during particle extraction from the large mosaic images. Even with well-trained techniques to segment and separate char particles into individual images, it remains inevitable that some char information will be lost during this process, either as fragments that could not be effectively repaired or as touching particle agglomerates. By implementing a version of the Pacman Model

on the whole sample mosaic before separation, all the char material would be analysed as well as drastically reducing the overall processing time of the model system by removing the separation phase. Whilst the morphology of the individual chars cannot be considered in the simulation as described in Section 6.3.2.1, this method could still be used by power generators as a quick and useful comparative tool for simulating the burnout of different char samples as illustrated in Figure 6.13 where a basic version of model was applied to mosaics of the five Australian coal samples. The general burnout trend observed from manually obtained refire data is maintained when the Pacman Model is implemented on the whole mosaic image, with coal 5 burning out the fastest with coal 3 the slowest. Whilst the same resolution cannot be obtained as with individual particle analysis, the whole mosaic program could still be a useful comparative tool for power generators.

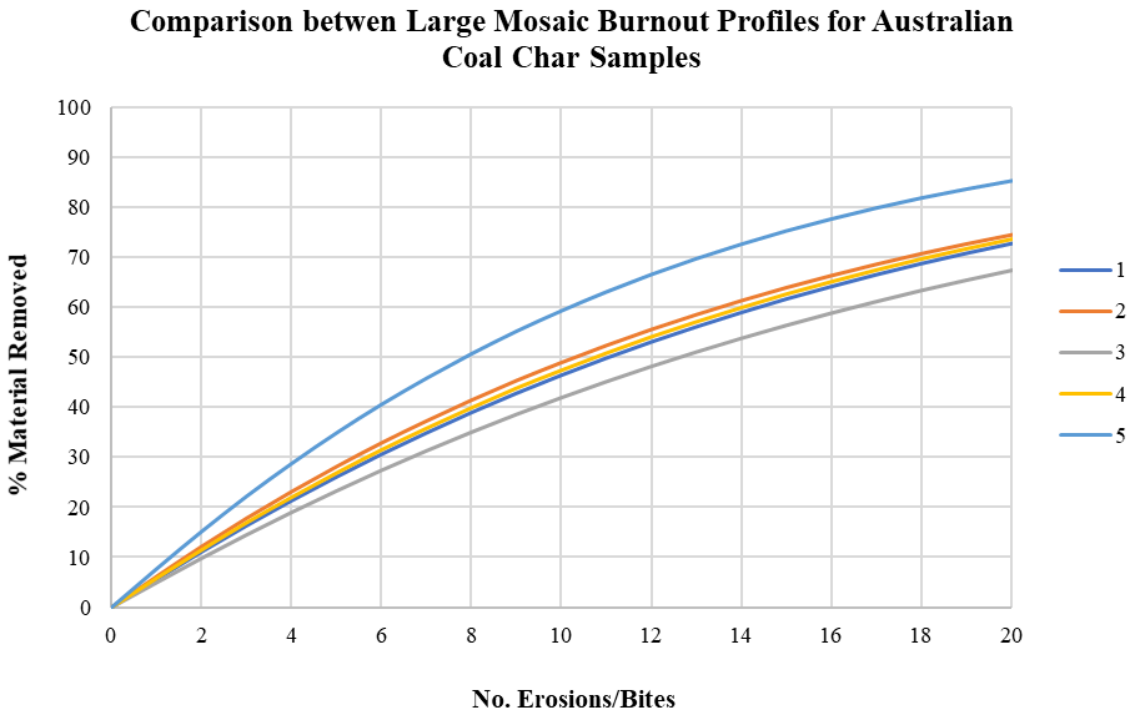


Figure 6.13 *– Comparison of the simulated whole mosaic burnouts*

6.4.1.2. Char Morphology Distributions

In addition to providing power generators with predicted burnout information, simulating local changes in individual char structure during combustion enables the proportion of the remaining char material distributions at different resident times. These properties can be visualised in various ways (i.e. changes in char porosity, particle size, available surface area vs time etc). Combining some of these parameters, an overall distribution of carboneous material that will be converted and char material remaining for each individual particle after combustion can be predicted and visualised as shown in Figures 6.14d, 6.15d, 6.16d, 6.17d and 6.18d. The amount of char material converted at various stages of combustion can also be visualised in Figures respective Figures a-c. This information could inform a generator as to the likely carbon loss in ash and whether any remaining material is distributed evenly between many small particles nearing burnout completion or condensed as larger and less numerous solid particles which are likely to be deposited in the fly/bottom ash.

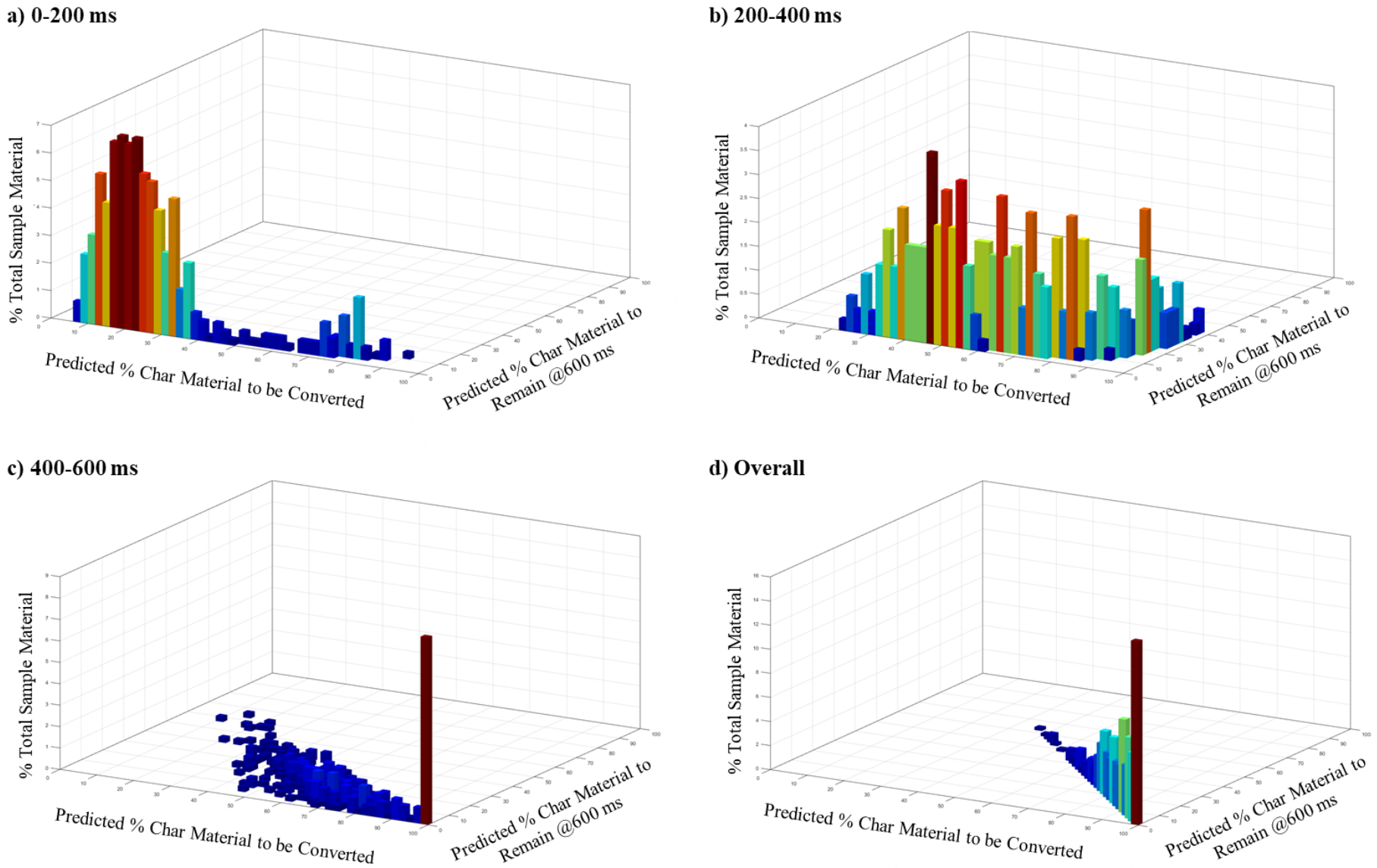


Figure 6.14 *– Predicted distribution of remaining carboneous material at (a) 200, (b) 400 (c) 600 ms for Australian coal sample 1*

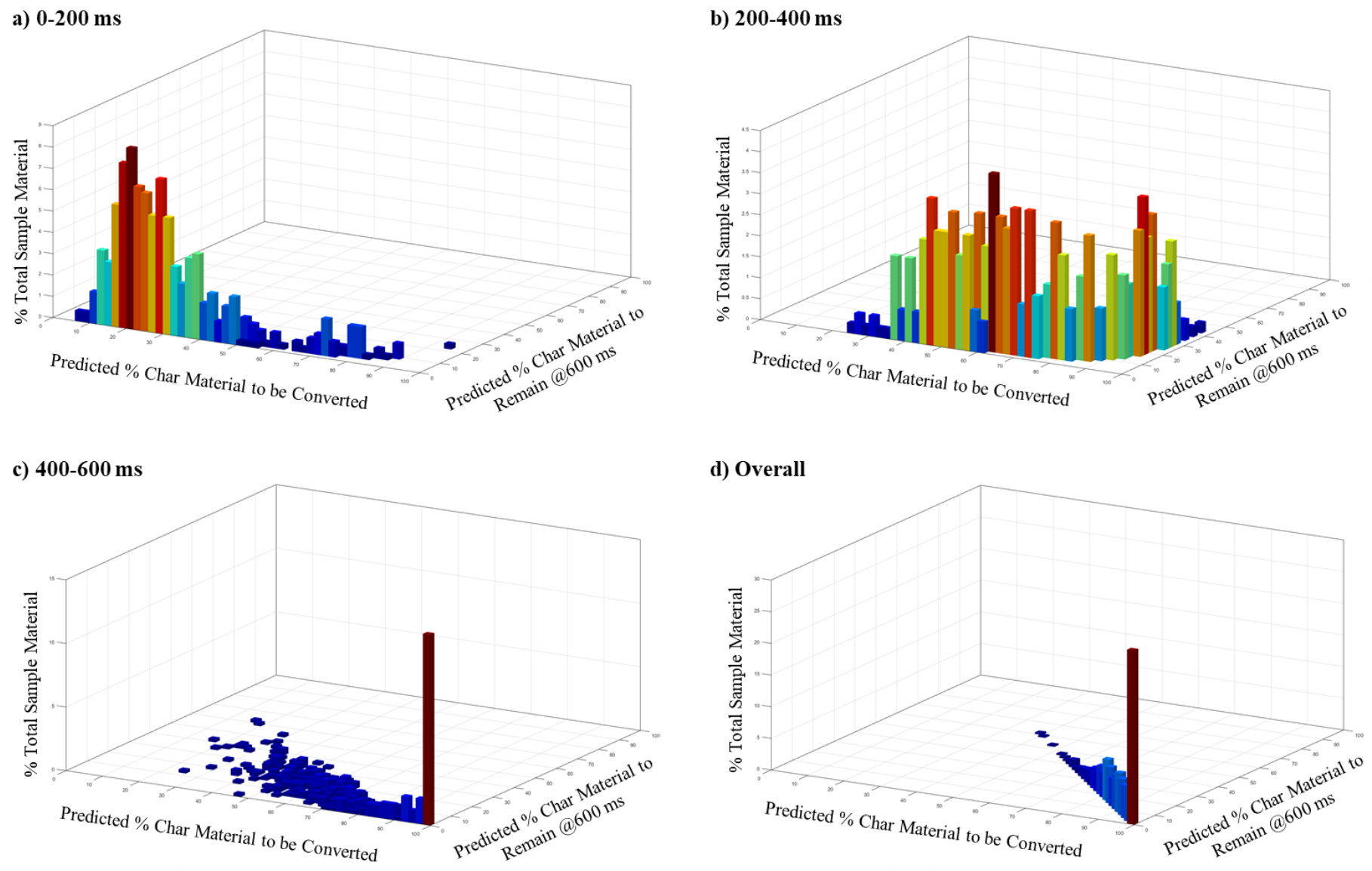


Figure 6.15 *– Predicted distribution of remaining carboneous material at (a) 200, (b) 400 (c) 600 ms for Australian coal sample 2*

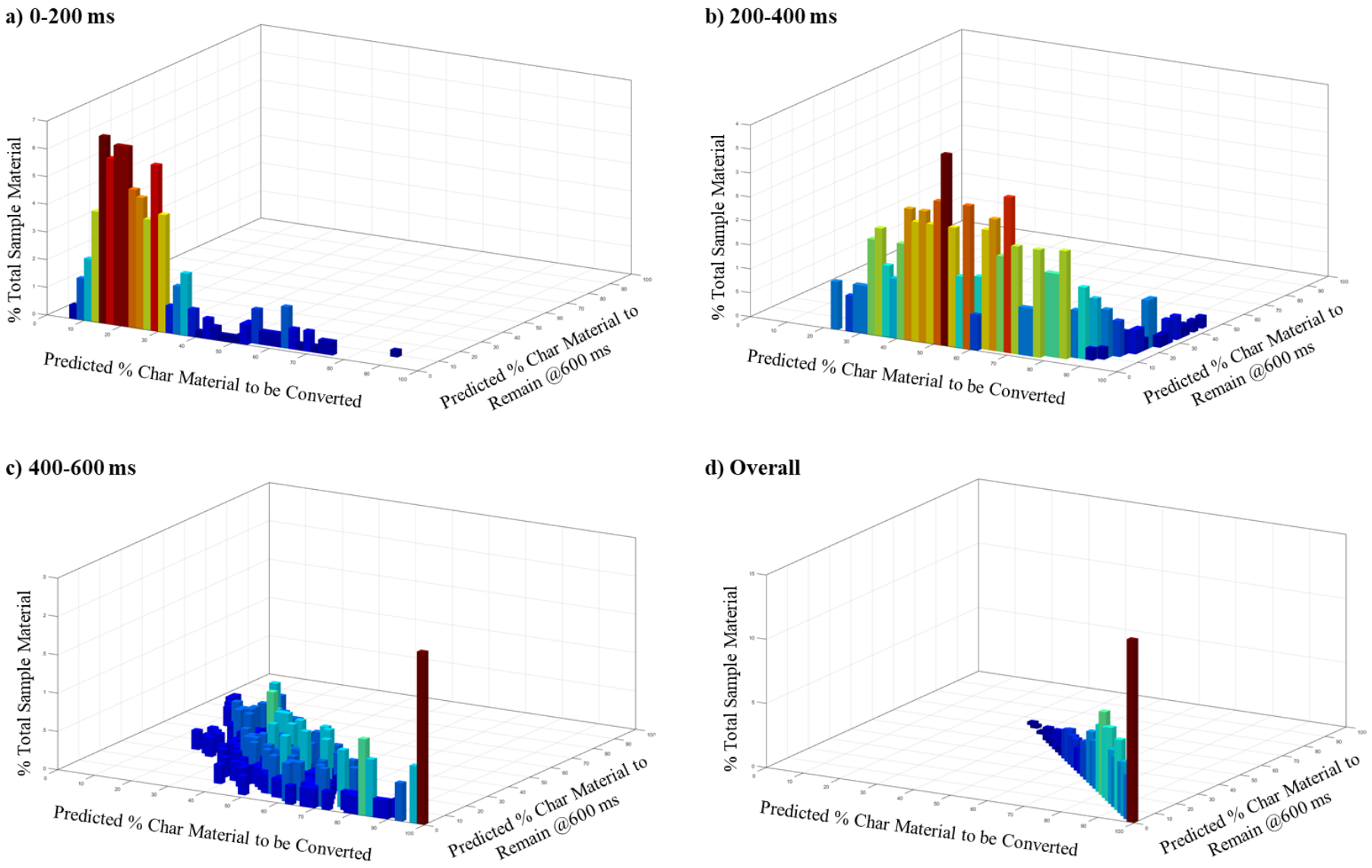


Figure 6.16 *– Predicted distribution of remaining carboneous material at (a) 200, (b) 400 (c) 600 ms for Australian coal sample 3*

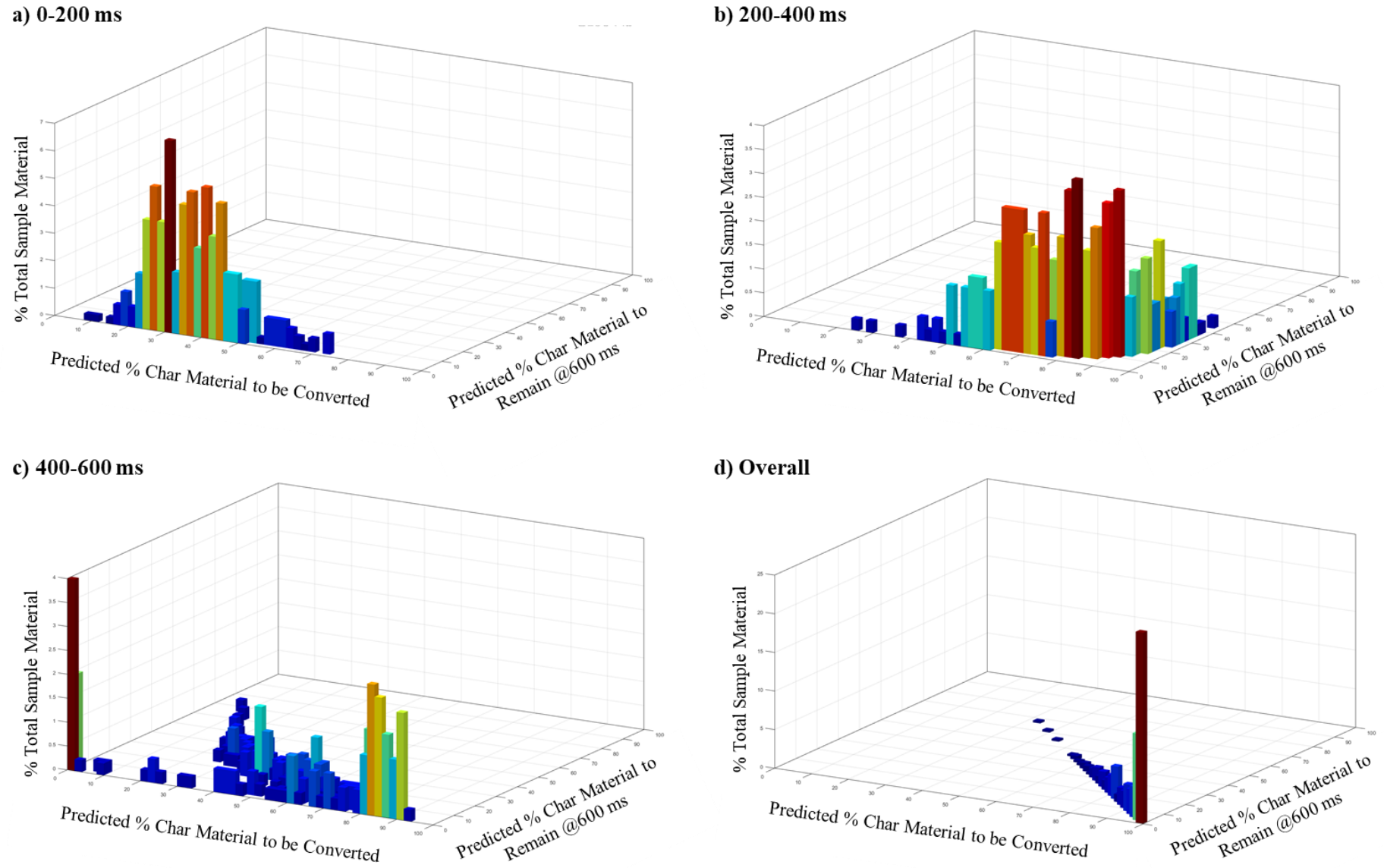


Figure 6.17 *– Predicted distribution of remaining carboneous material at (a) 200, (b) 400 (c) 600 ms for Australian coal sample 4*

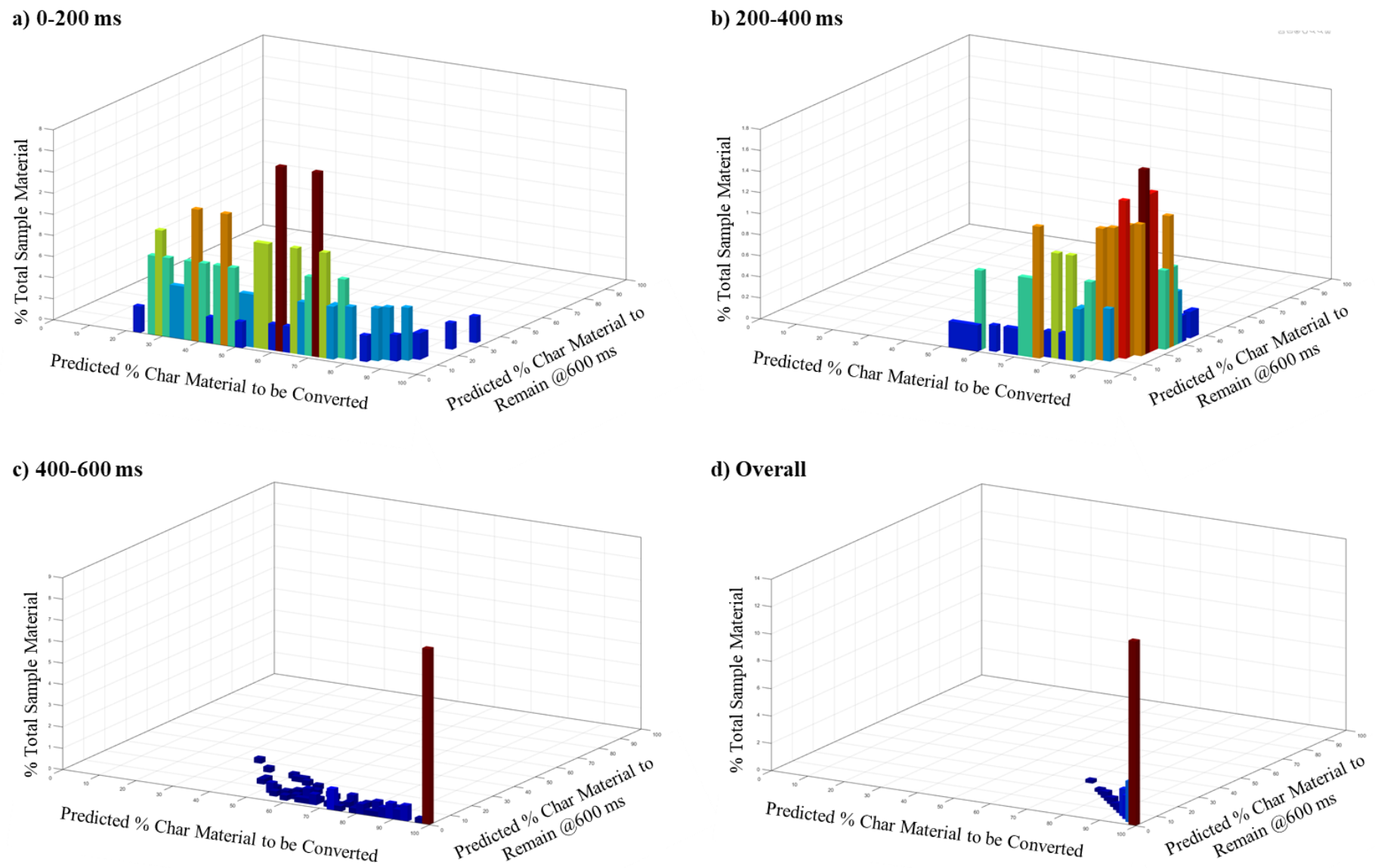


Figure 6.18 *– Predicted distribution of remaining carboneous material at (a) 200, (b) 400 (c) 600 ms for Australian coal sample 5*

6.5. Conclusions

This Chapter describes the testing and refinement of an automated image-based coal char burnout model capable of simulating char oxidation on individual char structures. In addition to burnout simulation data, the model can be applied to whole mosaic images as a rapid burnout comparison tool for power generators and provide carboneous material distribution information at different residence times. The inclusion of different char morphology factors confirms previous findings that different char types burn out in markedly different ways due to the significant difference in their geometric structures, and that one effective way of measuring this and providing a better description of mass and heat transfers during combustion is by measuring local changes in char structure throughout the combustion process.

CHAPTER 7. Using Advanced Image Analysis Techniques to Predict and Detect Variations in Char Structure and Reactivity as a Result of Coal Oxidation

As coal is usually stockpiled before combustion, the fuel is open to weathering and atmospheric oxidation. This can potentially alter the organic and mineral constituents and result in deterioration of a fuel's combustion potential. (Kus et al., 2017; Marchioni, 1983; Pisupati et al., 1991; M. M. Wu et al., 1988). The possible effects of oxidation upon coal have already been discussed in greater detail in Section 2.6, and the various structural changes to functional groups are thought to result in increased volatile content and decreased calorific content (Crelling, 2008; Monthioux & Landais, 1988). Whilst oxidation may produce changes within maceral groups, such as the formation of oxidation rims and surface cracks and cause a coal to behave differently, maceral composition is not thought to be effected (Chandra, 1982; Kus et al., 2017). Thus, the probability of detecting a problem before the event is low.

In this work, five artificially oxidised coal samples were analysed using the advanced image analysis techniques described in Chapters 4, 5 and 6. All 5 coals were prepared by sieving pulverised fuel samples in an alpine jet sieve. Initially a single 53µm sieve was used in order to remove the fines, after which a single size fraction of +53-106µm was produced.

Ten 2 gram portions of each coal were weighed out. All 50 samples (10 samples for each coal) were then placed inside an oven at ambient temperature. After 24 hours one sample of each coal was removed, and the oven allowed to heat up to 50^{o}C at a ramp rate of approximately 2^{o}C per minute. In this way the oven was heated from 25 to 250^{o}C

over a period of 10 days with graduated intervals of 25ºC. One sample from each coal type was removed after 24 hours at any given temperature. The whole oxidation procedure took 11 days from taking the initial removal at 25ºC to the final sample being removed after 24 hours at 250ºC. Each sample was stored in an air tight container after removal from the oven.

Sample manual maceral composition, proximate analysis, rank analysis, manual char morphology classification and char intrinsic reactivity were all performed by as part of the same study and used to both assess the effect of coal oxidation and to test the suitability and accuracy of the image analysis methods implemented in this Chapter.

The purpose of this investigation was not to directly simulate natural oxidation, since this is complex and variable, but to investigate how coal characteristics respond to temperature, and how these new properties effect the structure and reactivity of the respective pyrolysed chars. This Chapter describes the analysis of these coals and their daughter chars using traditional laboratory techniques (proximate analysis, calorific content, manual maceral composition, rank, manual char characterisation) and the image analysis techniques discussed in Chapter 4, 5 and 6 to both validate and investigate the suitability of using these methods as potential tools for power generators to detect subtle changes in coal properties that may impact coal combustion potential.

7.1. The Effect of Oxidation on Coal Properties

7.1.1. Oxidation and Proximate Composition

The five coals were chosen to represent a wide range of volatile contents and petrographic contents (Table 7.1). The fuel ratio (volatiles over fixed carbon, on a dry ash free basis) ranged from 1.1 to 3.0 and all five coals have been previously used in the generation of electricity in power stations around the world.

The full proximate analysis can be seen in Table 7.2. Moisture levels appeared to rise with all five coals. Since oxidation is known to increase the hydrophilicity of coal (Cox & Nelson, 1984; Nelson & Chen, 2007), the increase seen in Table 7.2 is not unusual.

Table 7.1 – Compositional details of coal set 3

Coal Sample	**Fila Mistra**	**La Jagua**	**Bentinck**	**Trans Natal**	**Klein Kopje**
Origin	Indonesia	Venezuela	UK	South Africa	South Africa
Vitrinite	96.8	87.2	86.6	56.4	31.6
Liptinite	1.6	1.6	4.8	4.8	3.4
Inertinite	1.6	11.2	7.6	38.8	65.0
% Unreactives	0.3	1.3	1.8	17.2	29.5
Rank	0.50	0.49	0.65	0.62	0.63
Fuel Ratio	1.28	1.67	1.94	2.27	2.98

On a dry basis, volatile content and ash show an increase between 25 ^{o}C and 250 ^{o}C for all 5 coals. Fixed carbon appears to decrease correspondingly. The point at which compositional changes can be seen appears to be dependent on the coal type. Bentinck shows a sudden change at approximately 175 ^{o}C whilst the other coals exhibit a more linear change. Klein Kopje changes gradually over the full range of oxidation

temperatures. Trans Natal begins to alter at about 125 ^{o}C. Fila Mistra shows the least tendency to alter. Figure 7.1 shows how fuel ratio changes with increasing oxidation temperature. A clear trend of decreasing fuel ratio with increasing temperature is apparent. Each coal displays a break point showing a non-linear increase with temperature, and this break point seems to correlate with coal type. The highest inertinite coal, Klein Kopje, shows a decrease in fuel ratio over the whole range. Trans Natal and Bentinck begin to fall at about 125 ^{o}C. La Jagua starts to fall after 150 ^{o}C, and Fila Mistra drops after 175 ^{o}C. The difference between the final fuel ratio values is much narrower than at 25 ^{o}C. Oxidation appears to cause the chemical properties of coals to converge.

Table 7.2 - Proximate Analysis Results for the Oxidation coals (as received basis)

		Oxidation Temperature (ºC)									
Coal Sample		**25**	**50**	**75**	**100**	**125**	**150**	**175**	**200**	**225**	**250**
	Moisture	6.2	5.2	4.3	3.8	3.5	4.4	5.3	7.2	8.4	9.3
Fila Mistra	Volatiles	36.1	35.0	36.4	35.5	36.5	34.4	35.1	38.6	38.8	38.2
	Carbon	46.1	48.7	47.9	48.8	49.5	49.5	46.4	42.0	39.5	38.6
	Ash	11.6	11.1	11.4	12.0	10.6	11.8	13.2	12.1	13.3	13.9
	Moisture	2.4	2.6	2.8	1.9	2.6	3.1	4.8	3.8	7.7	4.9
La Jagua	Volatiles	34.0	33.8	32.9	33.7	33.9	32.5	35.1	37.9	37.8	39.8
	Carbon	56.9	56.3	55.9	55.2	57.6	55.0	52.1	51.8	45.0	43.5
	Ash	6.7	7.3	8.4	9.1	5.9	9.4	8.0	6.5	9.5	11.8
	Moisture	2.7	2.2	1.8	2.2	2.1	3.9	1.5	2.3	6.4	5.9
Bentinck	Volatiles	27.0	25.2	26.7	25.7	23.9	24.9	29.4	31.9	32.8	31.9
	Carbon	52.6	52.8	52.2	54.0	54.2	52.8	53.6	46.8	40.5	38.5
	Ash	17.7	19.9	19.4	18.1	19.7	18.3	15.5	19.0	20.3	23.7
	Moisture	2.3	2.8	2.6	2.6	2.6	2.6	4.1	3.4	3.1	6.7
Trans Natal	Volatiles	24.3	25.5	24.8	23.6	23.7	26.7	29.0	30.2	33.1	31.1
	Carbon	55.2	55.2	55.0	52.0	55.4	55.6	51.4	47.8	44.7	40.3
	Ash	18.1	16.5	17.6	21.8	18.2	15.2	15.4	18.5	19.2	21.9
	Moisture	1.6	1.6	1.7	2.0	2.6	2.5	1.7	3.5	4.8	5.2
Klein Kopje	Volatiles	20.1	20.7	20.9	20.8	23.7	23.0	24.4	26.8	28.6	28.8
	Carbon	59.9	57.7	58.0	57.2	55.4	54.0	53.6	50.2	46.8	44.1
	Ash	18.4	20.0	19.4	20.0	18.2	20.5	20.3	19.5	19.7	21.9

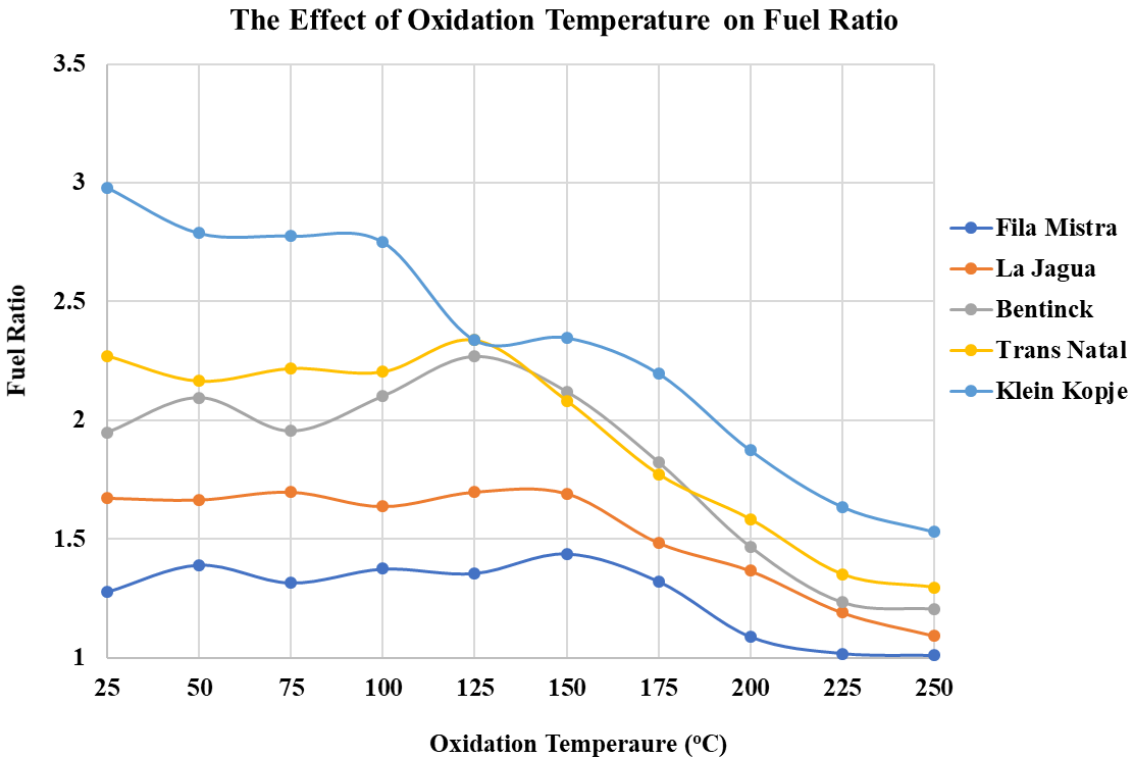


Figure 7.1 *– The effect of oxidation temperature on fuel ratio*

As mentioned previously, other studies also noted that volatile content increased as a result of oxidation (Monthioux & Landais, 1988). It appears that below 300 °C, volatile content will increase as a result of the elimination of oxygen bearing functional groups that are known to increase the thermostability of the coal matrix (Gracia M., 1993). Above 300 °C this trend disappears. The impact of this phenomena should be apparent in the characteristics of the chars produced in the drop-tube furnace discussed in Section 7.2.

7.1.2. Oxidation and Vitrinite Reflectance

The rank analysis results are shown in Table 7.3. The vitrinite reflectance of all 5 coals increases as oxidation temperature increases. The rank values for the initial 5 coals were all relatively low. The final coal samples, oxidised at 250 °C, all had values of

approximately 1.0%. This amounts to an almost 100% increase in the vitrinite reflectance of each sample. The break point appears to be around 150 ^{o}C, where the relative change in Rank value from one temperature to the next increases significantly. The impact of this effect is unusual since all five coals remain as medium to high volatile coals, despite being heated to 250 ^{o}C. The reflectance of vitrinite is often used as an index for the Rank of the coal, hence the reason for 'rank' being the term for vitrinite reflectance. Clearly, in this case, rank does not really correlate to the proximate characteristics of the coals.

Table 7.3 – Rank values with changing oxidation temperature

	Oxidation Temperature (^{o}C)									
Coal Sample	**25**	**50**	**75**	**100**	**125**	**150**	**175**	**200**	**225**	**250**
Fila Mistra	0.50	0.52	0.51	0.52	0.57	0.60	0.68	0.78	0.89	0.96
La Jagua	0.49	0.53	0.54	0.55	0.57	0.59	0.65	0.79	0.83	1.01
Bentinck	0.65	0.64	0.67	0.67	0.71	0.78	0.77	0.88	0.94	1.04
Trans Natal	0.62	0.60	0.64	0.61	0.65	0.70	0.74	0.86	0.91	1.03
Klein Kopje	0.63	0.68	0.65	0.69	0.71	0.72	0.77	0.86	0.92	1.08

7.1.3. Oxidation and Maceral Composition

It has been stated that oxidation does not cause significant changes in maceral composition (Kus et al., 2017). However, liptinite may behave differently from vitrinite and inertinite at specific temperatures (Yun & Meuzelaar, 1988). Table 7.4 shows the results for all 5 coals over the oxidation temperature range. Fila Mistra appears to lose all inertinite, as well as all liptinite at about 200 ^{o}C. The inertinite in Fila Mistra has a relatively low reflectance compared other standard Northern Hemisphere coals. As the

overall reflectance of the coal increased, the criteria for distinguishing between vitrinite and inertinite diminished which may explain the apparent disappearance of inertinite. At about 200 ºC, all 5 coals showed a reduction in liptinite content. Like Fila Mistra, this may not necessarily mean that liptinite is no longer present, but that it became more difficult to distinguish from its vitrinite/inertinite matrix.

Table 7.4 – Manual Maceral Analysis

		Oxidation Temperature (ºC)									
Coal	**Maceral**	**25**	**50**	**75**	**100**	**125**	**150**	**175**	**200**	**225**	**250**
Fila Mistra	Vitrinite	97	96	97	96	97	97	96	98	100	100
	Liptinite	2	2	1	2	2	1	2	1	0	0
	Semi-Fusinite	0	0	1	0	1	1	2	1	0	0
	Fusinite	2	2	1	2	0	1	0	0	0	0
La Jagua	Vitrinite	87	88	90	89	88	89	89	89	90	88
	Liptinite	2	2	2	1	2	2	2	1	0	0
	Semi-Fusinite	4	4	4	4	4	3	4	4	4	5
	Fusinite	7	6	4	5	6	6	5	6	7	7
Bentinck	Vitrinite	87	88	88	89	90	90	88	89	91	88
	Liptinite	4	4	5	4	3	3	4	2	0	0
	Semi-Fusinite	3	2	0	1	1	2	4	4	4	6
	Fusinite	7	6	7	6	6	5	4	5	5	7
Trans Natal	Vitrinite	56	57	55	55	53	54	51	55	60	47
	Liptinite	5	4	5	4	3	4	3	1	0	1
	Semi-Fusinite	31	27	25	24	25	27	29	29	30	42
	Fusinite	8	12	15	18	18	16	17	16	10	10
Klein Kopje	Vitrinite	32	34	32	31	28	32	30	31	31	28
	Liptinite	3	2	2	3	4	3	2	1	0	0
	Semi-Fusinite	51	50	52	51	52	50	52	56	58	58
	Fusinite	14	14	14	15	16	16	15	12	11	14

Large mosaic images of each coal sample were then analysed using the automated maceral analysis tool described in Chapter 4. The correlation between manual maceral

analysis and maceral composition is shown in Figure 7.2 and the full data set is attached as Table 1 in Appendix 4. Generally automated results correlated well with manually determined maceral distributions with a R^2 value of 0.9952. For high vitrinite coals Fila Mistra, La Jagua and Bentinck, the maximum variance observed was 3%. For Trans Natal and Klein Kopje the average variance was higher at 5-10%, as the transition point between vitrinite and semi-Fusinite becomes harder to resolve and the larger proportion of inertinite increases potential error. These results are consistent with those observed in Chapter 4 and most automated classifications fall within standard prescribed by ISO standard, indicating that the automated method can generally detect subtle changes in reflectance well.

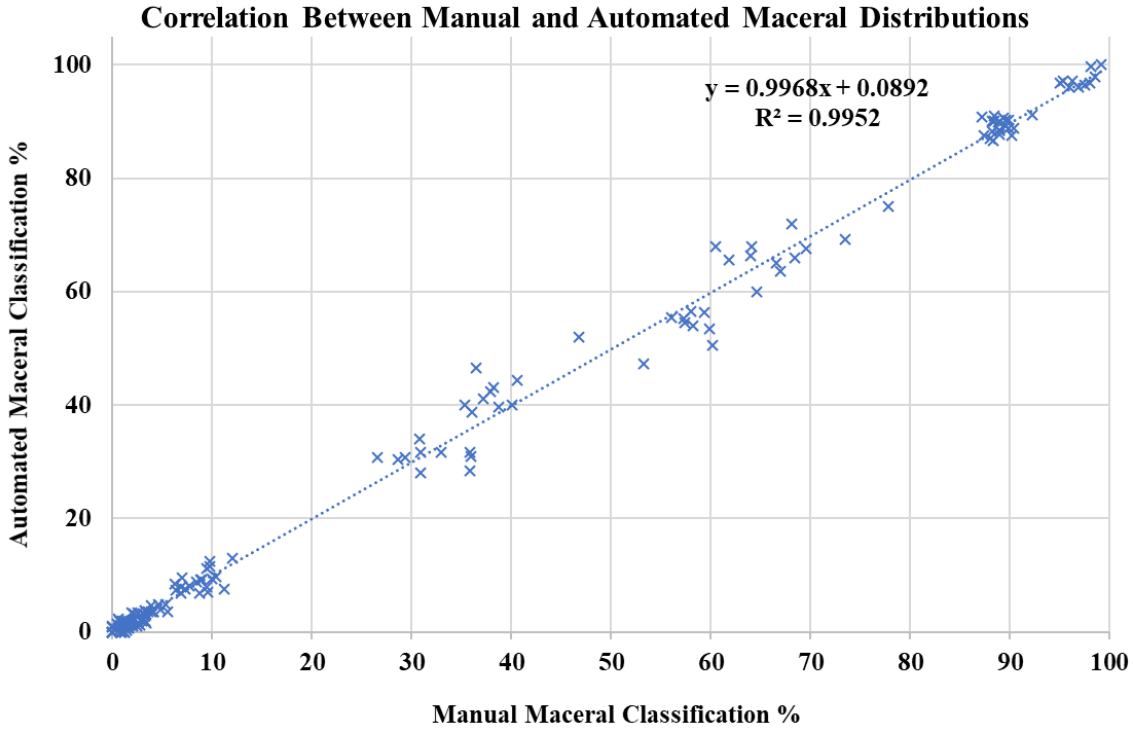


***Figure 7.2** – Correlation between manually obtained maceral distributions and those derived using the automated system*

7.1.4. % Unreactives

The % Unreactives derived from the Reactivity Assessment, is the cumulative percentage of coal material (all macerals) that has a reflectance greater than 70 grey scale units. The % Unreactives for each coal sample can be seen in Table 7.5. The results show that Bentinck, Fila Mistra and La Jagua do not change significantly until 225 ^{o}C. The value for 250 ^{o}C shows a large non-linear increase. The % Unreactives for Klein Kopje and Trans Natal exhibit a more profound increase over the whole temperature range. This in some ways is like the effect seen in the fuel ratio changes. Klein Kopje showed a trend of steadily decreasing fuel ratio over the whole range, whereas the other coals were more reluctant to show any definite change until the higher temperatures where reached.

Table 7.5 - % Unreactives for the oxidised coals

	Oxidation Temperature (^{o}C)									
Coal Sample	**25**	**50**	**75**	**100**	**125**	**150**	**175**	**200**	**225**	**250**
La Jagua	3	1	4	4	3	7	5	6	6	15
Bentinck	3	4	2	2	2	5	5	6	5	5
Fila Mistra	1	1	1	0	1	0	1	1	6	9
Klein Kopje	37	32	36	37	33	38	47	44	51	56
Trans Natal	3	1	4	3	4	3	2	18	19	16

Since the rank of each coal is clearly increasing, as seen in Table 7.3, it may seem odd that the % Unreactives does not increase in line with rank changes. The explanation is related to the method used to obtain the % Unreactives from the reactivity assessment profile. Figure 7.3 shows how the cumulative profile for Bentinck coal moves from left to right, as a result of increasing oxidation temperature. A coal like La Jagua and Fila

Mistra would produce steep sided distribution curves as illustrated in Figures 7.4 and 7.5 respectively. With increasing oxidation temperature, this uniform profile moves up the grey scale axis (X-axis) and it is not until the final oxidation temperatures that a significant change is seen in the %Unreactives. The curves for Klein Kopje (Figure 7.6) and Trans Natal (Figure 7.7) are markedly different, due to their high inertinite content, their curves are much flatter, which results in a much higher % Unreactives recorded at all temperatures.

The use of a simple cut-off, as opposed to a more complex summary of the reflectance information (found in the Reactivity Assessment profile) may prove to be too simplistic a measure with oxidised coals as is demonstrated below in Section 7.2.2, where a %unreactives cut off is implemented as part of the char morphology prediction program as coals with a similar %Unreactives should produce equal amounts of thin walled chars with a relatively high intrinsic reactivity.

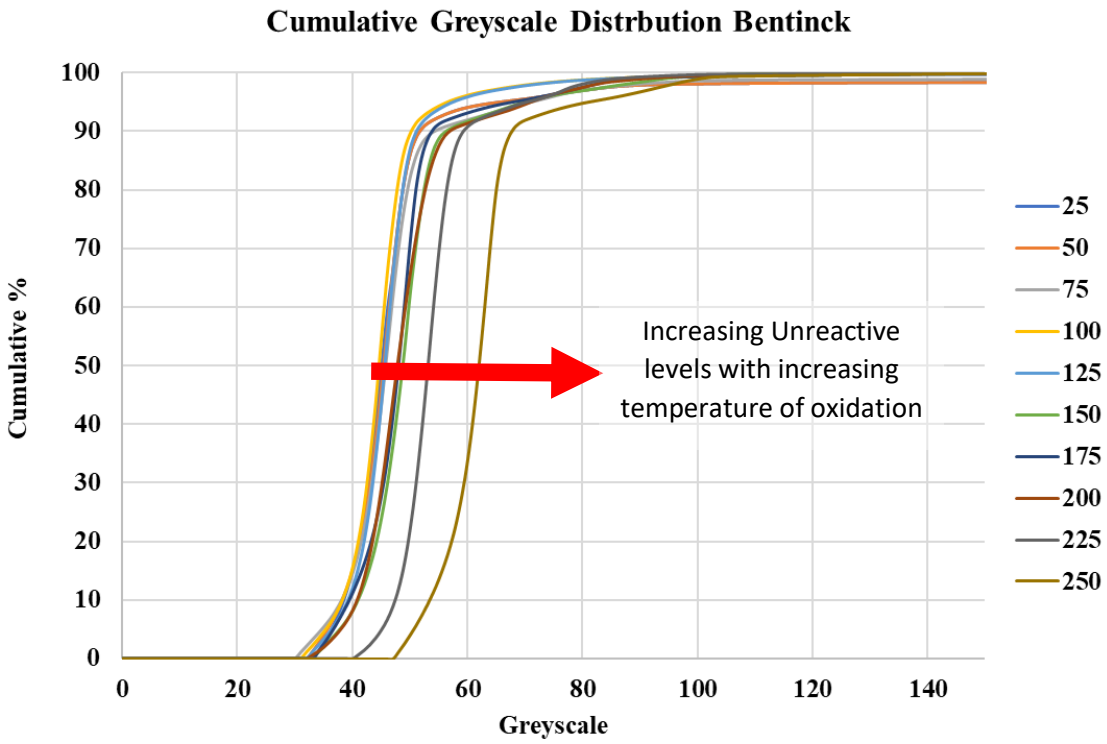


Figure 7.3 *– Cumulative greyscale distribution curves for Bentinck coal with increasing oxidation temperature*

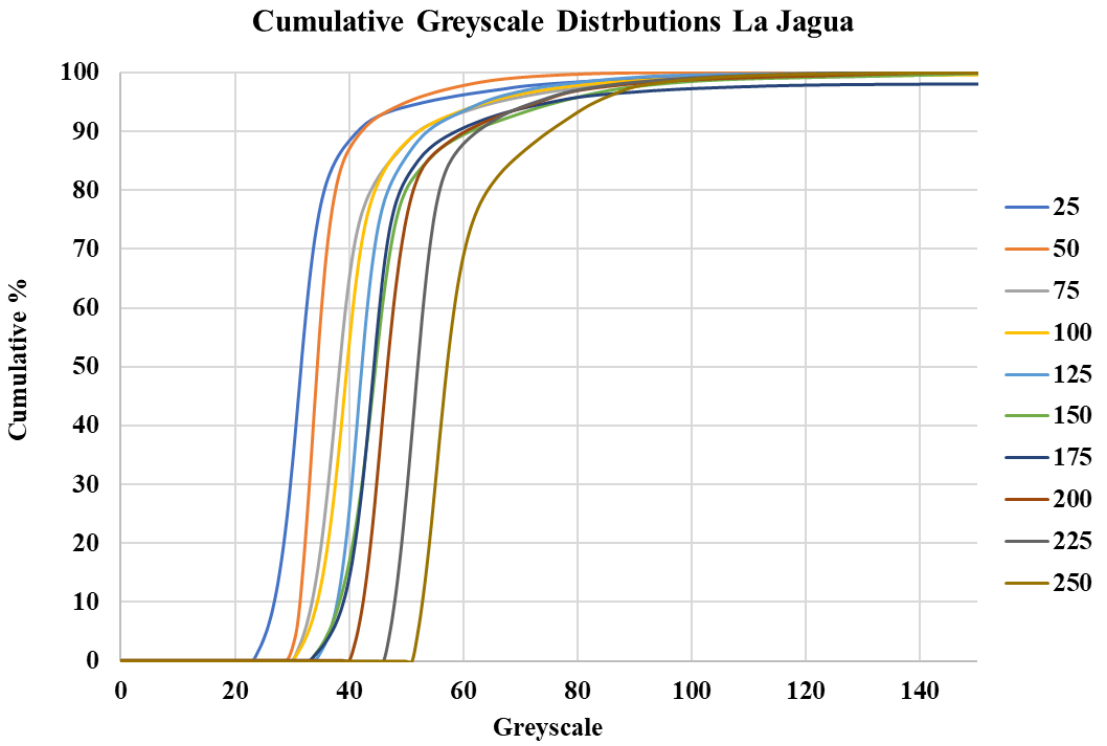


Figure 7.4 *– Cumulative greyscale distribution curves for La Jagua coal with increasing oxidation temperature*

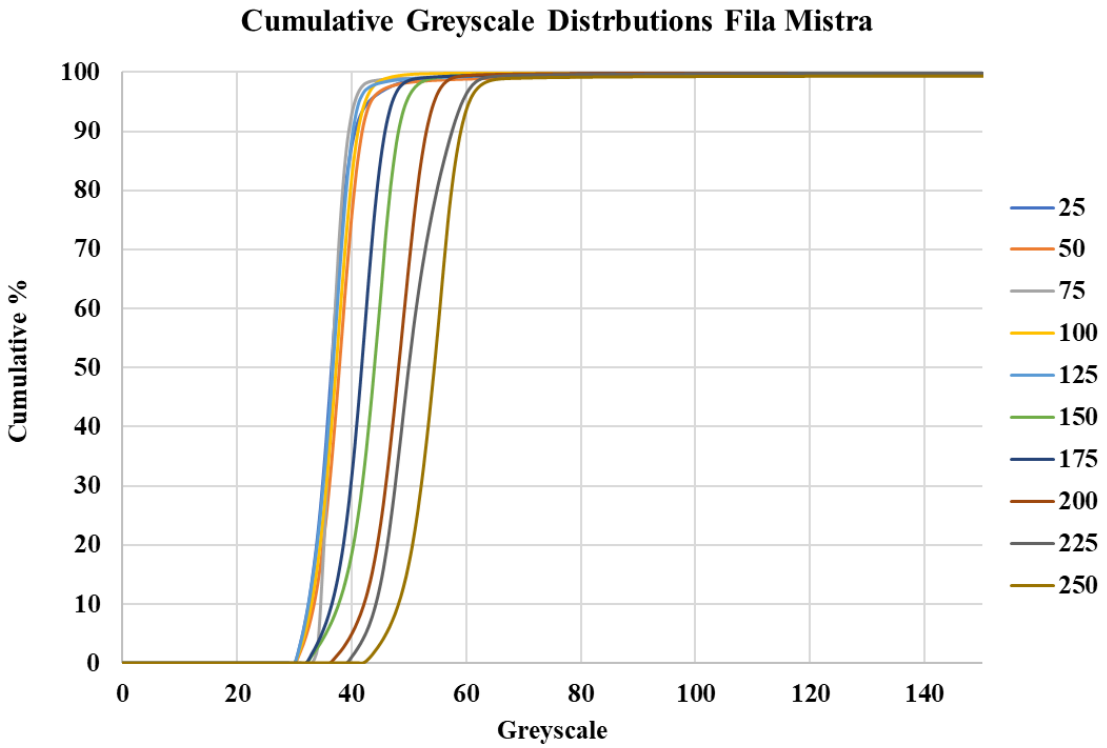


Figure 7.5 *– Cumulative greyscale distribution curves for Fila Mistra coal with increasing oxidation temperature*

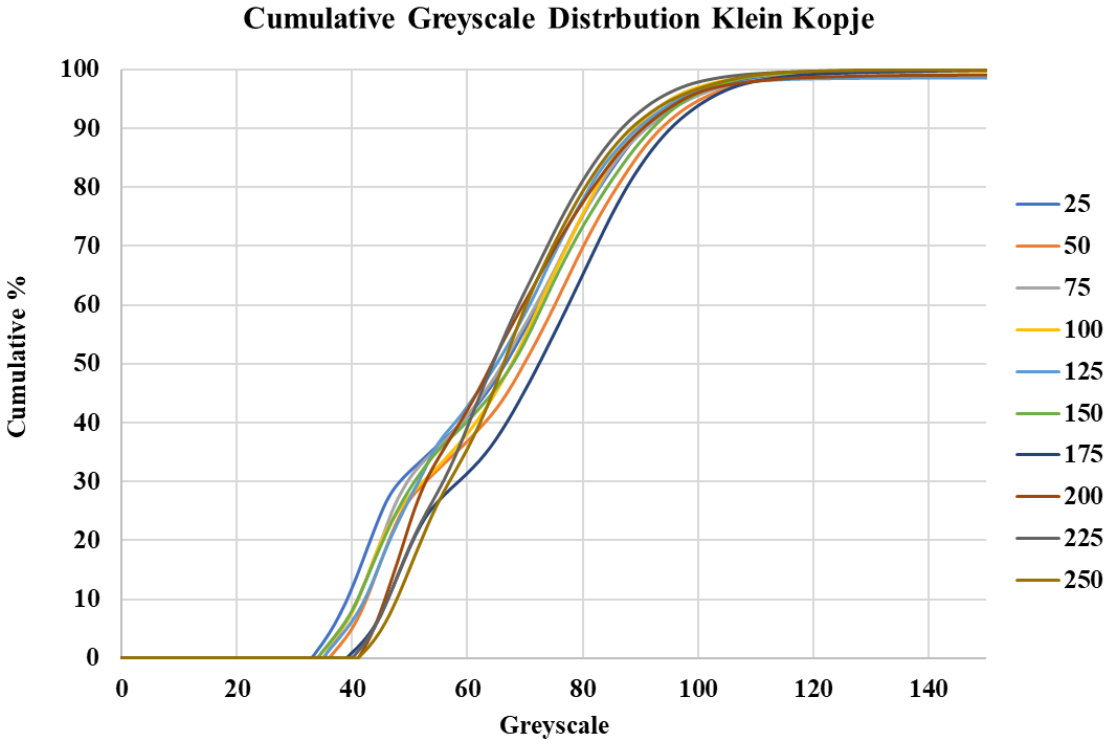


Figure 7.6 *– Cumulative greyscale distribution curves for Klein Kopje coal with increasing oxidation temperature*

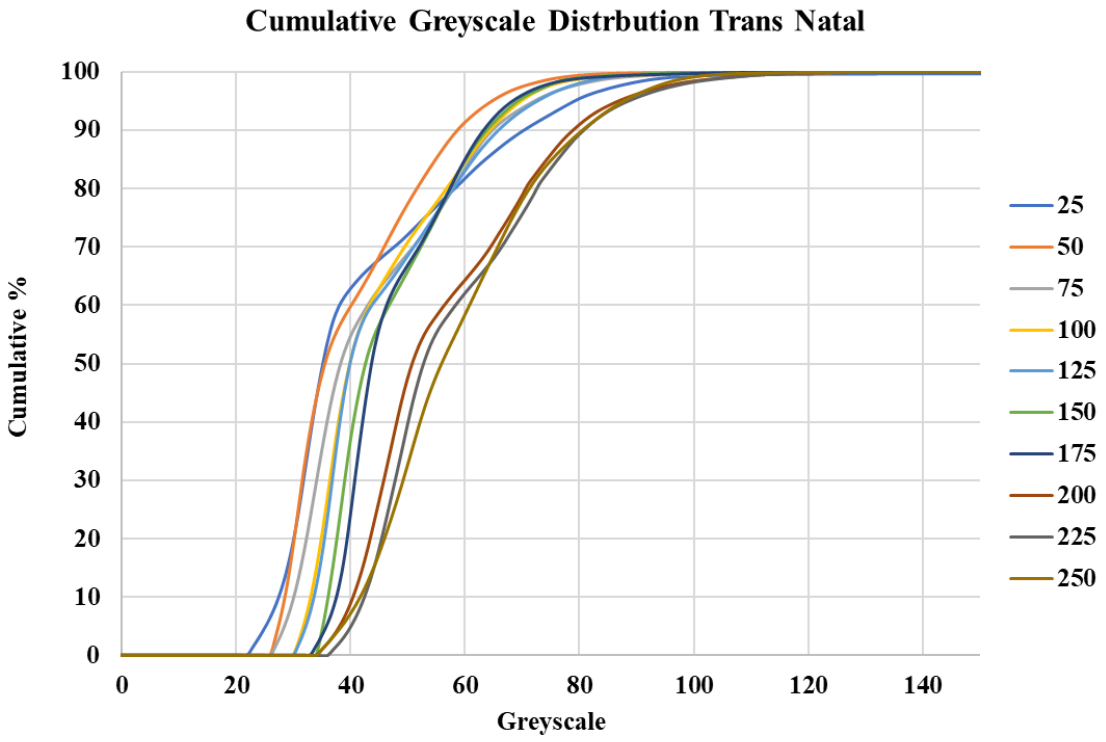


Figure 7.7 *– Cumulative greyscale distribution curves for Trans Natal coal with increasing oxidation temperature*

7.2. The Effect of Oxidation on Char Properties

7.2.1. Oxidation and Char Morphology

As the oxidation temperature increases, any change in the type of chars produced would indicate structural and physical changes in the initial coal. The morphological appearance of each char sample at different oxidation temperatures was measured using traditional manual point counting and the automated classification system described in Chapter 5. Figures 7.8-12 compare the results from both methods and visualise the changing char morphology observed with increasing oxidation temperature (TS =

Tenuisphere, CS = Crassisphere, TN = Tenuinetwork, CN = Crassinetwork and S = Solids). Detailed results are attached as Tables 2 and 3 in Appendix 4.

The char morphology distributions obtained using the automated system generally matched very closely with those obtained manually with a maximum variance of 15% observed, with most results varying between 0-10%. Generally, the automated system underclassified tenuispheres compared to the manual results. The likely reason being, that these thinner chars are more suspectable to fracturing during the sample preparation and are more likely to remain unrepaired and disregarded by the program. This under classification was only minor and the overall variability is akin to that observed during development of the system in Chapter 5 and illustrates that the automated system is sensitive enough to detect subtle changes in char morphology distribution with increasing oxidation temperature.

In terms of the oxidation temperature trends themselves, there are distinct differences in char morphology distribution observed with increasing oxidation temperature in all 5 coal samples. Fila Mistra clearly begins to change from thin walled chars to form thicker crassi- chars. A break point exists at 150 ^{o}C, where the equilibrium in char types begins to radically change and crassinetworks become far more prevalent. By 250 ^{o}C more thick-walled chars exist than thin walled. The quantity of Solids is low and remains low throughout all temperatures.

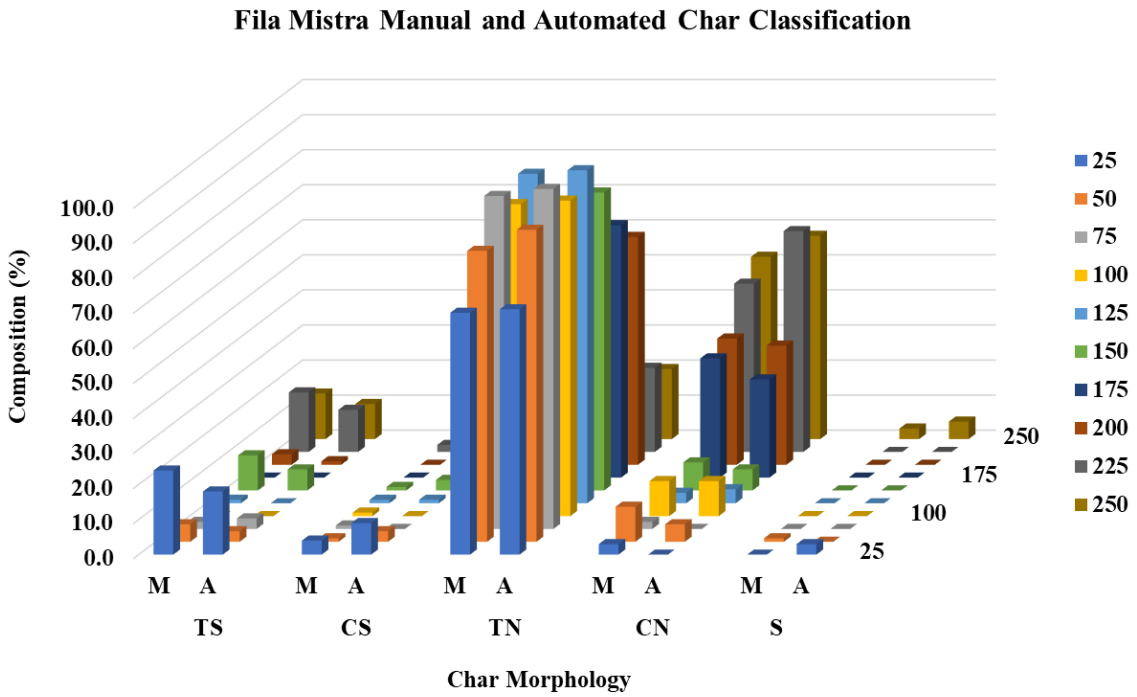


Figure 7.8 *– Comparison between manual and automated char classification results for Fila Mistra*

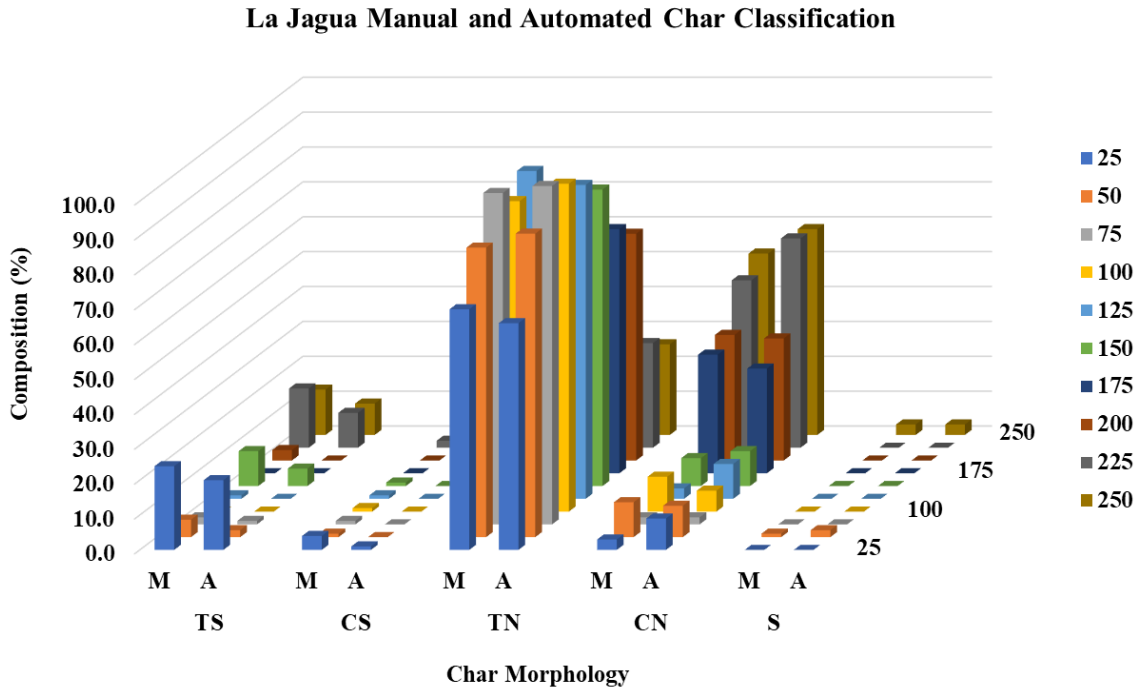


Figure 7.9 *– Comparison between manual and automated char classification results for La Jagua*

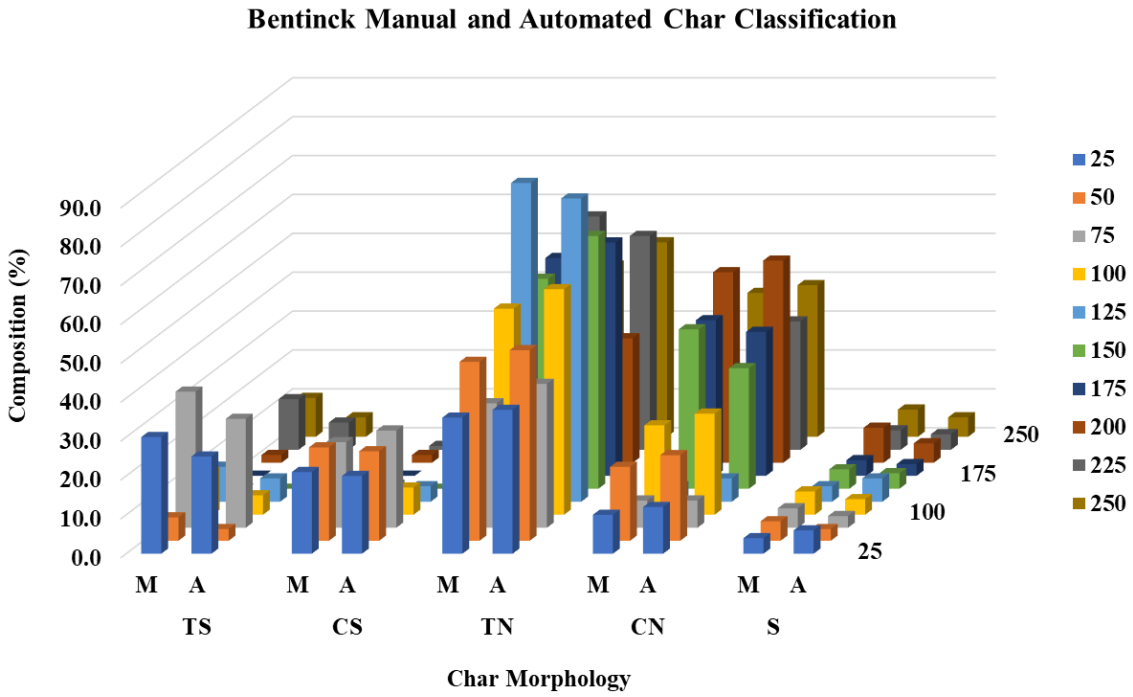


Figure 7.10 *– Comparison between manual and automated char classification results for Bentinck*

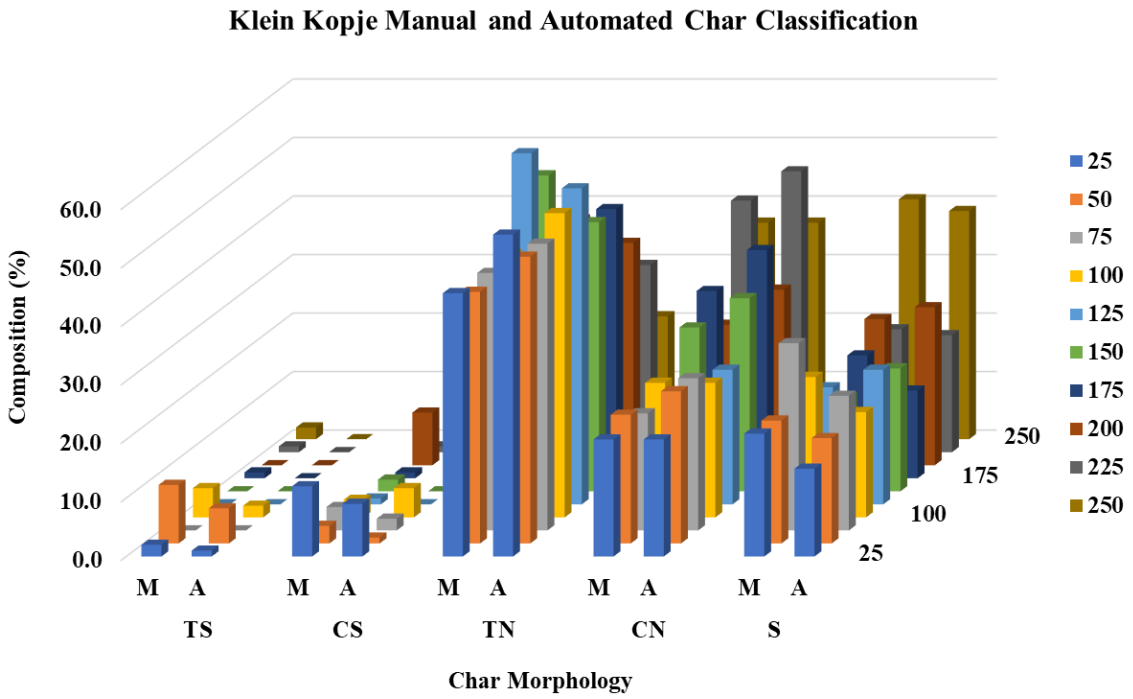


Figure 7.11 *– Comparison between manual and automated char classification results for Klein Kopje*

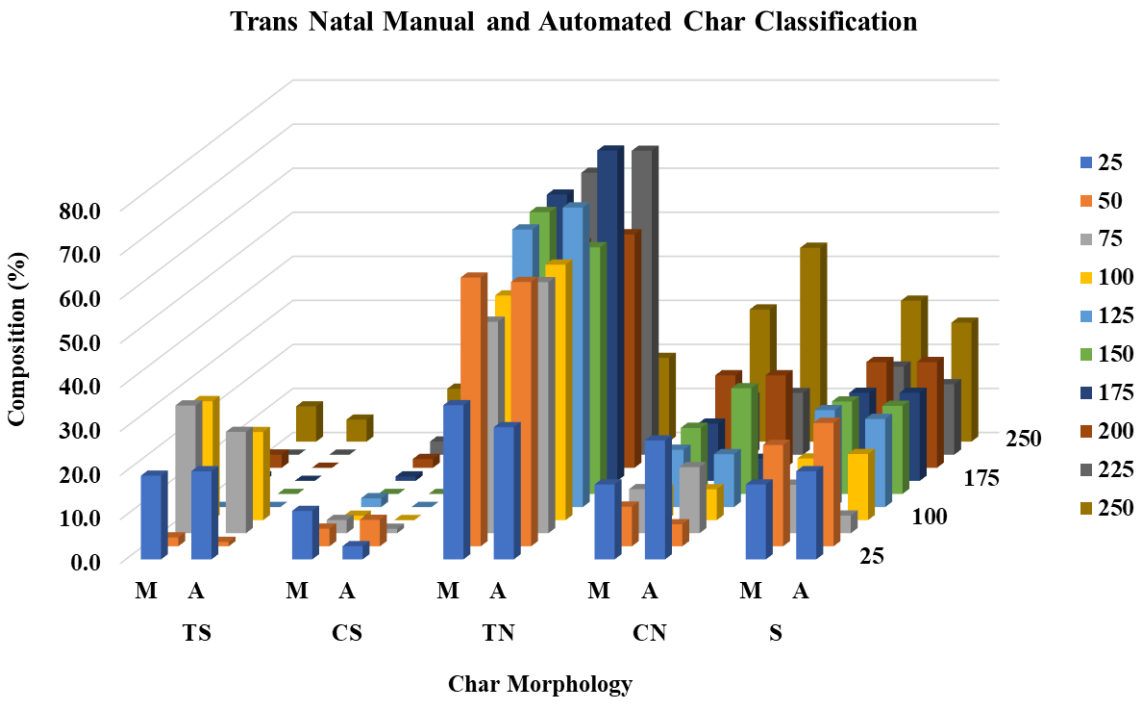


Figure 7.12 *– Comparison between manual and automated char classification results for Trans Natal*

La Jagua shows a break point at about 175 ºC. A conversion of the thin material from Tenuispheres to Tenuinetworks tends to precede this sudden change i.e. from 25 ºC to the breakpoint there is an increased prevalence in thin networks before a sharp increase in thick and solid chars generated. Most of the other char samples also undergo this same transition and tend to become thinner before the break point as (crassispheres decrease and tenuinetworks increase). Fila Mistra did not show the same tendency to thin out below the break point, but this is because most Fila Mistra chars already had thin walls. Bentinck formed more Solids although the total amount formed was still quite low, relative to the other char types.

Trans Natal chars appear to thin out between 25 ºC and 200 ºC. The break point seems to be at 225 ºC. The quantity of Solids also appears to rise over the temperature range. This may be due to reduced fluidity of low reflectance semi-fusinite which can form

fusinoids instead of crassinetworks or tenuinetworks. The lack of fluidity is known to affect the behaviour of the inertinite maceral (Thomas, 1989).

Between 25 ^{o}C and 125 ^{o}C, Klein Kopje appears to thin out. Solids rise from 20% to 40% although their presence in the sample between 25 ^{o}C and 225 ^{o}C seems erratic. The quantity of solid type chars does not rise significantly, and Klein Kopje also has little tendency to form spheres of any kind. This means that most chars are either tenuinetworks, crassinetworks or fusinoids. These three categories can converge, since it is the degree of fluidity that enables a particle to vesiculate into a tenuinetwork instead of a crassinetwork. As with Trans Natal, the ability of a low reflectance inertinite based particle to form a crassinetwork instead of a fusinoid is related to its ability to plasticise. As the oxidation increases beyond 125 ^{o}C, the decrease in tenuinetworks is made up with increasing crassinetworks and fusinoids. The subjectivity of char analysis, as it is, can also make the differentiation between tenuinetworks and fusinoids difficult.

All 5 coals show that oxidation at the most severe temperatures (greater than 250 ^{o}C) result in thicker walled chars that show a lower overall porosity. The behaviour in between 25 ^{o}C and these high temperatures appears to depend on the initial coal type.

7.2.2. Predicted Char Morphology

Individual coal particles separated from each coal mosaic were analysed and the daughter char morphology predicted using the system described in Chapter 4. Figures 7.13-17 display a comparison of the manual and predicted morphology results with increasing oxidation temperature. (TS = Tenuisphere, CS = Crassisphere, TN = Tenuinetwork, CN = Crassinetwork and S = Solids). A full breakdown of the results is attached as Table 4 in Appendix 4.

For coals oxidised at temperatures between 25 ^{o}C and 150 ^{o}C the degree of agreement between manual and predicted char morphologies is generally very good with an average variance of between 0-7% observed as shown in Figure 7.18. The exception to this is Bentick, where the predictive system consistently overpredicts the proportion of tenuispheres. This is due to the steep greyscale distribution and relatively small increase in rank with increasing oxidation temperature (illustrated by the steep and condensed line grouping in Figure 7.3) meaning that most coal particles didn't exceed the %Unreactives cut off to predict tenuinetworks instead of spheres.

For oxidising temperatures of 175 ^{o}C and above the variance between manual and predicted results increases greatly for Fila Mistra, La Jagua and Bentick, which corresponds with the break points discussed earlier where thick walls become far more prevalent than thinner morphologies. It appears that the predicted program is ill suited to detecting this point and can no longer make accurate char morphology predictions for these three coals. This is due to the implementation of a simple cut-off for %Unreactives as opposed to a more complex summary of the reflectance information (found in the Reactivity Assessment profile) and appears too simplistic a measure when dealing with coals which approach and then surpass this cut off during oxidation as coals with a similar %Unreactives should produce equal amounts of thin and thick walled chars. Char predictions for Klein Kopje and Trans Natal remained generally good across the whole range of oxidation temperatures, in part this is unsurprising as Klein Kopje was one of the coals used in the initial development and training of the system. Another reason is that a large percentage of particles for both South African coals already met the %Unreactives threshold before any oxidation occurred and response from the system to increasing unreactives was not required as with the other coal samples.

The predictive system is to some degree effective at providing power generators with information concerning predicted char morphology of oxidised coal samples and that accuracy and reliability could be improved by introducing a more comprehensive measure of changing %Unreactives.

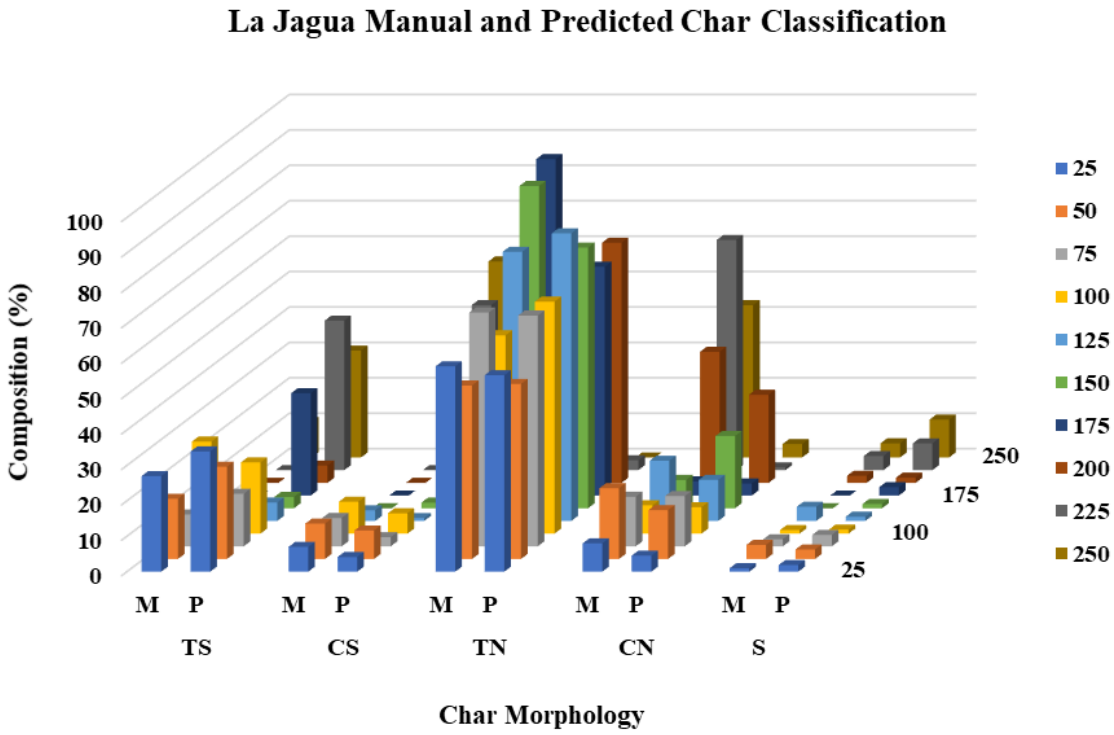


Figure 7.13 *- Comparison between manual and predicted char classification results for La Jagua*

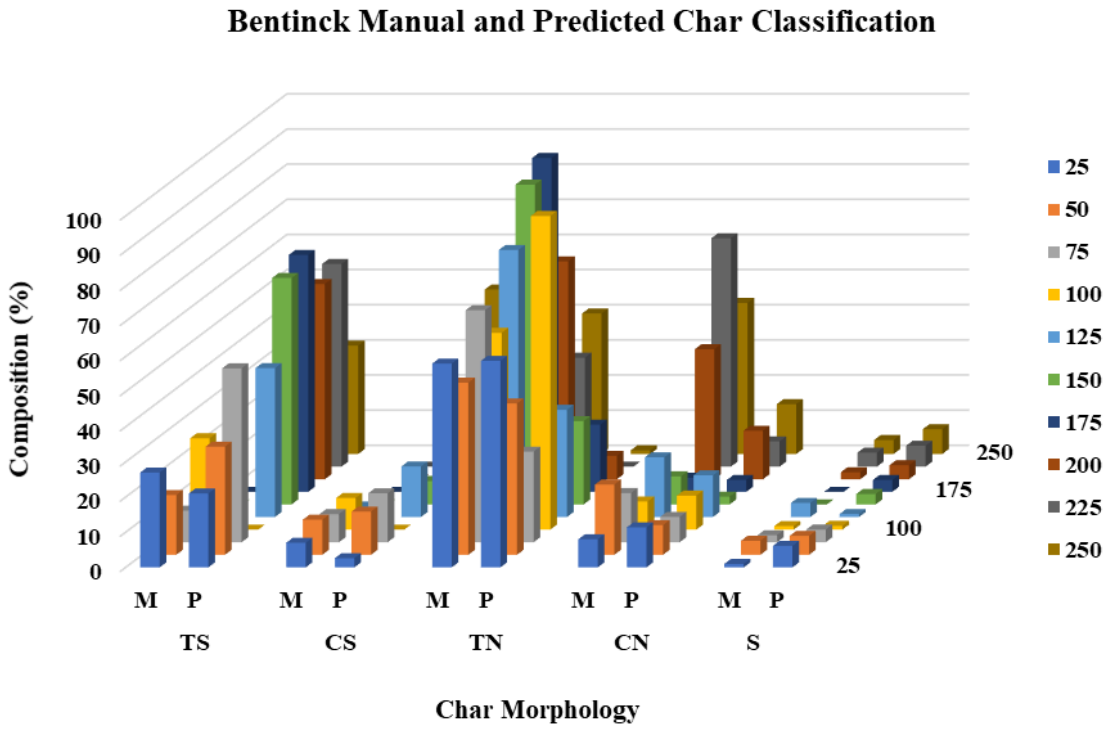


Figure 7.14 *- Comparison between manual and predicted char classification results for Bentinck*

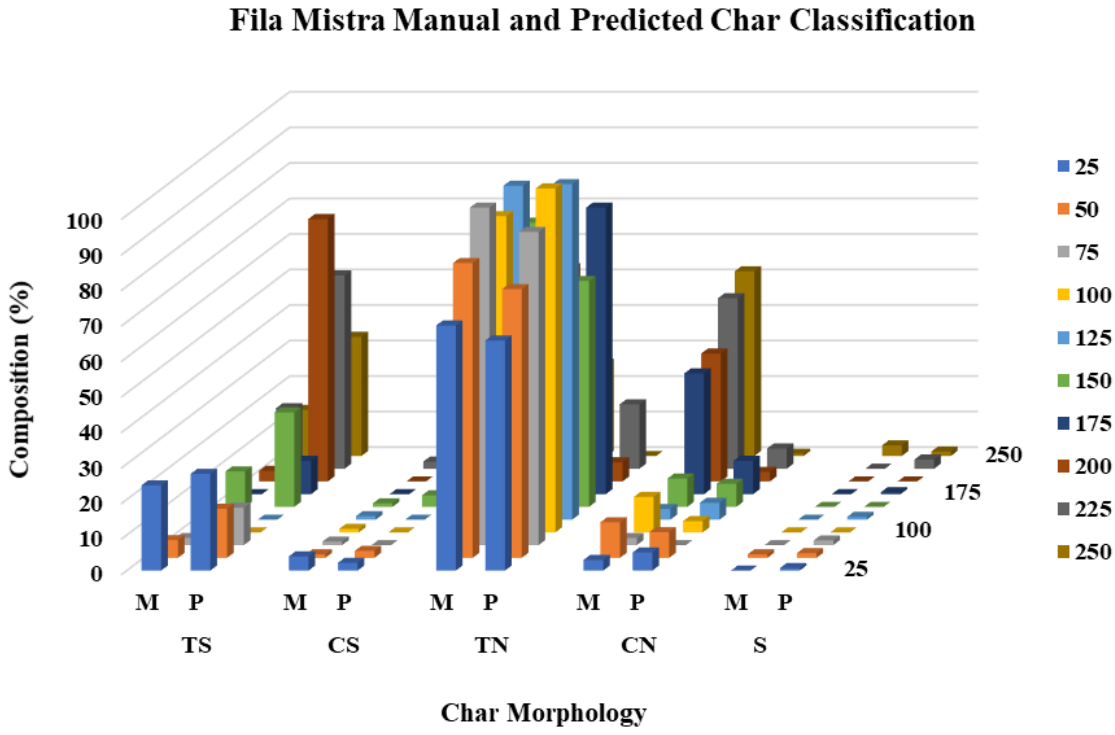


Figure 7.15 *- Comparison between manual and predicted char classification results for Fila Mistra*

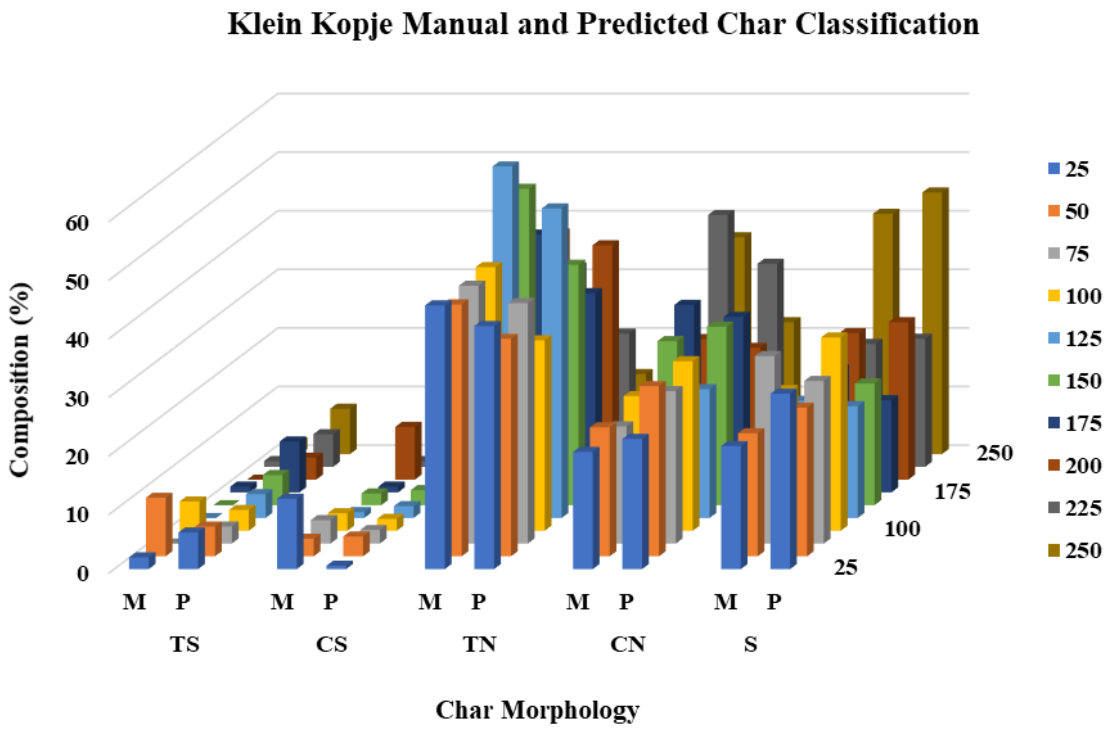


Figure 7.16 *- Comparison between manual and predicted char classification results for Klein Kopje*

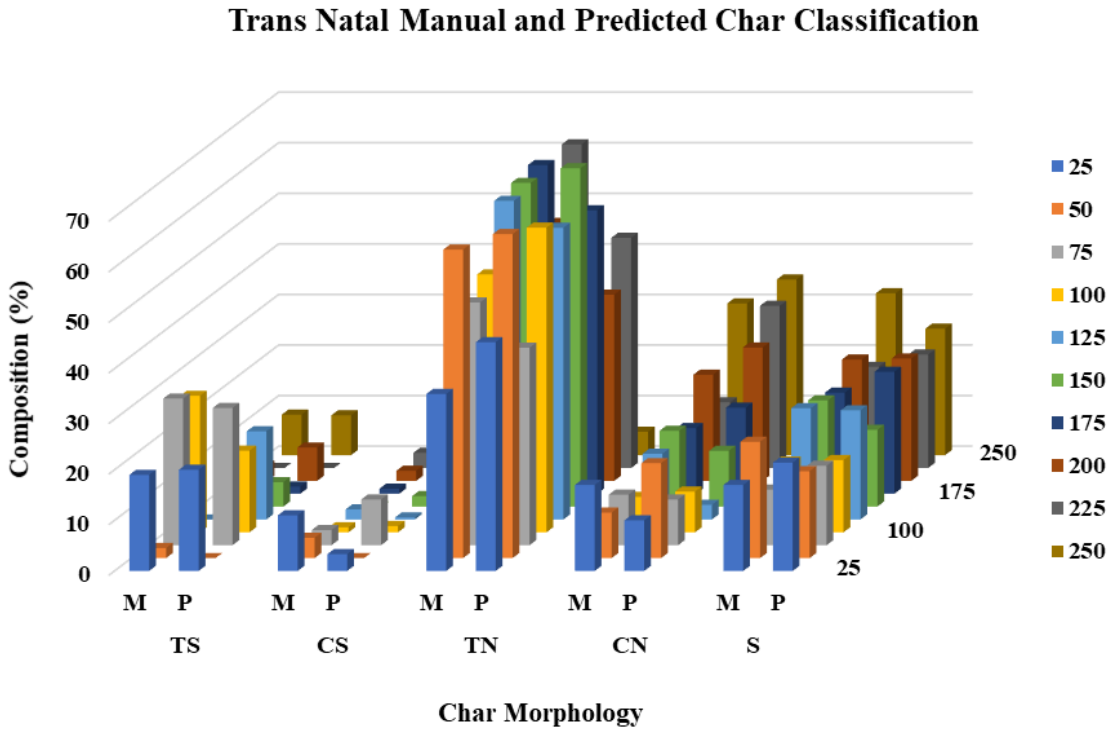


Figure 7.17 *- Comparison between manual and predicted char classification results for Trans Natal*

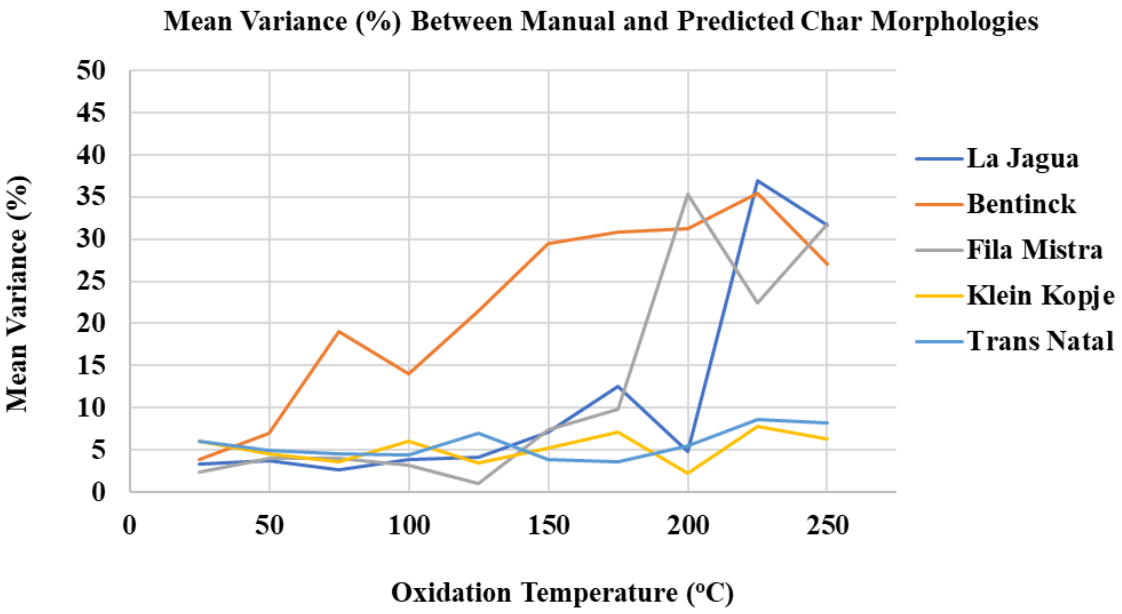


Figure 7.18 *– Relationship between increasing oxidation temperature and the variance between manual and predicted char morphology*

7.2.3. Oxidation and Intrinsic Reactivity

Table 7.6 shows the intrinsic reactivity (peak temp) results for the chars produced in the drop-tube furnace. Figure 7.19 shows the change in burnout temperature as coal oxidation increases. With Klein Kopje, Trans Natal and Bentinck, it is possible to see a gradual decrease in burnout temperature over the oxidation range. La Jagua shows a similar decrease, but with a break at 150 °C. Fila Mistra does not really show any definite trend with oxidation temperature. The fact that the chars from the most oxidised coals produced chars that were relatively more 'reactive', is surprising. It might be expected that since oxidised coals are poorer burners, that oxidised coals would give low reactivities (in the form of higher burnout temperatures).

Table 7.6 - Intrinsic Reactivity Values

	Peak Temperature at Oxidation Temperature (°C)									
Char Sample	**25**	**50**	**75**	**100**	**125**	**150**	**175**	**200**	**225**	**250**
La Jagua	613	615	617	610	604	590	602	606	599	599
Bentinck	612	612	611	606	593	594	596	596	588	590
Fila Mistra	559	554	558	551	553	551	558	566	555	565
Klein Kopje	643	641	640	637	635	626	627	624	622	623
Trans Natal	632	628	629	625	623	618	618	618	615	615

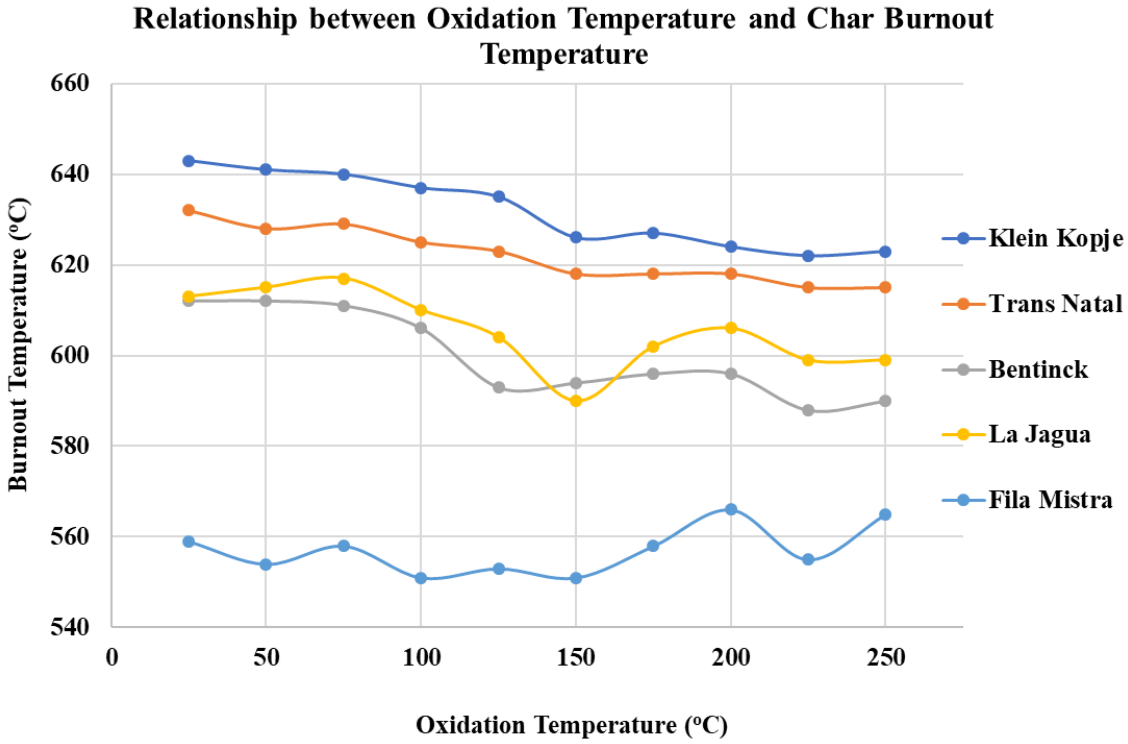


Figure 7.19 *– Relationship between char oxidation temperature and burnout temperature*

The effect on peak temperature is less clear. Fila Mistra, as with burnout temperature, appears to increase slightly. La Jagua, Bentinck and Trans Natal are either unaffected

or decrease marginally. Klein Kopje shows an increase in peak temperature between 25^{o}C and 250 ^{o}C. Since the peak temperature increases and the burnout temperature decreases, the peaks appear to be converging, becoming less distinguished. The exact reason for this is not known although it is possible that the proportion of 'reactive' components in a coal influences the size and position of the second peak as well as its own, and vice versa.

The burnout temperatures correlate with % Unreactives, in that Klein Kopje has the highest % Unreactives and has the lowest intrinsic reactivity. Fila Mistra has the highest % Unreactives and has a high intrinsic reactivity. At 250 ^{o}C, the same distribution is seen. Fila Mistra has a burnout temperature of 565 ^{o}C, whereas the Klein Kopje char gives 623 ^{o}C. The results from the other three coals are distributed in-between.

7.3. Predicted Char Burnout

Any trends of char thinning, or thickening seen with the manual and automated morphology analysis and the impact this would have on char combustion should also be detectable using the predicted char burnout method developed in Chapter 6. Combustion was simulated on all 50 char samples using the 'Pacman Burnout Simulation' and the predicted burnouts with increasing oxidation temperature are shown in Figures 7.20-24.

As discussed in Section 7.2.1, some of the coals appear to undergo a thinning process before a break point is reached and the prevalence of thick-walled chars increases dramatically. As the Pacman model erodes char material away iteratively, char wall thickness can therefore be directly related to the rate of simulated burnout. Bentinck, La Jagua, Trans Natal and Klein Kopje all appear to undergo the initial thinning process

illustrated by a faster simulated burnout before a break point where burnout efficiency is predicted to decrease dramatically. For Bentinck, the rate of simulated burnout for sample oxidised at 50 ^{o}C and 75 ^{o}C exceeds that for 25 ^{o}C before the rate begins to gradually slow before dramatically decreasing at 175 ^{o}C. Similar is observed for Klein Kopje, Trans Natal and La Jagua samples, however the break points are less dramatic and appear to be more gradual. The simulated burnout of Fila Mistra differs as most of the initial char material generated at 25 ^{o}C was already thin.

The predicted burnout simulations support the changes observed in char morphology with increasing oxidisation temperature discussed earlier. Whereas char classification can only provide morphology distribution information, burnout simulations can show the degree of morphology change with increasing oxidation temperature and the directly impact on char burnout.

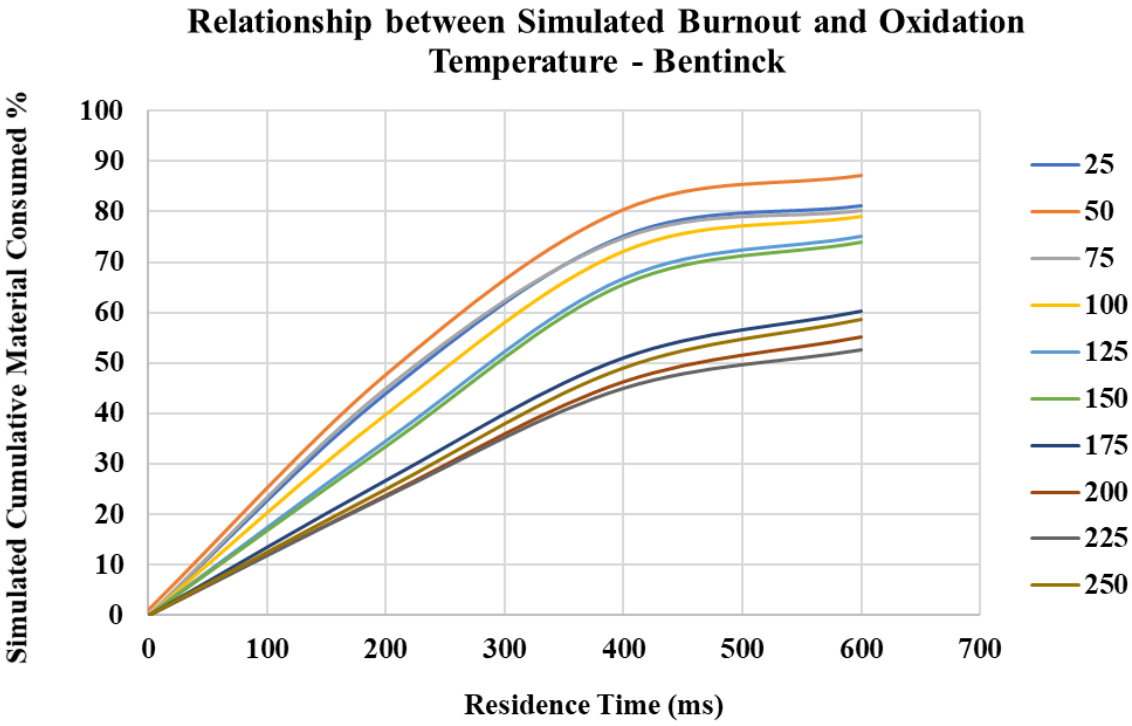


Figure 7.20 *– Relationship between increasing oxidising temperature and simulated char burnout Bentinck*

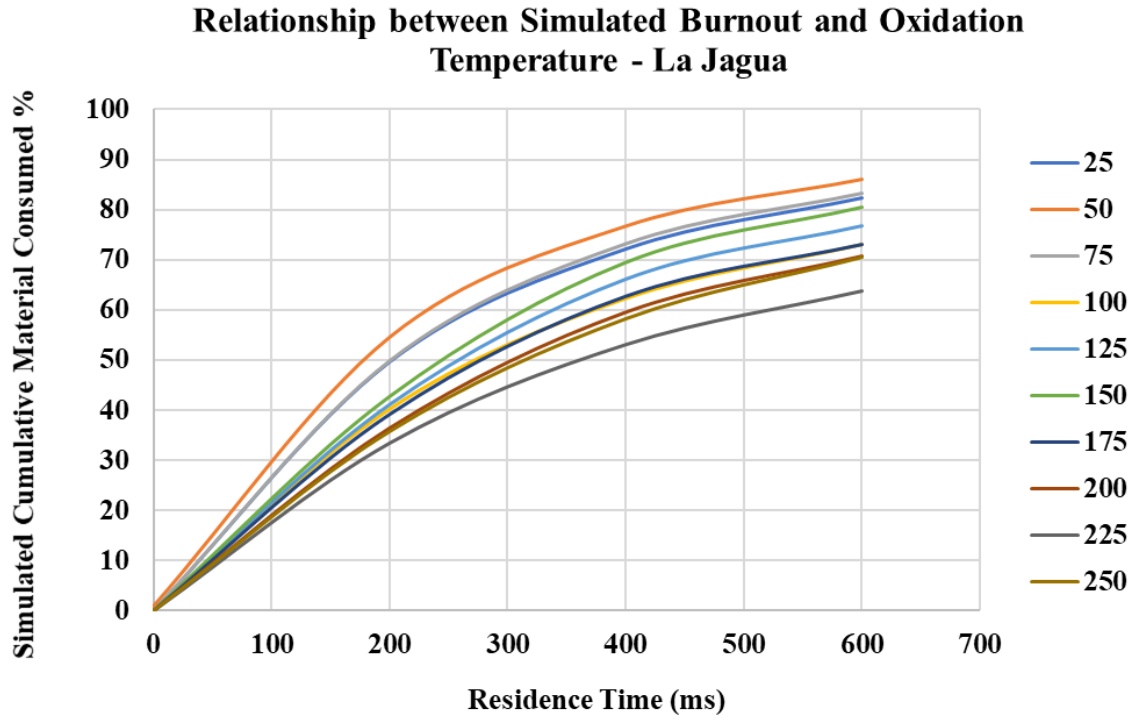


Figure 7.21 *– Relationship between increasing oxidising temperature and simulated char burnout La Jagua*

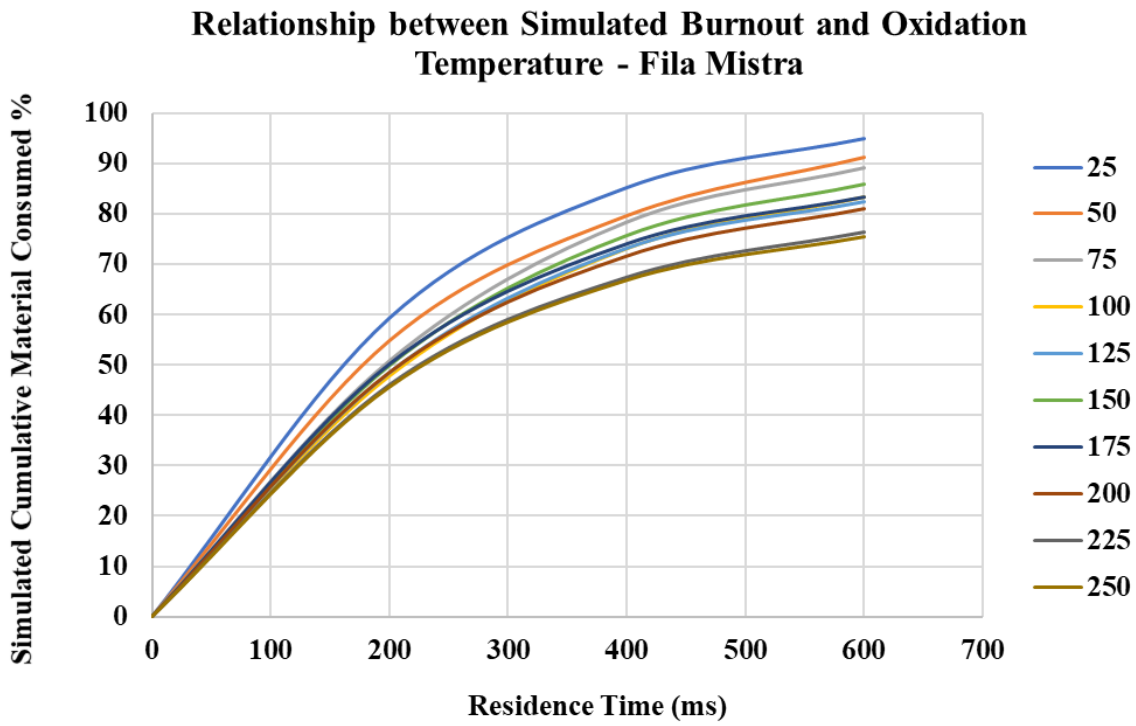


Figure 7.22 *– Relationship between increasing oxidising temperature and simulated char burnout Fila Mistra*

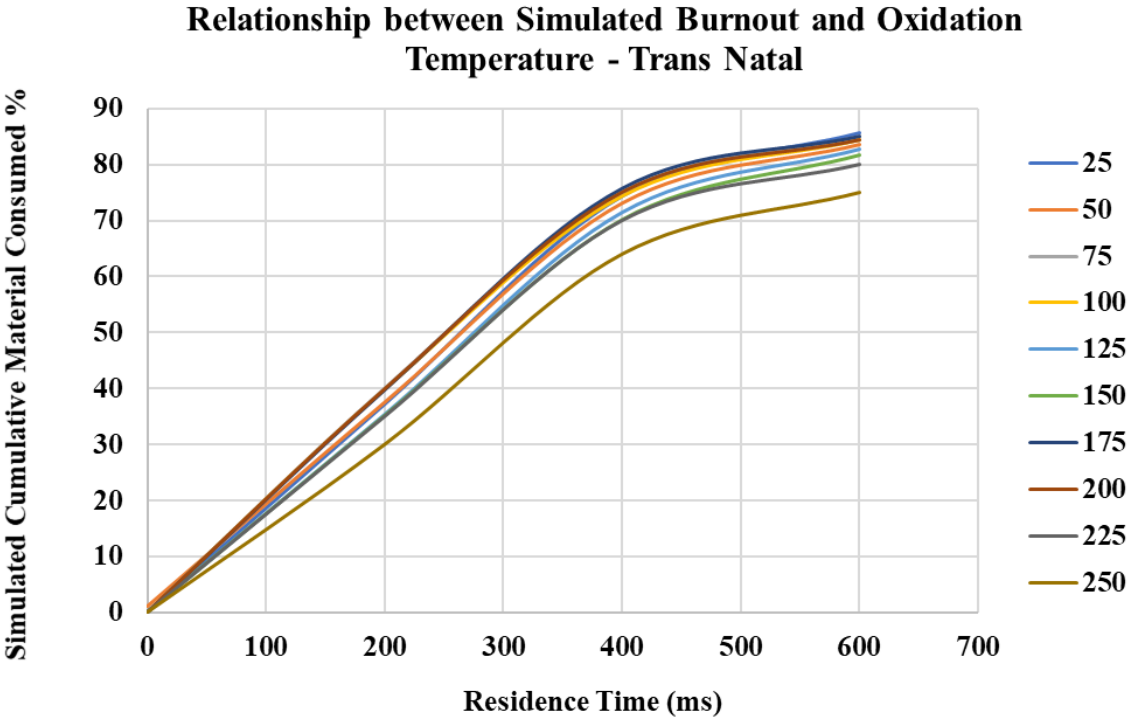


Figure 7.23 *– Relationship between increasing oxidising temperature and simulated char burnout Trans Natal*

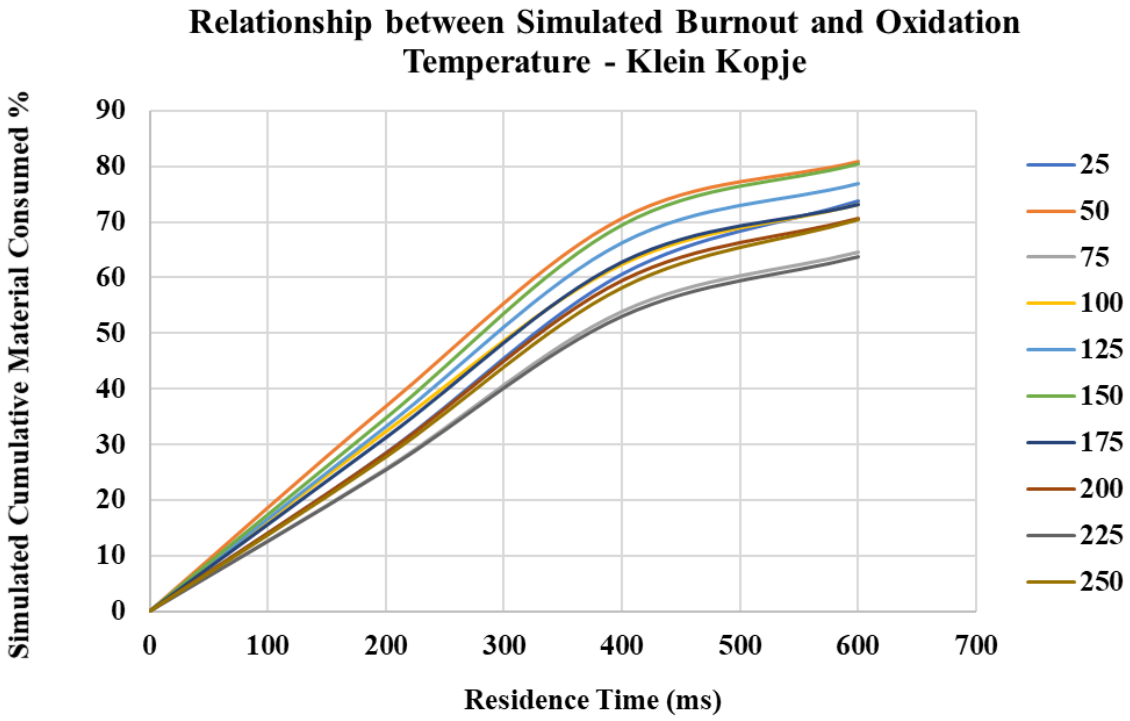


Figure 7.24 *– Relationship between increasing oxidising temperature and simulated char burnout Klein Kopje*

7.4. Conclusions

The aim of this work was to implement a suite of advanced image analysis techniques to observe the relative effect of oxidation on both coal and char properties and to test the accuracy and versatility of the methods for analysing subtle changes in coal and char samples. This work represented a novel image-based investigation into the properties of heat affected coal samples and the way that these properties dictate daughter char properties. Coal oxidation and its effect on char behaviour is significant with temperatures as low as 75 ^{o}C could be observed by the analysis of whole mosaic images and the properties of individually analysed particles.

The maceral analysis of all 5 coals changed with oxidation only with the loss of liptinite, and this was only at the higher temperatures (above 200 ^{o}C). The rank of each coal sample gradually increased with temperature and it was shown that this and the maceral distributions could be accurately monitored using the automated maceral thresholding method described in Chapter 4. It was observed that after 125 ^{o}C, the increase appeared to be quite large. The % Unreactives did not show this same tendency to increase over the whole temperature range. Only the two South African coals gave a gradual increase in %Unreactives. The position and size of the initial reactive constituents in the coal appeared to be paramount in determining whether the %Unreactives increased significantly. The initial vitrinite peaks for Fila Mistra, Bentinck and La Jagua were all so far below the cut-off threshold, that the % Unreactives did not change till around 200 ^{o}C. This had a significant impact on the predicted char morphologies as the system utilizes a set of single cut-off %Unreactives values for predicting thin or thick-walled morphologies and as a result, above a certain oxidation temperature (approx. 175 ^{o}C), could not accurately predict the continued thickening in char morphologies.

Results obtained from the automated char classification method described in Chapter 5 agreed well with those of manual analysis. The morphology of the chars produced from the oxidised coals also showed some unexpected trends. The char samples appeared to ‘thin out’ over the middle range of temperatures. However, the chars then became thicker again as the oxidation temperature continued to increase. The chars from the coals prepared at 250 ^{o}C were consistently thicker than the original coal sample (25 ^{o}C), but the behaviour in-between was non-uniform, depending on the initial coal type. As the system could detect these changes in char wall thickness, it appears that that the thresholds set for discrimination between different morphologies appear to be relatively accurate.

The ‘Pacman Burnout Model’ described in Chapter 6 was used to predict the burnout profiles of each oxidised coal sample chars. It was observed that predicted burnout rate increased for those samples than appeared to undergo a ‘thinning’ process, before a sudden increase in char wall thickness at a ‘break point’ temperature, characterised by a far slower predicted char burnout above this temperature. The exact point varied between the samples but can be approximated at between 150-200 ^{o}C. In addition to this, the intrinsic reactivity analysis of a char appeared to be dependant both on the degree of oxidation, as well as the type of coal used. Burnout temperature decreased as oxidation increased, indicating an increase in char reactivity. This was not expected, although it seems logical since the reduced fluidity of the coal would reduce the carbonisation of the char in the drop-tube, so it seems that oxidation does not reduce the ability of a particle to burnout, but merely increases the time required to burnout completely. These observations were counterintuitive but provides some interesting issues that need further consideration. The oxidation process doesn’t appear to render the particles ‘less reactive’ from an intrinsic chemical view point, but their overall tendency to form thicker chars explains the general observation that oxidised coals do not burn as well as non-oxidised coals. In short, the coal particles do not form unreactive chars. Rather, they form thicker more reactive chars that take longer to burn as a result of combustion being diffusion limited where thicker walls take longer to burnout.

Overall, it has also been shown that a suite of rapidly implementable image analysis techniques can also be employed to obtain similar observations to manually obtained data and, in some instances such as char structure analysis, provide a greater level of detail including char wall-thickness measurements and simulate burnout information without the need for a trained operator.

CHAPTER 8. Conclusions and Future Work

8.1 Research Summary

This thesis set out to develop a suite of novel automated image analysis techniques to characterise and predict the burnout potential of pulverised coal fuel. In total, four new IA techniques were developed to (1) separate and determine the maceral distribution of individual coal particles, (2) predict daughter char morphology, (3) analyse and classify 'real' combustion intermediates and (4) simulate their burnout. These techniques were then used to investigate the effects of weathering on coal stockpiles and to illustrate the potential capabilities of advanced image analysis for monitoring coal stockpiles.

8.1.1. Automated Maceral Classification

A new image-based rapid fuel characterisation system was developed that can automatically segregate coal particles into maceral groups from large mosaic images. The predicted maceral composition vs actual composition appeared to be within standard prescribed by ISO standard.

8.1.2. Char Morphology Prediction

The system then uses the information gathered from individual coal particles including reactivity, inertinite content and vitrinite reflectance to predict the distribution of major char morphologies, matching closely with actual chars generated using a drop-tube furnace. This data could be used in the future by generators who are interested in predicting combustion characteristics of unknown coals prior to purchase.

8.1.3. Automated Char Analysis and Char Classification

A fully automated image analysis technique for the separation, assessment and morphological classification of char particles into one of six morphological categories was also developed. The system displayed similar classification capabilities and enhanced processing speed compared to previous binary morphological analysis work and superior precision compared to machine learning and porosity based-systems. There is also the potential to expand the current capability to include mixed porous/dense structures in the future. One key feature of the program is the versatility of the wall mending process that, without distorting the char structure or morphological features, can rebuild even substantially splintered structures and appears to be effective on chars of various sizes.

8.1.4. Char Burnout Simulations

A novel image-based kinetics free char combustion model, the “Pacman Model”, capable of simulating char oxidation on individual char structures was developed. In addition to burnout simulation data, the model can be applied to whole mosaic images as a rapid burnout comparison tool for power generators and provide carboneous material distribution information at different residence times.

8.1.5. Implementing Image Analysis Techniques

The aforementioned suite of image analysis techniques was implemented to observe the relative effect of oxidation on both coal and char properties and to test the accuracy and versatility of the methods for analysing subtle changes in coal and char samples. This work represented a novel image-based investigation into the properties of heat affected

coal samples and the way that these properties dictate daughter char properties. It was shown that rapidly implementable image analysis techniques can be effectively employed to obtain similar observations to manually obtained data and, in some instances, such as char structure analysis, provide a greater level of detail to power generators.

8.2. Future Work

As techniques to classify individual coal particles, predict daughter char morphology and simulate burnout have been developed, a logical next step would be the development of a tool to generate artificial char structures from information obtained from individual coal particles. This would close the loop and remove the need to spend time and money generating char particles in a drop-tube furnace. A detailed array of information could then be rapidly obtained from a single large mosaic image of a coal fuel, without the need for any experimental work.

Another key potential development would be the incorporation of mineral data. As mineral detection using traditional microscopy has already been shown using air objectives (Comino et al., 2010), incorporating both maceral and mineral detection methods, particularly on the same polished surface, has the potential to offer interesting new information - including the size and position of mineral types in relation to macerals, sub-macerals and even microlithotypes. This mineral data could then be combined with particle parameters obtained from other IA techniques to provide precipitator collection efficiencies along with the expected levels of carbon in ash.

References

Ahmaruzzaman, M. (2010). A review on the utilization of fly ash. *Progress in Energy and Combustion Science, 36*(3), 327-363. doi:https://doi.org/10.1016/j.pecs.2009.11.003

Alvarez, D. L., E. (2001). Atlas of Char Occurrences. *Combustion Working Group, Commission III. ICCP*.

Avila, C., Pang, C. H., Wu, T., & Lester, E. (2011). Morphology and reactivity characteristics of char biomass particles. *Bioresource technology, 102*(8), 5237-5243. doi:10.1016/j.biortech.2011.01.071

Awangga, R. M. (2018). K Means Clustering and Meanshift Analysis for Grouping the Data of Coal Term in Puslitbang tekMIRA. *TELKOMNIKA, 16*, 1351-1357. doi:DOI: 10.12928/TELKOMNIKA.v16i3.8910

Bailey, J. G. (1990). A char morphology system with applications to coal combustion. *Fuel, 69*(2), 225-239. doi:https://doi.org/10.1016/0016-2361(90)90179-T

Benfell, K. E., Liu, G.-S., Roberts, D. G., Harris, D. J., Lucas, J. A., Bailey, J. G., & Wall, T. F. (2000). Modeling char combustion: The influence of parent coal petrography and pyrolysis pressure on the structure and intrinsic reactivity of its char. *Proceedings of the Combustion Institute, 28*(2), 2233-2241. doi:https://doi.org/10.1016/S0082-0784(00)80633-5

Bengtsson, M. (1986). Combustion behavior for a range of coals of various origins and petrographic composition. *Coal science and technology*.

Bengtsson, M. (1987). Combustion behaviour for a coal containing a high proportion of pseudovitrinite. *Fuel Processing Technology, 15*, 201-212. doi:https://doi.org/10.1016/0378-3820(87)90045-2

Bhatia, S. K., & Perlmutter, D. D. (1980). A random pore model for fluid-solid reactions: I. Isothermal, kinetic control. *AIChE Journal, 26*(3), 379-386. doi:10.1002/aic.690260308

Bhattacharjee, U., & Kandpal, T. (2002). Potential of fly ash utilisation in India. *Energy, 27*, 151-166. doi:10.1016/S0360-5442(01)00065-2

British Petroleum. (2016). *Statistical Review of World Energy*. Retrieved from https://www.bp.com/en/global/corporate/energy-economics/statistical-review-of-world-energy.html

Bustin, R. M. (1991). Quantifying macerals: Some statistical and practical considerations. *International Journal of Coal Geology, 17*(3), 213-238. doi:https://doi.org/10.1016/0166-5162(91)90033-F

C.E.S.A.C. (2003). *The Future of Coal.* Retrieved from https://web.mit.edu/coal/

Canada, S. C., G.; Cable, R.; Brosseau, D. & Price, H. . (2004). *Parabolic Trough Organic Rankine Cycle Power Plant,*. Paper presented at the DOE Solar Energy Technologies, Denver, Colorado.

Chandra, D. (1982). Oxidized coals. *Stach's Textbook of Coal Petrology*, 198-205.

Chao, E. C. T., Minkin, J. A., & Thompson, C. L. (1982). Application of automated image analysis to coal petrography. *International Journal of Coal Geology, 2*(2), 113-150. doi:https://doi.org/10.1016/0166-5162(82)90002-7

Chaubey. (2016). Comparison of The Local and Global Thresholding Methods in Image Segmentation. *World Journal of Research and Review, 2*(1), 1-4.

Chaves, D., Fernández-Robles, L., Bernal, J., Alegre, E., & Trujillo, M. (2018). Automatic characterisation of chars from the combustion of pulverised coals using machine vision. *Powder Technology, 338*, 110-118. doi:https://doi.org/10.1016/j.powtec.2018.06.035

Cloke, M., Lester, E., Allen, M., & Miles, N. (1995). *Automated maceral analysis using fluorescence microscopy and image analysis* (Vol. 74).

Cloke, M., Lester, E., & Belghazi, A. (2002). *Characterisation of the properties of size fractions from ten world coals and their chars produced in a drop-tube furnace* (Vol. 81).

Cloke, M., Lester, E., & Gibb, W. (1997). Characterization of coal with respect to carbon burnout in p.f.-fired boilers. *Fuel, 76*(13), 1257-1267. doi:https://doi.org/10.1016/S0016-2361(97)00016-1

Cloke, M., Lester, E., & Thompson, A. W. (2002). Combustion characteristics of coals using a drop-tube furnace. *Fuel, 81*(6), 727-735. doi:http://dx.doi.org/10.1016/S0016-2361(01)00199-5

Cloke, M., Wu, T., Barranco, R., & Lester, E. (2003). Char characterisation and its application in a coal burnout model☆. *Fuel, 82*(15), 1989-2000. doi:https://doi.org/10.1016/S0016-2361(03)00155-8

Comino, P., Warren, K., & O'Brien, G. (2010). *Applying the Coal Grain Analysis (CGA) method on liberation studies in coal*.

Cox, J. L., & Nelson, C. R. (1984). *COAL WEATHERING: CAUSES, EFFECTS AND IMPLICATIONS.* Paper presented at the ACS Division of Fuel Chemistry, Preprints.

Crelling, J. C. (2008). Chapter 7 - Coal Carbonization. In I. Suárez-Ruiz & J. C. Crelling (Eds.), *Applied Coal Petrology* (pp. 173-192). Burlington: Elsevier.

David, P., & Fermont, W. (1993). *Application of colour image analysis in coal petrology* (Vol. 20).

Directive 2008/50/EC of the European Parliament and of the Council of 21 May 2008 on ambient air quality and cleaner air for Europe, (2008).

Gilfillan, A., Lester, E., Cloke, M., & Snape, C. (1999). Structure and reactivity of density separated coal fractions. *Fuel, 78*, 1639-1644. doi:10.1016/S0016-2361(99)00110-6

Gilot, P., Brillard, A., Brilhac, J.-F., & Schönnenbeck, C. (2017). A Simplified Model Accounting for the Combustion of Pulverized Coal Char Particles in a Drop Tube Furnace. *Energy & Fuels, 31*(10), 11391-11403. doi:10.1021/acs.energyfuels.7b01756

Gracia M., G. J. R., Barrero M.L., García A.B., Martinez-Alonso A., Tascón (1993). Comparative Mijssbauer study of the effects of natural weathering and artificial oxidation on iron minerals present in coal *Nuclear Instruments and Methods in Physics Research, B76*, 191-194.

H.S.Prasantha. (2010). Medical Image Segmentation. *International Journal on Computer Science and Engineering, Vol. 02*(No. 04), 1209-1121.

Hapugoda, P., Krahenbuhl, G., O'Brien, G., & Warren, K. (2015). *A New Method for Obtaining Detailed Mineral Information on Individual Coal Particles at the size that they are used in Coke Making*.

Hurt, R., Sun, J.-K., & Lunden, M. (1998). A Kinetic Model of Carbon Burnout in Pulverized Coal Combustion. *Combustion and flame, 113*(1), 181-197. doi:https://doi.org/10.1016/S0010-2180(97)00240-X

Hurt, R. H., & Calo, J. M. (2001). Semi-global intrinsic kinetics for char combustion modeling. *Combustion and flame, 125*(3), 1138-1149. doi:https://doi.org/10.1016/S0010-2180(01)00234-6

Hurt, R. H., & Davis, K. A. (1994). Near-extinction and final burnout in coal combustion. *Symposium (International) on Combustion, 25*(1), 561-568. doi:https://doi.org/10.1016/S0082-0784(06)80686-7

ICCP. (2001). The new inertinite classification (ICCP System 1994). *Fuel, 80*(4), 459-471. doi:https://doi.org/10.1016/S0016-2361(00)00102-2

IE.Agency. (2017). *Coal Report 2017: Analysis and Forecasts to 2022*. Retrieved from https://www.iea.org/coal2017/

IE.Agency. (2008). *Scenarios and Strategies to 2050.* Retrieved from https://www.iea.org/weo2018/scenarios/

IE.Agency. (2015). 2015. *World Energy Outlook*. Retrieved from https://www.iea.org/weo/

IEA. (2018). *Coal 2018: Analysis and forecasts to 2023*. Retrieved from https://www.iea.org/coal2018/

Institution, T. B. S. (1981). British Standard (BS) 6177, 1981. Petrographic analysis of bituminous coal and anthracite Part 2: Method of preparing coal samples for petrographic analysis. Database Section, BSI.

Institution, T. B. S. (1982). British Standard (BS) 6127, 1982. Petrographic analysis of bituminous coal and anthracite, Part 3: Method of determining maceral group composition of bituminous coal and anthracite. Database Section, BSI.

Jayaranjan, M. L. D., van Hullebusch, E., & Annachhatre, A. (2014). *Reuse Options for Coal Fired Power Plant Bottom Ash and Fly Ash* (Vol. 13).

Jones, R. B., Morley, C., & McCourt, C. B. (1985). *MACERAL EFFECTS ON THE MORPHOLOGY AND COMBUSTION OF COAL CHAR*.

Jones, R. B., Morley, C., & McCourt, C. B. (2019). *MACERAL EFFECTS ON THE MORPHOLOGY AND COMBUSTION OF COAL CHAR*.

Kass, M., Witkin, A., & Terzopoulos, D. (1988). Snakes: Active contour models. *International Journal of Computer Vision, 1*(4), 321-331. doi:10.1007/BF00133570

Kus, J., Misz-Kennan, M., & Iccp. (2017). Coal weathering and laboratory (artificial) coal oxidation. *International Journal of Coal Geology, 171*, 12-36. doi:https://doi.org/10.1016/j.coal.2016.11.016

Le Manquais, K., Snape, C. E., McRobbie, I., & Barker, J. (2011). Evaluating the Combustion Reactivity of Drop Tube Furnace and Thermogravimetric Analysis Coal Chars with a Selection of Metal Additives. *Energy & Fuels, 25*(3), 981-989. doi:10.1021/ef101577z

Lee, B., Song, J.-H., Lee, C.-S., Chang, Y.-J., & Jeon, C. H. (2009). *Effect of Coal Properties on Combustion Characteristics in a Pulverized Coal Fired Furnace* (Vol. 33)

Lester, E., Allen, M., Cloke, M., & J. Miles, N. (1994). An automated image analysis system for major maceral group analysis in coals. *Fuel, 73*(11), 1729-1734. doi:https://doi.org/10.1016/0016-2361(94)90160-0

Lester, E., Allen, M., Cloke, M., & Miles, N. (1994). *An automated image analysis system for major maceral group analysis in coals* (Vol. 73).

Lester, E., Alvarez, D., Borrego, A., Valentim, B., Flores, D., A. Clift, D., . . . S. Milenkova, K. (2010). The procedure used to develop a coal char classification—Commission III Combustion Working Group of the International Committee for Coal and Organic Petrology. *International Journal of Coal Geology - INT J COAL GEOL, 81*, 333-342. doi:10.1016/j.coal.2009.10.015

Lester, E., & Cloke, M. (1999). *Characterisation of coals and their respective chars formed at 1300°C in a drop tube furnace* (Vol. 78).

Lester, E., Cloke, M., & Allen, M. (1996). Char Characterization Using Image Analysis Techniques. *Energy & Fuels, 10*(3), 696-703. doi:10.1021/ef9501713

Lester, E. G., M.; Thompson, A. (2007). A method for source apportionment in biomass/coal blends using thermogravimetric analysis. *Anal. Appl. Pyrolysis, 80*, 111-117.

Lunden, M. M., Yang, N. Y. C., Headley, T. J., & Shaddix, C. R. (1998). Mineral-char interactions during char combustion of a high-volatile coal. *Symposium (International) on Combustion, 27*(2), 1695-1702. doi:https://doi.org/10.1016/S0082-0784(98)80009-X

Ma, L., & Mitchell, R. (2009). Modeling char oxidation behavior under Zone II burning conditions at elevated pressures. *Combustion and flame, 156*(1), 37-50. doi:https://doi.org/10.1016/j.combustflame.2008.06.015

Marchioni, D. L. (1983). The detection of weathering in coal by petrographic, rheologic and chemical methods. *International Journal of Coal Geology, 2*(3), 231-259. doi:https://doi.org/10.1016/0166-5162(83)90002-2

Metcalf., G. (2009). Design of a Carbon Tax. *The."Harv. Envtl. L. Rev., 33*(499).

Metz, B., Davidson, O., de Coninck, H., Loos, M., & Meyer, L. (2005). IPCC Special Report on Carbon dioxide Capture and Storage. *Policy Stud.*

Michele, G. D., Riccardi, J., & Lopez-Doriga, E. (1994). Influence of Coal Type and Operating Conditions on the Formation of Incomplete Combustion Products. Pilot Plant Experiments AU - BONFANTI, L. *Combustion Science and Technology, 101*(1-6), 505-525. doi:10.1080/00102209408951890

Monthioux, M., & Landais, P. (1988). Natural and artificial maturations of a coal series: infrared spectrometry study. *Energy & Fuels, 2*(6), 794-801. doi:10.1021/ef00012a012

Murphy, J. J., & Shaddix, C. R. (2010). Effect of reactivity loss on apparent reaction order of burning char particles. *Combustion and flame, 157*(3), 535-539. doi:https://doi.org/10.1016/j.combustflame.2009.09.013

Nandi, B. N., Brown, T. D., & Lee, G. K. (1977). Inert coal macerals in combustion. *Fuel, 56*(2), 125-130. doi:https://doi.org/10.1016/0016-2361(77)90130-2

Nelson, M. I., & Chen, X. D. (2007) Survey of experimental work on the self-heating and spontaneous combustion of coal. In*: Vol. 18. GSA Reviews in Engineering Geology* (pp. 31-83).

Nihalani, S. A., Mishra, Y., & Juremalani, J. (2018). Emission Control Technologies for Thermal Power Plants. *IOP Conference Series: Materials Science and Engineering, 330*, 012122. doi:10.1088/1757-899x/330/1/012122

Niu, Y., & Shaddix, C. R. (2015). A sophisticated model to predict ash inhibition during combustion of pulverized char particles. *Proceedings of the Combustion Institute, 35*(1), 561-569. doi:https://doi.org/10.1016/j.proci.2014.05.077

O'Brien, G., Jenkins, B., Ofori, P., & Ferguson, K. (2007). *Semi-automated petrographic assessment of coal by coal grain analysis* (Vol. 20).

Oka, N., Murayama, T., Matsuoka, H., Yamada, S., Yamada, T., Shinozaki, S., . . . Thomas, C. G. (1987). The influence of rank and maceral composition on ignition and char burnout of pulverized coal. *Fuel Processing Technology, 15*, 213-224. doi:https://doi.org/10.1016/0378-3820(87)90046-4

Oka, N. M., T.; Matsuoka, H.; Yamada, S.; Yamada, T.; Shinozaki, S.; Shibaoka, M.; Thomas, . (1987). The influence of rank and maceral composition on ingnition and char burnout of pulverized coal *C. Fuel Process Technol, 15*, 213-224.

Otsu, N. (1979). A Threshold Selection Method from Gray-Level Histograms. *IEEE Transactions on Systems, Man, and Cybernetics, 9*(1), 62-66. doi:10.1109/TSMC.1979.4310076

P., J. (2016). *A new classification system for biomass and waste materials for their use in combustion. .* University of Nottingham,

Payá, J., Monzó, J., Borrachero, M. V., Perris, E., & Amahjour, F. (1998). Thermogravimetric Methods for Determining Carbon Content in Fly Ashes. *Cement and Concrete Research, 28*(5), 675-686. doi:https://doi.org/10.1016/S0008-8846(98)00030-1

Perkins, J., Williams, O., Wu, T., & Lester, E. (2020). Automated image analysis techniques to characterise pulverised coal particles and predict combustion char morphology. *Fuel, 259*, 116022. doi:https://doi.org/10.1016/j.fuel.2019.116022

Pisupati, S. V., Scaroni, A. W., & Stoessner, R. D. (1991). Combustion characteristics of naturally weathered (in situ) bituminous coals. *Fuel Processing Technology, 28*(1), 49-66. doi:https://doi.org/10.1016/0378-3820(91)90092-Q

Pyatenko, A. T., Bukhman, S. V., Lebedinskii, V. S., Nasarov, V. M., & Tolmachev, I. Y. (1992). Experimental investigation of single coal particle devolatilization by laser heating. *Fuel, 71*(6), 701-704. doi:https://doi.org/10.1016/0016-2361(92)90175-N

Rafael C. Gonzalez, R. E. W. (2007). *Digital Image Processing,* (2nd ed.): Pearson Dducation.

Ricke, K., Drouet, L., Caldeira, K., & Tavoni, M. (2018). Country-level social cost of carbon. *Nature Climate Change, 8*(10), 895-900. doi:10.1038/s41558-018-0282-y

Riepe, W., & Steller, M. (1984). Characterization of coal and coal blends by automatic image analysis: Use of the Leitz texture analysis system. *Fuel, 63*(3), 313-317. doi:https://doi.org/10.1016/0016-2361(84)90006-1

Rubin, E., Chen, C., & Rao, A. (2007). Cost and performance of fossil fuel power plants with CO2 capture and storage. *Energy Policy, 35*, 4444-4454. doi:10.1016/j.enpol.2007.03.009

Senneca, O. (2008). Burning and physico-chemical characteristics of carbon in ash from a coal fired power plant. *Fuel, 87*(7), 1207-1216. doi:https://doi.org/10.1016/j.fuel.2007.07.033

Smith, S. E., Neavel, R. C., Hippo, E. J., & Miller, R. N. (1981). DTGA combustion of coals in the Exxon coal library. *Fuel, 60*(6), 458-462. doi:https://doi.org/10.1016/0016-2361(81)90103-4

Smoot, L. D. (1993). *Fundamentals of coal combustion : for clean and efficient use*. Amsterdam; New York: Elsevier.

Stach, E., & Murchison, D. (1982). *Stach's Textbook of coal petrology*. Berlin; Stuttgart: Borntraeger.

Su, S., Pohl, J. H., Holcombe, D., & Hart, J. A. (2001). A proposed maceral index to predict combustion behavior of coal. *Fuel, 80*(5), 699-706. doi:https://doi.org/10.1016/S0016-2361(00)00137-X

Suárez-Ruiz, I., & Ward, C. R. (2008). Chapter 2 - Basic Factors Controlling Coal Quality and Technological Behavior of Coal. In I. Suárez-Ruiz & J. C. Crelling (Eds.), *Applied Coal Petrology* (pp. 19-59).

Thomas, C. G., Shibaoka, M., Gawronski, E., Gosnell, M.E., Ponganant, D., Brunckhorst, L.F. & Salehi, M.R. (1989). *Swelling and plasticity of inertinite in pf combustion.* Paper presented at the 1989 International Conference on Coal Science. Tokyo.

Unsworth, J. F., Barratt, D. J., & Roberts, P. T. (1991). *Coal quality and combustion performance : an international perspective*. Amsterdam; New York; Thornton: Elsevier ; Shell Research.

Wells, W. F., & Smoot, L. D. (1991). Relation between reactivity and structure for coals and chars. *Fuel, 70*(3), 454-458. doi:https://doi.org/10.1016/0016-2361(91)90138-Z

Wu, M. M., Robbins, G. A., Winschel, R. A., & Burke, F. P. (1988). Low-temperature coal weathering: its chemical nature and effects on coal properties. *Energy & Fuels, 2*(2), 150-157. doi:10.1021/ef00008a009

Wu, T., Lester, E., & Cloke, M. (2006a). Advanced Automated Char Image Analysis Techniques. *Energy & Fuels, 20*(3), 1211-1219. doi:10.1021/ef050360d

Wu, T., Lester, E., & Cloke, M. (2006b). A Burnout Prediction Model Based around Char Morphology. *Energy & Fuels, 20*(3), 1175-1183. doi:10.1021/ef050101o

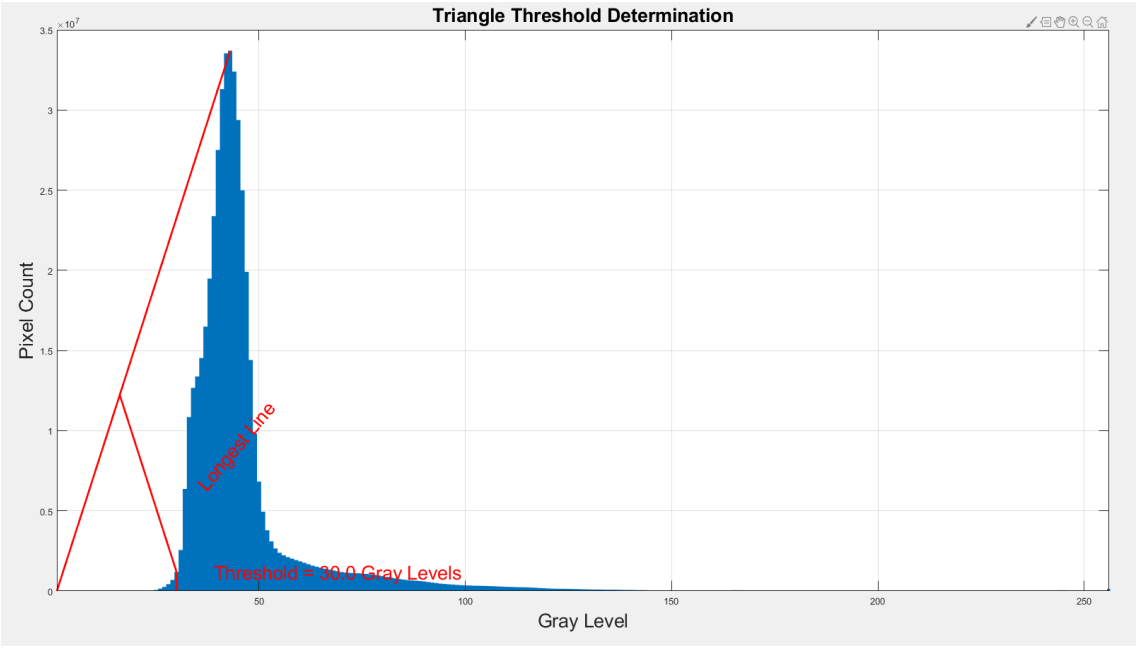
Yu, J., Lucas, J., Strezov, V., & Wall, T. (2003). Swelling and Char Structures from Density Fractions of Pulverized Coal. *Energy & Fuels, 17*(5), 1160-1174. doi:10.1021/ef030022h

Yun, Y., & Meuzelaar, H. (1988). *ACS Div. Fuel Chem. Prepr., 33*(3), 75.

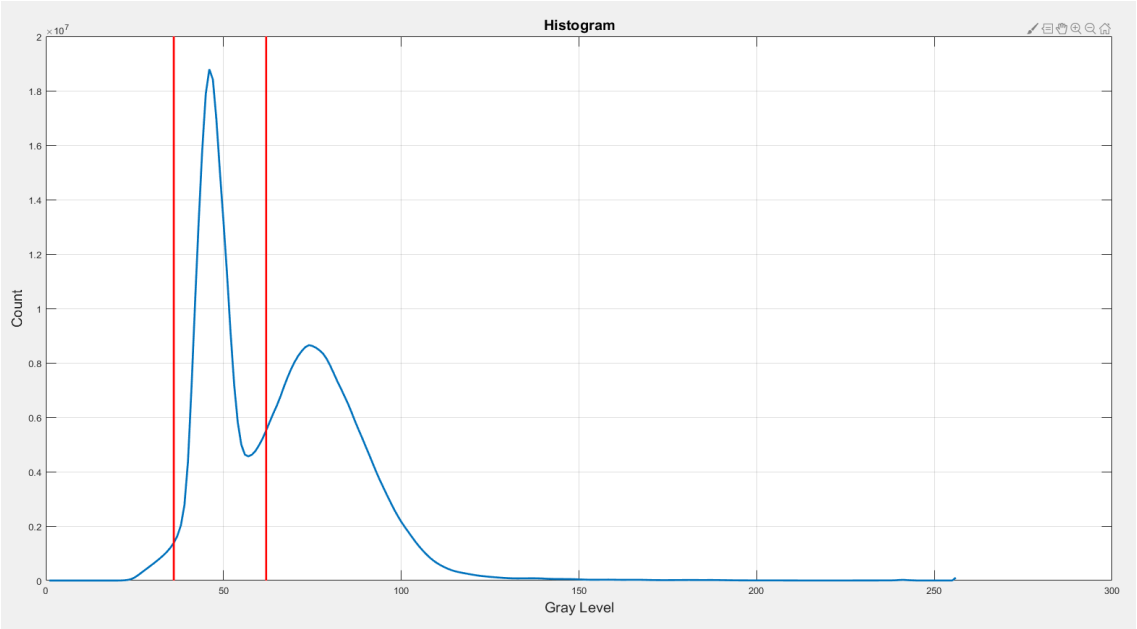
Zhang, D. (2013). 1 - Introduction to advanced and ultra-supercritical fossil fuel power plants. In D. Zhang (Ed.), *Ultra-Supercritical Coal Power Plants* (pp. 1-20): Woodhead Publishing.

Zhang, Y., McKechnie, J., Cormier, D., Lyng, R., Mabee, W., Ogino, A., & Maclean, H. (2009). Life Cycle Emissions and Cost of Producing Electricity from Coal, Natural Gas, and Wood Pellets in Ontario, Canada. *Environmental science & technology, 44*, 538-544. doi:10.1021/es902555a

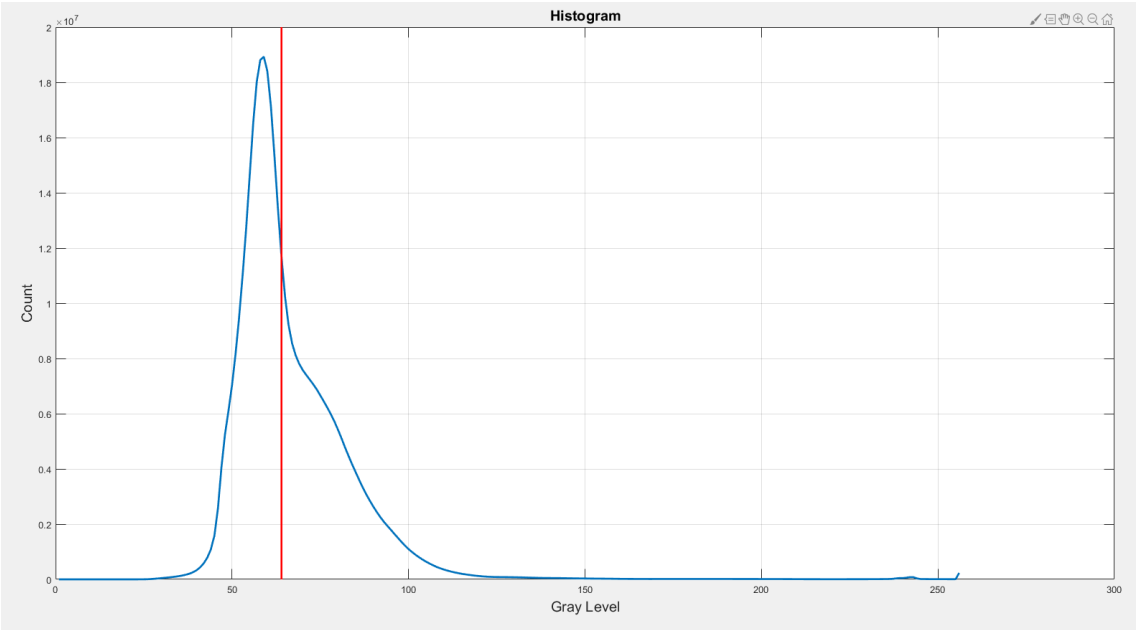
Appendix A. Journal Paper Supplemental Data



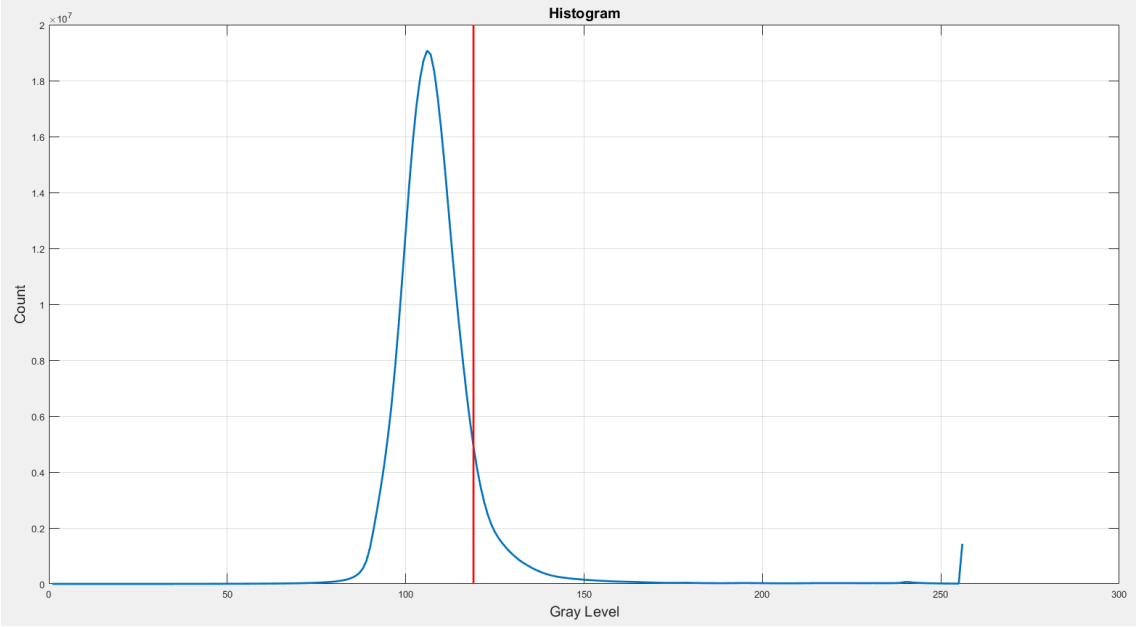
Appended Figure A.1 *- Liptinite threshold via triangle method*



Appended Figure A.2 *- Liptinite and inertinite thresholds for bi modal distribution*



Appended Figure A.3 *- Thresholds for overlapping vitrinite and semi-fusinite peaks*



Appended Figure A.4 *- Thresholds for very high reflectance sample*

Appended Table A.1 – Proximate analysis of 12 samples.

	Moisture %	Volatiles %	Fixed Carbon %	Ash %	Fuel Ratio	Vitrinite Reflectance
CALENTURITAS	5.4	38.4	51.2	5.0	1.3	0.54
LA LOMA	3.9	31.1	48.5	16.5	1.6	0.51
RUSSIAN	2.9	34.9	53.1	9.1	1.5	0.58
KLEIN KOPJE	2.3	24.4	58.4	14.9	2.4	0.76
OSTRAVA	0.6	28.6	59.6	11.2	2.1	0.93
WELSH 1	0.7	7.0	61.9	30.4	8.8	2.46
CHINESE COKE	0.0	1.1	84.8	14.1	75.6	7.01
VIETNEMESE	0.9	7.5	66.1	25.4	8.8	2.99
EL CERREJON	2.8	35.8	53.5	7.9	1.5	0.57
INDONESIAN	3.2	30.8	50.0	16.0	1.6	0.62
WELSH 2	0.7	7.5	84.7	7.1	11.2	2.41
ZONDAG	4.6	25.9	61.7	7.8	2.4	0.61

Appended Table A.2 – Comparison between manual and automated system maceral distributions ***M = manual/P = Predicted**

	LIPTINITE		VITRINITE		INERTINITE	
	M %	P %	M %	P %	M %	P %
CALENTURITAS	1.2	0.9	85.2	89.6	13.6	9.5
LA LOMA	0.0	0.2	88.4	87.5	11.6	12.3
RUSSIAN	3.2	3.8	72.0	88.6	24.8	7.6
KLEIN KOPJE	1.0	0.4	57.0	57.3	42.0	42.3
OSTRAVA	6.2	5.7	49.4	50.2	44.4	44.1
WELSH 1	0.0	0.1	49.6	61.4	50.4	38.5
CHINESE COKE	N/A	N/A	N/A	N/A	N/A	N/A
VIETNEMESE	0.0	0.0	97.6	97.5	2.4	2.5
EL CERREJON	0.4	0.4	91.2	90.4	8.4	9.2
INDONESIAN	3.0	0.4	84.0	83.0	13.0	16.6
WELSH 2	0.0	0.0	84.2	89.8	15.8	10.2
ZONDAG	1.0	1.1	48.0	46.4	51.0	52.5

Appended Table A.3 – Predicted vs Manual char morphologies ***M = manual/P = Predicted**

MORPHOLOGY	TENUISPHERE		TENUINETWORK		CRASSISPHERE		CRASSINETWORK		FUSINOID		SOLID	
	M %	P %	M %	P %	M %	P %	M %	P %	M %	P %	M %	P %
CALENTURITAS	8.4	6.1	25.6	26.8	45.2	51.3	16.4	15.6	3.2	0.1	1.2	0.0
LA LOMA	21.2	5.6	40.4	48.1	26.4	26.6	6.0	15.9	4.4	0.0	1.6	3.8
RUSSIAN	13.6	16.0	13.6	12.7	40.4	41.5	14.4	19.3	11.6	10.2	6.4	1.4
KLEIN KOPJE	9.2	3.5	12.0	15.6	22.0	27.4	36.0	29.1	13.2	0.9	7.6	23.6
OSTRAVA	6.4	6.1	4.4	0.0	56.0	52.6	22.8	22.1	9.6	10.5	0.8	8.7
WELSH 1	4.0	0.0	8.0	10.8	9.2	0.0	6.0	16.3	12	15.1	60.8	57.8
CHINESE COKE	0.8	0.0	2.4	0.0	2.0	0.0	5.0	12.3	70	2.9	20.0	84.8
VIETNEMESE	0.8	0.0	0.4	0.0	6.0	0.0	8.8	10.7	2.4	3.9	81.6	85.4
EL CERREJON	23.6	11.7	8.0	15.3	46.4	45.6	19.2	26.9	2.4	0.2	0.4	0.3
INDONESIAN	20.8	10.7	24.4	36.0	26.8	31.9	10.0	10.8	14.4	0.7	3.6	10.0
WELSH 2	0.4	0.0	0.4	1.1	6.4	0.0	24.8	29.3	1.2	63.1	66.8	6.5
ZONDAG	1.2	1.1	38.8	38.5	5.6	13.5	30.0	29.2	17.6	14.2	6.8	3.5

Appended Table A.4 – Predicted vs Manual Char morphology main groups ***M = manual/P = Predicted**

MORPHOLOGY	THIN		THICK		SOLID	
	M %	P %	M %	P %	M %	P %
CALENTURITAS	34.0	32.9	61.6	67.0	4.4	0.1
LA LOMA	61.6	53.7	32.4	42.5	6.0	3.8
RUSSIAN	27.2	28.6	54.8	60.7	18.0	11.6
KLEIN KOPJE	21.2	19.0	58.0	56.5	20.8	24.5
OSTRAVA	10.8	6.1	78.8	74.7	10.4	19.2
WELSH 1	12.0	10.8	15.2	16.3	72.8	72.8
CHINESE COKE	3.2	0.0	7.0	12.3	90.0	87.7
VIETNEMESE	1.2	0.0	14.8	10.7	84.0	89.3
EL CERREJON	31.6	27	65.6	72.5	2.8	0.5
INDONESIAN	45.2	46.6	36.8	42.7	18.0	10.7
WELSH 2	0.8	1.1	31.2	29.3	68.0	69.6
ZONDAG	40.0	39.6	35.6	42.7	24.4	17.8

Program Script A.1 – Coal Mosaic Segmentation & Particle Separation

```
% Load coal mosaic & convert to grayscale
MosaicInput = imread('X.tif');
Mosaic = rgb2gray(MosaicInput);

% Input pixel size for later calculations
Micron_Per_Pixel = 0.1288;


% L is the labelling matrix, defined by points chosen in the ImageSegmenter app
Mosaic_Mask = lazysnapping(Mosaic,L,foremask,backmask);


% Overlay background mask with original for next step
Initial_Segmented_Mosaic = Mosaic;
Initial_Segmented_Mosaic(Mosaic_Mask ~= 1) =
Mosaic_Mask(Mosaic_Mask_Finished ~= 1);


% Use clustering (KMEAN, no. clusters = 12) to remove remaining background
blemishes within particle boundaries
ClusterMask = imsegkmeans(Initial_Segmented_Mosaic,12);
Cluster_Mosaic = labeloverlay(Initial_Segmented_Mosaic,ClusterMask);
imwrite(Cluster_Mosaic,'X_Cluster.tif');

% Specific cluster groups removed using ImageSegmenter GUI & save new mask
imwrite(BW, 'X_Mask_Initial.tif');

% Invert & Clean Up to remove small pixels
Mosaic_Mask = imcomplement(BW);
Mosaic_Mask = bwareaopen(Mosaic_Mask,2000);
imshow(Mosaic_Mask);


% Implement Watershed function to separate particles

% Run distance transform on mask
D = -bwdist(~Mosaic_Mask);
imshow(D,[]);

% Run initial watershed function
Ld = watershed(D);
imshow(label2rgb(Ld))

% Use watershed ridge lines to segment binary image = raw segmentation
Mosaic_Mask_2 = Mosaic_Mask;
Mosaic_Mask_2(Ld == 0) = 0;
imshow(Mosaic_Mask_2);
```

```
 % Combat over-segmentation by filtering out small local minima
Mosaic_Mask_3 = imextendedmin(D,14);
imshowpair(Mosaic_Mask,Mosaic_Mask_3,'blend');

% Modify distance transform with main minima only & repeat watershed
D2 = imimposemin(D,Mosaic_Mask_3);
Ld2 = watershed(D2);
Mosaic_Mask_4 = Mosaic_Mask;
Mosaic_Mask_4(Ld2 == 0) = 0;
imshow(Mosaic_Mask_4);

% Scrap again & Save image
Mosaic_Mask_Finished = bwareaopen(Mosaic_Mask_4,2000);
imwrite(Mosaic_Mask_Finished, 'X_Mosaic_Mask_Finished.tif');


% Original Mosaic Overlay
Mosaic_Mask_Finished = imread('X_Mosaic_Mask_Finished.tif');

% Resize mask to original image if needed
A = Mosaic;
B = Mosaic_Mask_Finished;

% Resize Mask & Original Image & Get size of existing Mosaic.
[rowsA colsA numberOfColorChannelsA] = size(A);

% Get size of existing image B.
[rowsB colsB numberOfColorChannelsB] = size(B);

% See if lateral sizes match.
if rowsB ~= rowsA || colsA ~= colsB

% Size of B does not match A, so resize B to match A's size.
B = imresize(B, [rowsA colsA]);
end
Mosaic_Mask_Finished = B;

% Overlay mask & original mosaic to remove background
Segmented_Mosaic = Mosaic;
Segmented_Mosaic(Mosaic_Mask_Finished ~= 1) =
Mosaic_Mask_Finished(Mosaic_Mask_Finished ~= 1);

% Save masked mosaic
imwrite(Segmented_Mosaic, 'X_Segmented.tif');
[pixelCounts grayLevels] = imhist(Segmented_Mosaic);

%%
Segmented_Mosaic = imread('X_Segmented.tif');
[pixelCounts grayLevels] = imhist(Segmented_Mosaic);
imhist(Segmented_Mosaic);
```

```
% LABEL & SAVE INDIVIDUAL PARTICLES

% Label mosaic mask & compute properties
Labeled_Coal_Mosaic = bwlabel(Segmented_Mosaic, 8);
Coal_Particle_Measurements = regionprops(Labeled_Coal_Mosaic,'all');
Number_Particles = size(Coal_Particle_Measurements, 1);

% Assign boundaries of each particle, cut & save individual images
Mask_Boundaries = bwboundaries(Segmented_Mosaic);
Number_Boundaries = size(Mask_Boundaries, 1);
for k = 1 : Number_Boundaries
   thisBoundary = Mask_Boundaries{k};
end
 for k = 1 : Number_Particles
      thisParticleBoundingBox = Coal_Particle_Measurements(k).BoundingBox;
      subImage = imcrop(Mosaic, thisParticleBoundingBox);
      subImageMask = imcrop(Segmented_Mosaic, thisParticleBoundingBox);
      SubImageFinal = subImage;
      SubImageFinal(subImageMask ~= 1) = subImageMask(subImageMask ~= 1);
      SubImageFinal = im2double(SubImageFinal);
      imwrite(SubImageFinal,sprintf('Coal_Particle%d.png',k)
```

Program Script A.2 – Automated Maceral Analysis Script

```
% Read grey levels determined in script 1a
pixelCounts = xlsread('X_Greylevels.xlsx');

% Duplicate for later functions
Save = pixelCounts;

% Remove background pixels & count remaining total
pixelCounts(1) = 0;
TotalPixels = sum(pixelCounts);

% Plot histogram for closer inspection if desired
plot(pixelCounts, '-', 'LineWidth', 2);
xlabel('Gray Level', 'FontSize', 15);
ylabel('Count', 'FontSize', 15);
title('Histogram', 'FontSize', 15);
grid on;
set(gcf, 'Units', 'Normalized', 'OuterPosition', [0, 0.04, 1, 0.96]);

% Find Vitrinite peak greylevel
[maxCount, glAtMaxCount] = max(pixelCounts);
Vitrinite_Peak = glAtMaxCount;
```

```
% Find Liptinite Threshold
Liptinite_Threshold = triangle_threshold_Lip(pixelCounts, 'L');
% Find Inertinite Threshold options

 % Determine what percentage of material within 10% vitrinite peak
 Vitrinite10 = sum(pixelCounts(Vitrinite_Peak:Vitrinite_Peak+10));
 Vitrinite_10_Percentage = (Vitrinite10/TotalPixels)*100;

 % Find 28% of peak value
 temp = pixelCounts;
 temp(1:glAtMaxCount) = maxCount;
 gl = find(temp < 0.28 * maxCount, 1, 'first');

 % Determine any minima between vitrinite & semi-fusinite peaks
Minima = triangle_threshold_Inert(pixelCounts, 'R');
pixelCounts = Save;
pixelCounts(1) = 0;

 % Find minima <gl histogram value
 CutBin = gl+1;
 pixelCounts(CutBin:end) = 0;
 MinimaCut = triangle_threshold_Inert(pixelCounts, 'R');
 pixelCounts = Save;
 pixelCounts(1) = 0;

% Determine which inertinite threshold value to use dependant on histogram shape &
assign % composition
if Vitrinite10 >35
Inertinite_Threshold = triangle_threshold_Inert(pixelCounts, 'R');
elseif Minima <gl;
Minima = Inertinite_Threshold;
else
gl = Inertinite_Threshold;
end

pixelCounts(1) = 0;
VitriniteTotal = sum(pixelCounts(Liptinite_Threshold:Inertinite_Threshold));
VitrinitePercentage = (VitriniteTotal/TotalPixels)*100;
LiptiniteTotal = sum(pixelCounts(1:Liptinite_Threshold));
LiptinitePercentage = (VitriniteTotal/TotalPixels)*100;
InertiniteTotal = sum(pixelCounts(Inertinite_Threshold:end));
InertinitePercentage = (VitriniteTotal/TotalPixels)*100;

% Plot thresholds on histogram
plot(pixelCounts, '-', 'LineWidth', 2);
xlabel('Gray Level', 'FontSize', 15);
ylabel('Count', 'FontSize', 15);
title('Histogram', 'FontSize', 15);
grid on;
```

```
set(gcf, 'Units', 'Normalized', 'OuterPosition', [0, 0.04, 1, 0.96]);
line([Inertinite_Threshold, Inertinite_Threshold], ylim, 'Color', 'r', 'LineWidth', 2);
line([Liptinite_Threshold, Liptinite_Threshold], ylim, 'Color', 'r', 'LineWidth', 2);
```

Program Script A.3 – Coal Particle Analysis and Char Prediction

```
% Upload particles into processing loop
for A = 1:X %Number_Particles
try
CoalFilename = sprintf('Coal_Particle%d.png', A);
fullFileName = fullfile(pwd, CoalFilename);
 if exist(fullFileName, 'file')
Coal_Particle = imread(fullFileName);
 else
    continue
 end
Coal_Particle = addborder(Coal_Particle, 5, 1, 'outer');

% Remove border particles & select primary particle in image only
Coal_Particle = imfilter(Coal_Particle,1);


% Calculate histogram peak value
Coal_Particle_Array = im2double(Coal_Particle);
idx = Coal_Particle_Array > 0;
[pixelCounts, grayLevels] = imhist(Coal_Particle_Array(idx));
pixelCounts(2) = 0;
[maxCount, indexOfMax] = max(pixelCounts);
PEAK = grayLevels(indexOfMax);
PEAK = PEAK*255;

% Percentage unreactives threshold input
UnreactivesThreshParticle = Coal_Particle >= X & Coal_Particle <= 255;

% Count pixels for maceral distributions
Pixel_Total = sum(pixelCounts);

% Calculate Vitrinite pixel count and percentage
TruePixelsCountV = sum(VitriniteThreshParticle(:));
VITRINITE = TruePixelsCountV/Pixel_Total;

% Calculate %Unreactives pixel count and percentage
TruePixelsCountU = sum(UnreactivesThreshParticle(:));
UNREACTIVES = TruePixelsCountU/Pixel_Total;

% Calculate inertinite pixel count and percentage
Pixel_Total = sum(pixelCounts);
```

```
TruePixelsCountI = sum(InertiniteThreshParticle(:));
INERTINITE = TruePixelsCountI/Pixel_Total;

% Clean up any remaining noise & identify no. of inertinite fragments
InertiniteThreshParticleFilter = bwareaopen(InertiniteThreshParticle, 250);
Coal_Inertinite_Measurements = regionprops(InertiniteThreshParticleFilter,'all');
INERTITEFRAGMENTS = size(Coal_Inertinite_Measurements, 1);

% Calculate mean distance of 3 largest fragments to particle border & isolate
fragments, invert and binarize for analysis
Coal_Particle_Mask = imbinarize(Coal_Particle);
Coal_Particle_Mask = bwareafilt(Coal_Particle_Mask,1);
Particle_Fragments = InertiniteThreshParticleFilter;
Particle_Fragments(Coal_Particle_Mask ~= 1) =
Coal_Particle_Mask(Coal_Particle_Mask ~= 1);

Particle_Fragments = ~Particle_Fragments;
Particle_Fragments = 1-Particle_Fragments;
Particle_Fragments = (Particle_Fragments == 0);

% Overlay fragments on top of filled particle outline
Coal_Particle_Mask_Whole = imfill(Coal_Particle_Mask, 'holes');
Particle_Fragments_Combination = Coal_Particle_Mask_Whole;
Particle_Fragments_Combination(Particle_Fragments ~= 1) =
Particle_Fragments(Particle_Fragments ~= 1);

% Count number of boundaries
boundaries = bwboundaries(Particle_Fragments_Combination);
numberOfBoundariesFragment = size(boundaries, 1);

if INERTITEFRAGMENTS >3
   boundary1 = boundaries{1};
   boundary2 = boundaries{2};
   boundary3 = boundaries{3};
   boundary4 = boundaries{4};
   boundary1x = boundary1(:, 2);
   boundary1y = boundary1(:, 1);
   x1=1;
   y1=1;
   x2=1;
   y2=1;
   overallMinDistance1 = inf;

% For every point in boundary 2, find the distance to every point in boundary 1.
   for k = 1 : size(boundary2, 1)
      % Pick the next point on boundary 2.
      boundary2x = boundary2(k, 2);
      boundary2y = boundary2(k, 1);
      % For this point, compute distances from it to all points in boundary 1.
```

```
        allDistances = sqrt((boundary1x - boundary2x).^2 + (boundary1y -
boundary2y).^2);
        % Find closest point, min distance.
        [minDistance(k), indexOfMin] = min(allDistances);
            if minDistance(k) < overallMinDistance1
            x1 = boundary1x(indexOfMin);
            y1 = boundary1y(indexOfMin);
            x2 = boundary2x;
            y2 = boundary2y;
            overallMinDistance1 = minDistance(k);
            end
    end

 %Find the overall min distance fragment 1
    minDistance1 = min(minDistance);

    overallMinDistance2 = inf;

 % For every point in boundary 3, find the distance to every point in boundary 1.
    for k = 1 : size(boundary3, 1)
        % Pick the next point on boundary 3.
        boundary3x = boundary3(k, 2);
        boundary3y = boundary3(k, 1);
        % For this point, compute distances from it to all points in boundary 1.
        allDistances2 = sqrt((boundary1x - boundary3x).^2 + (boundary1y -
boundary3y).^2);
        % Find closest point, min distance.
        [minDistance2(k), indexOfMin2] = min(allDistances2);
            if minDistance2(k) < overallMinDistance2
            x1 = boundary1x(indexOfMin2);
            y1 = boundary1y(indexOfMin2);
            x3 = boundary3x;
            y3 = boundary3y;
            overallMinDistance2 = minDistance2(k);
            end

    end
    % Find the overall min distance fragment 3
    minDistance2 = min(minDistance2);

    overallMinDistance3 = inf;

 % For every point in boundary 2, find the distance to every point in boundary 1.
    for k = 1 : size(boundary4, 1)
        % Pick the next point on boundary 2.
        boundary4x = boundary4(k, 2);
        boundary4y = boundary4(k, 1);
        % For this point, compute distances from it to all points in boundary 1.
        allDistances3 = sqrt((boundary1x - boundary4x).^2 + (boundary1y -
boundary4y).^2);
```

```
        % Find closest point, min distance.
        [minDistance3(k), indexOfMin3] = min(allDistances3);
           if minDistance3(k) < overallMinDistance3
           x1 = boundary1x(indexOfMin3);
           y1 = boundary1y(indexOfMin3);
           x2 = boundary4x;
           y2 = boundary4y;
           overallMinDistance3 = minDistance3(k);
           end
    end

    % Find the overall min distance fragement 3
    minDistance3 = min(minDistance3);

% Calculate fragment prox in microns
FRAGMENTPROX = (minDistance1+minDistance2+minDistance3)/3;
FRAGMENTPROX = FRAGMENTPROX*0.1288;

else
    FRAGMENTPROX = 0;

end

% Calculate porosity of particle

 % Get intial pixel count & save image
  numberOfPixelsPorosity = numel(Coal_Particle_Mask);
  numberOfTruePixelsPorosity = sum(Coal_Particle_Mask(:));
  P1 = numberOfTruePixelsPorosity;

 % Fill particle
  Filled_Coal_Whole = imfill (Coal_Particle_Mask, 'holes');
  numberOfPixelsPorosity = numel(Coal_Particle_Mask);
  numberOfTruePixelsPorosity = sum(Filled_Coal_Whole(:));

 % Count pixels of porous vs filled chars
  P2 = numberOfTruePixelsPorosity;
  PorosityCalc = (P2-P1)/P2;
  Porosity = PorosityCalc*100;
  POROSITY = Porosity;

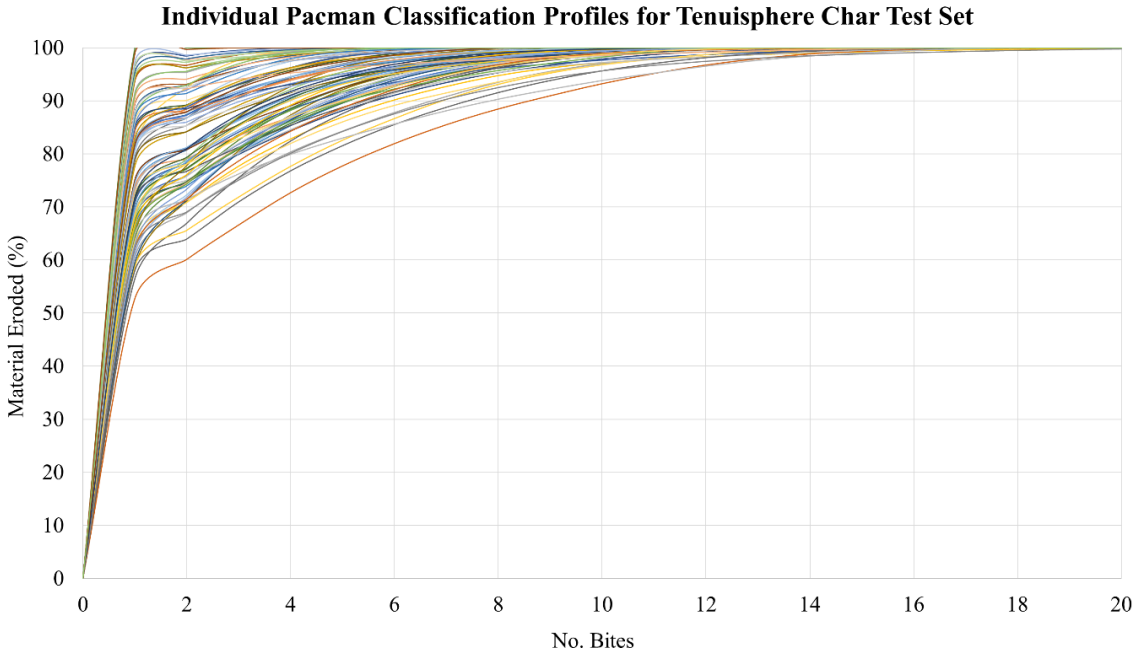
 % Calculate size of particle (in microns)
 SIZE1 = regionprops(Coal_Particle_Mask,'MajorAxisLength');
 SIZE = struct2table(SIZE1);
 SIZE = table2cell(SIZE);
 SIZE = cell2mat(SIZE);
 SIZE = SIZE *0.1288;


% DECISION TREE & OUTPUT DATA
```

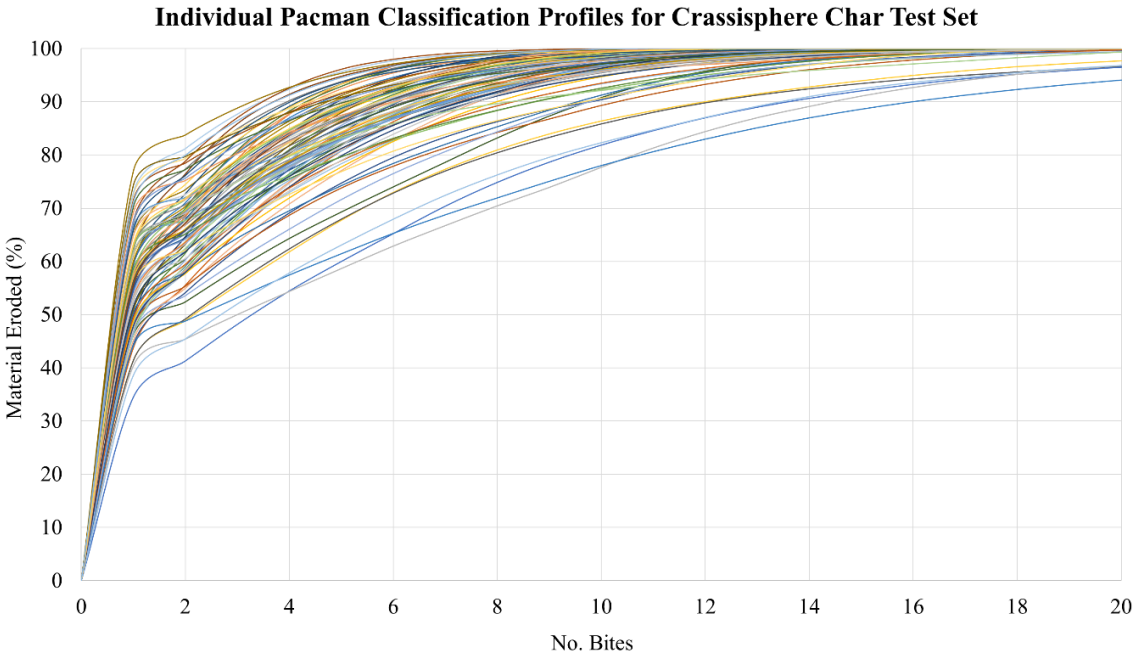
```
% Load variables into table for classification
load('Coal_Prediction_Tree.mat');
Table_Classification = table(PEAK,POROSITY, FRAGMENTPROX, SIZE,
INERTITEFRAGMENTS, INERTINITE,UNREACTIVES);

% Run classification % save
yfit = Coal_Prediction_Tree.predictFcn(Table_Classification);
Class = double(yfit);
dlmwrite('X.txt',Class,'-append','delimiter','','roffset',1);
type('X.txt');
Coal_Classification_Data = dlmread('X.txt');
end
% End of individual analysis loop. Repeat for next particle
end
```

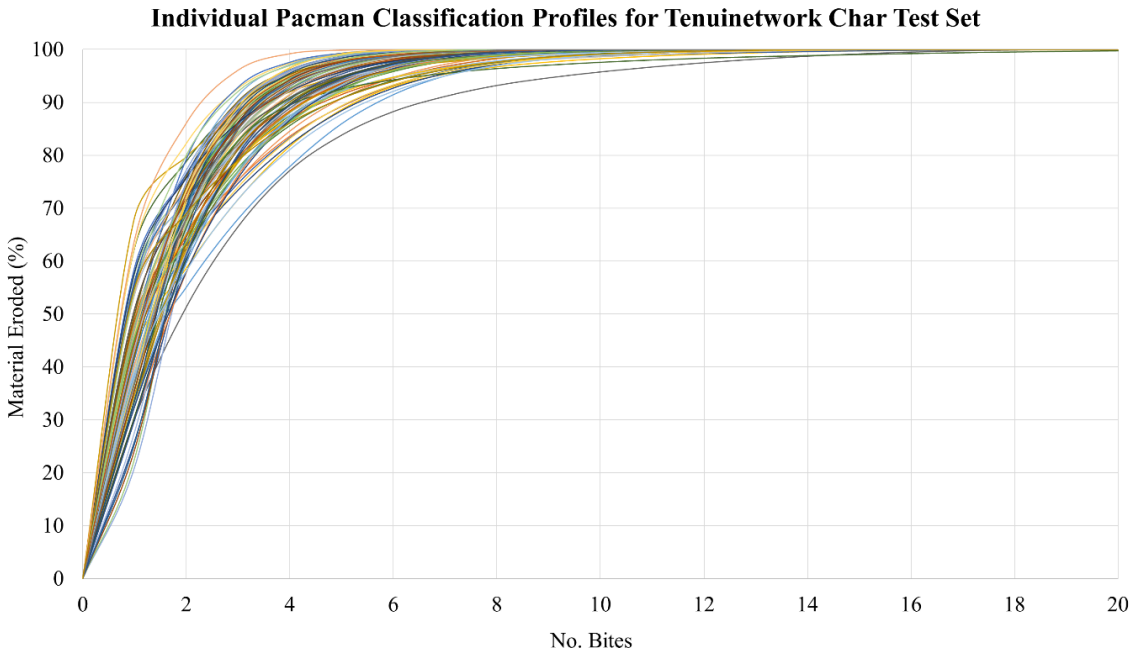
Appendix B. Automated Char Analysis Data



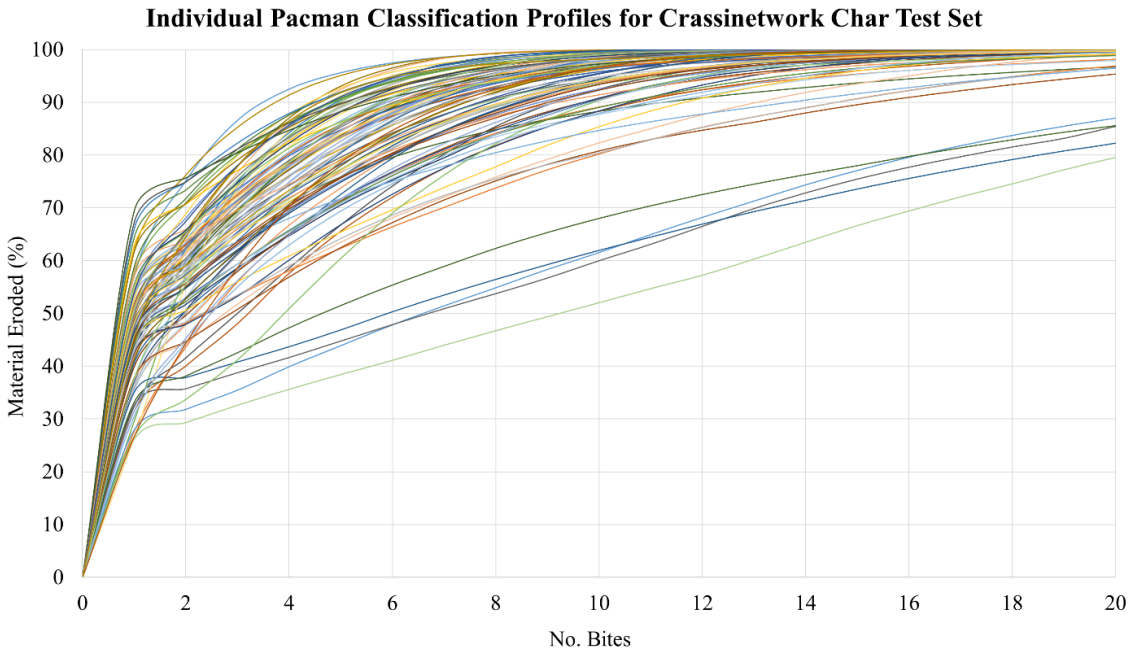
Appended Figure B.1 *- Individual Pacman Erosion Profiles for Tenuisphere test chars*



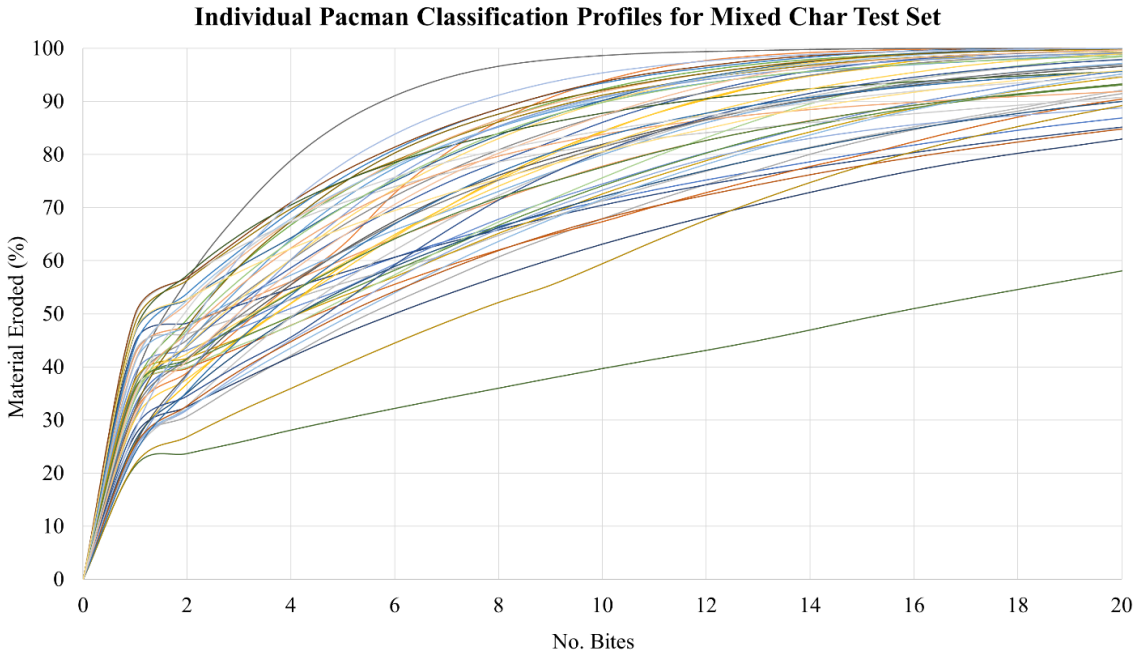
Appended Figure B.2 *- Individual Pacman Erosion Profiles for Crassisphere test chars*



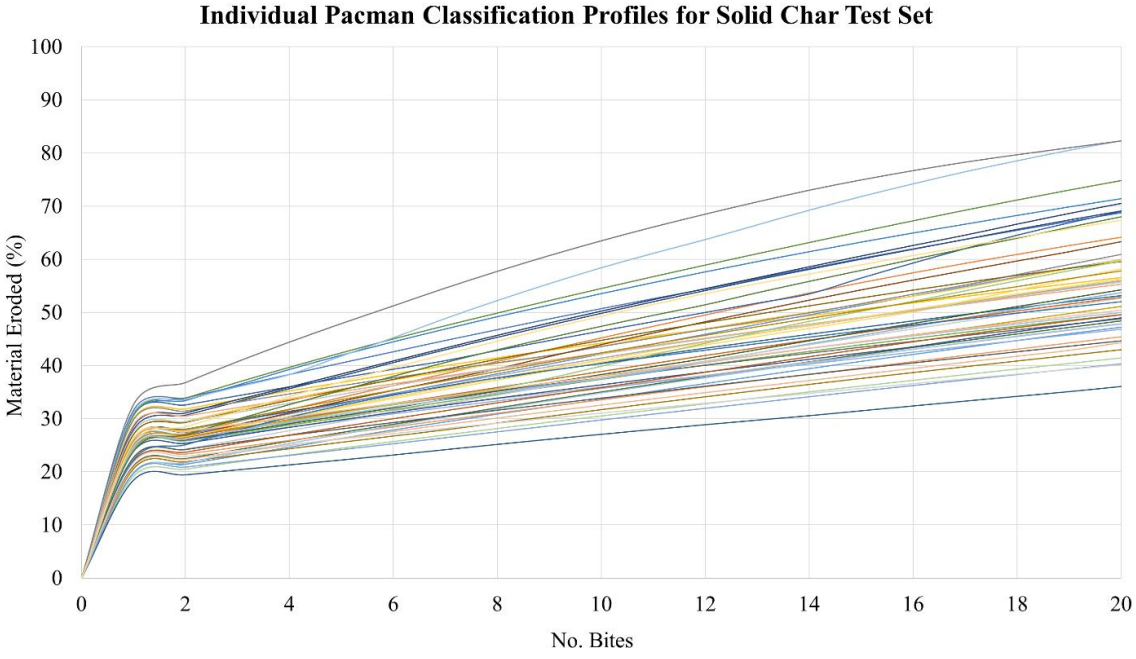
Appended Figure B.3 **-** *Individual Pacman Erosion Profiles for Tenuinetwork test chars*



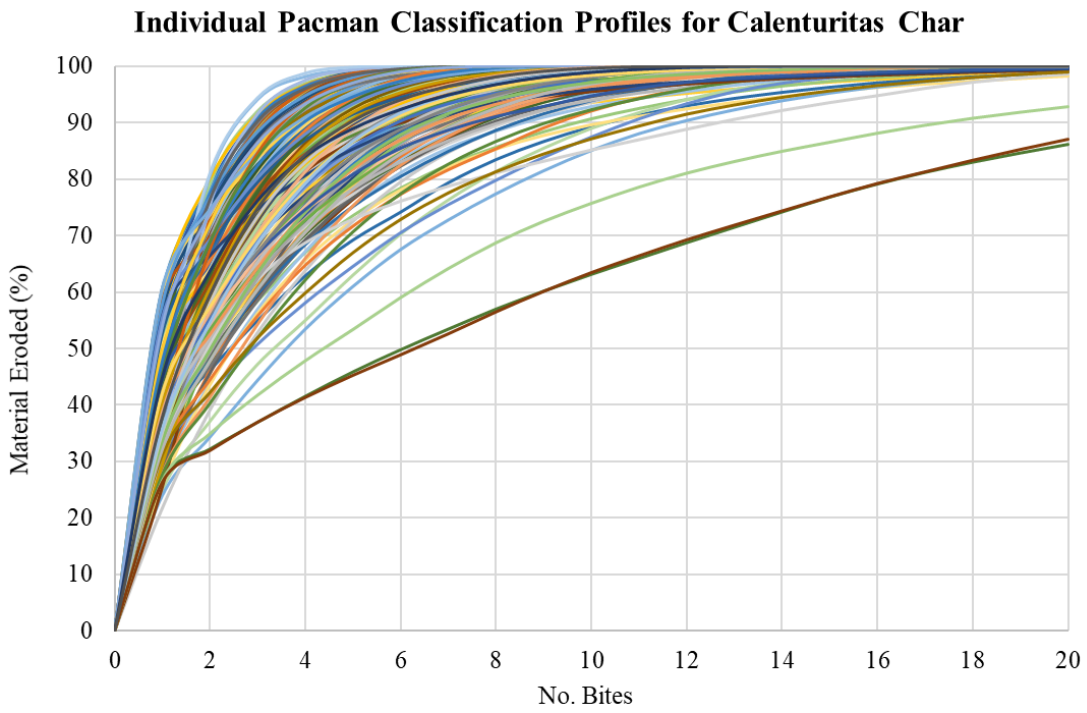
Appended Figure B.4 **-** *Individual Pacman Erosion Profiles for Crassinetwork test chars*



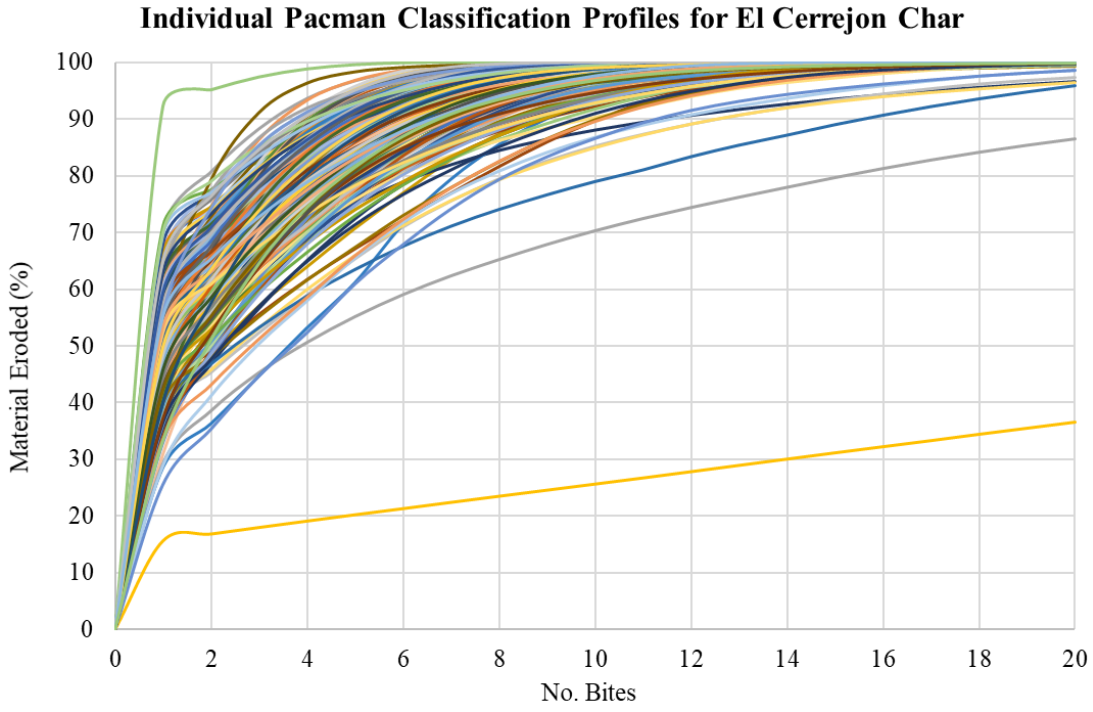
Appended Figure B.5 *- Individual Pacman Erosion Profiles for Mixed test chars*



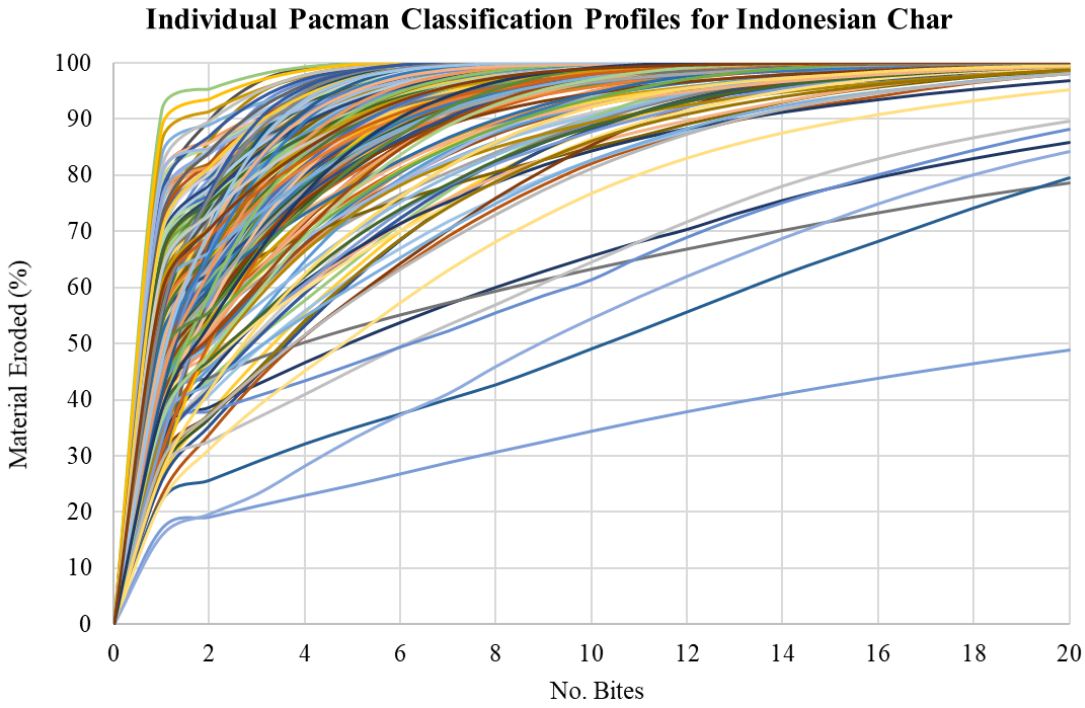
Appended Figure B.6 *- Individual Pacman Erosion Profiles for Solid test chars*



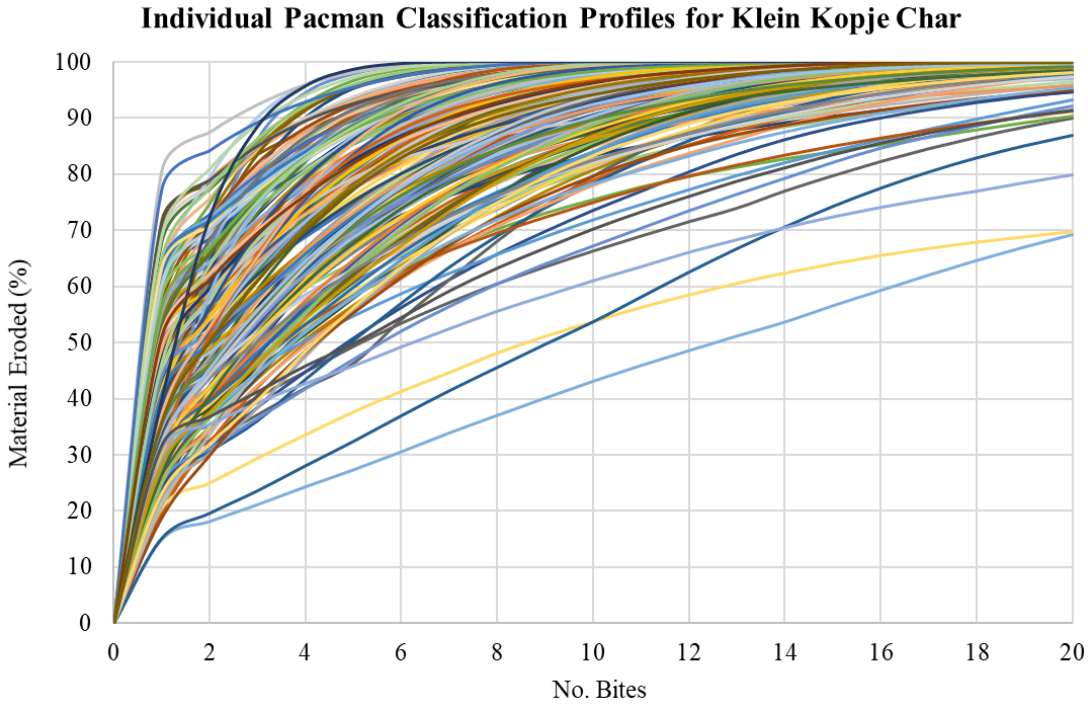
Appended Figure B.7 *- Individual Pacman Erosion Profiles for Calenturitas Char sample*



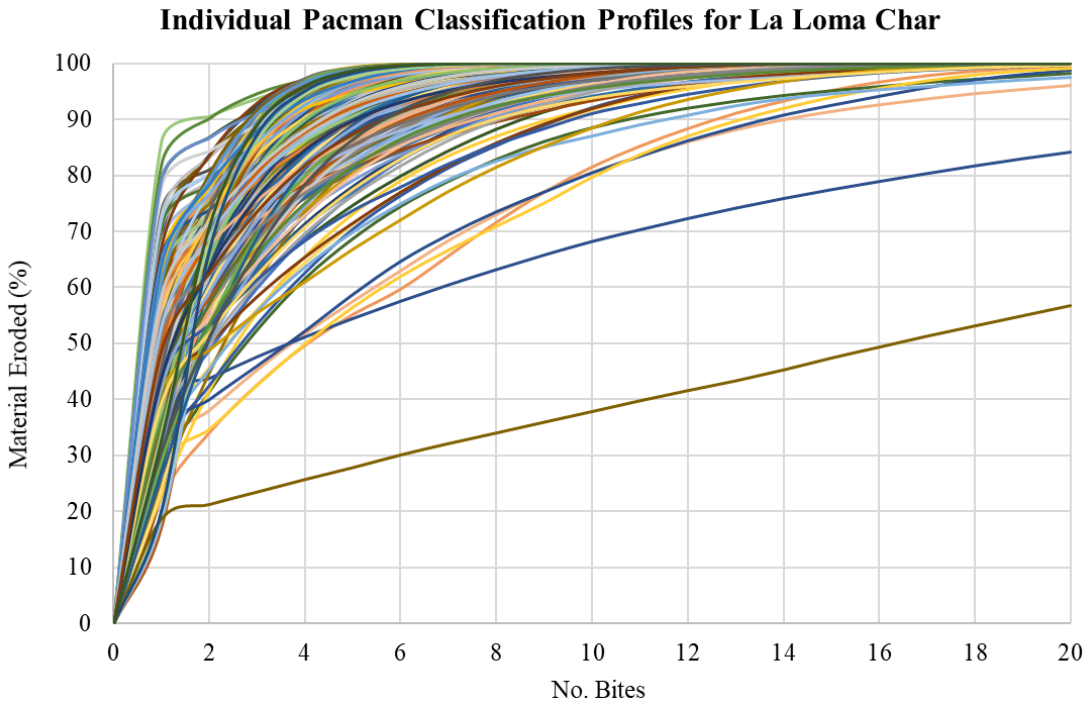
Appended Figure B.8 *- Individual Pacman Erosion Profiles for El Cerrejon Char sample*



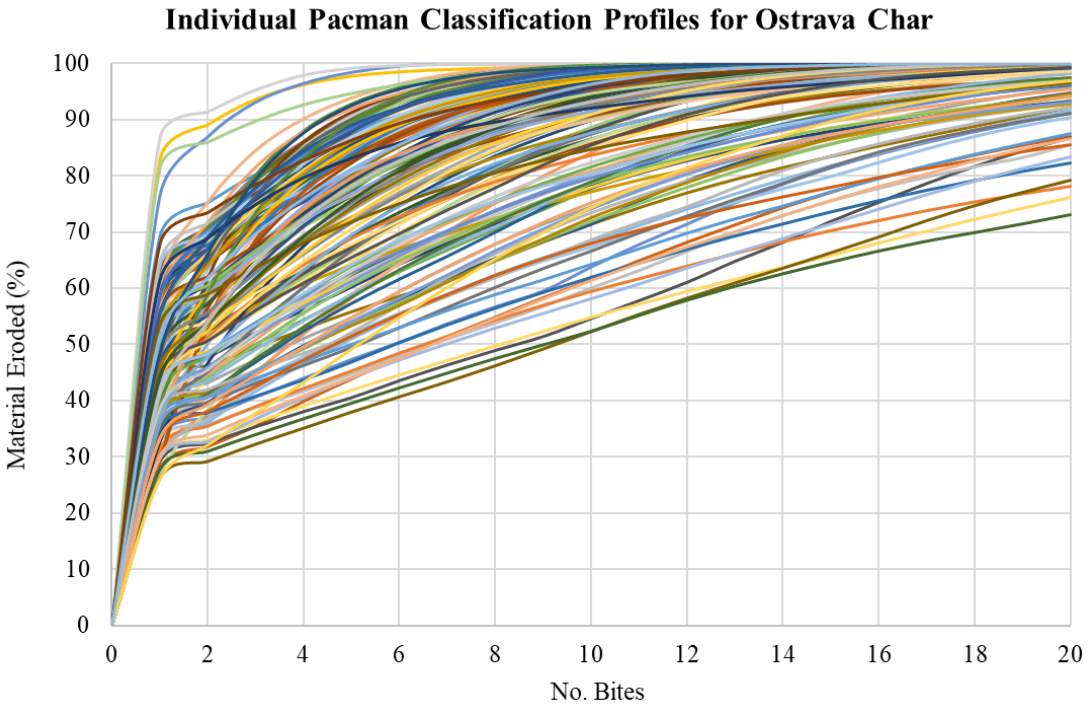
Appended Figure B.9 *- Individual Pacman Erosion Profiles for Indonesian Char sample*



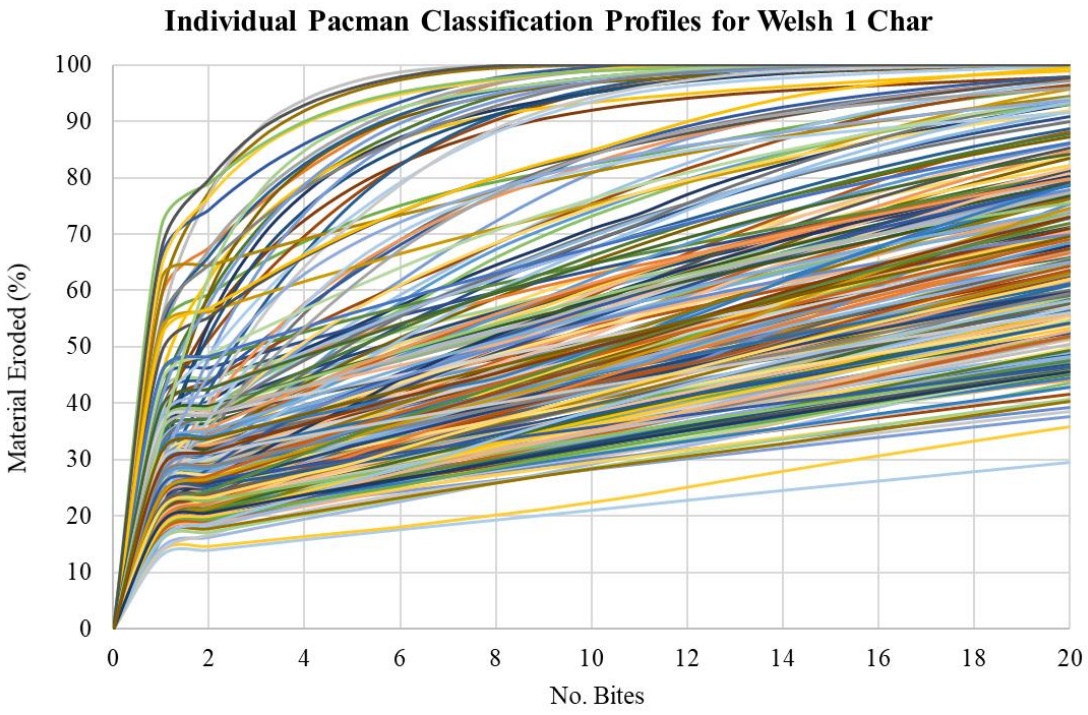
Appended Figure B.10 *- Individual Pacman Erosion Profiles for Klein Kopje Char sample*



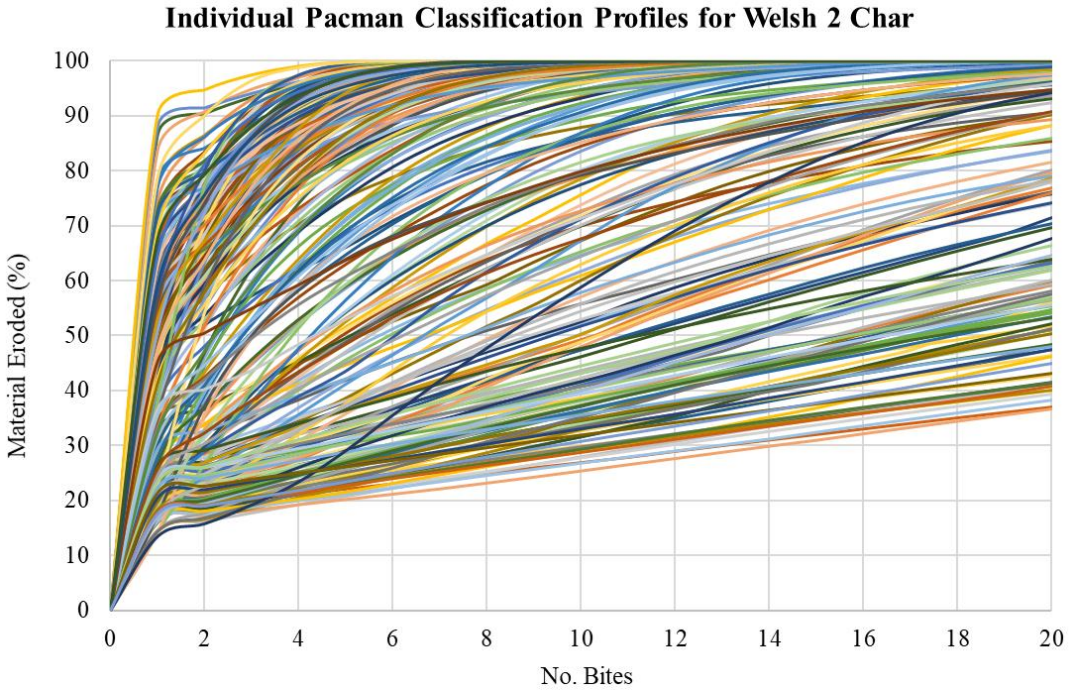
Appended Figure B.11 - *Individual Pacman Erosion Profiles for La Loma Char sample*



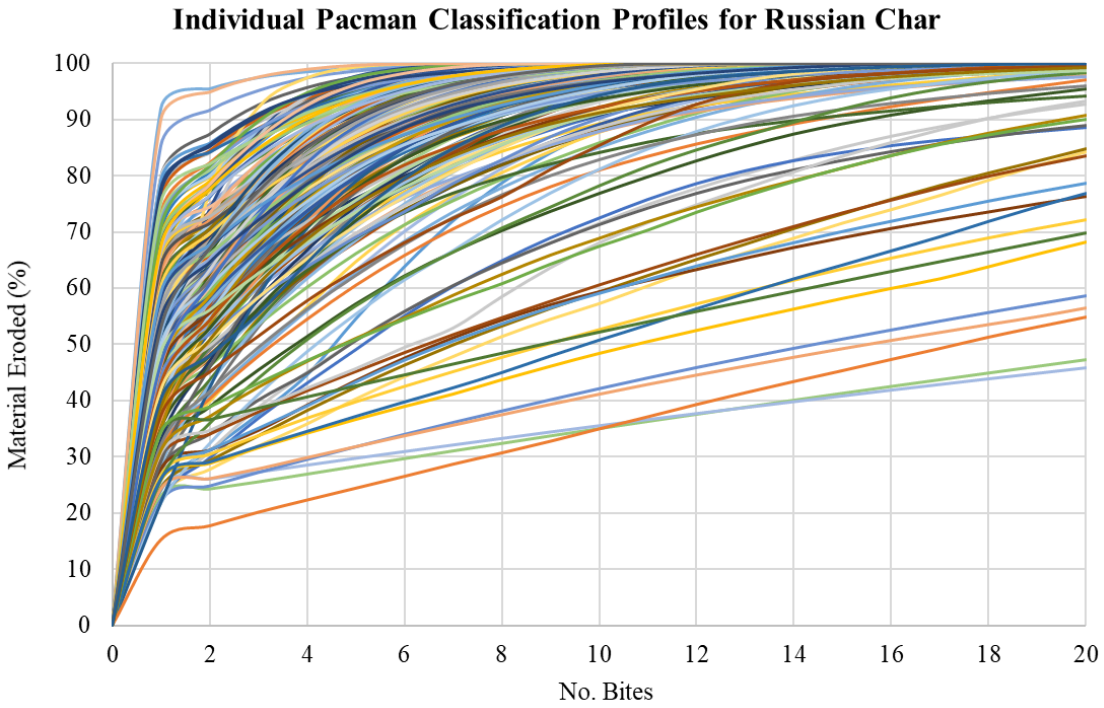
Appended Figure B.12 - *Individual Pacman Erosion Profiles for Ostrava Char sample*



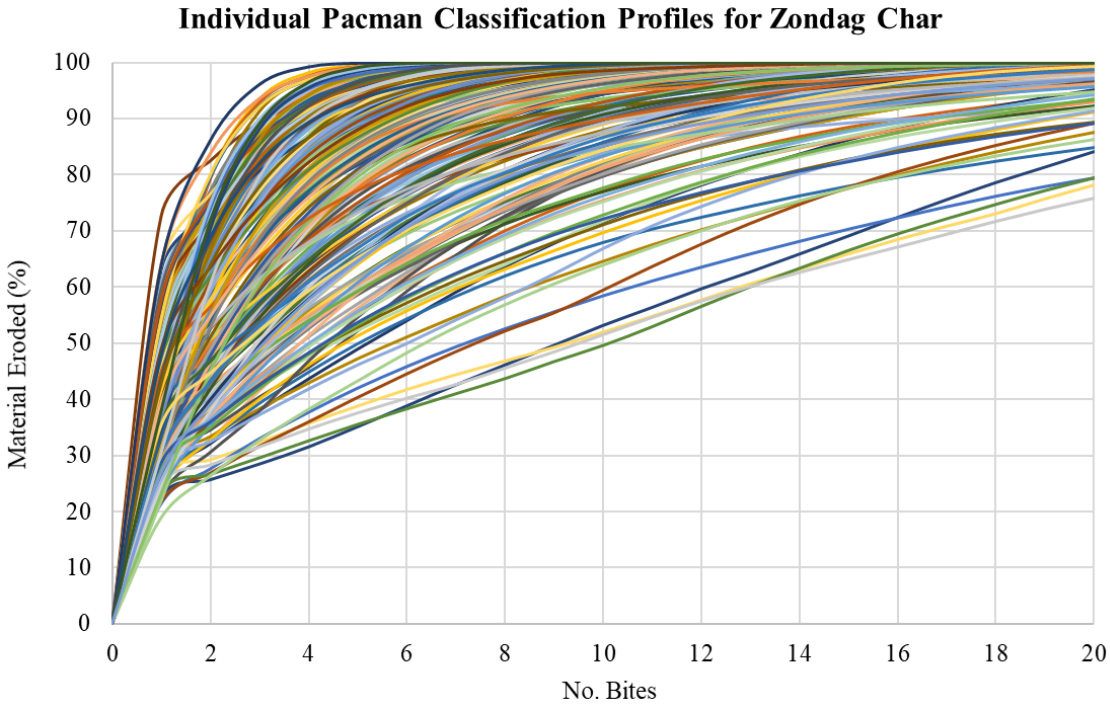
Appended Figure B.13 - *Individual Pacman Erosion Profiles for Welsh 1 Char sample*



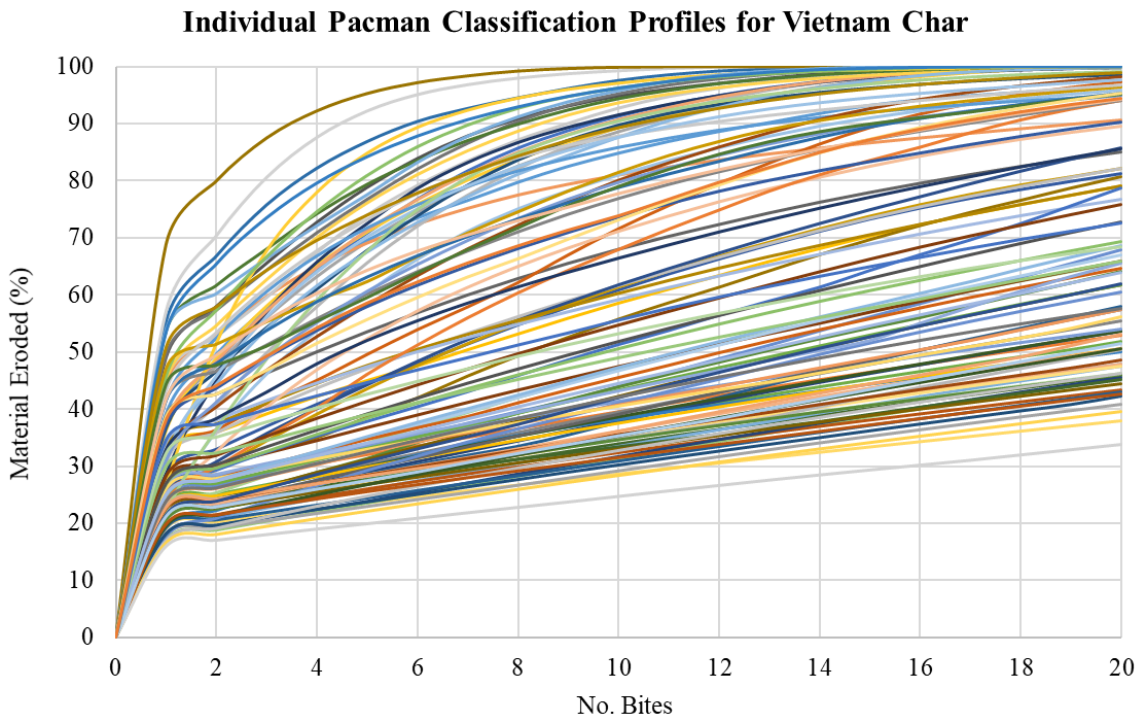
Appended Figure B.14 - *Individual Pacman Erosion Profiles for Welsh 2 Char sample*



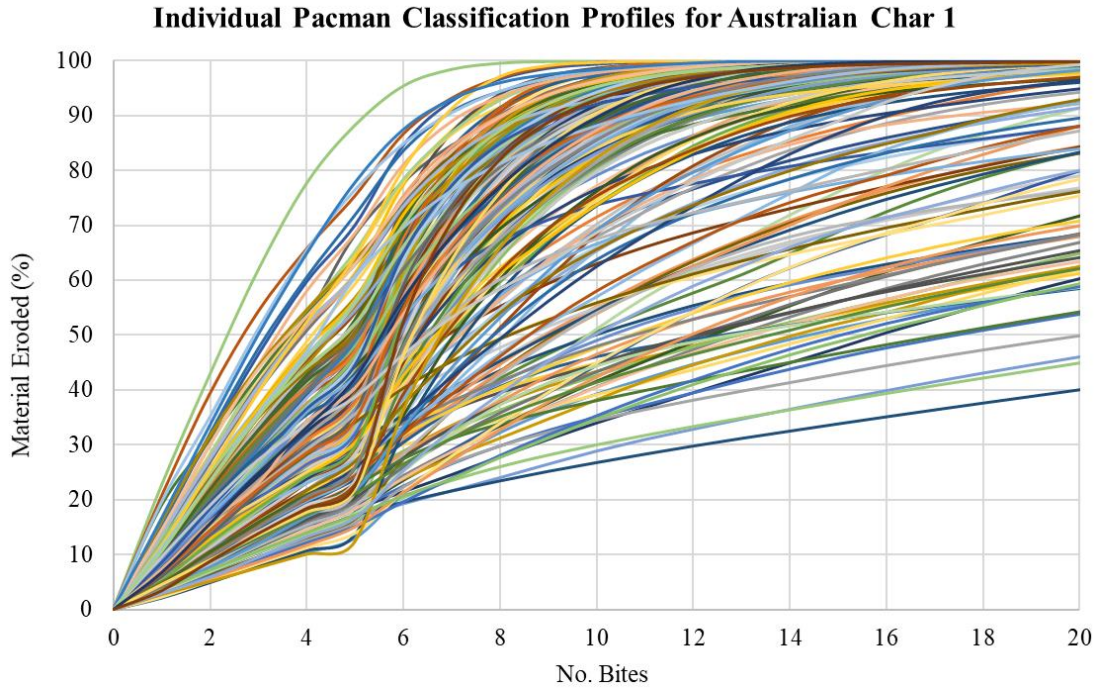
Appended Figure B.15 *- Individual Pacman Erosion Profiles for Russian Char sample*



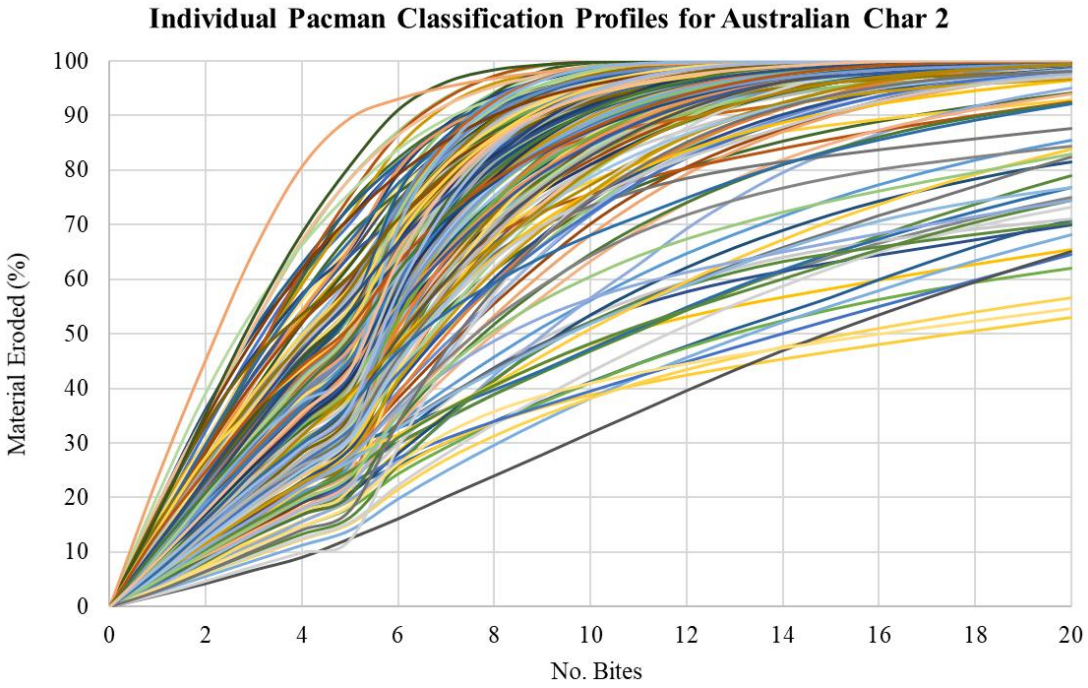
Appended Figure B.16 *- Individual Pacman Erosion Profiles for Zondag Char sample*



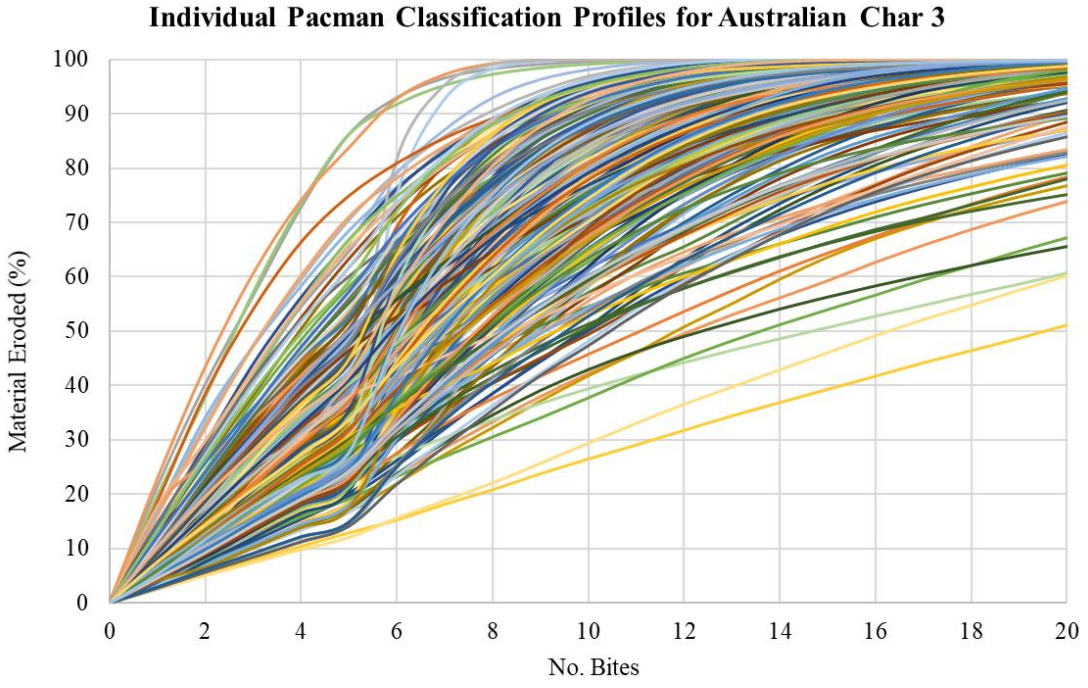
Appended Figure B.17 - *Individual Pacman Erosion Profiles for Vietnamese Char sample*



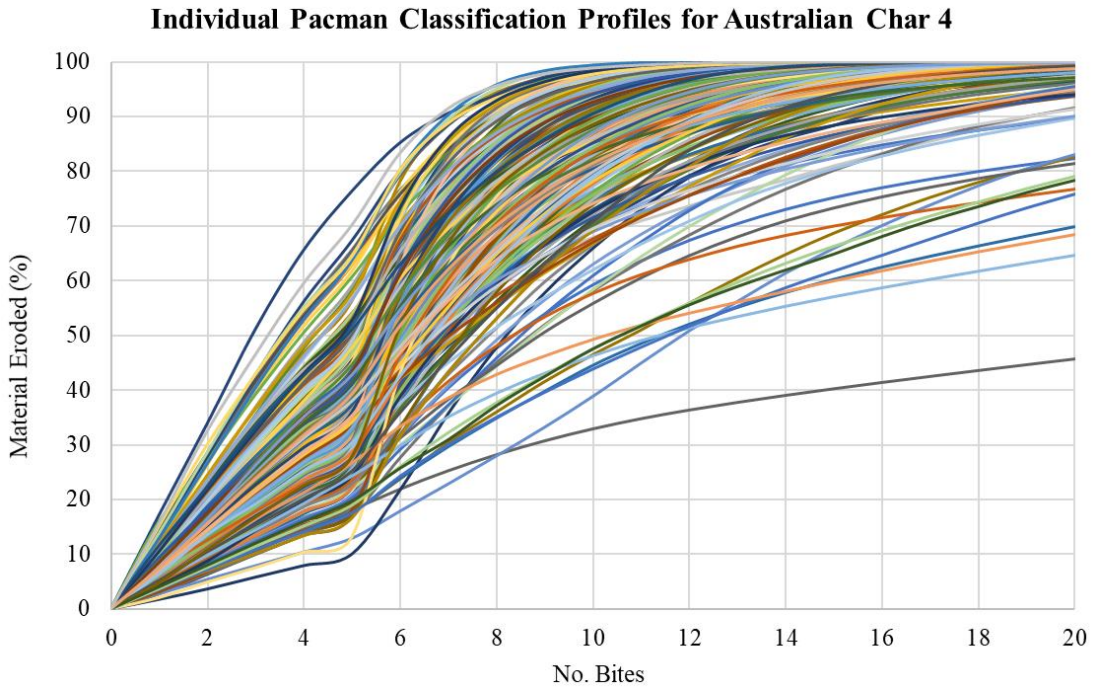
Appended Figure B.18 - *Individual Pacman Erosion Profiles for Australian Char 1 sample*



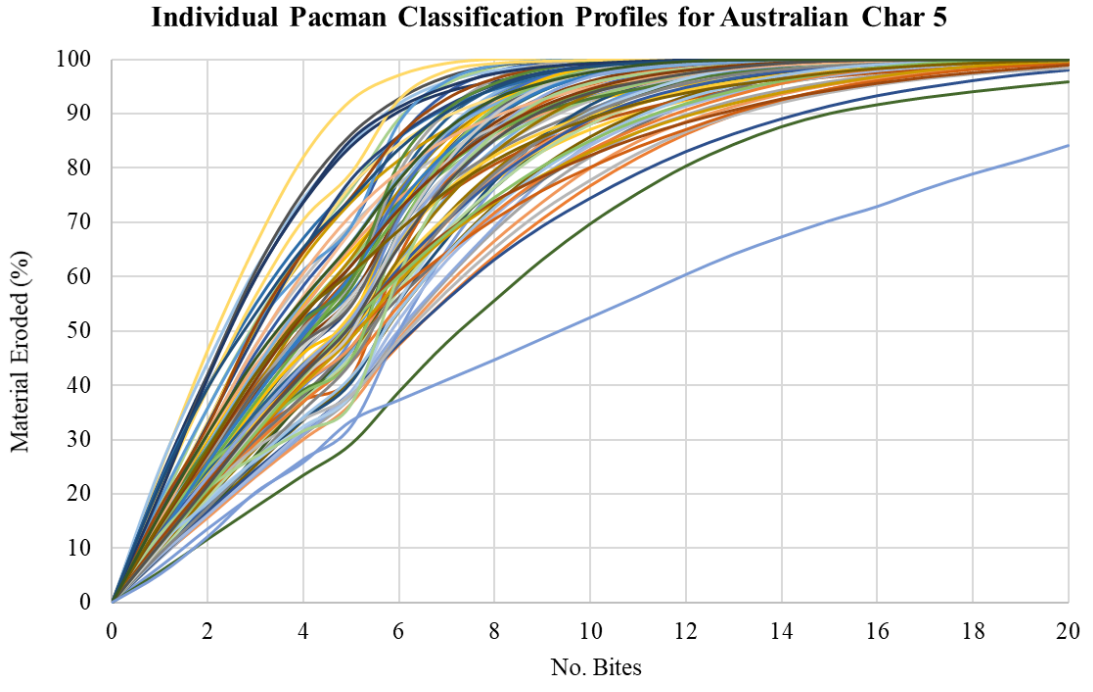
Appended Figure B.19 - *Individual Pacman Erosion Profiles for Australian Char 2 sample*



Appended Figure B.20 - *Individual Pacman Erosion Profiles for Australian Char 3 sample*



Appended Figure B.21 - *Individual Pacman Erosion Profiles for Australian Char 4 sample*



Appended Figure B.22 - *Individual Pacman Erosion Profiles for Australian Char 5 sample*

Appended Table B.1 – *Predicted vs Manual char morphologies for coal set 2 (106-125 µm)* ***M = manual/P = Predicted***

SAMPLE	CHAR MORPHOLOGY											
	TENUISPHERE		TENUINETWORK		CRASSISPHERE		CRASSINETWORK		FUSINOID		SOLID	
	M %	A%	M %	A%	M %	A%	M %	A%	M %	A%	M %	A%
1	6.0	5.8	6.0	11.6	35.1	38.8	27.5	20.7	18.8	14.5	6.6	8.7
2	3.4	9.5	14.0	11.6	47.3	44.6	16.7	15.1	12.9	13.3	5.7	6.0
3	14.3	7.3	9.0	6.5	46.8	50.4	16.5	19.5	10.0	13.7	3.4	2.7
4	9.2	5.9	10.2	5.9	55.2	68.2	8.8	10.6	14.4	9.0	2.2	0.4
5	35.1	38.5	9.8	4.4	53.9	53.8	1.0	2.2	0.2	0.0	0.0	1.1
INDONESIAN	0.5	0.0	22.8	29.7	5.4	2.7	46.5	45.9	14.9	18.9	9.9	2.7
OSTRAVA	8.0	7.6	6.0	5.1	44.6	51.9	16.3	12.7	21.1	19.0	4.0	3.8
EL CERREJON	27.2	33.9	6.0	3.4	55.2	52.5	8.8	5.1	2.4	1.7	0.4	3.4
VIETNEMESE	0.0	0.0	0.0	0.0	0.0	0.0	0.0	0.0	0.8	4.3	99.2	95.7

Program Script B.1 – Implementation of Otsu's Method

```
function threshold = otsu_2D(hists, total)
maximum = 0.0;
threshold = 0;
helperVec = 0:255;
mu_t0 = sum(sum(repmat(helperVec',1,256).*hists));
mu_t1 = sum(sum(repmat(helperVec,256,1).*hists));
p_0 = zeros(256);
mu_i = p_0;
mu_j = p_0;
for ii = 1:256
   for jj = 1:256
      if jj == 1
         if ii == 1
            p_0(1,1) = hists(1,1);
         else
            p_0(ii,1) = p_0(ii-1,1) + hists(ii,1);
            mu_i(ii,1) = mu_i(ii-1,1)+(ii-1)*hists(ii,1);
            mu_j(ii,1) = mu_j(ii-1,1);
         end
      else
         p_0(ii,jj) = p_0(ii,jj-1)+p_0(ii-1,jj)-p_0(ii-1,jj-1)+hists(ii,jj);
         mu_i(ii,jj) = mu_i(ii,jj-1)+mu_i(ii-1,jj)-mu_i(ii-1,jj-1)+(ii-1)*hists(ii,jj);
         mu_j(ii,jj) = mu_j(ii,jj-1)+mu_j(ii-1,jj)-mu_j(ii-1,jj-1)+(jj-1)*hists(ii,jj);
      end

      if (p_0(ii,jj) == 0)
         continue;
      end
      if (p_0(ii,jj) == total)
         break;
      end
      tr = ((mu_i(ii,jj)-p_0(ii,jj)*mu_t0)^2 + (mu_j(ii,jj)-
p_0(ii,jj)*mu_t1)^2)/(p_0(ii,jj)*(1-p_0(ii,jj)));

      if ( tr >= maximum )
         threshold = ii;
         maximum = tr;
      end
   end
end
```

Program Script B.2 – Individual Char Analysis and Classification

```
POROSITY = [1];
PORESIZEPERCENTAGE1 = [1];
THICKNESS_1 = [1];
THICKNESS_10 = [1];
THICKNESS_15 = [1];
DIFF12 = [1];
Size_1 = [1];

CharDataWhole = zeros(1, 22);
CharData = 0;
Table_Classification = table(POROSITY,
PORESIZEPERCENTAGE1,THICKNESS_1,DIFF12,THICKNESS_10,
THICKNESS_15, Size_1);

for A = 1:1000;

CharFilename = sprintf('Char_Sample (%d).png', A);
  fullFileName = fullfile(pwd, CharFilename);
  if exist(fullFileName, 'file')
    Char_Particle = imread(fullFileName);
  else
     continue
  end

  tf = isa(Char_Particle,'logical');
   if tf == 0;
  Char_Particle = rgb2gray(Char_Particle);
  Char_Particle = imbinarize(Char_Particle);
  Char_Particle_Logical = addborder(Char_Particle, 5, 0, 'outer');
  Char = im2uint8(Char_Particle_Logical);
   else
      Char_Particle_Logical = addborder(Char_Particle, 5, 0, 'outer');
      Char = im2uint8(Char_Particle_Logical);
   end

Char_Particle_Logical = bwareaopen(Char_Particle_Logical,25);
Char_ParticleBin = Char_Particle_Logical;
numberOfPixels = numel(Char_ParticleBin);
numberOfTruePixels = sum(Char_ParticleBin(:));
n = numberOfTruePixels;
CharData = n;
n_0 = n;

% Mend Walls
mask = bwconvhull(Char_Particle_Logical, 'Union');
bw = activecontour(Char, mask, 500, 'edge','ContractionBias',0.03,
'SmoothFactor',0.2);
```

```
CharPerim = bwperim(bw, 8);
CharPerimDilate = imdilate(CharPerim, strel('disk',3));
Char_Mend = imfuse(Char_Particle_Logical,CharPerimDilate,'blend');

Char_Image = imbinarize(Char_Mend);


%Percentage Porosity Calculation

 % Get intial pixel count & save image
 numberOfTruePixels = sum(Char_Image(:));
 P1 = numberOfTruePixels;

 % Fill particle
 Filled_Char_Whole = imfill (Char_Image, 'holes');
 numberOfTruePixels = sum(Filled_Char_Whole(:));


 % Size Filter (60 um)
 Size = regionprops(Filled_Char_Whole,'MajorAxisLength');
 Size = struct2array(Size);
 Size_1 = max(Size);


 % Count pixels of porous vs filled chars
 P2 = numberOfTruePixels;
 PorosityCalc = (P2-P1)/P2;
 POROSITY = PorosityCalc*100;
 CharArea = bwarea(Filled_Char_Whole);


% ***PORE ANALYSIS - Mean Pore Size, Feret Max & Roundness***
 se = strel('disk',75);
 Char_Image2 = imclose(Char_Image,se);

% Fill & Invert Whole Char Image for background identification
 Char_Image_Whole_Background = imfill(Char_Image2, 'holes');
 Char_Image_Whole_Background = ~Char_Image_Whole_Background;
 Char_Image_Whole_Background = 1-Char_Image_Whole_Background;
 Char_Image_Whole_Background_Invert = (Char_Image_Whole_Background == 0);

% Invert just Char Wall for pore identification
 Char_Image2 = ~Char_Image2;
 Char_Image2 = 1-Char_Image2;
 Char_Image_Whole_Invert = (Char_Image2 == 0);

% Overlay the background and char images and burn together
 Pores_Only = imoverlay (Char_Image2, Char_Image_Whole_Background_Invert,
'white');
```

```
Pores_Only = rgb2gray(Pores_Only);
Pores_Only = imbinarize (Pores_Only);

% Invert Back & Label pores for measurement
Pores_Only = ~Pores_Only;
Pores_Only = 1-Pores_Only;
Pores_Only_Invert = (Pores_Only == 0);
Pores_Only_Invert = bwareaopen(Pores_Only_Invert, 30);
Pore_Measurements = regionprops('table',Pores_Only_Invert,'All');
Number_Pores = size(Pore_Measurements, 1);

t = regionprops('table',Pores_Only_Invert,'Area');
LargestPoreValues = table2array(t);

Array_High_1 = maxk(LargestPoreValues,1,1);
TF = isempty(Array_High_1);
if TF == 1
PORESIZEPERCENTAGE1 = 0;
else
Table_High_1 = array2table(Array_High_1,'VariableNames',{'Area'});
Mean_Pore_Size = mean(Table_High_1.Area);
PORESIZEPERCENTAGE1 = (Mean_Pore_Size/P2)*100;
end


% Pacman Method 1
for k = 1:1
CharMask = bwconvhull(Char_ParticleBin, 'Union');
SegmentedChar = activecontour(Char, CharMask, 300, 'edge','ContractionBias',0.2,
'SmoothFactor',0.2);
CharPerimeter = bwperim(SegmentedChar, 8);
CharPerimeterDilate = imdilate(CharPerimeter,strel('disk',21));
Segout = Char;
Segout(CharPerimeterDilate) = 0;
CharNew = cat(1, Segout);
CharNewBin = imbinarize(CharNew);
numberOfPixels = numel(CharNewBin);
numberOfTruePixels = sum(CharNewBin(:));
n = numberOfTruePixels;
CharData = [CharData, n];
Char = CharNew;
Char_ParticleBin = imbinarize(Char);

end

% Pacman Method 2
for k = 1:20
CharMask = bwconvhull(Char_ParticleBin, 'Union');
SegmentedChar = activecontour(Char, CharMask, 300, 'edge','ContractionBias',0.8,
'SmoothFactor',0.2);
```

```
CharPerimeter = bwperim(SegmentedChar, 8);
CharPerimeter = imdilate(CharPerimeter,strel('disk',2));
Segout = Char_ParticleBin;
Segout(CharPerimeter) = 0;
CharNew = cat(1, Segout);

numberOfPixels = numel(CharNew);
numberOfTruePixels = sum(CharNew(:));
n = numberOfTruePixels;
CharData = [CharData, n];
Char_ParticleBin = CharNew;
end
CharDataWhole_TS = [CharDataWhole_TS;CharData];

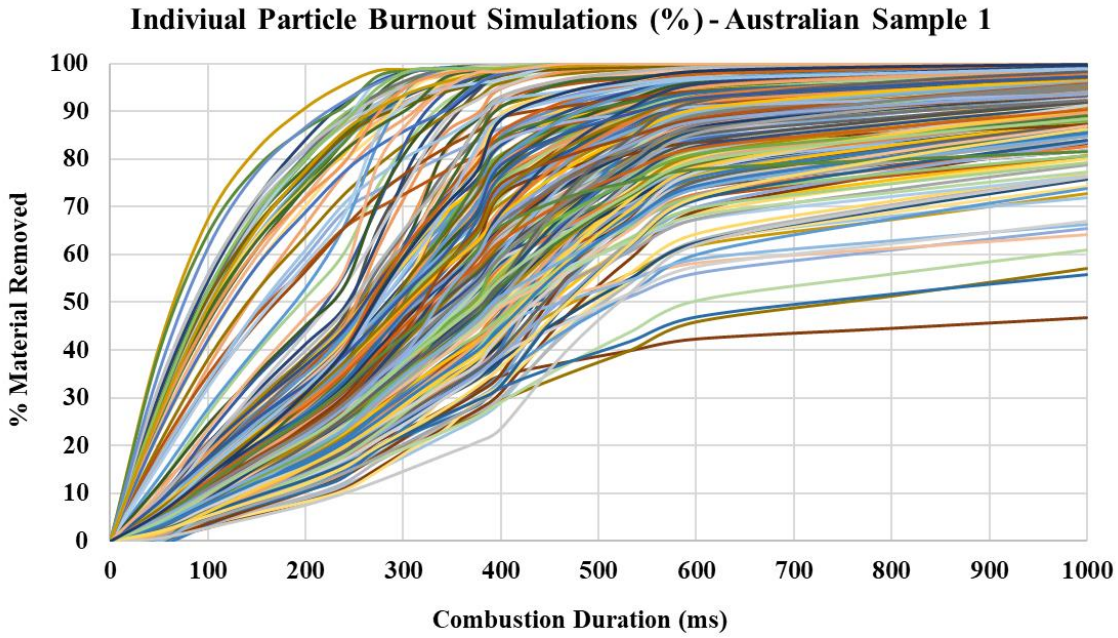
n_1 = CharData(2);
n_2 = CharData(3);
n_10 = CharData(11);
n_15 = CharData(16);

THICKNESS_1 = (n_1/n_0)*100;
THICKNESS_2 = (n_2/n_0)*100;
THICKNESS_10 = (n_10/n_0)*100;
THICKNESS_15 = (n_15/n_0)*100;
DIFF12 = THICKNESS_1-THICKNESS_2;

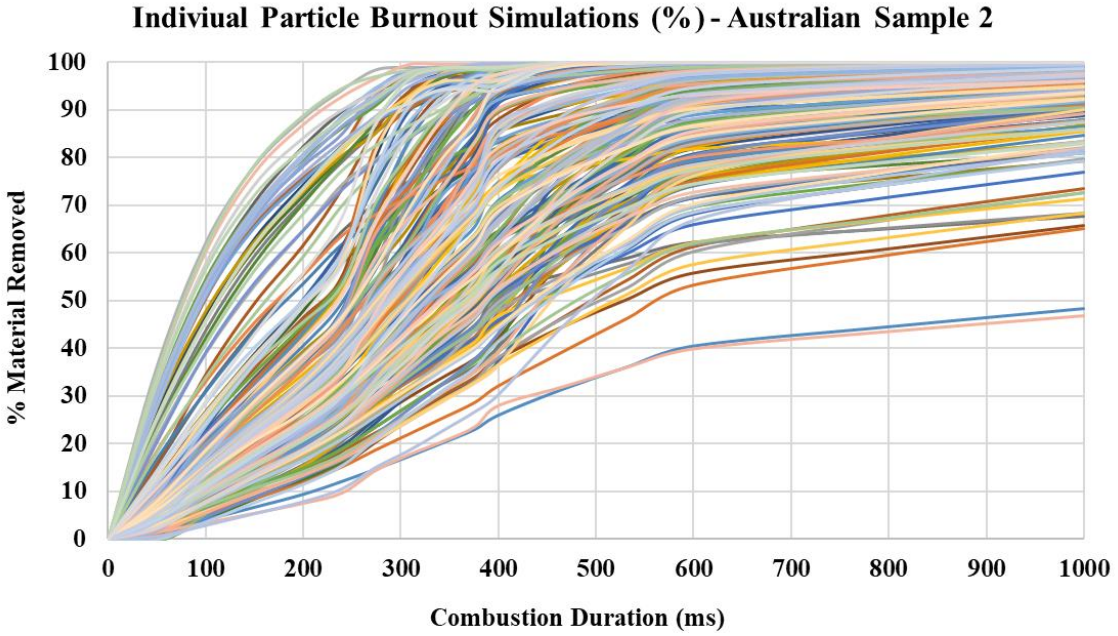

% Construct dataset and run logic tree
Table_Classification = table(POROSITY,
PORESIZEPERCENTAGE1,THICKNESS_1,DIFF12,THICKNESS_10,
THICKNESS_15, Size_1);
Table_Classification = [Table_Classification; Table_Classification];
yfit = Char_Classification_Tree.predictFcn(Table_Classification);
Class = double(yfit);
dlmwrite('X.txt',Class,'-append','delimiter','','roffset',1);
type('X.txt');
Char_Classification = dlmread('X.txt');

end
```

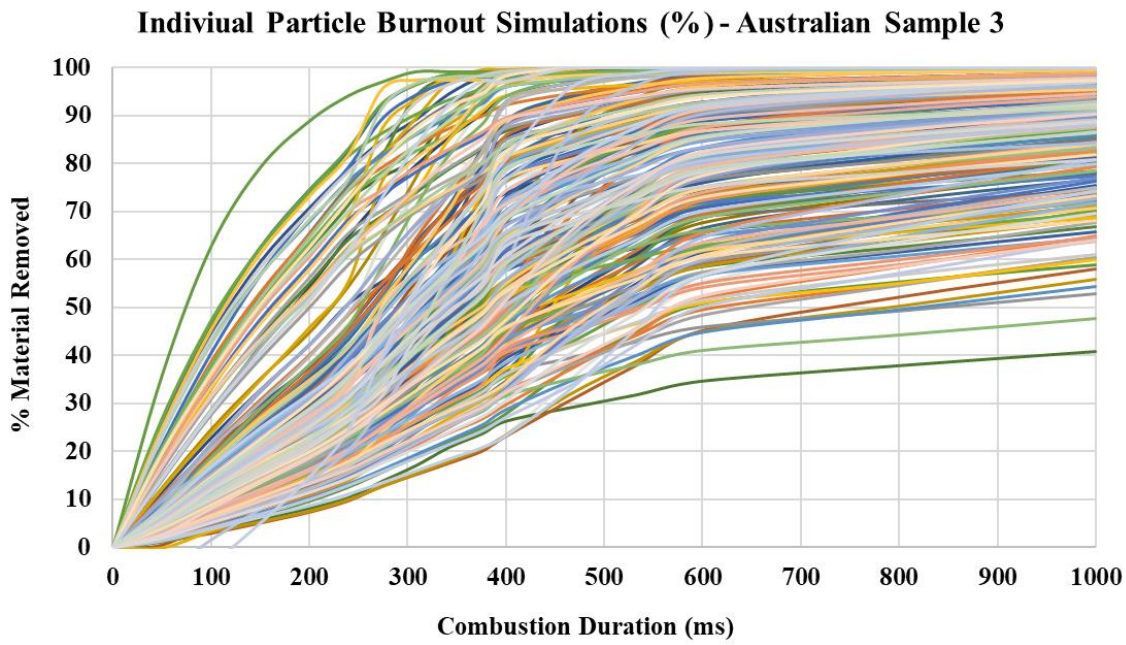
Appendix C. Burnout Simulation Profiles



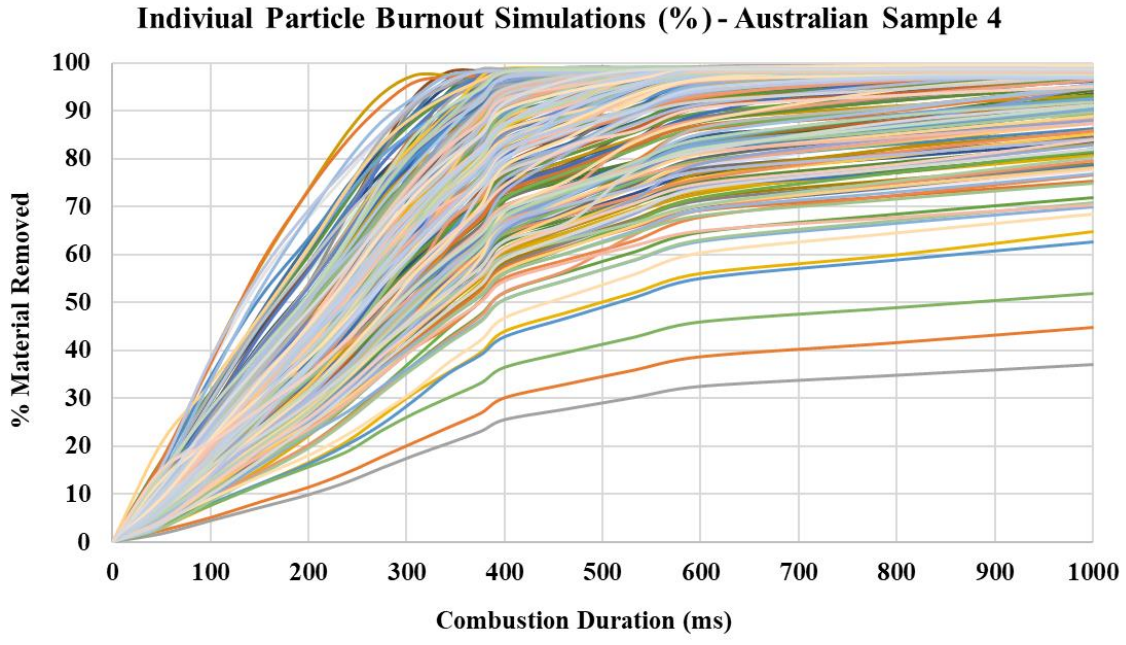
Appended Figure C.1 *– Individual particle percentage burnouts for Australian sample 1*



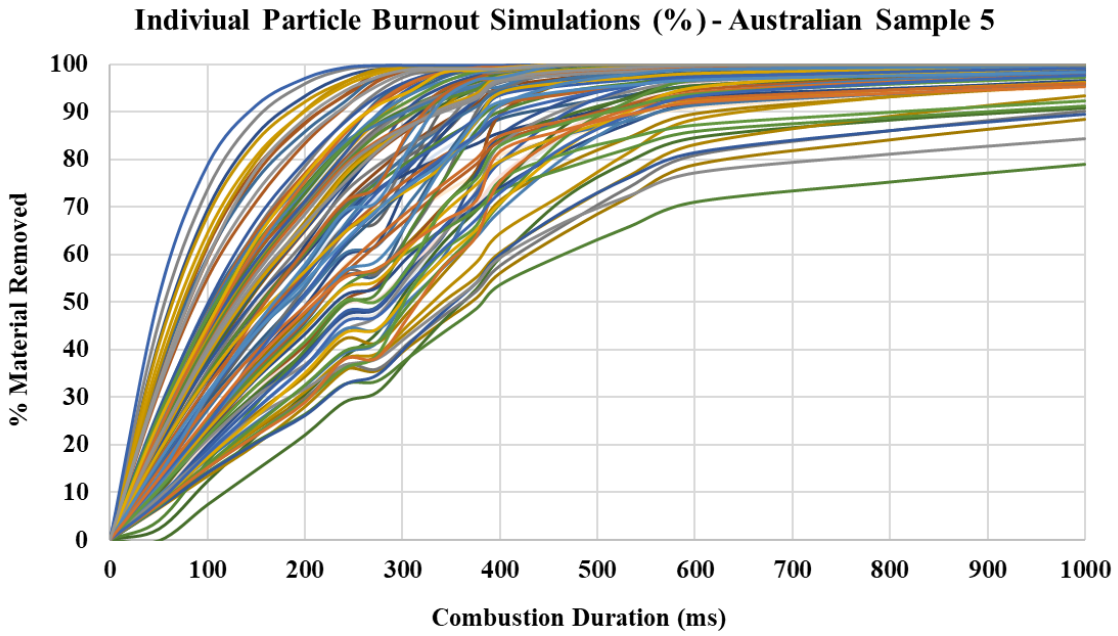
Appended Figure C.2 *– Individual particle percentage burnouts for Australian sample 2*



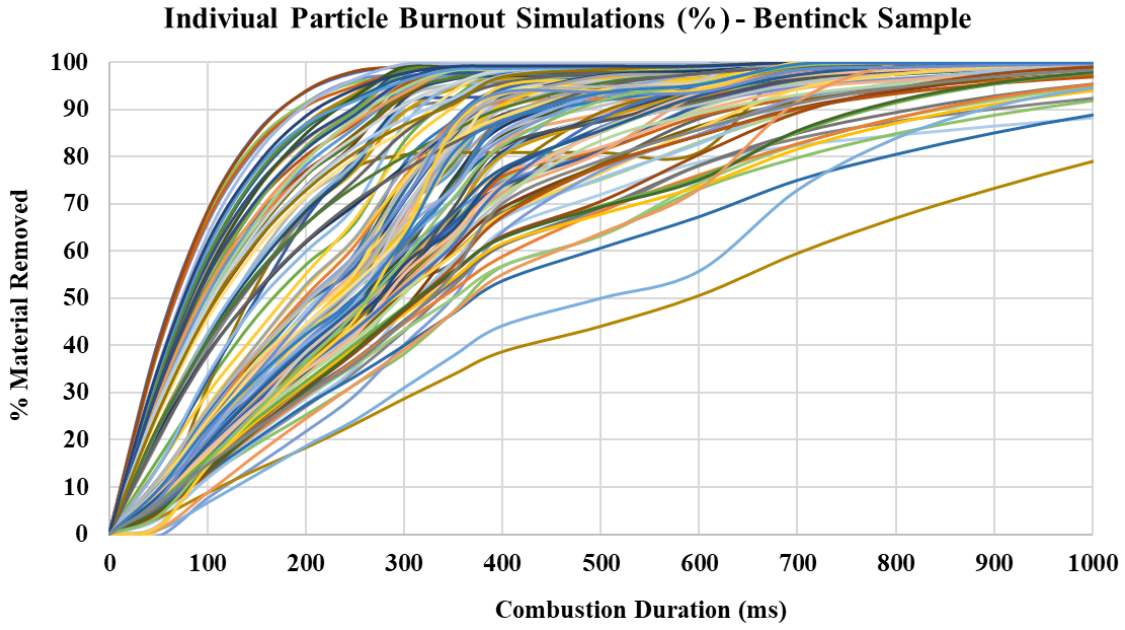
Appended Figure C.3 *– Individual particle percentage burnouts for Australian sample 3*



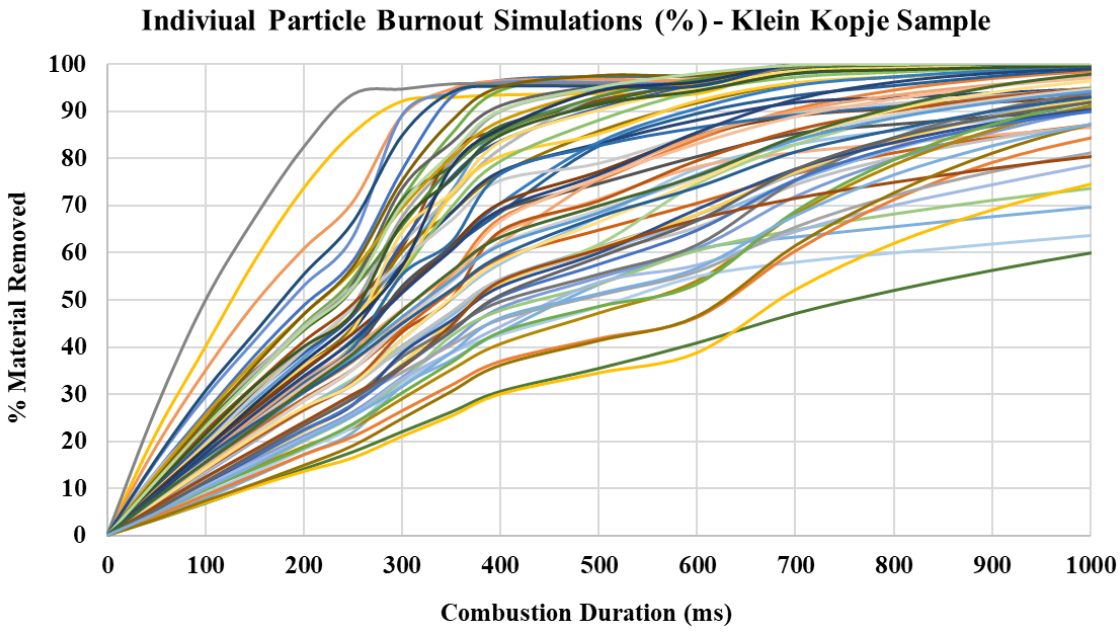
Appended Figure C.4 *– Individual particle percentage burnouts for Australian sample 4*



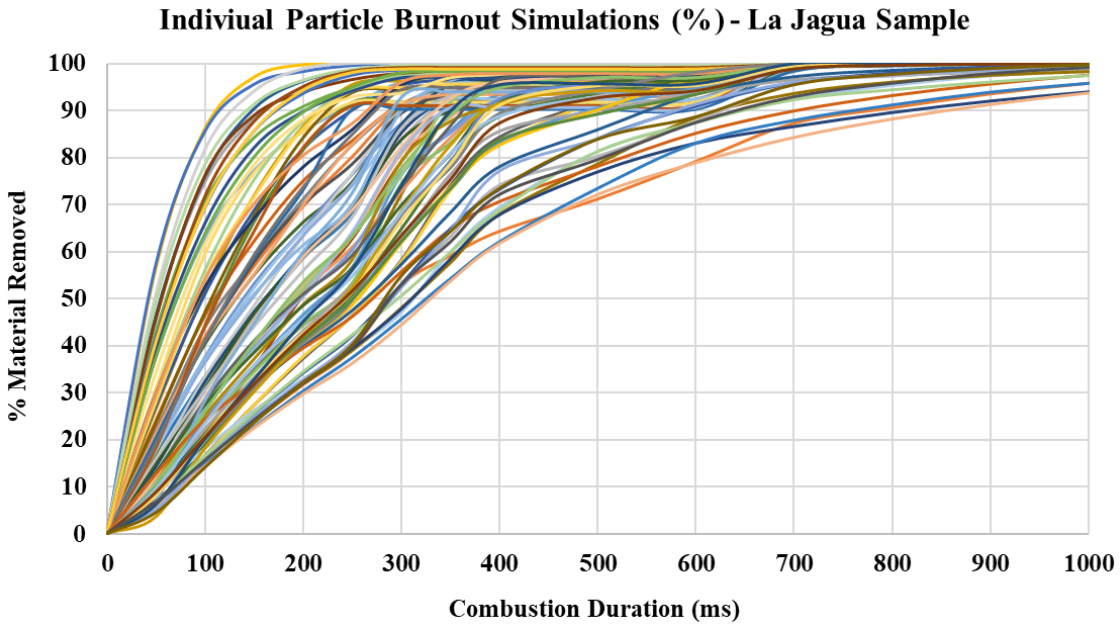
Appended Figure C.5 *– Individual particle percentage burnout for Australian sample 5*



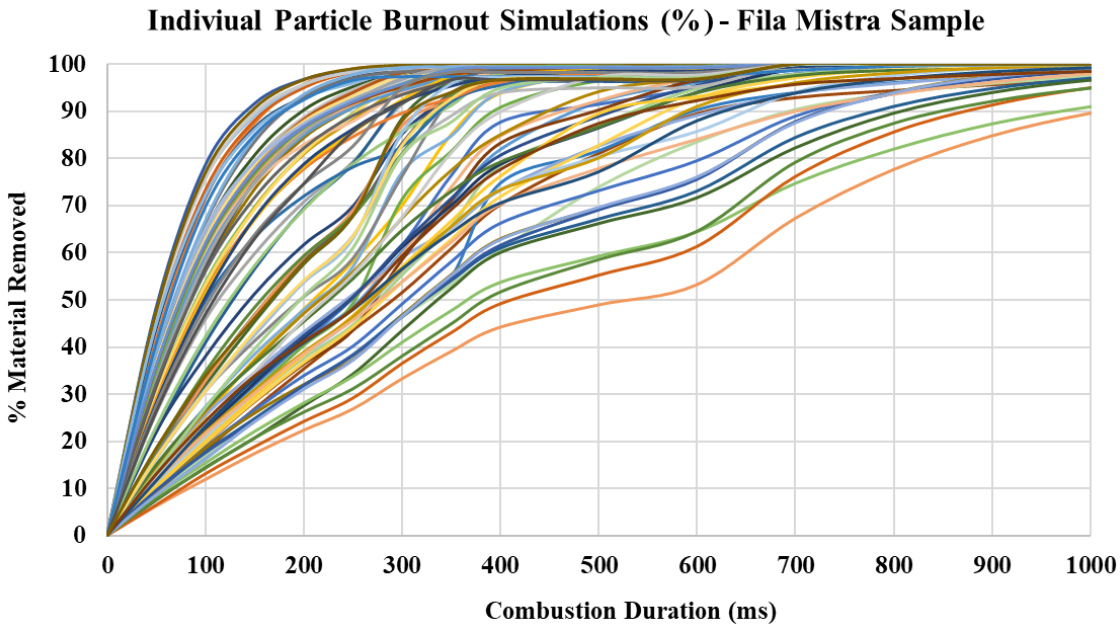
Appended Figure C.6 *– Individual particle percentage burnout for Bentinck sample*



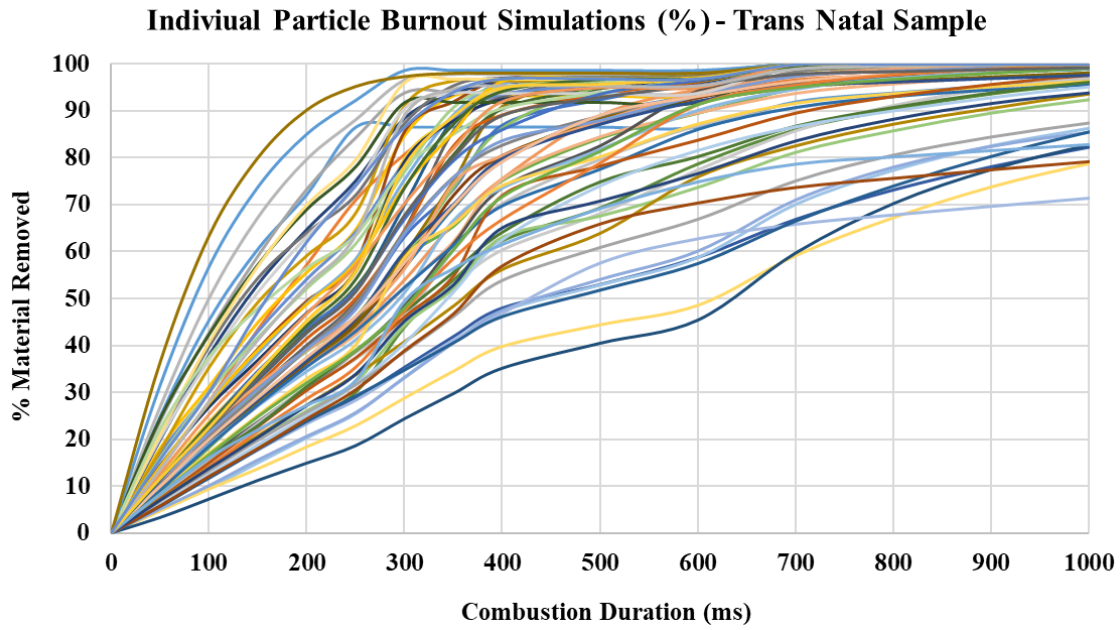
Appended Figure C.7 *– Individual particle percentage burnout for Klein Kopje sample*



Appended Figure C.8 *– Individual particle percentage burnout for La Jagua sample*



Appended Figure C.9 *– Individual particle percentage burnout for Fila Mistra Sample*



Appended Figure C.10 *– Individual particle percentage burnout for Trans Natal Sample*

Program Script C.1 – Burnout Simulation Script

```
CharDataWhole_X = zeros(1, 16);
CharData = 0;

% Char Particle upload & burnout simulation loop
for A = 1: Number_of_Particles;

CharFilename = sprintf('X_Particle%d.png', A);
  fullFileName = fullfile(pwd, CharFilename);
  if exist(fullFileName, 'file')
    Char_Particle = imread(fullFileName);
  else
      continue
  end

  tf = isa(Char_Particle,'logical');
   if tf == 0
  Char_Particle = rgb2gray(Char_Particle);
  Char_Particle = imbinarize(Char_Particle);
  Char_Particle_Logical = addborder(Char_Particle, 5, 0, 'outer');
  Char = im2uint8(Char_Particle_Logical);
   else
       Char_Particle_Logical = addborder(Char_Particle, 5, 0,
'outer');
       Char = im2uint8(Char_Particle_Logical);
   end

Char_Particle_Logical = bwareaopen(Char_Particle_Logical,25);
Char_ParticleBin = Char_Particle_Logical;
numberOfPixels = numel(Char_ParticleBin);
numberOfTruePixels = sum(Char_ParticleBin(:));

% Initial Pixel Count
n = numberOfTruePixels;
CharData = n;
n_0 = n;

% Morphology assessment section - Mend Char Walls + Determine
Sphere/Other
mask = bwconvhull(Char_Particle_Logical, 'Union');
bw = activecontour(Char, mask, 500, 'edge','ContractionBias',0.03,
'SmoothFactor',0.2);
CharPerim = bwperim(bw, 8);
CharPerimDilate = imdilate(CharPerim, strel('disk',3));
Char_Mend = imfuse(Char_Particle_Logical,CharPerimDilate,'blend');
Char_Image = imbinarize(Char_Mend);
% Get intial pixel count & save image
  numberOfTruePixels = sum(Char_Image(:));
  P1 = numberOfTruePixels;
  % Fill particle
  Filled_Char_Whole = imfill (Char_Image, 'holes');
  numberOfTruePixels = sum(Filled_Char_Whole(:));
  % Size Filter (60 um)
  Size = regionprops(Filled_Char_Whole,'MajorAxisLength');
  Size = struct2array(Size);
  Size_1 = max(Size);
  % Count pixels of porous vs filled chars
  P2 = numberOfTruePixels;
```

```
  PorosityCalc = (P2-P1)/P2;
  POROSITY = PorosityCalc*100;
  CharArea = bwarea(Filled_Char_Whole);
se = strel('disk',75);
Char_Image2 = imclose(Char_Image,se);
Char_Image_Whole_Background = imfill(Char_Image2, 'holes');
Char_Image_Whole_Background = ~Char_Image_Whole_Background;
Char_Image_Whole_Background = 1-Char_Image_Whole_Background;
Char_Image_Whole_Background_Invert = (Char_Image_Whole_Background ==
0);
Char_Image2 = ~Char_Image2;
Char_Image2 = 1-Char_Image2;
Char_Image_Whole_Invert = (Char_Image2 == 0);
Pores_Only = imoverlay (Char_Image2,
Char_Image_Whole_Background_Invert, 'white');
Pores_Only = rgb2gray(Pores_Only);
Pores_Only = imbinarize (Pores_Only);
Pores_Only = ~Pores_Only;
Pores_Only = 1-Pores_Only;
Pores_Only_Invert = (Pores_Only == 0);
Pores_Only_Invert = bwareaopen(Pores_Only_Invert, 30);
Pore_Measurements = regionprops('table',Pores_Only_Invert,'All');
Number_Pores = size(Pore_Measurements, 1);
t = regionprops('table',Pores_Only_Invert,'Area');
LargestPoreValues = table2array(t);
  Array_High_1 = maxk(LargestPoreValues,1,1);
  TF = isempty(Array_High_1);
  if TF == 1
  PORESIZEPERCENTAGE1 = 0;
  else
  Table_High_1 = array2table(Array_High_1,'VariableNames',{'Area'});
  Mean_Pore_Size = mean(Table_High_1.Area);
  PORESIZEPERCENTAGE1 = (Mean_Pore_Size/P2)*100;
  end


if PORESIZEPERCENTAGE1 >35;
  for k = 1:5
CharMask = bwconvhull(Char_ParticleBin, 'Union');
SegmentedChar = activecontour(Char, CharMask, 300,
'edge','ContractionBias',1.0, 'SmoothFactor',0.2);
CharPerimeter = bwperim(Char_Image_Fill, 8);
%CharPerimeter = imdilate(CharPerimeter,strel('disk',2));
Segout = Char_ParticleBin;
Segout(CharPerimeter) = 0;
CharNew = cat(1, Segout);

numberOfPixels = numel(CharNew);
numberOfTruePixels = sum(CharNew(:));
n = numberOfTruePixels;
CharData = [CharData, n];
Char_ParticleBin = CharNew;
Char_ParticleBin = bwareaopen(Char_ParticleBin, 25);
  end
Char = im2uint8(Char_ParticleBin);
else
for k = 1:5
CharMask = bwconvhull(Char_ParticleBin, 'Union');
SegmentedChar = activecontour(Char, CharMask, 300,
'edge','ContractionBias',0.05, 'SmoothFactor',0.2);
CharPerimeter = bwperim(SegmentedChar, 8);
```

```
CharPerimeterDilate = imdilate(CharPerimeter,strel('disk',3));
Segout = Char;
Segout(CharPerimeterDilate) = 0;
CharNew = cat(1, Segout);
CharNewBin = imbinarize(CharNew);
numberOfPixels = numel(CharNewBin);
numberOfTruePixels = sum(CharNewBin(:));
n = numberOfTruePixels;
CharData = [CharData, n];
Char = CharNew;
Char_ParticleBin = imbinarize(Char);
Char_ParticleBin = bwareaopen(Char_ParticleBin, 25);
end
end


for k = 1:5
CharMask = bwconvhull(Char_ParticleBin, 'Union');
SegmentedChar = activecontour(Char, CharMask, 300,
'edge','ContractionBias',a, 'SmoothFactor',0.2);
CharPerimeter = bwperim(SegmentedChar, 8);
CharPerimeterDilate = imdilate(CharPerimeter,strel('disk',2));
Segout = Char;
Segout(CharPerimeterDilate) = 0;
CharNew = cat(1, Segout);
CharNewBin = imbinarize(CharNew);
numberOfPixels = numel(CharNewBin);
numberOfTruePixels = sum(CharNewBin(:));
n = numberOfTruePixels;
CharData = [CharData, n];
Char = CharNew;
Char_ParticleBin = imbinarize(Char);
Char_ParticleBin = bwareaopen(Char_ParticleBin, 25);
end

for k = 1:5
Char_Image_Fill = imfill(Char_ParticleBin, 'holes');
CharPerimeter = bwperim(Char_Image_Fill, 8);
Segout = Char_ParticleBin;
Segout(CharPerimeter) = 0;
CharNew = cat(1, Segout);

numberOfPixels = numel(CharNew);
numberOfTruePixels = sum(CharNew(:));
n = numberOfTruePixels;
CharData = [CharData, n];
Char_ParticleBin = CharNew;
Char_ParticleBin = bwareaopen(Char_ParticleBin, 25);
end
CharDataWhole_X = [CharDataWhole_X;CharData];
end
```